Unlocking planetesimal histories using refined thermal evolution and dynamo generation models

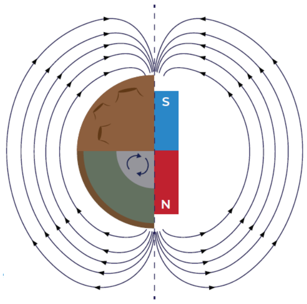

Hannah Sanderson

Exeter College

University of Oxford

A thesis submitted for the degree of

Doctor of Philosophy

July 2025

+ΡՐՐE ΛᚹΔE

For my wife

Acknowledgements

Firstly, huge thanks go to my supervisors James Bryson and Claire Nichols for guiding and supporting me throughout my DPhil. Thank you for always asking ‘why?’, pointing out weird things in my plots, and making me think about the bigger picture. I have appreciated the balance between freedom to explore my own ideas and your regular constructive feedback. You have challenged and encouraged me to become a better scientist in every way. I have really enjoyed working with you and look forward to continuing to collaborate.

As well as my supervisors, I have been very fortunate to have many mentors who have given me valuable scientific and career advice. Thank you to Adina Pusok, Amy Bonsor, Andrew Walker, Clara Maurel, Conall MacNiocaill, Francis Nimmo, Ina Plesa, Laura Rogers, Maylis Landeau, and Rich Katz. A special mention goes to Chris Davies for his painstaking and constructive feedback on my dynamo generation model that underpins this thesis. Also particular thanks goes to Kathryn Dodds for explaining her model in so much detail at the beginning of my DPhil, looking out for me at conferences, and listening to my complaints about coding bugs. Hopefully we can be involved in more ‘misadventures’ together!

I have learnt so much from the research group meetings I have attended during my DPhil: Early Earth and Planetary, Foalab and Computational Geoscience. I really appreciate everyone in these research groups for answering my many questions, for teaching me about such a wide range of research, and for giving me feedback on my work. When I eventually have my own research group, I hope to emulate aspects of all these groups. Extra thanks go to the Early Earth and Planetary Group for creating such a supportive atmosphere in group meetings (and for baking lots of tasty cake).

While my research focuses on tiny, ancient, space rocks, I wanted to stay connected to the wider world. Thanks to Sarah Hilton for helping me create my outreach workshop and to Charlie Rex for helping me to deliver it to as many schools as possible. Every time I see a school student get excited about planets, it reminds me how cool my job is. I’m also grateful for all the teaching experiences I’ve had during my doctorate and for my students for engaging with my enthusiasm about everything from vector fields to pillow basalts. Co-founding and co-leading the LGBTQIA+ affinity

group alongside Rebecca Colquhoun, gave me the chance to make the department a more inclusive place. Thank you so much to Rebecca for taking on this challenge with me and to Laura Stevens for supporting us throughout. Thanks to all affinity group members past and present — you are great friends and the group would literally not exist without you.

There are many people who helped me remember there was life outside my thesis. Huge thanks to office 20.17: ‘it’s nice to be around human remains again’ Ally; ‘progress is being made but at the cost of my sanity’ Harri; ‘everyone gets the butts’ Kate; ‘next time I have a dream about lithium I may cry’ Lewis; and ‘life can’t always be roses and dandelions’ Lot. Our quote wall, tea breaks, football chats, and research rants made me excited to come to the office every day. Also, thanks Bei Bei, Bram, Hamish, Jeanette, Nikki, Rebecca, Rhiannon, Sarah, Sofia, Vicky, Vikki, and many others for the coffee and lunch time chats, ice-cream trips, climbing adventures, conference antics, and board games nights. I’m also lucky to have had the support of my friends outside of Oxford, who could remind me about life outside the DPhil bubble. Playing for East Oxford Football Club and Oxford University Wheelchair Basketball Club was also a vital way to destress.

Finally, I could not have completed this DPhil without the support of my immediate and extended family. Fiona, I’m so grateful that our DPhils finally allowed us to move in together (and get married!). Thank you for putting up with all of my unnecessary stress, being a sounding board for all my work dilemmas, and for reminding me to be silly sometimes. Eleanor, thank you for putting up with your infuriatingly nerdy older sister and always being there for me. Mum and Dad, thank you for supporting my interest in space from such a young age and always trying your best to understand my research. I may not want to be an astronaut anymore, but being a planetary scientist is even better (and a lot less stressful for Mum than me being strapped to a rocket!).

Funding This research was funded by a NERC studentship (NE/S007474/1) and an Exonian Graduate Scholarship from Exeter College. I would also like to thank the Royal Astronomical Society and Exeter College for student travel grants that enabled me to attend multiple conferences during my DPhil.

Abstract

Accreting in the first few million years of the Solar System, planetesimals recorded conditions in the protoplanetary disk and formed the building blocks of the rocky planets. The meteorite paleomagnetic record carries key insights into the thermal history of planetesimals and their extent of differentiation. In this thesis, I use thermal evolution and dynamo generation models to translate meteorite magnetisations into planetesimal properties.

I begin by presenting a new 1D planetesimal thermal evolution and dynamo generation model. This magnetic field generation model is the first of a differentiated, mantled planetesimal that includes both mantle convection and sub-eutectic core solidification. It reconsiders previous assumptions about mantle convection, mantle viscosity, and core solidification, and includes a unified description of dynamo generation by thermal and compositional convection.

I first utilise this model to explore the effect of mantle viscosity, core composition and planetesimal size on dynamo generation. I find that variations in these properties lead to more variable timings of different planetesimal magnetic field generation mechanisms than previously thought. As a result, the meteorite paleomagnetic record cannot be split into three distinct epochs (nebula field, thermal dynamos, compositional dynamos). This alters the information we can glean from the meteorite paleomagnetic record about the early Solar System.

Next, I predict possible differences in dynamo generation for inner and outer Solar System planetesimals by exploring the effect of mantle water content and core size on dynamo generation. I find a stark contrast in magnetic field histories between dry, reduced and wet, oxidised planetesimals. Comparison with the existing paleomagnetic record suggests inner Solar System planetesimals formed in moderately reducing conditions and degassed water efficiently during differentiation. Future measurements of outer Solar System meteorites could determine whether planetesimals in this region formed in more oxidising conditions and retained more water during differentiation.

Finally, I utilise the time-resolved paleomagnetic records of the Main Group pallasites and IIE irons to determine their parent body properties. I find that these bodies were likely large with approximately equal core and mantle thicknesses, and

these meteorites originated from close to the surface. As a result, these meteorites consisting of both metal and silicate are more likely to have formed via impacts than eruptions of core material into the mantle.

Overall, I combine refined thermal evolution and dynamo generation models with meteorite paleomagnetism to deepen our understanding of the evolution of planetesimals. Furthermore, I establish the potential of future meteorite paleomagnetic measurements combined with thermal modelling to reveal new insights about the protoplanetary disk, in which these planetary building blocks formed.

Statement of Originality

My thesis was supervised by James Bryson and Claire Nichols. For all chapters, I developed the methodology and software, produced the results and wrote the first drafts. They provided written and verbal feedback on chapter drafts. The following chapters have been published already.

Chapter 2: A refined, thermal evolution and dynamo generation model This chapter was originally published as H. R. Sanderson, J. F. J. Bryson, C. I. O. Nichols, and C. J. Davies, 'Unlocking planetesimal magnetic field histories: A refined, versatile model for thermal evolution and dynamo generation', Icarus, vol. 425, p. 116323, Jan. 2025, doi: 10.1016/j.icarus.2024.116323. Chris Davies provided written and verbal feedback on paper drafts.

Chapter 3: Early and elongated epochs of planetesimal dynamo generation This chapter was was originally published as H. R. Sanderson, J. F. J. Bryson, and C. I. O. Nichols, 'Early and elongated epochs of planetesimal dynamo generation', Earth and Planetary Science Letters, vol. 648, p. 119083, Dec. 2024, doi: 10.1016/j.epsl.2024.119083.

Portions of the introductions of these publications have been moved to Chapter 1 and the introductions of Chapters 2 and 3 have been amended to avoid repetition and to ensure a clear narrative throughout the thesis.

Contents

List of Figures

List of Tables

Chapter 1

Introduction

Internally-generated magnetic fields are widespread throughout the Solar System. All the planets, except Mars and Venus, as well as Jupiter's largest moon, Ganymede, generate a magnetic field at the present day (Stevenson, 2010; Soderlund et al., 2025). These magnetic fields provide unique insights into the composition, structure, and dynamics of planetary interiors. In the gas and ice giants, magnetic fields are thought to be generated in metallic hydrogen and superionic water layers, respectively, while in rocky planets and moons, these fields are generated in partially molten, iron-rich cores (Schubert and Soderlund, 2011; Soderlund et al., 2025). In all scenarios, the dynamo-generating region must be a fluid, in which flow is sufficiently vigorous to generate a magnetic field. Remanent magnetisations in rocks can shed light on earlier periods of magnetic field generation for terrestrial bodies. Samples from Apollo and Chang'e-5 and remote observations of the Moon (Wieczorek et al., 2022; Cai et al., 2025), and observations of Mars by missions, such as MAVEN and InSight (e.g., Mittelholz et al., 2018; Johnson et al., 2020b), have demonstrated that both bodies generated magnetic fields in their past. These magnetic records have raised questions about the thermal evolution of both these bodies. For example, what interior process drove the intermittent, high intensity magnetic field epoch on the Moon 3.5–3.9 Ga ago (Weiss and Tikoo, 2014; Evans and Tikoo, 2022; Jung et al., 2024)? Why is there a hemispherical dichotomy in Mars' crustal magnetisation (Mittelholz et al., 2020; Mittelholz and Johnson, 2022)?

This thesis focuses on interpreting magnetic fields recorded in meteorites — fragments of the earliest forming rocky bodies in the Solar System called planetesimals. Planetesimals were the building blocks of Earth and the other rocky planets, so their composition and interior evolution influenced final planetary compositions. For example, higher than expected abundances of highly siderophile elements in the Earth's mantle are attributed to the accretion of large, differentiated planetesimals at the tail end of Earth's accretion (e.g., Bottke et al., 2010; Marchi et al., 2018). Differentiated planetesimals have similar interiors to the rocky planets, but evolve on much more rapid timescales (millions rather than billions of years) due to their smaller sizes. Therefore, planetesimals provide an opportunity to understand the whole thermal evolution of a rocky body from high melt fraction at differentiation through to complete mantle and core solidification. Planetesimals also allow us to understand a wider range of thermal processes in rocky body interiors, because they experience stagnant lid convection rather than plate tectonics (Sterenborg and Crowley, 2012; Bryson et al., 2019a) as well as inward rather than outward core crystallisation (Gubbins, 1977; Williams, 2009; Dodds et al., 2025). Since dynamo generation depends on the structure and thermal state of a planetesimal's interior, meteorite magnetisations can reveal the extent of differentiation within planetesimals and the timescales of their thermal evolution. In this thesis, I use thermal evolution and dynamo generation models to interpret the meteorite paleomagnetic record enabling me to shed light on the interior structures and evolution of differentiated planetesimals, and the composition of the protoplanetary disk.

In this introduction, I will begin by defining a planetesimal and providing an overview of the meteorite record that we use to understand them (Section 1.1). I will then explain possible sources of meteorite magnetisations (Section 1.2.1), with a focus on planetesimal dynamo generation (Section 1.2.2). Next, I will describe the thermal evolution models used to understand planetesimal dynamo generation (Section 1.2.3) and summarise the results of previous studies. Finally, I will outline the key questions in this thesis and how they are addressed in subsequent chapters (Section 1.3).

1.1 Planetesimals and meteorites

1.1.1 Planetesimal and planet formation

The Sun formed from the gravitational collapse of part of a giant molecular cloud — a region of the galaxy with an increased density of gas and dust (McKee and Ostriker, 2007). After the formation of the Sun, the angular momentum of the remaining gas and dust flattened this material into a protoplanetary disk around the Sun (Williams and Cieza, 2011). The first solids to condense in the disk after the ignition of the Sun were highly refractory solids called calcium-aluminium inclusions (CAIs). Therefore, the formation time of CAIs is used as the reference time for the beginning of the Solar System (Connelly et al., 2012).

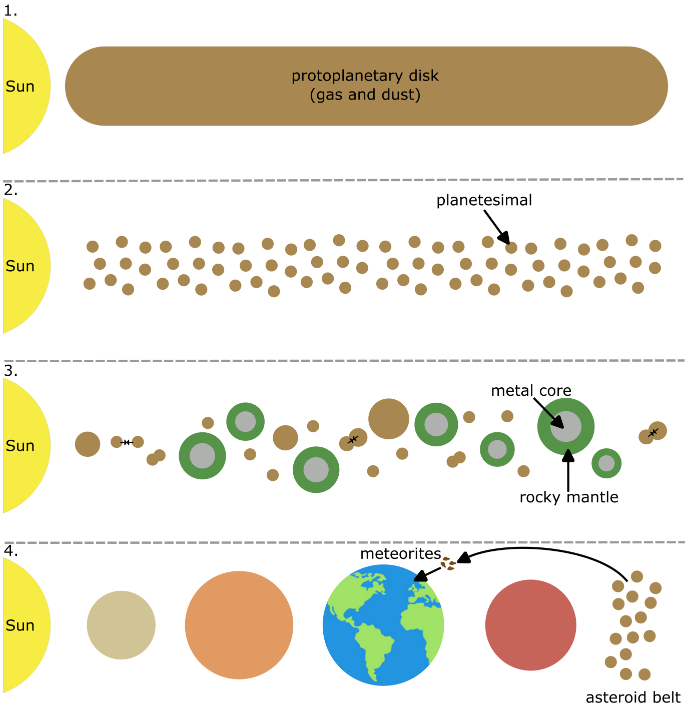

Figure 1.1: Schematic illustrating the relationship between planetesimals, planets, asteroids and meteorites.

Within the protoplanetary disk, processes such as radial drift (Drążkowska et al., 2016) and/or condensation lines (Drążkowska and Dullemond, 2018; Morbidelli et al., 2022) formed regions with an increased dust-to-gas ratio and high densities of pebbles (solids large enough to be marginally coupled to the gas; Drążkowska et al., 2022). Self-gravitating clumps of pebbles then collapsed due to a streaming instability to form ~ 100 km radius planetesimals (Johansen et al., 2014). Once formed, planetesimals underwent successive collisions and mergers to form larger planetesimals, the terrestrial planets (Morbidelli et al., 2025), and the cores for the formation of the gas and ice giants by pebble accretion (Lambrechts et al., 2014; Drążkowska et al., 2022).

1.1.2 Planetesimal interior structure

The interior structure of a planetesimal (Figure 1.2) is determined by its size and accretion time. To differentiate, a planetesimal must be large enough (> 100 km for differentiation via rain-out; Lichtenberg et al., 2021) to retain heat and have formed early enough to have sufficient heating from radiogenic ^{26}Al. Planetesimals that accreted < 1.5 million years (Ma) after CAI formation fully differentiated, while planetesimals that formed 1.5–2 Ma after CAI formation partially differentiated (Lichtenberg et al., 2019b; Monnereau et al., 2023). Gradual accretion also could have formed partially differentiated bodies with an 'onion shell' structure consisting of differentiated centres overlaid by layers of decreasingly thermally metamorphosed material (Elkins-Tanton et al., 2011; Weiss and Elkins-Tanton, 2013; Dodds et al., 2021). In bodies that accreted 2–4 Ma after CAI formation beyond the water condensation line, there was insufficient ^{26}Al for metal-silicate differentiation, but there was enough heat to melt water-ice, leading to aqueous alteration (Doyle et al., 2015; Courville et al., 2022). Collisions between planetesimals were frequent in the early Solar System (Asphaug, 2009) and also could have affected planetesimal interior structure. For instance, collisions could strip the mantle from a differentiated planetesimal (Asphaug and Reufer, 2014), mix the core of one differentiated planetesimal into the mantle of another (e.g., Ruzicka, 2014; Maurel et al., 2020; Kruijer et al., 2022), or completely disrupt planetesimals that then reaccreted into porous rubble piles (e.g., Nakamura et al., 2022).

1.1.3 Planetesimal observations and samples

Asteroids are planetesimals that were not accreted into planets. Although they are now cold and geologically inactive, their orbits, size, shape, composition, and surface features provide clues to their evolution in the early Solar System (Bottke and Morbidelli, 2017; Vernazza and Beck, 2017). Many observations of asteroids are from ground- and space-based telescopes. For example, radar can be used to determine an asteroid's shape (e.g., Shepard et al., 2017) and reflectance spectra help determine an asteroid's surface composition (e.g., Dibb et al., 2023). Asteroid flybys, such as Galileo (Chapman et al., 1996), and orbital missions, such as Dawn (Raymond et al., 2017; Rayman, 2022), have provided us with much higher resolution data. For example, gravity field measurements of Vesta confirmed the asteroid is differentiated (Raymond et al., 2017). The Psyche and LUCY missions, en-route to a metal-rich asteroid and the Trojan asteroids, respectively, will soon provide insights about two more types of asteroids (Elkins-Tanton et al., 2020; Levison et al., 2021).

Until recently, the only samples from planetesimals were meteorites — fragments produced in planetesimal collisions that subsequently strike Earth and survive entry through the atmosphere to reach the surface. In 2005, the Hayabusa mission was the first to return a sample (< 1 g) from an asteroid (Nakamura et al., 2011). Recently, research on asteroid samples has been transformed by the Hayabusa 2 and OSIRIS-REx missions that returned a combined ~ 128 g of material between them from rubble pile asteroids Ryugu and Bennu, respectively (Tachibana et al., 2022; Lauretta et al.,

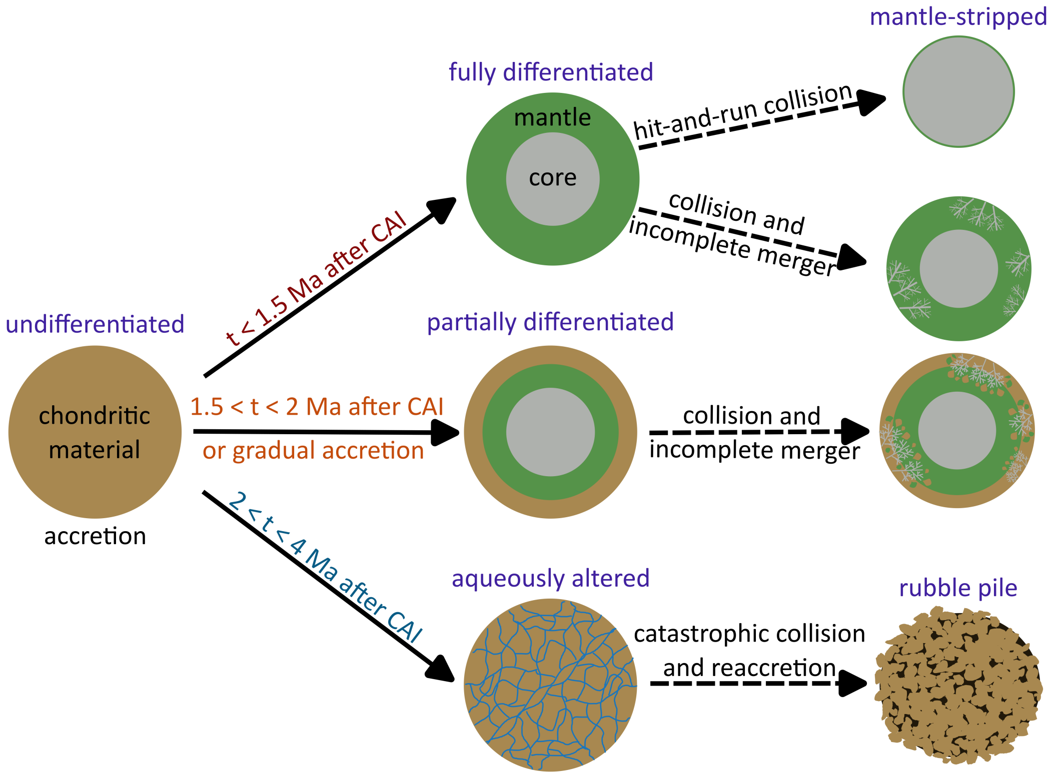

Figure 1.2: Possible planetesimal interior structures and their evolution depending on accretion time and collisional history. Possible interior structures are written in purple. Solid lines indicate the deterministic evolution of a planetesimal's interior, depending on its accretion time. Dashed lines indicate stochastic collisional processes, which could further alter a planetesimal's interior.

2024). These samples provide a valuable point of comparison between meteorite and asteroid observations. For example, they have revealed a compositional discrepancy between asteroids and meteorites with similar spectra (e.g., Amano et al., 2023). However, these missions have exclusively visited rubble pile asteroids, so can only provide information about the evolution of undifferentiated planetesimals.

1.1.4 Meteorite classification

Meteorites are split into two categories, chondrites and achondrites, based on their degree of thermal processing (Figure 1.3). Chondrites are unmelted meteorites with a distinctive texture consisting of a matrix of fine-grained dust that surrounds phases formed by thermal processing in the protoplanetary disk (Krot et al., 2014). They take their name from sub-milimetre, spherical melt inclusions called chondrules. Achondrites experienced partial or complete melting and differentiation, erasing their pre-existing chondritic textures (Krot et al., 2014). Achondrites can be split into three further categories based on composition: irons, stony-irons and rocky achondrites for meteorites consisting of pure metal, a roughly equal mixture of metal and silicate and predominantly silicate, respectively (Krot et al., 2014). There are two types of iron meteorite: magmatic that are silicate free and have compositions reflecting fractional crystallisation; and non-magmatic that contain silicates and do not follow fractional crystallisation trends (Scott, 2020). Rocky achondrites can also be split into two groups: primitive that experienced extreme thermal metamorphism, but very low degrees of partial melting; and differentiated that experienced a high degree of partial melting and differentiation (Mittlefehldt, 2007).

Meteorites can also be split into two isotopic categories, non-carbonaceous (NC) and carbonaceous (CC) (Warren, 2011; Kruijer et al., 2020; Bermingham et al., 2020). Based on their isotopic similarity to the terrestrial planets (Warren, 2011) and the lack of water in NC chondrites (e.g., Alexander, 2019b), NC meteorites are thought to originate from the inner Solar System (interior to Jupiter's orbit and the water condensation line). CC meteorites are thought to originate from the outer Solar System beyond the water condensation line based on the water contents of CC chondrites (e.g., Alexander, 2019a). NC and CC examples of every meteorite category have been found (e.g. Krot et al., 2014; Greenwood et al., 2006; Sanborn et al., 2019). Within the NC chondrites, the enstatite chondrites (EC) formed in more reducing conditions, closer to the Sun than the ordinary chondrites (OC) and R chondrites (Weisberg and Kimura, 2012).

Within these categories, meteorites with similar nucleosynthetic isotopic compositions, bulk chemistry, mineralogy and petrology form a *group* (Figure 1.3) and are thought to originate from the same parent body (Krot et al., 2014). Although most meteorite parent bodies are planetesimals, some groups originate from the Moon and Mars (Udry et al., 2020; Joy et al., 2023). Only the howardite, eucrite and diogenite (HED) meteorites have been linked to a specific surviving planetesimal (asteroid (4) Vesta; McSween et al., 2012). Meteorites that are not sufficiently similar to any others are called *ungrouped*, but can still be broadly classified as CC or NC, as well as chondritic or achondritic. There are different naming conventions for meteorite groups based on the meteorite category (Krot et al., 2014). Carbonaceous chondrite groups are named C–, where – denotes the first letter of the first identified meteorite for that group e.g., CM chondrites are Mighei-like. The ordinary chondrite groups are named based on their metal content: High (H), Low (L) or Low Low (LL). Meteorites which fall in between these classes get an intermediate designation e.g. L/LL. Enstatite chondrites are named similarly (EH or EL). Iron meteorite groups were initially named with a roman numeral from I–IV indicating decreasing Ga and Ge concentration (Goldberg et al., 1951; Lovering et al., 1957) and a capital letter was subsequently appended to further subdivide them e.g. IIE (Wasson, 1967). The group names for other achondrites are either based on the location where the first identified meteorite for the group was found or after scientists e.g., angrites are named after Angra dos Reis, Brazil (Keil, 2012) and pallasites are named after naturalist Peter Pallas (Pallas, 1778; Chladni, 1794). Pallasites are further subdivided into the Main Group and Eagle Station groups (Greenwood et al., 2017) and ungrouped pallasites (Krot et al., 2014).

The origin of the NC-CC dichotomy is one of the biggest questions in planet formation (Kruijer et al., 2020; Bermingham et al., 2020). The different isotopic compositions of NC and CC meteorites reflects the changing composition of material infalling onto the protoplanetary disk in the first 4 Ma of Solar System formation (e.g., Yang and Ciesla, 2012; Nanne et al., 2019; Burkhardt et al., 2019). Some process prevented homogenisation of this material within the disk and led to formation of planetesimals in two compositionally distinct regions. Several possibilities have been suggested for this process including: a pressure barrier between the reservoirs caused by Jupiter's formation (e.g., Nanne et al., 2019; Kruijer et al., 2020); formation of planetesimals at different condensation lines (e.g., Izidoro et al., 2022; Morbidelli et al., 2022); or migration of the water condensation line (e.g., Drążkowska and Dullemond, 2018; Lichtenberg et al., 2021). The process that formed the isotopic

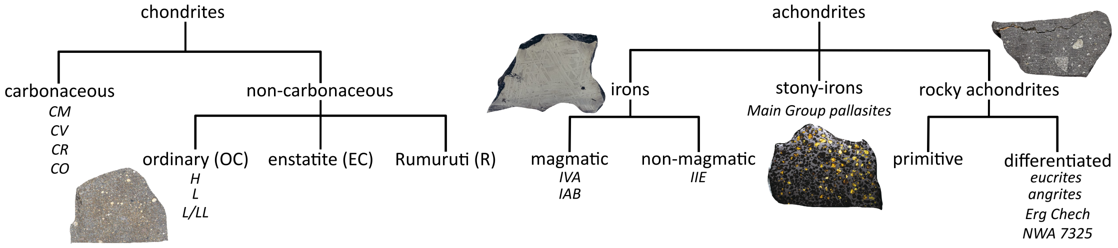

Figure 1.3: Overview of meteorite classification scheme. Meteorite groups which have been measured paleomagnetically are listed under their relevant categories. NWA 7325 and Erg Chech are both ungrouped meteorites. Meteorite images credit: The Trustees of the Natural History Museum, London, UK.

dichotomy could have led to other differences between NC and CC planetesimals, such as water content (e.g., Alexander et al., 2018; McCubbin and Barnes, 2019). Several quantities have been investigated to elucidate differences between these reservoirs, including planetesimal accretion times (Spitzer et al., 2021; Hellmann et al., 2024) and iron meteorite oxidation states (Rubin, 2018; Hilton et al., 2022; Zhang et al., 2024). The ability for meteorite paleomagnetism to shed light on these differences has not yet been considered. Earths's isotopic composition indicates that Earth accreted both NC (~95%) and CC (~ 5%), chondritic and achondritic material (Dauphas et al., 2024; Nimmo et al., 2024). Therefore, understanding the formation of planetesimals in these reservoirs and differences between them is vital for understanding the Earth's formation.

1.1.5 Meteorite records of magnetic fields

NC and CC chondrites and NC achondrites have had their paleomagnetic remanences measured (Figure 1.4). There are three types of magnetic remanence relevant to meteorite paleomagnetism: thermal remanent magnetisation (TRM), chemical remanent magnetisation (CRM) and chemical transformation remanent magnetisation (CTRM). A TRM is recorded when a magnetic mineral is heated and then cooled through its blocking temperature (the temperature at which a magnetisation becomes stable for a given time period) in the presence of a magnetic field (Tauxe, 2010). On a planetesimal, this can occur due to impact heating (e.g., Bryson et al., 2020a; Fu et al., 2012) or radiogenic heating (e.g., Wang et al., 2017). A CRM is recorded when a magnetic mineral is formed during a chemical reaction either replacing an existing mineral (pseudomorphic CRM) or precipitating from solution (grain growth CRM) in the presence of a magnetic field (Tauxe, 2010). CRMs in the meteorite record formed by aqueous alteration of chondritic material (e.g., Cournede et al., 2015). It can be difficult to obtain an accurate paleointensity (strength of the primordial field) from a CRM, because pseudomorphic CRMs may partially inherit a magnetisation from precursor minerals (Bryson et al., 2023). CRMs also acquire a paleomagnetic remanence over a longer timescale than a TRM, so their paleointensities represent a temporal average of the primordial field (Cournede et al., 2015; Bryson et al., 2020a). A CTRM is recorded when a material becomes a stable magnetic recorder following a phase transformation. Iron or stony-iron meteorites record CTRMs in cloudy zones; a microstructure that forms as part of the characteristic FeNi Widmanstätten pattern by spinodal decomposition as the alloy cools below 593 K at cooling rates $< 10,000\,\mathrm{K Ma^{-1}}$ (Einsle et al., 2018; Maurel et al., 2019). TRMs and CRMs can both be measured for bulk meteorite samples (e.g., Carporzen et al., 2011) or for individual phases, such as chondrules (Fu et al., 2014b; Borlina et al., 2021). CTRMs in cloudy zones are only detectable by imaging the distribution of magnetisation directions in the cloudy zone directly (e.g., Bryson et al., 2015; Nichols et al., 2016).

Paleomagnetic remanences can be dated radiometrically if the closure temperature of the radiometric system is close to either the blocking temperature of the magnetised mineral recording a TRM or the formation temperature of the mineralogy recording a CRM/CTRM. For example, the $^{40}\mathrm{Ar}/^{39}\mathrm{Ar}$ system in 0.1-1 mm feldspars has the same closure temperature ($\sim 600\,\mathrm{K}$) as the temperature of cloudy zone remanence acquisition (Bogard et al., 2000; Maurel et al., 2020). For samples where radiometric dating is not possible or extrapolation from a dated closure temperature to the Curie temperature is required, thermal evolution and dynamo generation models can be used to predict the timing of remanence acquisition.

1.2 Magnetic fields in the early Solar System

1.2.1 Sources of meteorite magnetisations

Four possible sources have been proposed for meteorite magnetisations: the nebula field in the protoplanetary disc, which existed prior to ~4–5 Ma after CAI formation (e.g., Fu et al., 2014a; Wang et al., 2017; Fu et al., 2020; Borlina et al., 2021; Bryson et al., 2023; Maurel and Gattacceca, 2024); internally generated dynamos (e.g., Tarduno et al., 2012; Wang et al., 2017; Bryson et al., 2019b); impact generated fields (Muxworthy et al., 2017); and the solar wind (Tarduno et al., 2017; O'Brien et al., 2020). Magnetisation from the solar wind has been proposed to be three to four orders of magnitude too weak to explain meteorite paleomagnetic remanences (Oran

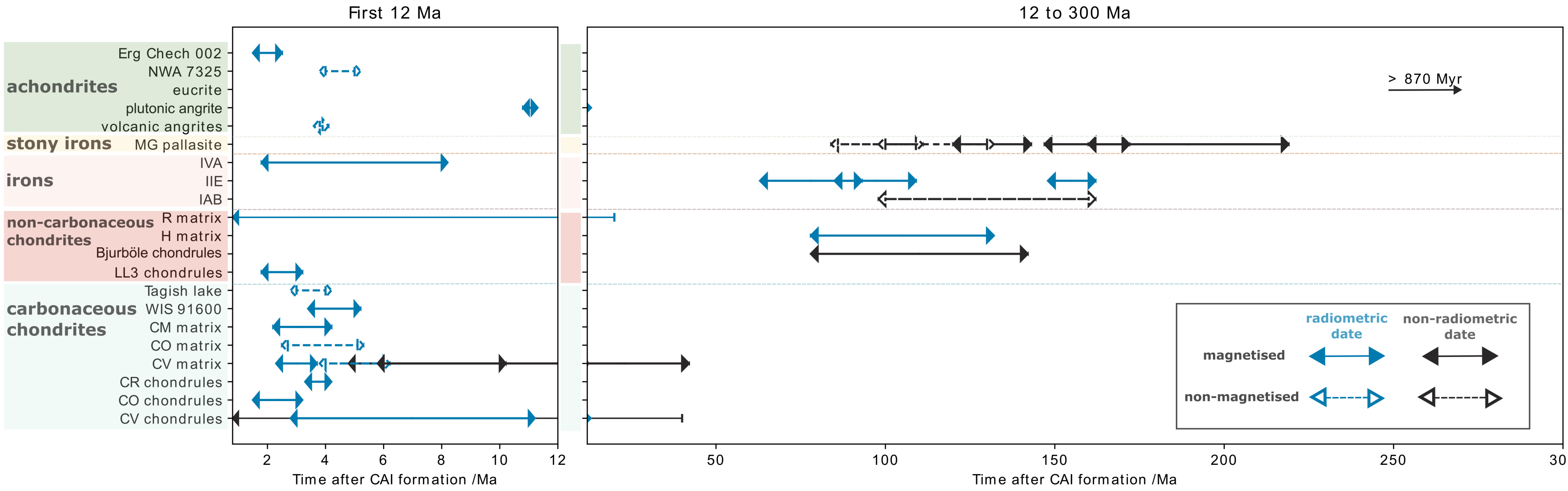

Figure 1.4: The meteorite paleomagnetic record. Blue and red boxes indicate undifferentiated (chondritic) meteorite groups and green, yellow and pink boxes indicate differentiated (achondritic) meteorite groups. Blue and black arrows represent magnetic remanences dated using radiometric methods and thermal evolution models, respectively. Solid arrows with filled caps indicate magnetised samples and dashed arrows with unfilled caps indicate unmagnetised samples. For the angrites, the time range is so short that only the arrowheads are visible. Multiple measurements for the same meteorite group are combined, but measurements of bulk magnetisation vs chondrules are kept separate to distinguish between pre-accretionary and post-accretionary remanences. Unlike the other chondrules, the CV chondrules remanence is not pre-accretionary, because the CV chondrules have experienced aqueous alteration, thermal metamorphism, and possibly brecciation (Fu et al., 2014a; Shah et al., 2017). The data table shown in this plot and references for each measurement can be found in Table B.2 and B.3.

et al., 2018) and impact fields could only be recorded in highly shocked meteorites that cooled sufficiently quickly (Muxworthy et al., 2017). Therefore, these two sources will not be discussed further.

The nebula field was generated by charged material orbiting in the protoplanetary disk. This field affected stellar accretion from the protoplanetary disk (Wardle, 2007; Weiss et al., 2021) and may have influenced disk structure (Hu et al., 2019). Paleomagentic records of the nebula field can help us understand disk lifetime (Wang et al., 2017; Borlina et al., 2022), structure and strength of the disk field (Cournede et al., 2015; Borlina et al., 2021; Bryson et al., 2023), movement of solids within the disk (Bryson et al., 2020a,b), and stellar accretion rate (Weiss et al., 2021). Remanences from the nebula field can be identified by randomly oriented chondrule magnetisation directions (e.g., Fu et al., 2020). This thesis focuses on internally generated dynamo fields, but as a corollary can shed light on paleomagnetic records of the nebula field.

1.2.2 Driving mechanisms for dynamo generation

A dynamo is the transfer of kinetic to magnetic energy through the motion of an electrically conductive fluid (Soderlund et al., 2025). In rocky bodies, dynamos are generated in molten, metallic cores and can be driven by buoyancy or by mechanical forcing (Landeau et al., 2022). Additionally, dynamos could be generated in silicate magma oceans (e.g. Scheinberg et al., 2018; Stixrude et al., 2020; Lherm et al., 2024), but this depends on the highly debated electrical conductivity of silicate at high temperatures and pressures (e.g., Pommier et al., 2015; Stixrude et al., 2020; Guarguaglini et al., 2021). Rotation is also required to give the flow a net helicity and ensure a large-scale magnetic field (Stanley, 2016).

Tides, libration, and precession can drive dynamos in planetary cores by dissipating orbital and rotational energy into the core via turbulence (Le Bars et al., 2015). These mechanisms could have driven the early geodynamo (e.g., Landeau et al., 2022) and lunar dynamo (e.g., Le Bars et al., 2011; Cébron et al., 2019). However, mechanical driving is not relevant for planetesimals because they cannot sustain libration or precession over timescales $\geq 10\,\mathrm{kyr}$ (Burns et al., 1973; Dodds et al., 2021), and they are too small and too far from the Sun for them to experience significant tidal deformation.

Instead, planetesimal dynamos can only be generated by buoyancy-driven flows: thermal, compositional, or thermo-compositional convection. Thermal convection is driven by temperature-induced density differences and requires a superadiabatic heat flux across the core-mantle boundary (CMB). Compositional convection is driven by chemically induced density differences resulting from core solidification (e.g., Gubbins, 1977; Scheinberg et al., 2016) or light-element precipitation as the core cools (e.g., Badro et al., 2016; O'Rourke and Stevenson, 2016). For example, at the present day, the Earth's magnetic field is driven by partitioning of buoyant, incompatible light elements from the solidifying inner core into the liquid outer core, which rise and drive convection in the liquid outer core (Braginsky, 1963; Gubbins, 1977; Nimmo, 2007). In planetesimals, the mechanism for driving a compositional dynamo is debated. Planetesimal cores solidify inwards because the pressure gradient of the liquidus is shallower than the core adiabat (Williams, 2009; Dodds et al., 2025). Therefore, for core solidification to generate compositional convection, the dense solid phase must sink towards the centre of the planetesimal disrupting the stable stratification of light-element enriched fluid at the CMB. Several mechanisms for generating dynamos from inward core solidification have been proposed including: iron snow (Rückriemen et al., 2015; Scheinberg et al., 2016); viscous delamination of solid iron from the CMB (Neufeld et al., 2019); and formation of unstable iron dendrites (Scheinberg et al., 2016). In viscous delamination and dendritic solidification, solid iron sinks as large blobs ($\sim 1\,\mathrm{km}$), while in iron snow solid iron crystallises as small particles ($\sim 10^{-2}\,\mathrm{mm}$). These crystals either fall through the core without remelting (Dodds et al., 2025) or remelt at a depth determined by the adiabatic temperature gradient and form an iron-rich fluid that continues to sink to the centre (Rückriemen et al., 2015).

1.2.3 Thermal evolution and dynamo generation models

Planetesimal thermal evolution and dynamo generation models can predict when thermal and compositional dynamos would have been active on a planetesimal. These predictions can be compared to meteorite magnetic remanences and meteorite thermochronology to determine whether remanences have a thermal (e.g., Wang et al., 2017) or compositional (e.g., Maurel et al., 2021) dynamo origin. These models can also help determine whether ancient, bulk paleomagnetic remanences were imparted by dynamo or nebula fields (e.g., Cournede et al., 2015; Maurel and Gattacceca, 2024). As well as interpreting the source of meteorite paleomagnetic remanences, planetesimal thermal evolution and dynamo generation models can be used to recover a range of parent body sizes and interior properties that generated the recorded field (e.g., Bryson et al., 2019b). If a remanence cannot be dated, thermal models can also be used to estimate the age at which the magnetisation was acquired. For example, in the Main Group pallasites, metallographic cooling rates are combined with thermal models to predict a meteorite's depth on a parent body, and then the age of the magnetisation is calculated from when that depth cooled through the temperature of remanence acquisition (e.g., Tarduno et al., 2012; Bryson et al., 2015; Nichols et al., 2021).

Previous studies have used a variety of thermal and dynamo models to constrain the properties of meteorite parent bodies, including the CV chondrites (Elkins-Tanton et al., 2011), H chondrites (Bryson et al., 2019b), angrites (Dodds et al., 2021), IIE irons (Maurel et al., 2021), and Main Group pallasites (e.g., Tarduno et al., 2012; Bryson et al., 2015; Nichols et al., 2021). Additionally, these previous models have led to broad insights about planetesimal evolution. They have been used to argue that some planetesimals were partially differentiated (Elkins-Tanton et al., 2011; Maurel et al., 2019, 2021) and that planetesimals could have generated magnetic fields through core solidification (Nimmo, 2009; Scheinberg et al., 2016; Neufeld et al., 2019). They have also predicted the range of planetesimal sizes that can generate a dynamo (e.g. > 340 km; Bryson et al., 2019a) and the timing and duration of planetesimal dynamos (4–30 Ma after CAI formation for thermal dynamos; Dodds et al., 2021). These timings have been used to define three, distinct origins for meteorite paleomagnetic remanences based on time: nebula fields < 4 Ma after CAI formation; thermal dynamos 4–30 Ma after CAI formation; and compositional dynamos > 35 Ma after CAI formation (Bryson et al., 2019a; Dodds et al., 2021).

1.2.3.1 Model set-up

Previous thermal evolution and dynamo generation models for planetesimals were 1D, spherically symmetric, and adopted two possible interior structures. Models focussed on mantle-stripped planetesimals (Scheinberg et al., 2016; Neufeld et al., 2019) or magnetic field generation by core solidification (Nimmo, 2009) only modelled thermal evolution of the core, while all other models consist of a coupled mantle and core (Elkins-Tanton et al., 2011; Sterenborg and Crowley, 2012; Bryson et al., 2019a; Dodds et al., 2021). Mantle heat transport is either modelled as purely conductive (Elkins-Tanton et al., 2011; Murphy Quinlan et al., 2021) or also includes stagnant lid convection (Sterenborg and Crowley, 2012; Bryson et al., 2019a; Dodds et al., 2021). Magnetic field generation is not modelled explicitly due to the high computational cost of magnetohydrodynamic (MHD) simulations. Instead, two different criteria for dynamo generation have been adopted in previous models: positive CMB heat flux (Elkins-Tanton et al., 2011); and, more commonly, the value of the magnetic Reynolds number (e.g., Sterenborg and Crowley, 2012; Bryson et al., 2019a). The magnetic Reynolds number is a dimensionless parameter that characterises the balance between magnetic induction and diffusion in the core. If the magnetic Reynolds number is above a critical value (10–100) a dynamo can be generated (Christensen and Aubert, 2006). Scaling laws derived from MHD simulations are used to relate the buoyancy flux across the CMB in a thermal evolution model to the magnetic Reynolds number and magnetic field strength (e.g., Aubert et al., 2009; Davies et al., 2022). The core is assumed to consist of Fe-FeS (e.g. Nimmo, 2009; Bryson et al., 2019a; Scheinberg et al., 2016), based on sulfur's siderophile behaviour (Poirier, 1994; Li and Fei, 2014); the sulfur contents of chondrites (Kracher and Wasson, 1982; Bercovici et al., 2022); and models of iron meteorite fractional crystallisation (Ulff-Møller, 1998; Chabot, 2004; Goldstein et al., 2009). The presence of other light elements, such as O, C, Si (Bromiley, 2023), is neglected for two reasons. Firstly, the thermal conductivity and density of iron alloys containing multiple light elements is poorly constrained (Pommier et al., 2020). Secondly, the abundance of light elements, other than sulfur, in planetesimal cores is very sensitive to oxygen fugacity, planetesimal bulk composition, differentiation mechanism and fluid immiscibility, so is difficult to calculate (Poirier, 1994; Rubie et al., 2015; Bromiley, 2023; Bromiley et al., 2024).

1.2.3.2 Limitations in previous modelling approaches

In the existing literature, each model iteration included a new degree of complexity, such as parametrised mantle convection (Sterenborg and Crowley, 2012), multi-stage accretion (Bryson et al., 2019a), gradual accretion (Dodds et al., 2021), or core thermal stratification (Dodds et al., 2021). However, the assumptions in previous models about mantle heat transport, core composition and core solidification, and their implementations of scaling laws for magnetic field generation limit the conclusions they can make about the meteorite paleomagnetic record, as discussed below.

For a planetesimal to generate a magnetic field, its core must be cooling rapidly or must have cooled enough to begin solidifying. Both these dynamo generation mechanisms depend on the heat flux from the core into the mantle, which is set by the mantle cooling rate. Several assumptions in previous models affected mantle cooling rate by controlling the vigour and duration of mantle convection. Firstly, previous models used scaling laws for stagnant lid thickness that include basal and surface heat fluxes but no internal heating (Solomatov, 1995), despite the importance of radiogenic ^{26}Al in planetesimal evolution (Hevey and Sanders, 2006; Sahijpal et al., 2007). Secondly, the boundary layer thickness at the base of the convecting mantle was approximated from scaling laws for the stagnant lid thickness (Bryson et al., 2019a; Dodds et al., 2021). Thirdly, constants in boundary layer scaling laws were fixed and therefore insensitive to changes in the viscosity (Dodds et al., 2021) or mantle viscosity models' simplified behaviour at high melt fractions (Sterenborg and Crowley, 2012). Finally, using a critical Rayleigh number criterion for the cessation of convection led to unphysical spikes in CMB heat flux at the cessation of convection and an unrealistic pause in core cooling (Bryson et al., 2019a). These assumptions need revisiting, because they influence the cessation of the thermal dynamo and the onset of core crystallisation and limit our ability to explore how mantle viscosity affects dynamo generation.

Previous models were also limited in their treatment of core composition. They neglected ^{60}Fe in the core, because ^{60}Fe had a minimal effect on core temperature for ^{60}Fe abundances measured at the time (Henke et al., 2013). However, recent work has highlighted that there are large discrepancies between in-situ and bulk meteorite measurements of ^{60}Fe (Kodolányi et al., 2022a,b) and abundances vary between different meteorite groups (Tang and Dauphas, 2012; Cook et al., 2021). Some measurements suggest ^{60}Fe abundance could be an order of magnitude higher than previously thought (Cook et al., 2021). Including ^{60}Fe will increase the heat available to drive the dynamo at early times, possibly changing the onset time of thermal dynamos. Additionally, mantled, convective models that include core solidification only considered Fe-FeS eutectic core compositions (Bryson et al., 2019a) due to the challenges in modelling planetesimal core solidification (Section 1.2.2). However, eutectic core compositions cannot drive a compositional dynamo because there is no compositional difference, and hence minimal density difference, between the solid and liquid phases. Since several meteorite parent bodies are thought to record dynamo fields from core solidification, assuming a eutectic composition limits the information we can extract about parent body core size and core composition from the meteorite record.

The magnetic field strength predictions from previous models have also been restricted. Most models predicted the duration of the dynamo using the magnetic Reynolds number, but did not predict magnetic field strengths due to uncertainties in how to relate field strengths to the vigour of convection (e.g., Elkins-Tanton et al., 2011; Sterenborg and Crowley, 2012). This limits the information that can be obtained from measured meteorite paleointensities. Models also did not consider thermal and compositional drivers of the dynamo at the same time: models for mantled planetesimals either only studied early thermal dynamos until the end of mantle convection (Sterenborg and Crowley, 2012; Dodds et al., 2021) or only modelled compositional dynamos during core solidification in planetesimals with conductive mantles

(Bryson et al., 2015; Nichols et al., 2021). The only model that discussed both driving mechanisms used the duration of eutectic core solidification as a proxy for when a compositional dynamo could be generated, and used different scaling laws to estimate magnetic Reynolds numbers for thermal and compositional dynamos (Bryson et al., 2019a). Considering thermal and compositional dynamo generation separately limits our ability to delineate between different dynamo generation mechanisms in the meteorite record and predict gaps in dynamo generation. Furthermore, without explicitly modelling dynamo generation during core solidification it is difficult to establish the range of planetesimal radii, core sizes and core compositions for which compositional dynamo generation is possible.

1.3 Key questions and thesis outline

Although previous models have provided many insights about planetesimal evolution, their assumptions about mantle convection and core solidification outlined above mean there are several outstanding questions:

1. What are the effects of mantle heat transfer and core composition on planetesimal dynamo generation? (Chapter 2 and Chapter 3)
2. Are previous interpretations of the meteorite paleomagnetic record still valid when mantle viscosity, core composition and compositional dynamo generation are properly accounted for? (Chapter 3)
3. Could meteorite paleomagnetism reveal differences in water content and oxidation state between NC and CC planetesimals? (Chapter 4)
4. What can a time-resolved paleomagnetic record tell us about the size, structure, and composition of a meteorite parent body? (Chapter 5)

In this thesis, I combine numerical models of planetesimal thermal evolution and dynamo generation with meteorite paleomagnetic measurements to address these questions.

As discussed above, previous thermal evolution and dynamo generation models have several limitations. Therefore, I begin this thesis by developing a refined thermal evolution and dynamo generation model (Chapter 2), which I use to explore the meteorite paleomagnetic record in subsequent chapters. Key refinements in this model include: an improved description of mantle convection and mantle viscosity, a parametrisation for inward core solidification, and a combined thermal and compositional buoyancy flux that allows both drivers of dynamo generation to be considered simultaneously. I use an example thermal and dynamo history to discuss differences to previous modelling approaches.

In Chapter 3, I use this model to explore the effect of individual planetesimal parameters on dynamo generation (Question 1). I vary mantle viscosity parameters and planetesimal radius to understand the effect of mantle heat transfer on dynamo generation. I also explore the importance of core composition through the abundance of radiogenic ^{60}Fe and initial core sulfur content. I use the results of this parameter variation to redefine the epochs of magnetic field generation in the meteorite record (Question 2). Developing an insight into the controls of these parameters on dynamo generation provides a foundation for subsequent chapters, where these parameters are varied to predict the dynamo histories of individual parent bodies.

To explore possible differences in dynamo generation between NC and CC differentiated planetesimals, in Chapter 4, I investigate the effect of mantle water content and core size — proxies for redox state — on dynamo generation. After understanding the effects of these individual parameters and utilising the results of Chapter 3, I compare dynamo histories for dry, reduced and wet, oxidised planetesimal endmembers as possible analogues for NC and CC differentiated plantesimals, respectively. I use these results to discuss water retention during planetesimal differentiation and possible water contents of the NC and CC reservoirs during planetesimal formation (Question 3).

In Chapter 5, I model the thermal and paleomagnetic histories of the IIE iron and Main Group pallasite parent bodies. Following explorations of individual planetesimal parameters in previous chapters, I consider all possible combinations of parameters to determine the most likely properties of these bodies, including size, core radius fraction, and initial core sulfur content. This reveals the extent to which meteorite paleomagnetism can constrain the interior structure and composition of a meteorite parent body (Question 4). I also re-evaluate the formation depths of these meteorites and discuss the implications for the formation of these meteorites.

Finally, in Chapter 6, I relate the results of Chapters 2–5 back to the key questions of the thesis and discuss directions for future research.

Chapter 2

A refined thermal evolution and dynamo generation model

2.1 Introduction

Magnetic field generation in planetesimals depends on conditions in their interiors, such as the extent of differentiation, and the vigour of core and mantle convection. These conditions are controlled by a range of planetesimal properties, including mantle viscosity and core composition. Thermal evolution and dynamo generation models must account for variations in these properties when they are used to interpret the meteorite paleomagnetic record. Previous models (Nimmo, 2009; Sterenborg and Crowley, 2012; Bryson et al., 2019a; Dodds et al., 2021) made the same assumptions about fundamental aspects of mantle heat transport and core solidification and held parameters that control these processes constant. In this chapter, I present a refined, thermal evolution and dynamo generation model, in which the mathematical description of these key processes are reconsidered and in which parameters such as mantle viscosity and core sulfur content can be varied. This model will enable the effect of mantle heat transfer and core composition on dynamo generation to be understood.

Magnetic field generation requires rapid core cooling (superadiabatic CMB heat flux) or core solidification, for which heat must be moved from the core to the mantle. Therefore, the timing of magnetic field generation is intrinsically linked to mantle cooling. Unlike previous models, my chosen mantle convection scaling laws are suitable for a body with internal heating and surface and basal heat fluxes and have been benchmarked against 2D numerical simulations (Deschamps and Vilella, 2021; Thiriet et al., 2019). Mantle convection depends strongly on viscosity, so I have refined the viscosity law from previous models. My chosen mantle convection scaling laws also respond consistently to changes to viscosity parameters, which enables a full investigation of the effects of viscosity on dynamo generation. Moreover, my criterion for the cessation of mantle convection ensures smooth and more physically realistic behaviour in the CMB heat flux and the mantle temperature profiles when the mantle becomes fully conductive. In the core, I have also included heating from radiogenic ^{60}Fe, which may increase the core temperature and the heat flux into the mantle at early times.

Alongside mantle convection and variable viscosity, I also consider sub-eutectic core solidification (core sulfur content $< 33\,\mathrm{wt\%}$) for an Fe-FeS core composition. Modelling dynamo generation from planetesimal core solidification is challenging, because there are multiple possible mechanisms of core solidification (Section 1.2.2). Due to the uncertainty in solidification mechanism, previous models that included mantle convection used the time taken for eutectic core solidification as a proxy for when a compositional dynamo could be generated, even though eutectic solidification cannot drive a compositional dynamo (Bryson et al., 2019a). Additionally, these models used different magnetic field scaling laws for thermal compared to compositional dynamos and were not able to accommodate both mechanisms driving core flow simultaneously. Here, I have developed a model for magnetic field generation by sub-eutectic core solidification, which also considers the relative contribution of both thermal and compositional buoyancy to magnetic field generation during core solidification.

I begin this chapter by describing my refined, 1D, spherically symmetric thermal evolution model (Section 2.2). I show the results of an example run and discuss the effects of my model changes in Section 2.3. I justify my assumptions about accretion and differentiation, mantle melting, and core solidification in Sections 2.4, 2.5 and 2.6, respectively. Future applications of the model and areas for further refinement are addressed in Section 2.7, and I conclude in Section 2.8.

2.2 Thermal Evolution Model

2.2.1 Overview

The key stages in planetesimal thermal evolution are shown in Figure 2.1. After accretion, the planetesimal will heat up due to the decay of radiogenic ^{26}Al ($t_{1/2} = 0.717\,\mathrm{Ma}$; Neumann et al., 2012). If accreted sufficiently early (within 1.5–2.5 Ma of CAI formation; Neumann et al., 2012; Monnereau et al., 2023), the planetesimal reaches a high enough temperature that it can melt and differentiate, forming a core and mantle. During differentiation ^{26}Al partitions into the mantle, while radiogenic

^{60}Fe ($t_{1/2} = 2.62\,\mathrm{Ma}$; Ruedas, 2017) partitions into the core. These two isotopes then heat the mantle and the core, respectively, and the mantle becomes unstable to convection. The adiabatic gradient is small in planetesimals due to their small size, so I neglect the core adiabat in my core convection criterion and when determining the direction of heat flow across the CMB. If the mantle becomes hotter than the core (e.g. due to strong internal heating and low surface heat flux) the core is heated by the mantle from above and becomes thermally stratified at shallow depths (Dodds et al., 2021). Once the mantle is cooler than the core, the core also begins to cool. Since the CMB heat flux, F_{CMB}, is positive, core convection begins. If the magnetic Reynolds number, Re_{m}, is greater than a critical value this convection can lead to the onset of the dynamo. As the mantle cools, it becomes more viscous and mantle convection ceases and heat in the mantle is transported by conduction. Initially, the cessation of mantle convection decreases F_{CMB} and can lead to a subcritical Re_{m} and the cessation of the dynamo. Later, during mantle conduction, if F_{CMB} increases sufficiently, Re_{m} can become supercritical again and the dynamo can restart. Once the core cools below its liquidus, core solidification begins. This provides an additional buoyancy source for the core dynamo due to the rejection of light elements (e.g. carbon, sulfur) and can lead to a second period (or extend the first/second period) of dynamo generation. Dynamo generation is no longer possible once the core is fully solidified.

I describe my 1D, spherically symmetric model in detail in the following sections. I begin with my mantle viscosity model, then explain each stage in the thermal evolution and finish with magnetic field generation and the numerical implementation. Model assumptions are discussed in Sections 2.4, 2.5 and 2.6.

2.2.2 Mantle viscosity

Mantle viscosity varies over many orders of magnitude during a planetesimal's thermal evolution, due to variations in mantle temperature and melt fraction, and has a large impact on mantle cooling. It controls mantle boundary layer thicknesses during convection and the transition from mantle convection to conduction, which affects CMB heat flux and dynamo generation. In this model, I define a four-piece viscosity law to capture changing rheological behaviour with temperature, and ensure the viscosity law and convection parametrisations are self-consistent and can be fully adjusted to reflect uncertainties in viscosity parameters.

The temperature dependence of mantle viscosity is defined piece-wise with five control variables (Figure 2.2): critical melt fraction, ϕ_{C}, Arrhenius slope, β, melt

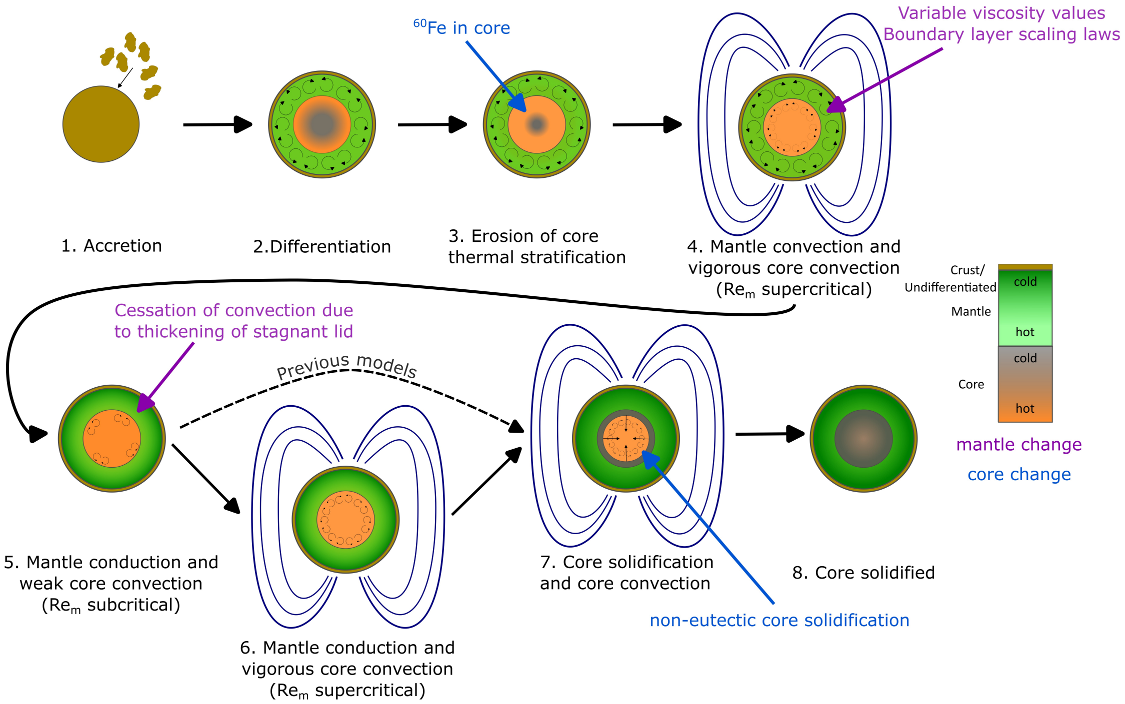

Figure 2.1: Schematic depicting the stages in my planetesimal thermal evolution model. Blue (core) and purple (mantle) labels highlight significant refinements adopted in my model compared to Sterenborg and Crowley (2012); Bryson et al. (2019a) and Dodds et al. (2021). Previous models only considered magnetic field generation after the end of mantle convection via core solidification (stage 7). However, my model allows for the possibility of two epochs of magnetic field generation prior to core solidification. Magnetic field generation can occur in stages 4, 6, and 7 if the magnetic Reynolds number exceeds a critical value. For low initial core sulfur contents, the core can start solidifying before the cessation of mantle convection and there may not be a pause in dynamo generation (stage 5).

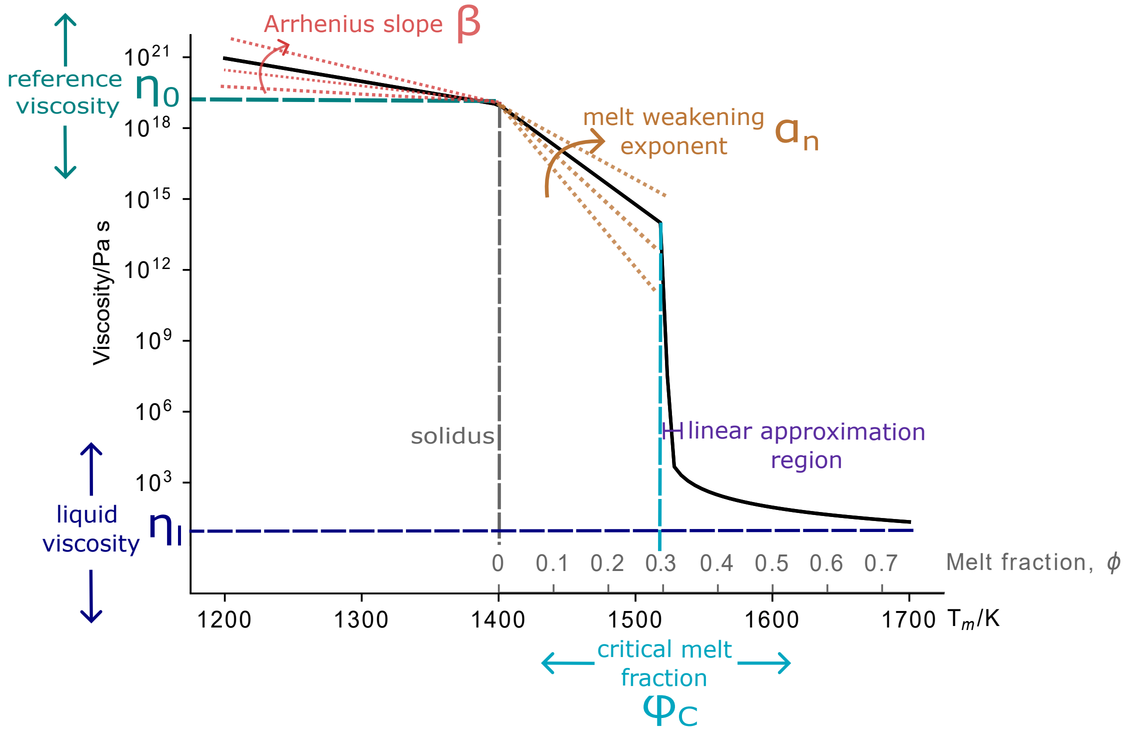

Figure 2.2: Variation of mantle viscosity with temperature (solid black line) for $\eta_0 = 10^{19}\,\mathrm{Pa\,s}$, $\phi_\mathrm{C} = 0.3$, $\beta = 0.0225\,\mathrm{K}^{-1}$ $\alpha_\mathrm{n} = 30$, and $\eta_\mathrm{l} = 10\,\mathrm{Pa\,s}$. The effect of varying each parameter is shown by the coloured arrows and lines. The grey, upper ticks on the horizontal axis indicates the equivalent melt fraction for temperatures above the solidus for mantle solidus and liquidus temperatures of 1400 K and 1800 K, respectively.

weakening exponent, α_{n}, reference viscosity at the solidus, η_0, and liquid viscosity, η_{l}:

$$\eta = \begin{cases} \eta_0 \exp\left(-\beta(T - T_{\mathrm{m,s}})\right) & T \leq T_{\mathrm{m,s}} \quad (2.1\mathrm{a}) \\ \eta_0 \exp\left(-(\beta + \frac{\alpha_{\mathrm{n}}}{T_{\mathrm{m,l}} - T_{\mathrm{m,s}}})(T - T_{\mathrm{m,s}})\right) & T_{\mathrm{m,s}} < T \leq T_{\phi_c} \quad (2.1\mathrm{b}) \\ \eta_{\mathrm{C}} 10^{\frac{\Delta\eta}{w}(T - T_{\phi_c})} & T_{\phi_c} < T < T_{\phi_c} + w \quad (2.1\mathrm{c}) \\ \eta_{\mathrm{l}} \left(\frac{\phi - \phi_C}{1 - \phi_C}\right)^{-2.5(1-\phi_C)} & T_{\phi_c} + w \leq T. \quad (2.1\mathrm{d}) \end{cases}$$

Here $T_{\mathrm{m,s}}$ and $T_{\mathrm{m,l}}$ are the mantle solidus and liquidus temperatures, respectively, T_{ϕ_c} is the temperature at ϕ_{C} and $\eta_{\mathrm{C}} = \eta(T_{\phi_c})$ is the viscosity at ϕ_{C}, which is calculated using Equation 2.1b. The melt fraction, ϕ is calculated assuming a linear liquidus approximation: $\phi = \frac{T - T_{\mathrm{m,s}}}{T_{\mathrm{m,l}} - T_{\mathrm{m,s}}}$. I do not specify a mantle composition and assume the same silicate solidus, $T_{\mathrm{m,s}} = 1400\,\mathrm{K}$, and liquidus, $T_{\mathrm{m,l}} = 1800\,\mathrm{K}$, values as Bryson et al. (2019a) and Dodds et al. (2021) (see Section 2.5.1). The mantle solidus and liquidus are pressure-independent constants, because the pressure variation in planetesimal mantles is small ($<50\,\mathrm{MPa}$).

Below the solidus, the viscosity has an Arrhenius temperature dependence (Equation 2.1a). This dependence is modelled using the Frank-Kamenetskii approximation at a reference temperature, T_{ref}, and reference viscosity, η_0, $\frac{E}{RT} \approx \frac{E(T - T_{\mathrm{ref}})}{R_{\mathrm{g}} T_{\mathrm{ref}}^2} = \beta(T - T_{\mathrm{m,s}})$, where E is the activation energy, $R_{\mathrm{g}} = 8.31\mathrm{JK}^{-1}\mathrm{mol}^{-1}$ is the gas constant, and the mantle solidus is taken as the reference temperature (Frank-Kamenetskii, 1969). Above the solidus, but below the critical melt fraction, this Arrhenius dependence has an additional melt weakening dependence $\alpha_{\mathrm{n}}\phi = \alpha_{\mathrm{n}} \frac{T - T_{\mathrm{m,s}}}{T_{\mathrm{m,l}} - T_{\mathrm{m,s}}}$ (Equation 2.1b). There is a sharp drop in viscosity at ϕ_{C} because melt surrounds any remaining solid phases and the material disaggregates. Above ϕ_{C}, viscosity is described by the Krieger-Dougherty relation (Faroughi and Huber, 2015; Sturtz et al., 2022b, Equation 2.1d), which tends to a constant liquid viscosity as the melt fraction approaches unity.

Equation 2.1c is an approximation using $\frac{\mathrm{d}\log_{10}\eta}{\mathrm{d}T} = \frac{\Delta\eta}{w}$ to ensure numerical stability at the rapid drop in viscosity at ϕ_{C}. w is the width of the region covered by this approximation, and is set to $5\,\mathrm{K}$ to minimise the approximated region, but ensure numerical stability. $\Delta\eta = \log_{10}(\eta(T_{\phi_c} + w)) - \log_{10}(\eta(T_{\phi_c}))$ is the logarithmic difference in the viscosity at ϕ_{C}, determined by Equation 2.1b, and the viscosity at $T_{\phi_c} + w$, determined by Equation 2.1d.

The Arrhenius temperature dependence (Equation 2.1a) determines the viscous temperature scale, $\frac{\Delta T}{f_{\mathrm{rh}}}$, which determines the fraction of the temperature difference across the convecting region that will control convection (Michaut and Neufeld, 2022;

Davaille and Jaupart, 1993)

$$f_{\mathrm{rh}} = -\frac{\mathrm{d}\eta(T_{\mathrm{m}})/dT}{\eta(T_{\mathrm{m}})}\Delta T. \tag{2.2}$$

In this definition, T_{m} is the temperature of the convecting region (the mantle) and ΔT is the temperature difference between the interior and the boundary (for the mantle $\Delta T = T_{\mathrm{m}} - T_{\mathrm{s}}$, where T_{s} is the surface temperature).

Compared to the three-piece model of Bryson et al. (2019a), this model has an order of magnitude narrower region approximated for numerical stability, w, and applies the Krieger-Dougherty relation to viscosity beyond ϕ_{C} rather than assuming a constant value. Unlike the tanh approximation employed by Dodds et al. (2021), it captures the change in slope at the solidus, has a steeper gradient in viscosity at ϕ_{C}, and can be adjusted using physically meaningful parameters.

2.2.3 Accretion

My model begins with instantaneous accretion of an undifferentiated mixture of silicates and Fe-FeS at 200 K at a specified time, t_{acc}, after CAI formation. The planetesimal surface temperature is fixed at an equilibrium temperature of 200 K throughout the simulation, because the range of planetesimal surface heat fluxes is small enough that its effect on the equilibrium surface temperature is negligible ($<$ 10 K; Dodds et al., 2021). At the plantesimal centre, $\frac{\partial T}{\partial r}\big|_{r=0} = 0$ throughout the simulation.

2.2.4 Before differentiation

After accretion, the planetesimal heats up due to decay of radiogenic ^{26}Al and ^{60}Fe. Heat is initially transported through the body by conduction

$$\rho_{\mathrm{ch}} c_{\mathrm{p,ch,eff}} \frac{\partial T}{\partial t} = \frac{1}{r^2}\frac{\partial}{\partial r}\left(k_{\mathrm{ch}} r^2 \frac{\partial T}{\partial r}\right) + \rho_{\mathrm{ch}} H, \tag{2.3}$$

where ρ is the density, c_p is the specific heat capacity, T is the temperature, r is the radius, t is the time, and k is the thermal conductivity. The subscript ch denotes the values for the undifferentiated, chondritic material. The undifferentiated planetesimal is assumed to have the same thermal properties as the silicate mantle (e.g., Elkins-Tanton et al., 2011; Bryson et al., 2019a) except for the density, which uses the bulk density of the planetesimal. Compaction and sintering of the planetesimal prior to differentiation are neglected and a constant thermal diffusivity is used throughout, because these processes only affect the planetesimal as it initially heats up from 200 K to 700 K (Yomogida and Matsui, 1984) and have a minimal effect on the overall thermal evolution. H is the radiogenic heating power per unit mass

$$H = H_{\mathrm{Al},0} f_{^{26}\mathrm{Al}} 0.01 X_{\mathrm{Al}} e^{-\frac{ln(2)t}{t_{1/2,\mathrm{Al}}}} + H_{\mathrm{Fe},0} f_{^{60}\mathrm{Fe}} 0.01 X_{\mathrm{Fe}} e^{-\frac{ln(2)t}{t_{1/2,\mathrm{Fe}}}}, \tag{2.4}$$

where $H_{i,0}$ is the heating power per unit mass of isotope i at the time of CAI formation, f_i is the radiogenic isotope abundance as a ratio to its most common stable isotope, X_i is the elemental abundance in wt % in the accreting material, and $t_{1/2,i}$ is the radiogenic isotope half life. The values chosen for each parameter are summarised in Table 2.1. Melting of metal and silicate as the planetesimal heats up is accounted for using a modified specific heat capacity (adapted from Merk et al., 2002; Dodds et al., 2021, for a mixture of metal and silicate).

$$c_{\mathrm{p,ch,eff}} = \begin{cases} c_{\mathrm{p,ch}} & T < T_{\mathrm{c,s}} \;\&\; T < T_{\mathrm{m,s}} \\ c_{\mathrm{p,ch}}\left(1 + \frac{0.01 X_{\mathrm{Fe}} L_c}{c_{\mathrm{p,ch}}(T_{\mathrm{c,l}} - T_{\mathrm{c,s}})}\right) & T_{\mathrm{c,s}} < T < T_{\mathrm{c,l}} \;\&\; T < T_{\mathrm{m,s}} \\ c_{\mathrm{p,ch}}\left(1 + \frac{0.01 X_{\mathrm{Fe}} L_c}{c_{\mathrm{p,ch}}(T_{\mathrm{c,l}} - T_{\mathrm{c,s}})} + \frac{0.01 X_{\mathrm{Si}} L_{\mathrm{m}}}{c_{\mathrm{p,ch}}(T_{\mathrm{m,l}} - T_{\mathrm{m,s}})}\right) & T_{\mathrm{c,s}} < T < T_{\mathrm{c,l}} \;\&\; T_{\mathrm{m,s}} < T < T_{\mathrm{m,l}} \\ c_{\mathrm{p,ch}}\left(1 + \frac{0.01 X_{\mathrm{Si}} L_{\mathrm{m}}}{c_{\mathrm{p,ch}}(T_{\mathrm{m,l}} - T_{\mathrm{m,s}})}\right) & T_{\mathrm{c,l}} > T \;\&\; T_{\mathrm{m,s}} < T < T_{\mathrm{m,l}} \end{cases} \tag{2.5}$$

Here X_{Fe} and X_{Si} are the Fe-FeS and silicate fraction in wt % in the accreted material, L_{c} and L_{m} are the latent heats of fusion of Fe-FeS and silicate, $T_{\mathrm{c,l}}$ and $T_{\mathrm{m,l}}$ are the Fe-FeS and silicate liquidi, and $T_{\mathrm{c,s}}$ and $T_{\mathrm{m,s}}$ are the Fe-FeS and silicate solidi. The Fe-FeS and silicate melt fractions are both calculated using the linear liquidus approximation. The sulfur content of the Fe-FeS system is set as an input parameter. For planetesimals with eutectic Fe-FeS compositions, the temperature is held fixed once the planetesimal temperature reaches the Fe-FeS solidus, until all the Fe-FeS is melted. In this scenario, the time evolution of the Fe-FeS melt fraction, ϕ_{Fe}, is calculated by replacing the term on the left hand side of Equation 2.3 by $\rho_{\mathrm{ch}} X_{\mathrm{Fe}} L_{\mathrm{Fe}} \frac{\partial \phi_{\mathrm{Fe}}}{\partial t}$ where $\rho_{\mathrm{ch}} X_{\mathrm{Fe}}$ is the density of Fe-FeS in the undifferentiated material.

Solid-state stagnant lid convection (Section 2.2.5.2) could begin prior to differentiation, as the body heats up. In this mode of convection, the stagnant lid is a conductive, immobile boundary layer at the surface of the planetesimal with a thickness δ_0 (Equation 2.7) and the interior beneath the lid convects (Figure 2.3). The interior is assumed to be isothermal, because pressure variation in the planetesimal is small enough for the adiabatic temperature gradient to be neglected. The interior temperature, T_i, evolves according to

$$\rho_{\mathrm{ch}} c_{\mathrm{p,ch}} V_i \frac{\partial T_i}{\partial t} = -F_{\mathrm{lid}} A_{\mathrm{lid}} + \rho_{\mathrm{ch}} V_i H, \tag{2.6}$$

where $F_{\text{lid}} = -k_{\text{ch}} \frac{\mathrm{d}T}{\mathrm{d}r}\Big|_{r=R-\delta_0}$, V_i is the volume of the interior, and A_{lid} is the surface area of the base of the stagnant lid (Solomatov, 1995). The stagnant lid continues to transport heat following Equation 2.3, assuming equal abundances of radiogenic elements in the interior and the lid, and decreases in thickness as the planetesimal heats up. If eutectic Fe-FeS melting occurs while the planetesimal is convecting, the left-hand side of Equation 2.6 is replaced by $\rho_{\text{ch}} X_{\text{Fe}} L_{\text{Fe}} \frac{\partial \phi_{\text{Fe}}}{\partial t}$. I assume solid-state stagnant lid convection can occur if δ_0 is less than 99% of the planetesimal radius, R.

Once the silicate melt fraction, ϕ, reaches the critical melt fraction, ϕ_{C}, there is a steep drop in the silicate viscosity and differentiation proceeds via rain-out, where the more dense, molten Fe-FeS settles through the less dense, low-viscosity silicate via Stokes settling. This process is rapid (10^4 years for mm size droplets, see Appendix A.5.2) and can be approximated as instantaneous. Differentiation via percolation prior to $\phi = \phi_{\text{C}}$ is neglected due to the uncertainties in the timescales for this process (see Section 2.4 and Appendix A.5.1). Due to the small internal pressure gradient, the body is almost isothermal and, for simplicity, the entire planetesimal is assumed to differentiate at the same time. My model assumes all Fe-FeS is fully molten before differentiation and that the core is initially liquid. In order to satisfy this assumption, the liquidus temperature for the initial core sulfur content of the Fe-FeS must be less than or equal to the temperature of ϕ_{C}. This limits the range of initial core sulfur contents (see Section 2.4.4.1).

At the point of differentiation, the body is assumed to instantly form an Fe-FeS core, with a radius half that of the body, $r_{\text{c}} = \frac{R}{2}$, with an overlying silicate mantle (Figure 2.3). The core and the mantle are isothermal at the temperature of the critical melt fraction, T_{ϕ_C}. All iron is assumed to partition into the core and all aluminium is assumed to stay in the mantle. This increases the concentration of ^{26}Al in the mantle and ^{60}Fe in the core compared to initial conditions. The initial core sulfur content, $X_{\text{S},0}$, is set by an input parameter and is the same as the sulfur content in Fe-FeS in the undifferentiated planetesimal.

2.2.5 After differentiation

2.2.5.1 Crust

The presence of a crust is simplified to the fixed surface temperature boundary condition. Only the surface node does not become hot enough to differentiate. Therefore, the thickness of any porous regolith is below the resolution of this model and has been neglected (Section 2.4.2).

2.2.5.2 Mantle

The mantle transports heat either via conduction or stagnant lid convection. In stagnant lid convection, the mantle is assumed to have an isothermal, convecting interior with a conductive boundary layer ('stagnant lid') below the surface and another above the CMB (Figure 2.3). In my adopted parametrisation, the stagnant lid thickness includes the thin mobile boundary layer at the base of the lid (Appendix A.1.2.1). I assume an empirically determined expression for stagnant lid thickness, δ_0, for a system with internal heating, heat flux at the top and bottom boundaries, temperature-dependent viscosity, and free-slip boundary conditions (Deschamps and Vilella, 2021)

$$\delta_0 = a_{\text{lid}}(R - r_{\text{c}})f_{\text{rh}}^{1.21}Ra^{-0.27}, \tag{2.7}$$

where a_{lid} is a empirically determined constant (0.633 for $\text{Ur} < 1$ and 0.667 for $\text{Ur} > 1$). Here Ur is the Urey ratio, which is the ratio of the power of internal heating, Q_{H}, to the power of cooling from the surface, Q_{S},

$$\text{Ur} = \frac{Q_{\text{H}}}{Q_{\text{S}}} = \frac{\rho_{\text{m}}V_{\text{m}}H_{\text{Al}}}{F_{\text{s}}A_{\text{s}}}, \tag{2.8}$$

where V_{m} is the volume of the mantle, F_{s}, and A_{s}, are the surface heat flux and surface area, respectively. In Equation 2.7, the Rayleigh number, Ra, is calculated using the interior mantle temperature

$$Ra = \frac{\rho_{\text{m}}\alpha_{\text{m}}g(R)\Delta T(R - r_{\text{c}})^3}{\kappa_{\text{m}}\eta}. \tag{2.9}$$

Here α_{m}, ρ_{m}, and κ_{m} are the thermal expansivity, density, and diffusivity of the mantle respectively, $\Delta T = T_{\text{m}} - T_{\text{s}}$ is the difference between the interior convective temperature, T_{m}, and the surface temperature T_{s}, $g(R)$ is the gravitational field strength at radius $r = R$, and the viscosity is calculated for the convecting interior temperature $\eta = \eta(T_{\text{m}})$. In this model, I adopt the middle value of silicate diffusivity, $9 \times 10^{-7}\text{m}^2\text{s}^{-1}$, used in previous work (6, 9 and $12{\times}10^{-7}\text{m}^2\text{s}^{-1}$; Bryson et al., 2019a), which corresponds to an ordinary chondrite composition. Equation 2.7 was derived neglecting melt weakening, therefore $f_{\text{rh}} = -\frac{\text{d}\eta(T_{\text{m}})/\text{d}T}{-\eta(T_{\text{m}})}\Delta T = \beta(T_{\text{m}} - T_s)$ based on the first piece of the viscosity law (Equation 2.1a).

The thickness of the CMB boundary layer at the base of the mantle, δ_l, is difficult to parametrise because it could be affected by downwelling material from the upper boundary layer interfering with its thermal structure (Thiriet et al., 2019). δ_l has been approximated in previous planetesimal models in two ways. First, δ_l has been

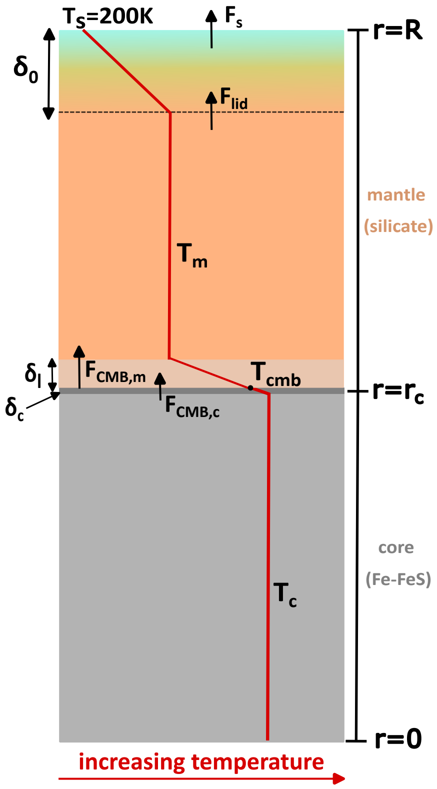

Figure 2.3: Schematic depicting my model setup for a convecting silicate mantle and a convecting Fe-FeS core. The core and mantle are two coupled reservoirs. The crust is approximated by the fixed surface temperature, $T_{\mathrm{s}} = 200\,\mathrm{K}$. The red line is the temperature profile in the planetesimal and temperature increases to the right. In this diagram, the mantle is convecting in the stagnant lid regime: the interior is isothermal and there are conductive boundary layers at the CMB, δ_l, and the surface, δ_0. The black dashed line denotes the base of the stagnant lid. The core has a thermal boundary layer at the CMB, δ_{c}. When the mantle and core are conductive, there is a temperature gradient throughout each layer instead. The balance of CMB heat fluxes ($F_{\mathrm{CMB,m}} = F_{\mathrm{CMB,c}}$) is used to calculate the CMB temperature T_{CMB}. The meaning of the symbols is given in Sections 2.2.5.2 and 2.2.5.3.

assumed to be equal thickness to the mobile layer in the stagnant lid at the surface (Bryson et al., 2019a). Second, δ_l has been calculated with the same parametrisation for lid thickness as the top boundary layer, but using $\Delta T = T_{\mathrm{CMB}} - T_{\mathrm{m}}$ rather than $\Delta T = T_{\mathrm{m}} - T_{\mathrm{s}}$ (Dodds et al., 2021). I have chosen to implement the CMB boundary layer scaling following Equation 13 in Thiriet et al. (2019), which has been benchmarked against 2D and 3D mantle convection simulations

$$\delta_l = (R - \delta_0 - r_{\mathrm{c}}) \left(\frac{Ra_{\mathrm{bl,crit}}}{Ra_{\mathrm{bl}}} \right)^{\frac{1}{3}}. \tag{2.10}$$

Here Ra_{bl} is the Rayleigh number in the boundary layer and $Ra_{\mathrm{bl,crit}}$ is the boundary layer critical Rayleigh number. Using equations 14 and 16 in Thiriet et al. (2019) to substitute for Ra_{bl} and $Ra_{\mathrm{bl,crit}}$ gives

$$\delta_l = 0.65(R - r_{\mathrm{c}})^{0.21} \left(\frac{\eta(T_{bl})}{(T_{\mathrm{CMB}} - T_{\mathrm{m}})g_{\mathrm{c}}} \right)^{\frac{1}{3}} \left(\frac{\eta(T_{\mathrm{m}})}{(T_{\mathrm{m}} - T_{\mathrm{s}})g(R)} \right)^{-0.07} \left(\frac{\kappa_{\mathrm{m}}}{\alpha_{\mathrm{m}}\rho_{\mathrm{m}}} \right)^{0.26}, \tag{2.11}$$

where T_{CMB} is the CMB temperature, and g_{c} is the gravitational field strength at the CMB. The temperature profile through the lower boundary layer is conductive and the temperature in the midpoint of the layer, $T_{\mathrm{bl}} = \frac{T_{\mathrm{m}} + T_{\mathrm{CMB}}}{2}$, is used to calculate Ra_{bl}. These boundary layer thicknesses control the heat flux from the CMB into the mantle during convection, $F^{\mathrm{conv}}_{\mathrm{CMB,m}}$

$$F^{\mathrm{conv}}_{\mathrm{CMB,m}} = \frac{-k_{\mathrm{m}}(T_{\mathrm{m}} - T_{\mathrm{CMB}})}{\delta_l} \tag{2.12}$$

and to the surface, F_{s}

$$F_{\mathrm{s}} = \frac{-k_{\mathrm{m}}(T_{\mathrm{s}} - T_{\mathrm{m}})}{\delta_0}. \tag{2.13}$$

Altogether, the thermal evolution of the convecting portion of the mantle is given by

$$\rho_{\mathrm{m}} c_{\mathrm{p,eff}} V_{\mathrm{m}} \frac{\partial T_{\mathrm{m}}}{\partial t} = -F_{\mathrm{lid}} A_{\mathrm{lid}} + F^{\mathrm{conv}}_{\mathrm{CMB,m}} A_{\mathrm{CMB}} + \rho_{\mathrm{m}} V_{\mathrm{m}} H_{\mathrm{Al}}. \tag{2.14}$$

Here, V_{m} is the volume of the convecting region; the silicate-modified specific heat capacity, $c_{\mathrm{p,eff}}$, is calculated at T_{m}; A_{lid} and A_{CMB} are the surface areas at the base of the stagnant lid and CMB, respectively; and $F_{\mathrm{lid}} = -k \frac{\mathrm{d}T}{\mathrm{d}r}\big|_{r=R-\delta_0}$ The silicate modified specific heat capacity, $c_{\mathrm{p,eff}}$, accounts for melting and solidification of silicate.

$$c_{\mathrm{p,eff}} = \begin{cases} c_{p,m} & T_{\mathrm{m}} < T_{\mathrm{m,s}} \\ c_{p,m}\left(1 + \frac{L}{c_{p,m}(T_{\mathrm{m,l}} - T_{\mathrm{m,s}})}\right) & T_{\mathrm{m,s}} < T_{\mathrm{m}} < T_{\mathrm{m,l}}. \end{cases} \tag{2.15}$$

Due to efficient heat loss by convection in the model, the mantle is never hotter than its liquidus temperature.

Heat is transported by conduction in the stagnant lid and the CMB boundary layer. As the mantle cools, both these layers thicken until the combined boundary layer thickness equal the thickness of the mantle, i.e., $\delta_0 + \delta_l = R - r_{\mathrm{c}}$. From this point, mantle convection ceases and the entire mantle cools conductively, such that the thermal evolution is dictated by

$$\rho_{\mathrm{m}} c_{\mathrm{p,eff}} \frac{\partial T}{\partial t} = \frac{1}{r^2} \frac{\partial}{\partial r} \left(k_{\mathrm{m}} r^2 \frac{\partial T}{\partial r} \right) + \rho_{\mathrm{m}} H_{\mathrm{Al}}. \tag{2.16}$$

In the conductive regime, the heat flux across the CMB into the mantle is given by

$$F^{\mathrm{cond}}_{\mathrm{CMB,m}} = -k_{\mathrm{m}} \left. \frac{\mathrm{d}T}{\mathrm{d}r} \right|_{r=r_{\mathrm{c}}^+} = -k_{\mathrm{m}} \frac{T^{\mathrm{m}}_{\mathrm{CMB+1}} - T_{\mathrm{CMB}}}{\Delta r}, \tag{2.17}$$

where $T^{\mathrm{m}}_{\mathrm{CMB+1}}$ and r_{c}^+ are the temperature and radius one node above the CMB, respectively, and Δr is the length of one grid cell in the simulation. T_{CMB} is determined by balancing the heat fluxes across the CMB ($F_{\mathrm{CMB,m}} = F_{\mathrm{CMB,c}}$).

2.2.5.3 Core

The thermal evolution of the core is coupled to the mantle by F_{CMB}. Due to the low pressure in planetesimal cores, the adiabatic temperature gradient is negligible ($T(r = r_{\mathrm{c}}) = 0.995T(r = 0)$ for a 250km core). Therefore, I assume the core is isothermal when convecting and that the criterion for core convection is $F_{\mathrm{CMB}} > 0$. At the beginning of the thermal evolution, the core and mantle are isothermal. If the abundance of ^{60}Fe in the core is low, the mantle experiences stronger radiogenic heating (from ^{26}Al) than the core. This increases the mantle temperature relative to the core and heat flows from the mantle to the core ($F_{\mathrm{CMB}} < 0$). The top of the core becomes thermally stratified, which inhibits core convection. While the core is thermally stratified, heat is transferred conductively as described by

$$\rho_{\mathrm{c}} c_{p,\mathrm{c}} \frac{\partial T}{\partial t} = \frac{1}{r^2} \frac{\partial}{\partial r} \left(k_{\mathrm{c}} r^2 \frac{\partial T}{\partial r} \right) + \rho_{\mathrm{m}} H_{\mathrm{Fe}}, \tag{2.18}$$

where $c_{p,\mathrm{c}}$ is core specific heat capacity, ρ_{c} is core density, k_{c} is core thermal conductivity, and $H_{\mathrm{Fe}} = H_{\mathrm{Fe},0} f_{^{60}\mathrm{Fe}} 0.01 X_{\mathrm{Fe}} e^{-\frac{ln(2)t}{t_{1/2,Fe}}}$ is heating from ^{60}Fe. An effective specific heat capacity is not used because the core begins molten and core solidification causes core convection, so is treated separately (see Section 2.2.5.4). The boundary conditions are a fixed CMB temperature using the temperature determined at the previous timestep (which is a reasonable approximation given the small timestep) and no temperature gradient at the centre of the body, i.e., $\left.\frac{\mathrm{d}T}{\mathrm{d}r}\right|_{r=0} = 0$. The conductive heat

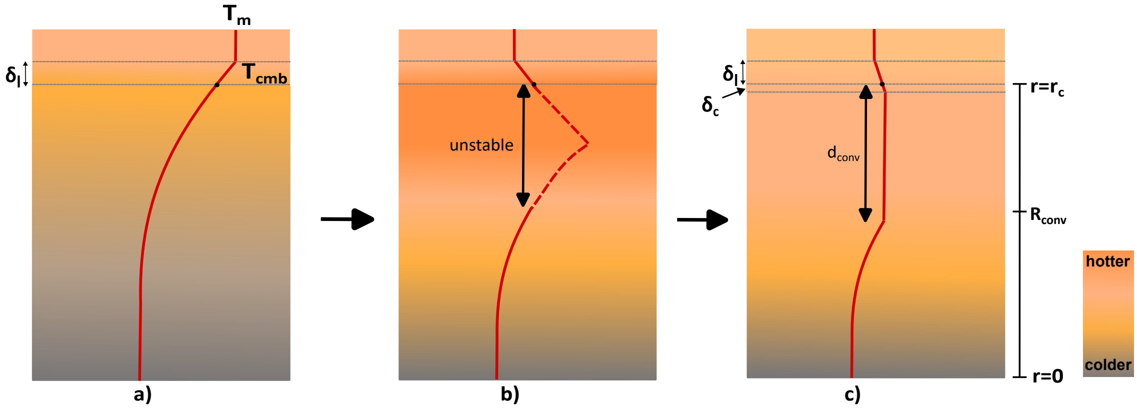

Figure 2.4: Schematic of the erosion of core thermal stratification by convective mixing of the unstable layer at the top of the core. The red lines indicate temperature profiles and temperature increases to the right. The dashed red line indicates the portion of the core that is unstable to convection. The top of the figure is the base of the convecting mantle above the CMB boundary layer in the mantle, δ_l, and CMB boundary layer in the core, δ_c. Time proceeds from left to right (a–c). Dashed lines indicate the mantle and core CMB boundary layers. The core CMB boundary layer (lower dashed layer) is only present when the core is convecting. Core thermal stratification is eroded either by mantle cooling (shifts the mantle temperature profile to the left relative to that of the core) or heating by ^{60}Fe in the core (shifts the core temperature profile to the right relative to the mantle). All symbols are defined in Section 2.2.5.3.

flux from the core to the CMB is given by

$$F^{\mathrm{cond}}_{\mathrm{CMB,c}} = -k_\mathrm{c}\frac{\mathrm{d}T}{\mathrm{d}r}\bigg|_{r=r_\mathrm{c}^-} = -k_\mathrm{c}\frac{T_\mathrm{CMB} - T^\mathrm{c}_{\mathrm{CMB}-1}}{\Delta r}, \tag{2.19}$$

where $T^\mathrm{c}_{\mathrm{CMB}-1}$ and r_c^- are the temperature and radius one node below the CMB, respectively. Once the CMB temperature is below the core temperature, either due to mantle cooling or core heating by ^{60}Fe, the top of the core begins to cool ($F_\mathrm{CMB} > 0$) and thermal stratification begins to erode (Figure 2.4). Positive F_CMB leads to the onset of convection in the upper portion of the core that is hotter than the CMB. As such, I assume this material convectively mixes down to the level of neutral buoyancy (the depth where core temperature is equal to the CMB temperature), d_conv. This forms an isothermal convecting layer, with temperature T_c, above a conductive region. This convective mixing continues until core thermal stratification is removed and the entire core is isothermal and convecting.

The temperature of the convecting portion of the core evolves according to

$$\rho_\mathrm{c} c_{p,\mathrm{c}} V_\mathrm{conv}\frac{\partial T_\mathrm{c}}{\partial t} = -F^{\mathrm{conv}}_{\mathrm{CMB,c}} A_\mathrm{CMB} + \rho_\mathrm{c} V_\mathrm{conv} H_\mathrm{Fe} + 4\pi R^2_\mathrm{conv} F_{R_\mathrm{conv}}, \tag{2.20}$$

where $R_{\text{conv}} = r_{\text{c}} - d_{\text{conv}}$, V_{conv} is the volume of the convecting portion of the core, and $A_{\text{CMB}} = 4\pi r_{\text{c}}^2$ is the CMB surface area (Dodds et al., 2021). While thermal stratification is being eroded, there is a heat flux into the convecting region from the conductive core beneath, $F_{R_{\text{conv}}} = -k_{\text{c}} \frac{\partial T}{\partial r}\big|_{r=R_{\text{conv}}}$, and the final term in Equation 2.20 is non-zero. When the core is convecting, a boundary layer, δ_{c}, forms at the top of the core. Although core rotation has a known effect on the convective boundary layer scaling law (Cheng et al., 2015), the combined effect of rotation, magnetic field generation and spherical geometry on heat transfer is unclear. Therefore, for simplicity, I assume the thickness of this boundary layer can be described by the non-rotating scaling (Schubert et al., 2001; Dodds et al., 2021)

$$\delta_{\text{c}} = \left(\frac{\kappa_{\text{c}} \eta_{\text{c}} Ra_{c,\text{iso}}}{\rho_{\text{c}} \alpha_{\text{c}} g_{\text{c}} (T_{\text{c}} - T_{\text{CMB}})} \right)^{\frac{1}{3}}, \tag{2.21}$$

where η_{c} and κ_{c} are the viscosity and thermal diffusivity of the core, respectively, and $Ra_{c,\text{iso}} = 1000$ (Schubert et al., 2001) is the critical Rayleigh number for isoviscous convection. The corresponding CMB heat flux is given by

$$F_{\text{CMB,c}}^{\text{conv}} = -k_{\text{c}} \frac{T_{\text{CMB}} - T_{\text{c}}}{\delta_{\text{c}}}. \tag{2.22}$$

2.2.5.4 Core solidification

Planetesimal CMBs are at lower pressures compared to Earth, so are likely to solidify inwards (Williams, 2009; Dodds et al., 2025). The mechanism of this inward solidification and its implications for dynamo generation are still being investigated, but could include formation of iron snow (Rückriemen et al., 2015; Davies and Pommier, 2018) formation of dendrites (Scheinberg et al., 2016) or viscous delamination of solid iron from the CMB (Neufeld et al., 2019). Previous models for mantled planetesimals that incorporate mantle convection either ended before core solidification (Elkins-Tanton et al., 2011; Sterenborg and Crowley, 2012; Dodds et al., 2021) or used eutectic core solidification to estimate the time period over which a compositional dynamo could be possible (Bryson et al., 2019a). To avoid the specificity of a particular core solidification model, I have chosen to use a parametrised model that captures two key changes in an inward solidifying core that will affect dynamo generation: (i) the decrease of convective lengthscale; (ii) the increase in sulfur content of the bulk liquid, assuming complete partitioning of sulfur into the liquid (Goldstein et al., 2009). This enables me to calculate a core solidification timescale and magnetic field strength during sub-eutectic core solidification.

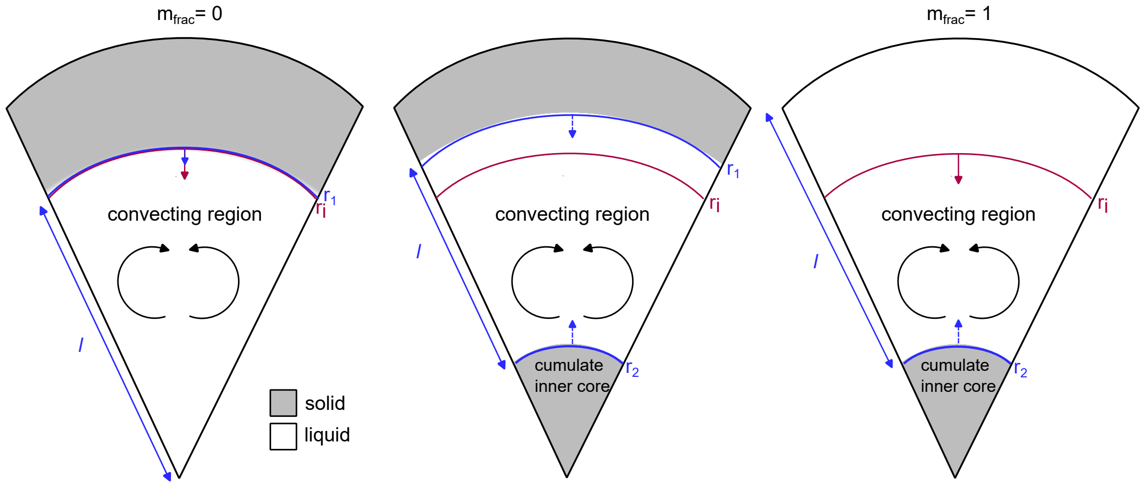

Figure 2.5: Schematic showing the geometry for core solidification. The amount of solidifying material is parametrised by r_i (magenta line) and the lengthscale for convection is give by $l = r_1 - r_2$. To account for the uncertainty in the mechanism of planetesimal core solidification I consider two endmember geometries (the middle scenario in the figure also depicts an intermediate geometry). In one endmember, m_{frac}= 0, the stable, solid portion of the core grows from the CMB inwards. In the other endmember, m_{frac}= 1, all solidified iron falls without remelting and forms a cumulate inner core. For m_{frac}= 0, the convective lengthscale decreases the slowest as the core solidifies, and for m_{frac}= 1, the convective lengthscale decreases the fastest. Due to the uncertainty in the mechanism for planetesimal core solidification, I do not prescribe how convection is driven in each scenario and just focus on the change in lengthscale. In both endmembers, the solid fraction in the solidified region is assumed to be 100%. For more details and discussion see Sections 2.2.5.4 and 2.6.1.

Core solidification is parametrised by a time-varying, inward moving boundary r_i, $\frac{\mathrm{d}r_i}{\mathrm{d}t} < 0$. The total material solidified is given by $M_{\mathrm{solid}} = \frac{4}{3}\pi\rho_{\mathrm{c}}(r_{\mathrm{c}}^3 - r_i^3)$. This solidified material can decrease the convective lengthscale of the core either due to formation of a solidified layer at the top of the core and/or due to the formation of a solid cumulate inner core formed by solidified material falling from r_i without remelting to the centre of the core (Scheinberg et al., 2016; Neufeld et al., 2019). To capture both of these possibilities, I vary the proportion of total solidified mass in the innermost core for a given r_i and time, M_{ic}, using a constant input parameter, $m_{\mathrm{frac}} = \frac{M_{\mathrm{ic}}}{M_{\mathrm{solid}}}$ (see Figure 2.5). Using $f = \frac{r_i}{r_{\mathrm{c}}}$ and conservation of mass, the resulting radii of the base of the solidified outer shell, r_1, and the solid innermost core, r_2, are given by

$$r_1 = r_{\mathrm{c}}(m_{\mathrm{frac}}(1 - f^3) + f^3)^{\frac{1}{3}}, \tag{2.23}$$

and

$$r_2 = r_{\mathrm{c}} m_{\mathrm{frac}}^{\frac{1}{3}}(1 - f^3)^{\frac{1}{3}}. \tag{2.24}$$

I show results for the two endmembers to explore the plausible range of geometric lengthscales: solidified outer layer only, $m_{\mathrm{frac}} = 0$; and solid inner core only, $m_{\mathrm{frac}} = 1$. Current dynamo theories suggest the convective lengthscale is some fixed fraction of this geometric lengthscale (Davidson, 2013; Aubert et al., 2017), but in this model I assume these lengthscales are the same (see Section 2.6.1). My model assumes the solidified portions of the core are completely solid and not a mushy layer, because self consistently calculating a solid fraction is overly complex given the uncertainties in core material properties (see Section 2.6.2).

The onset of solidification occurs when the temperature at the top of the core drops beneath the liquidus. Because compositional convection in the core will efficiently homogenise the temperature in the liquid core, the thermal conductivity of the solid portion is high, and the adiabatic gradient is minimal, the entire core is assumed to be isothermal at temperature T_{c} during solidification. During solidification, the heat flux across the CMB is balanced by secular cooling, radiogenic heating, and release of latent heat. Energy released due to changes in gravitational potential during solidification has a negligible effect on the time of core solidification (see Appendix A.3.2) and contributions due to planetary contraction are also negligible. The resulting thermal evolution of the core is expressed as

$$F_{\mathrm{CMB}} A_{\mathrm{CMB}} = M_{\mathrm{c}} H_{\mathrm{Fe}} - M_{\mathrm{c}} c_{p,c} \frac{\mathrm{d}T_{\mathrm{c}}}{\mathrm{d}t} - 4\pi r_i^2 \rho_{\mathrm{c}} L_{\mathrm{c}} \frac{\mathrm{d}r_i}{\mathrm{d}t}, \tag{2.25}$$

where L_c is the latent heat from solidification of iron and M_c is the total mass of the core (Nimmo, 2007). For an isothermal solidifying core, the rate of change of inner core boundary is given by

$$\frac{\mathrm{d}r_i}{\mathrm{d}t} = -\frac{1}{\rho_\mathrm{c} g_\mathrm{c} \frac{\mathrm{d}T_\mathrm{c,l}}{dP}} \frac{\mathrm{d}T_\mathrm{c}}{\mathrm{d}t}, \tag{2.26}$$

which is adapted to account for inward solidification and no core adiabat (Gubbins et al., 2003; Nimmo, 2009; Davies and Pommier, 2018). The sign of the pressure gradient of the liquidus, $\frac{\mathrm{d}T_\mathrm{c,l}}{\mathrm{d}P}$, determines whether $\frac{\mathrm{d}r_i}{\mathrm{d}t}$ is positive (outward solidification) or negative (inward solidification). As the core solidifies, I assume as an upper limit that sulfur partitions completely into the liquid portion of the core (Goldstein et al., 2009; Nichols et al., 2021), is homogeneously distributed, and this partitioning has a negligible effect on the total volume of the core. This enriches the liquid inner core relative to the initial sulfur content, $X_\mathrm{S,0}$, according to (Nichols et al., 2021)

$$X_\mathrm{S} = \frac{r_\mathrm{c}^3}{r_i^3} X_\mathrm{S,0} = \frac{1}{f^3} X_\mathrm{S,0}. \tag{2.27}$$

Once the core sulfur content reaches the eutectic (33 wt% S), the remaining liquid inner core will solidify as FeS. During eutectic solidification, there is no temperature change ($T_\mathrm{c} = 1260\,\mathrm{K}$) and the fraction of core solidified is determined by the removal of latent heat, as given by

$$\frac{\mathrm{d}r_i}{\mathrm{d}t} = -\frac{F_\mathrm{CMB} A_\mathrm{CMB} - M_\mathrm{c} H}{4\pi r_i^2 L_\mathrm{c} \rho_\mathrm{c}}. \tag{2.28}$$

Once the whole core has solidified ($r_i < 0.001$), the model run ends.

This model uses the Fe-FeS liquidus from Buono and Walker (2011), which depends on pressure and bulk sulfur content,

$$T_\mathrm{c,l}(X_\mathrm{S,mol}, P) = A(P)X_\mathrm{S,mol}^4 + B(P)X_\mathrm{S,mol}^3 + C(P)X_\mathrm{S,mol}^2 + D(P)X_\mathrm{S,mol} + E(P), \tag{2.29}$$

where the pressure, P, is in GPa and $X_\mathrm{S,mol} = \frac{X_\mathrm{S}}{100 - X_\mathrm{S}} \frac{M_\mathrm{r,Fe}}{M_\mathrm{r,S}}$ is the mole fraction of FeS in the core, $M_{\mathrm{r},i}$ are the molar masses of sulfur (32.07 amu) and iron (55.84 amu), respectively, and X_S is the core sulfur content in wt %. The pressure dependent coefficients are given by (Buono and Walker, 2011)

$$\begin{aligned}
A &= -2.4724P^4 + 28.025P^3 + 9.1404P^2 + 581.71P + 3394.8,\\
B &= 1.7978P^4 - 6.7881P^3 - 197.69P^2 - 271.69P - 8219.5,\\
C &= -0.1702P^4 - 9.3959P^3 + 163.53P^2 - 319.35P + 5698.6,\\
D &= -0.2308P^4 + 7.1P^3 - 64.118P^2 + 105.98P - 1621.9,\\
E &= 0.2302P^4 - 5.3688P^3 + 38.124P^2 - 46.681P + 1813.8.
\end{aligned} \tag{2.30}$$

This expression for the Fe-FeS liquidus is valid for sub-eutectic sulfur concentrations and pressures $< 10\,\mathrm{GPa}$. The pressure at a radius r in the core (assuming an incompressible core and mantle) is given by

$$P_\mathrm{c} = \frac{2\pi G}{3}\left[r_\mathrm{c}^2(\rho_\mathrm{c}^2 - \rho_\mathrm{m}^2) + R^2\rho_\mathrm{m}^2 + 2\rho_\mathrm{m}(\rho_\mathrm{c} - \rho_\mathrm{m})r_\mathrm{c}^2\left(1 - \frac{r_\mathrm{c}}{R}\right)\right]. \tag{2.31}$$

For a $\mathcal{O}(100\,\mathrm{km})$ radius body, the difference in pressure between the centre and the CMB is $\mathcal{O}(10^{-3}\,\mathrm{GPa})$; therefore, the central pressure is always used in the expression for the liquidus. The sulfur content used to calculate the liquidus and pressure gradient of the liquidus is updated as the core solidifies. Recently, Williams (2025) highlighted that the Buono and Walker (2011) liquidus may not be appropriate for planetesimals due to the inconsistency between the slope of the liquidus and experimental data for pure iron across a range of pressures. To investigate this issue, models were also run using a modified linear liquidus slope interpolated from the data in Williams (2025) (Dodds, pers. comm.). There was minimal difference in the duration and rate of core solidification, and the duration of dynamo generation between the two liquidus models (see Appendix A.3.4).

2.2.6 Magnetic field generation

2.2.6.1 Magnetic Reynolds number

The magnetic Reynolds number, Re_m, determines whether flow in a planetesimal core is vigorous enough to generate a magnetic field. This dimensionless number characterises the balance between magnetic induction and diffusion in the fluid and is given by

$$Re_\mathrm{m} = \frac{ul}{\lambda}, \tag{2.32}$$

where u and l are the characteristic speed and lengthscale of the flow and $\lambda = 1.3\,\mathrm{m^2 s^{-1}}$ (Weiss et al., 2010) is the magnetic diffusivity. If Re_m is greater than a critical value, a magnetic field can be generated. The minimum analytical critical value is 10 and numerical dynamo simulations suggest a critical value between 40–100 (Christensen and Aubert, 2006). To account for this uncertainty, I calculate three sets of dynamo onset and cessation times with critical Re_m values of 10, 40, and 100. λ depends on pressure, temperature and composition, but the appropriate value for a given set of conditions is uncertain (Pozzo et al., 2013; Konôpková et al., 2016; Tassin et al., 2021). In addition, measurements are limited to Earth-like conditions, i.e., much higher pressures and temperatures than in planetesimals. Therefore, I take

λ to be a constant between simulations and uncertainties in this parameter are considered by adopting multiple critical Re_m values. l is assumed to be the length over which convection can occur, $l = r_i - R_\mathrm{conv}$, which accounts for the possible existence of a stratified layer. In this model, I use the numerical scaling from Aubert et al. (2009) for the characteristic velocity, u,

$$u = c_u p^{0.42} \Omega l. \tag{2.33}$$

$c_u = 1.31$ is a constant (Aubert et al., 2009), Ω is the rotation rate of the planetesimal, and p is the convective power per unit volume. To enable comparison with previous work, I adopt a nominal rotation period of 10 hours ($\Omega = 1.7 \times 10^{-4}\mathrm{s}^{-1}$), which is a typical value for rotation periods of asteroids at the present day (Bryson et al., 2019a; Dodds et al., 2021). I use this characteristic velocity scaling law because it is not singular in the absence of an inner core so can be applied to inward solidification where a solid inner core is not present. Additionally, this law has been shown to agree with subsequent analytical derivations of dynamo scaling laws (Davidson, 2013). This also aligns with the work of Christensen (2015) who used this scaling law when determining the dimensional magnetic field strength of Ganymede.

2.2.6.2 Magnetic field strength

In planetesimal and planetary cores, the leading order force balance is geostrophic and the second order force balance controls dynamo generation (Aubert et al., 2017; Davies et al., 2022). In planetesimal cores, the Lorentz and buoyancy forces are the next strongest after the Coriolis force (Table A.1), which means the Magnetic-Archimedean-Coriolis (MAC) force balance is the relevant force balance for dynamo generation. For a core in MAC force balance, the magnetic dipole field at the CMB can be estimated as

$$B^\mathrm{dip}_\mathrm{CMB} = c_B f^{\frac{1}{2}}_\mathrm{ohm} p^{0.31} (\rho_\mathrm{c} \mu_0)^{\frac{1}{2}} \Omega l. \tag{2.34}$$

Here $f_\mathrm{ohm} = 1$ (Christensen, 2009) is the fraction of energy dissipated ohmically in the core, $\mu_0 = 4\pi \times 10^{-7}\mathrm{NA}^{-2}$ is the vacuum permeability and $c_B = 0.23$ is the median value of the scaling constant for CMB dipole field strength across the simulations assessed in Davies et al. (2022). The field strength decays from the CMB to the surface according to $B_\mathrm{surf} = \left(\frac{r_\mathrm{c}}{R}\right)^3 B^\mathrm{dip}_\mathrm{CMB}$. The exponents of the scaling law agree within error of the field strength scaling in Aubert et al. (2009), so this is consistent with the chosen characteristic velocity scaling. Additionally, the MAC force balance has been shown to best fit a large range of simulations of the geodynamo (Davies et al.,

2022) and scaling analysis suggests planetesimal dynamos are in a similar regime (see Table A.1).

2.2.6.3 Convective power and buoyancy flux

The scaling laws for both u and B require a dimensionless convective power per unit volume, p. This can be calculated using $p = \gamma Ra_Q$, where $\gamma = 3/5$ (Equation 18 in Aubert et al., 2009, for no inner shell and $f_i = 0$). Ra_Q is the flux based Rayleigh number given by

$$Ra_Q = \frac{g(r_i)Q_b}{4\pi\rho_\mathrm{c}\Omega^3 l^4}, \tag{2.35}$$

for a gravitational acceleration at the top of the convecting region, $g(r_i)$, and buoyancy flux, Q_b. The buoyancy flux combines the two possible contributions: thermal and compositional. Adapting from Buffett et al. (1996) (see Appendix A.3.1) for an inwardly solidifying core with $\frac{\mathrm{d}r_i}{\mathrm{d}t} < 0$, the buoyancy flux at the liquid inner core boundary r_i is given by

$$Q_b = 4\pi r_i^2 \left[\frac{\alpha_\mathrm{c} k_\mathrm{c}}{c_{p,c}} \left(-\left.\frac{\mathrm{d}T}{\mathrm{d}r}\right|_{r_i} - \frac{\alpha_\mathrm{c} g(r_i)}{c_{p,c}} T(r_i) \right) - \left(\Delta\rho + \frac{\alpha_\mathrm{c}\rho_\mathrm{c} L_\mathrm{c}}{c_{p,c}} \right) \frac{\mathrm{d}r_i}{\mathrm{d}t} \right], \tag{2.36}$$

where α_c is the core thermal expansivity. The first term in this equation represents the thermal buoyancy contribution from the superadiabatic heat flux at the upper boundary of the convecting region (i.e., the heat flux available to drive convection), assuming all the heat is advected by the flow. Although I have neglected the adiabatic gradient in the temperature structure of the convecting core, I retain the adiabatic heat flux in the expression for the buoyancy flux for consistency with previous literature (e.g., Lister, 2003; Rückriemen et al., 2015; Dodds et al., 2021). In my simulations, Re_m becomes subcritical before the CMB heat flux becomes subadiabatic and the adiabatic gradient is an order of magnitude smaller than the CMB heat flux when Re_m is supercritical. Therefore, including the adiabatic gradient will have minimal effect on the timings of dynamo generation.

The second term in Equation 2.36 is the compositional density difference and the latent heat release from the solidifying core. $\Delta\rho = \rho_\mathrm{Fe,s} - \rho_\mathrm{l}(X_\mathrm{S})$ is the density difference between the solidified iron $\rho_\mathrm{Fe,s} = 7800\,\mathrm{kgm^{-3}}$ (Bryson et al., 2015) and the liquid inner core, ρ_l, which is calculated using the relationship from Morard et al. (2018)

$$\rho_\mathrm{l} = (-3108X_\mathrm{S,at}^2 - 5176X_\mathrm{S,at} + 6950)(1 + \alpha_\mathrm{c}(1900 - 1600)), \tag{2.37}$$

where $X_{\mathrm{S,at}} = \left(1 + \frac{1-0.01X_{\mathrm{S}}}{0.01X_{\mathrm{S}}}\frac{M_{r,\mathrm{S}}}{M_{r,\mathrm{Fe}}}\right)^{-1}$ is atom % S and the core is assumed to only contain Fe and FeS. In Equation 2.37, the term in the first parentheses is the density from Morard et al. (2018) and the term in the second parentheses corrects for the fact the expression from Morard et al. (2018) was derived for ambient pressure at a temperature of 1900 K, whereas peak core temperatures are ~ 1600 K in my model. The change in core density due to core cooling below 1600 K to the eutectic (a further 3% difference in density) was neglected in order to simplify the model. Although I explore geometries for two possible endmembers for core solidification (Figure 2.5), I use the same density difference for both, because it is the correct order of magnitude and $\Delta\rho$ is raised to a fractional power in both Equations 2.33 and 2.34.

Prior to core solidification, Equations 2.35 and 2.36 are evaluated at the CMB ($r_i = r_{\mathrm{c}}$) and the second term in Equation 2.36 is zero. As the core solidifies inwards, these equations are evaluated at the liquid inner core boundary, r_i, which is the boundary of the convecting region. Once the eutectic composition is reached, the second term in Equation 2.36 is no longer calculated, because a compositional density difference is no longer generated by solidification. Combining thermal and compositional buoyancy flux contributions enables both drivers of convection to be considered simultaneously at all timesteps.

2.2.7 Numerical Implementation

My model is 1D and spherically symmetric. The one spatial dimension is radius, r, which runs from $r = 0$ at the centre of the planetesimal to $r = R$ at the surface. The model is run on a grid with fixed node spacing of $\Delta r = 500$ m following Bryson et al. (2019a) with the first node at the centre of the planetesimal and the last at the surface. The temperature change of convecting regions was calculated using the forward Euler method. The temperature in the conductive portion was calculated using matrix methods with a forward-in-time, centered-in-space (FTCS) stencil (see Appendix A.6). The boundary conditions are $\frac{dT}{dr}\big|_{r=0} = 0$, flux continuity at the CMB and a fixed surface temperature. The core conductive timescale, $\tau_{\mathrm{c,cond}} = \frac{(\Delta r)^2}{\kappa_{\mathrm{c}}}$, is a factor of ten shorter than the mantle conductive timescale. Therefore, the timestep was fixed to $\Delta t = 0.075\tau_{c,\mathrm{cond}}$ in order to resolve conduction in the core and mantle and ensure stability of the FTCS scheme, which is stable for $\Delta t \leq \frac{(\Delta r)^2}{2\kappa}$. To test the gridsize and timestep, four simulations were run for a 300 km body: one using the model gridsize and timestep, one for half the gridsize, one for two thirds the timestep, and one for one third the timestep. The results of the model were independent of the choice of timestep and gridsize (Appendix A.6).

2.2.8 Parameter values

The list of parameters used in the model are given in Table 2.1. The viscosity parameters are poorly constrained; the values here are the median value in a wide range (explored in more detail in Chapter 3). The range of possible initial core sulfur contents, $X_{\mathrm{S},0}$, primordial $^{60}\mathrm{Fe}/^{56}\mathrm{Fe}$, planetesimal radii, and accretion times are shown in Table 2.2. The maximum $X_{\mathrm{S},0}$ is assumed to be the eutectic composition and the minimum $X_{\mathrm{S},0}$ is based on the highest liquidus temperature for which all the Fe-FeS will be molten before differentiation for $\phi_{\mathrm{C}} = 0.3$ and $R = 300\,\mathrm{km}$. The eutectic sulfur content varies with pressure and was estimated as 33 wt% by finding the intersection of the liquidus with the eutectic temperature of 1260 K (Buono and Walker, 2011) for a 300 km radius planetesimal. Due to its presumed low concentration, previous studies have neglected radiogenic heating from $^{60}\mathrm{Fe}$. However, recent studies suggest the primordial $^{60}\mathrm{Fe}/^{56}\mathrm{Fe}$ could be as high as 6×10^{-7} (Cook et al., 2021). To incorporate this possible range, I adopt values from 0 to $6{\times}10^{-7}$. The minimum planetesimal radius is based on the lower limit for compositional dynamo generation (Nimmo, 2009), while the upper limit is approximately the radius of Ceres (470 km; Russell et al., 2016), the largest asteroid surviving today. Planetesimal accretion times affect the strength of radiogenic heating and must be within 2.5 Ma after CAI formation for there to be sufficient $^{26}\mathrm{Al}$ for full planetesimal differentiation (Neumann et al., 2012). Accretion earlier than 1.1 Ma after CAI formation reconciles best with my choice to neglect silicate melt migration (Monnereau et al., 2023, see Section 2.4).

2.3 Example Run

Results of an example run for a 500 km body that accreted 0.8 Ma after CAI formation with $^{60}\mathrm{Fe}/^{56}\mathrm{Fe} = 10^{-8}$ and $X_{\mathrm{S},0} = 29.85\,\mathrm{wt\%}$ are shown in Figures 2.6–2.9. The planetesimal radius and accretion time were chosen to enable comparison with the instantaneous accretion model (Case 1) from Dodds et al. (2021). The $X_{\mathrm{S},0}$ value is the median value for the range of $X_{\mathrm{S},0}$ that can be used in my model. Following a similar argument, I chose to use $^{60}\mathrm{Fe}/^{56}\mathrm{Fe} = 10^{-8}$ to produce a representative simulation. This $^{60}\mathrm{Fe}$ value is higher than that used in previous models ($^{60}\mathrm{Fe}/^{56}\mathrm{Fe} = 0$; Bryson et al., 2019a; Dodds et al., 2021), but is on the lower end of recently measured primordial

Symbol	Meaning	Value	Reference
Whole body parameters			
T_{s}	Surface temperature	$200\,\mathrm{K}$	*Bryson et al. (2019a)
Ω	Rotational frequency of planetesimal	$1.75 \times 10^{-4}\mathrm{s}^{-1}$	*Bryson et al. (2019a)
Undifferentiated material parameters			
ρ_{ch}	Density	$(\rho_{\mathrm{m}}(R^3 - r_{\mathrm{c}}^3) + \rho_{\mathrm{c}} r_{\mathrm{c}}^3)/R^3\ \mathrm{kgm}^{-3}$	
$c_{\mathrm{p,ch}}$	Specific heat capacity	$c_{p,m}$	Elkins-Tanton et al. (2011) Bryson et al. (2019a)
α_{ch}	Thermal expansivity	α_{m}	Elkins-Tanton et al. (2011) Bryson et al. (2019a)
k_{ch}	Thermal conductivity	$k_{\mathrm{m}} = \kappa_{\mathrm{m}} \rho_{\mathrm{m}} c_{\mathrm{p,m}}$	Elkins-Tanton et al. (2011) Bryson et al. (2019a)
Mantle parameters			
ρ_{m}	Density	$3000\,\mathrm{kgm}^{-3}$	Elkins-Tanton et al. (2011)
$c_{p,m}$	Specific heat capacity	$800\ \mathrm{Jkg}^{-1}\mathrm{K}^{-1}$	Ghosh and McSween (1999)
L_{m}	Latent heat of fusion	$400 \times 10^3\ \mathrm{Jkg}^{-1}$	*Ghosh and McSween (1998)
$T_{\mathrm{m,l}}$	Liquidus	$1800\,\mathrm{K}$	Dodds et al. (2021)
$T_{\mathrm{m,s}}$	Solidus	$1400\,\mathrm{K}$	Dodds et al. (2021)
α_{m}	Thermal expansivity	$4 \times 10^{-5}\,\mathrm{K}^{-1}$	*Nimmo and Stevenson (2000)
κ_{m}	Thermal diffusivity	$9 \times 10^{-7}\,\mathrm{m}^2\mathrm{s}^{-1}$	Dodds et al. (2021)
Ra_{c}	Critical Rayleigh number for isoviscous convection	1000	Schubert et al. (2001)
Viscosity parameters			
ϕ_{C}	Critical melt fraction	0.3	Scott and Kohlstedt (2006)
β	Arrhenius slope	$0.0225\,\mathrm{K}^{-1}$	E=366 kJ mol^{-1}, $T_{\mathrm{ref}} = 1600\,\mathrm{K}$ Hirth and Kohlstedt (2003)
α_{n}	Melt weakening exponent	30	Hirth and Kohlstedt (2003)
η_0	Reference viscosity	$10^{19}\,\mathrm{Pa\,s}$	Lichtenberg et al. (2019b)
η_{l}	Liquid viscosity	$10\,\mathrm{Pa\,s}$	Giordano et al. (2008)
Core parameters			
$\rho_{\mathrm{Fe},s}$	Solid iron density	$7800\,\mathrm{kgm}^{-3}$	Bryson et al. (2015)
$c_{p,c}$	Specific heat capacity	$850\ \mathrm{Jkg}^{-1}\mathrm{K}^{-1}$	*Bartels and Grove (1991)
L_{c}	Latent heat of fusion of core	$270 \times 10^3\ \mathrm{Jkg}^{-1}$	*Ghosh and McSween (1998)
$T_{\mathrm{c,s}}$	Fe-FeS solidus	$1260\,\mathrm{K}$	Buono and Walker (2011)
$X_{\mathrm{S,eut}}$	Eutectic sulfur content	33 wt %	Buono and Walker (2011), $R = 300\,\mathrm{km}$
α_{c}	Thermal expansivity	$9.2 \times 10^{-5}\,\mathrm{K}^{-1}$	*Nimmo (2009)
k_{c}	Thermal conductivity	$30\,\mathrm{Wm}^{-1}\mathrm{K}^{-1}$	*Opeil et al. (2010)
η_{c}	Viscosity	$0.01\,\mathrm{Pa\,s}$	*de Wijs et al. (1998)
λ	Magnetic diffusivity	$1.3\,\mathrm{m}^2\mathrm{s}^{-1}$	*Weiss et al. (2010)
f_{ohm}	Fraction of energy flux dissipated ohmically	1	Christensen (2009)
c_u	Convective velocity constant	1.31	Aubert et al. (2009)
c_b	Magnetic field strength constant	0.23	Davies et al. (2022)
Radiogenic heating parameters			
$H_{\mathrm{Al},0}$	Heating power of ^{26}Al at t=0 Ma after CAI formation.	$0.355\,\mathrm{Wkg}^{-1}$	*Castillo-Rogez et al. (2009)
$f_{^{26}\mathrm{Al}}$	^{26}Al/^{27}Al	5×10^{-5}	*MacPherson et al. (1995)
X_{Al}	wt % Al in accreting material	1.4	*Doyle et al. (2015)
$t_{1/2,\mathrm{Al}}$	^{26}Al half life	0.717 Ma	*Neumann et al. (2012)
$H_{\mathrm{Fe},0}$	Heating power of ^{60}Fe at t=0 Ma after CAI formation.	$0.0366\,\mathrm{Wkg}^{-1}$	Ruedas (2017)
X_{Fe}	wt % Fe in accreting material	22.4 wt %	Lodders (2021)
$t_{1/2,Fe}$	^{60}Fe half life	2.62 Ma	Ruedas (2017)

Table 2.1: All fixed parameters used in the model and their references. Blank reference indicates the value is chosen in this work. The choice of viscosity parameters is justified in Section 2.2.2. References with a * denote the that they were used in Dodds et al. (2021), but the original reference has been given here.

Symbol	Meaning	Value	Reference (if relevant)
Computational parameters			
Δr	Cell spacing	$500\,\mathrm{m}$	Bryson et al. (2019a)
Δt	Timestep	$0.075\frac{(\Delta r)^2}{\kappa_c}\ s$	
Variable parameters			
R	Planetesimal radius	$100\text{–}500\,\mathrm{km}$	
$X_{S,0}$	Initial core sulfur content	$26.7\text{–}33\,\mathrm{wt}\%$	
$f_{^{60}\mathrm{Fe}}$	$^{60}\mathrm{Fe}/^{56}\mathrm{Fe}$	$0-6\times10^{-7}$	Dodds et al. (2021) Cook et al. (2021)
t_{acc}	Accretion time	< 2.5 Ma after CAI formation	Neumann et al. (2012)

Table 2.2: Computational parameters and variable parameters for model runs. The choice of variable parameters is explained in Section 2.2.8. Accretion times are discussed further in Section 2.4.

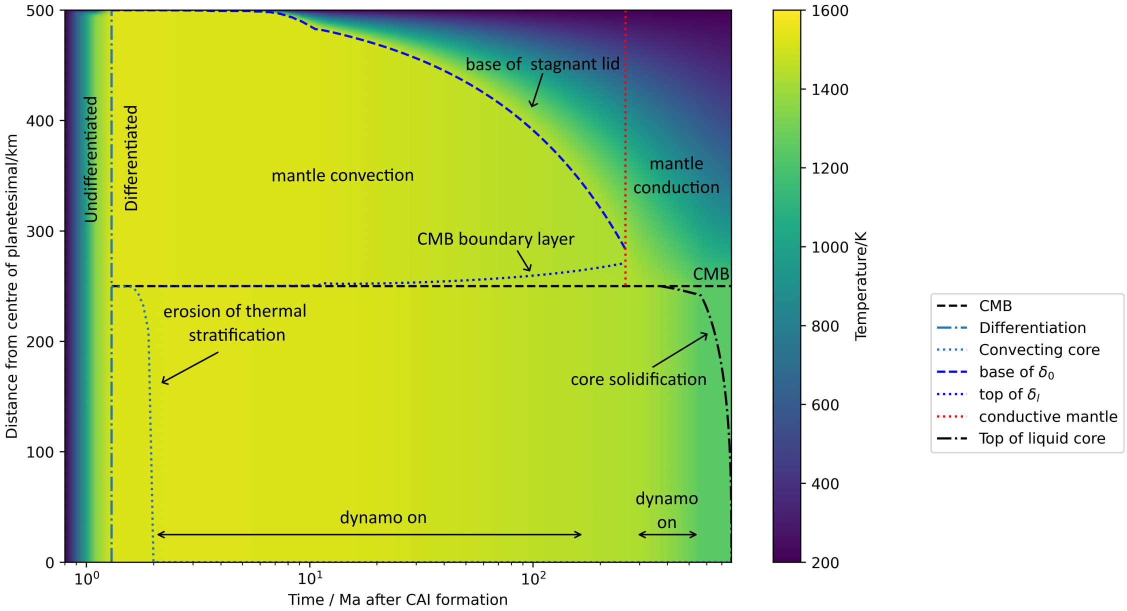

Figure 2.6: Annotated thermal profile for a 500 km radius planetesimal accreted at 0.8 Ma after CAI formation with $^{60}\mathrm{Fe}/^{56}\mathrm{Fe} = 10^{-8}$ and $X_{S,0} = 29.85\,\mathrm{wt}\%$. Prior to differentiation, the body heats up due to radiogenic heating by $^{26}\mathrm{Al}$. After differentiation, core thermal stratification is eroded rapidly due to heating by $^{60}\mathrm{Fe}$. The stagnant lid and CMB boundary layer thicken until the two boundary layers meet and convection ceases, which terminates the dynamo. The temperature gradient at the CMB steepens following the cessation of convection and the dynamo restarts prior to the onset of core solidification. The black horizontal arrows indicate the period of dynamo activity, their vertical position is arbitrary.

^{60}Fe/^{56}Fe values, which range from 10^{-8} to 6×10^{-7} (Cook et al., 2021). All fixed parameters are given in Table 2.1.

The thermal profile for this 500 km radius planetesimal is shown in Figure 2.6. The planetesimal reaches its critical melt fraction, ϕ_C, and differentiates at 1520 K, 1.2 Ma after CAI formation[1] (0.4 Ma after accretion). Once the planetesimal differentiates, the combined stagnant lid and CMB boundary layer thickness is less than the mantle

---

[1] The time resolution of this description is limited by the frequency at which model output is saved. Output is saved every 0.01 Ma prior to differentiation and every 0.1 Ma after differentiation. All times given are representative of the approximate time for these processes. Therefore times are given to a precision of 0.1 Ma from 1–10 Ma, 1 Ma for 10–100 Ma and 10 Ma for >100 Ma.

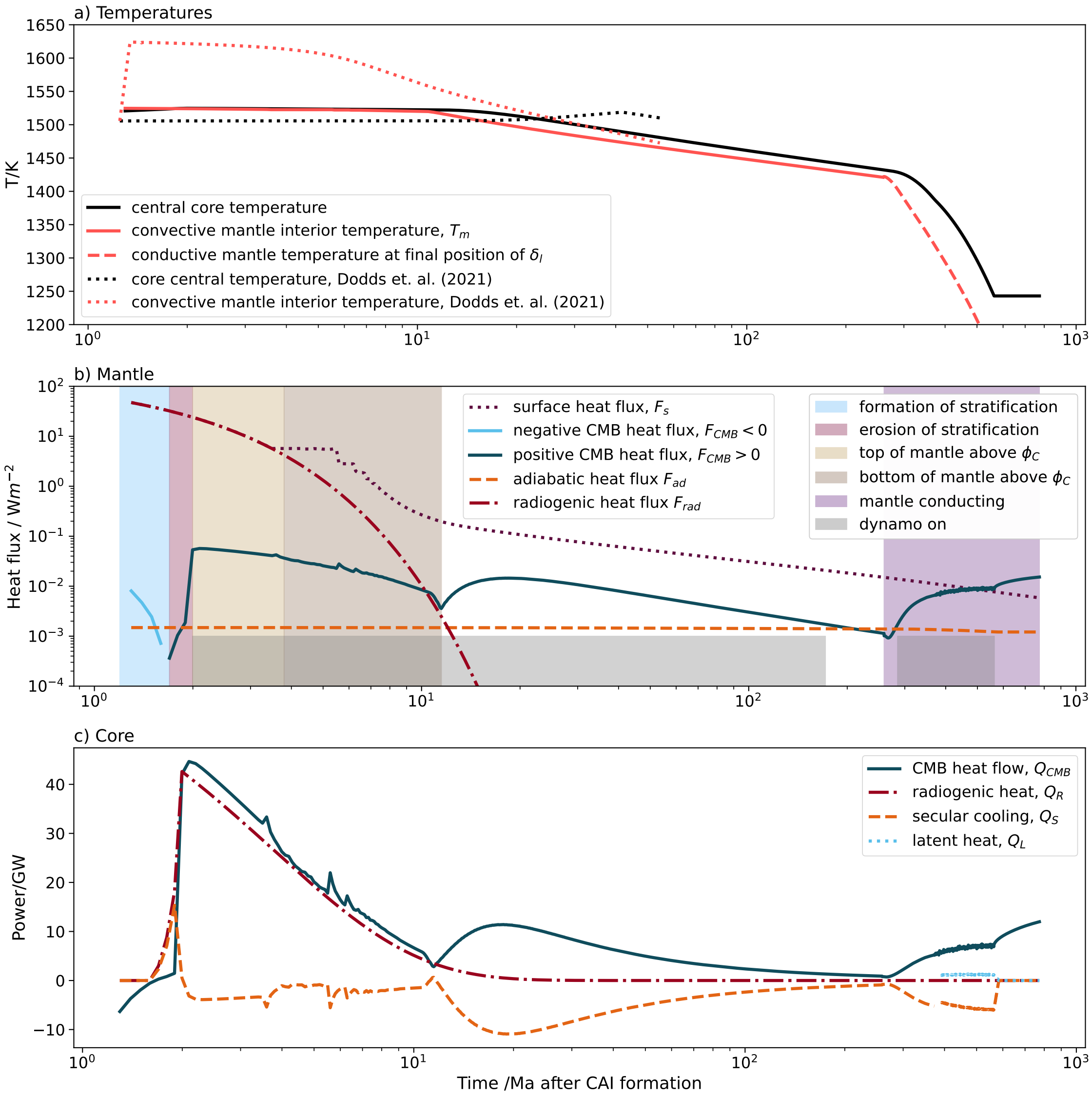

Figure 2.7: *see next page*

Figure 2.7 *(previous page)*: Temperatures (a) and mantle heat fluxes (b) and core power sources (c) for the same parameters as Figure 2.6: 500 km planetesimal accreted at 0.8 Ma after CAI formation with ^{60}Fe/^{56}Fe = 10^{-8} and $X_{\mathrm{S},0} = 29.85\,\mathrm{wt}\%$. In the upper panel, after the cessation of convection, the mantle temperature evolution at the position of the final mantle height of the CMB boundary layer is shown by the red, dashed line. For comparison, the central core temperature and convecting mantle temperature from Dodds et al. (2021) are shown by the dotted lines. The Dodds et al. (2021) temperature evolution is shorter, because their model ended after the cessation of mantle convection ($\sim$ 50 Ma in their model). In the middle panel, at the beginning of the thermal evolution, F_{CMB} is negative, because the mantle heats up faster than the core (blue box). The absolute value of F_{CMB} has been plotted for these times (light blue line). Before 3.8 Ma after CAI formation, the surface heat flux, F_{s}, matches the radiogenic heat flux, F_{rad}, because the top of the mantle is above the critical melt fraction and there is a negative feedback loop between mantle temperature and stagnant lid thickness (yellow-brown box). The downward spike in F_{CMB} at 13 Ma after CAI formation is due to the rapid thickening of the CMB boundary layer when the base of the mantle drops below the critical melt fraction. The horizontal plateaus and vertical drops in F_{s} and spikes in F_{CMB} prior to 13 Ma is a model artefact due to the discretisation of the stagnant lid, and I expect smooth curves in reality. The CMB heat flux, F_{CMB}, decreases with time and the dynamo turns off just before the cessation of convection due to the thickening of the CMB boundary layer. In the lower panel, the latent heat contribution only appears once the core begins solidifying. The latent heat release and secular cooling during core solidification are shown as a rolling average over 200 timesteps (20 Ma) to remove oscillations due to the discrete nature of the model.

thickness and the whole mantle convects. The mantle reaches a peak mantle temperature of 1525 K within 0.1 Ma of differentiation. At these early times, radiogenic heating from ^{26}Al is so strong that the dominant controls on mantle temperature are surface heat flux, F_{s}, and radiogenic heat flux, F_{rad} (see Figure 2.7, middle panel). When the mantle melt fraction is at or above ϕ_{C}, there is a negative feedback between F_{s} and temperature, because the planetesimal loses heat very efficiently. An increase in mantle temperature, due to high F_{rad}, causes the stagnant lid to thin, which in turn increases F_{s}, causing the mantle temperature to decrease. This results in a mantle peak temperature close to $T_{\phi_{\mathrm{C}}} = 1520\,\mathrm{K}$ and very thin stagnant lid ($\sim$100-700 m) and CMB boundary layers ($\sim$100 m) at early times. This feedback plays a role until 3.8 Ma after CAI formation (Figure 2.7). From 1.2–1.7 Ma after CAI formation the mantle is hotter than the core due to the faster decay of ^{26}Al in the mantle compared to ^{60}Fe in the core. From 1.7–2.0 Ma after CAI formation, core thermal stratification is eroded as radiogenic heating from ^{60}Fe increases the core temperature (Figure 2.7,

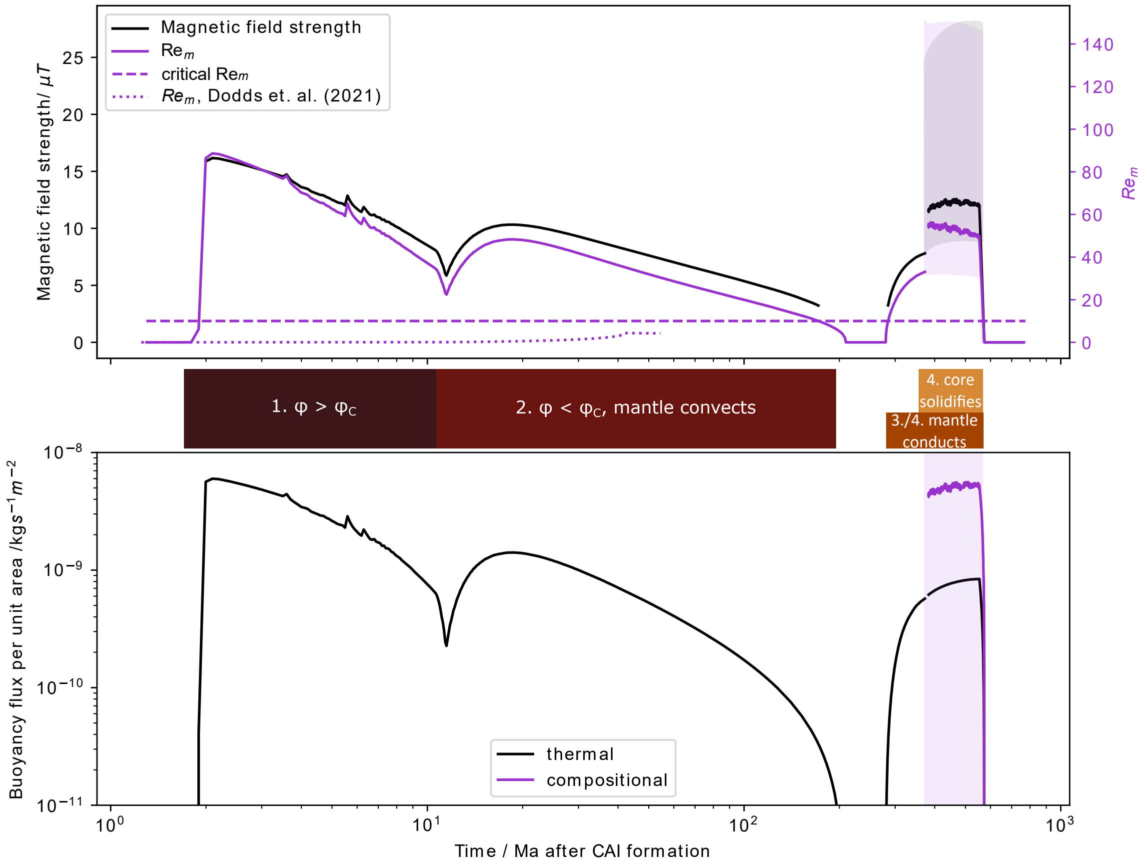

Figure 2.8: Predicted dipole magnetic field strength at the surface of the planetesimal and magnetic Reynolds number, Re_m, (upper panel) and buoyancy flux per unit area (lower panel) as a function of time for the same planetesimal as Figure 2.7. In the upper panel, the purple, horizontal dashed line is a critical Re_m of 10 and the dotted, purple line is the Re_m from Dodds et al. (2021). The longevity of core thermal stratification in Dodds et al. (2021) prevented their Re_m from becoming supercritical. The spikes in the traces prior to 13 Ma are model artefacts due to the discretisation of the stagnant lid. Due to the discrete nature of latent heat release in the model, the magnetic field strength and Re_m oscillate during core solidification. This oscillating output is shown by the faded grey and purple traces, and the rolling average over 200 output steps (20 Ma) is shown in bold. The small gap between the purely thermally driven dynamo and the average values for the thermo-compositional dynamo is due to the lag in the rolling average. The thermal and compositional buoyancy fluxes are shown in the lower panel. Again, the model compositional buoyancy flux (faded purple) and rolling average buoyancy flux (bright purple) are shown. Time is plotted logarithmically to make the early trends in magnetic field generation with time visible. The downward spike in magnetic field strength in the first epoch of dynamo generation occurs when the mantle cools sufficiently for its melt fraction, ϕ, to drop below the critical melt fraction, ϕ_C. The dynamo stops when mantle convection ceases and restarts prior to the onset of core solidification once the conductive temperature gradient at the CMB has steepened sufficiently. Core solidification very slightly increases magnetic field strength and Re_m.

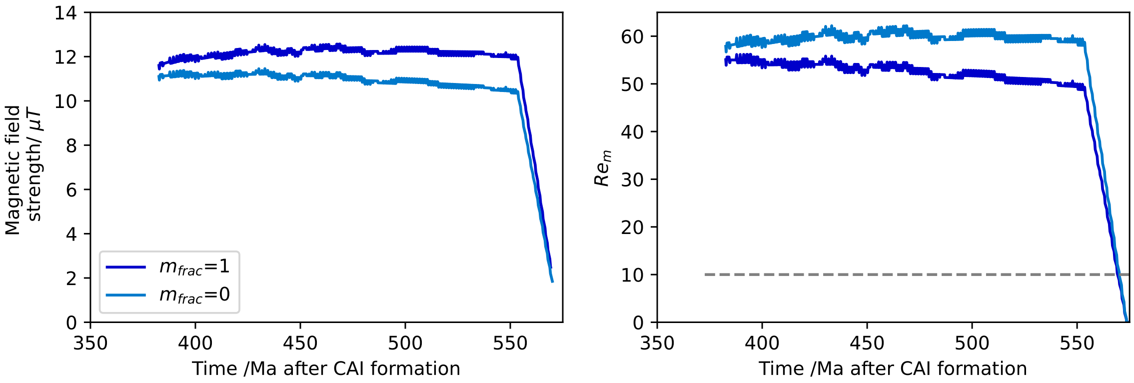

Figure 2.9: Magnetic field strength (left panel) and magnetic Reynolds number, Re_{m}, (right panel) for the two core solidification endmembers: no solidified material falls to the centre and no passive inner core forms, $m_{\mathrm{frac}}= 0$ (dark blue line); and all solidified material falls to the centre to form a passively growing inner core, $m_{\mathrm{frac}}= 1$ (light blue line). The lines indicate a rolling average over 20 Ma. Magnetic field strength is slightly increased and Re_{m} is slightly decreased in the presence of a passively growing inner core, but the difference between the two endmembers is minimal.

top panel). Once core thermal stratification has been eroded, the core begins to convect. Re_{m} is immediately supercritical, so magnetic field generation begins 2.0 Ma after CAI formation. At 4.3 Ma after CAI formation, the temperature at the top of the mantle drops below $T_{\phi_{\mathrm{C}}}$ and the stagnant lid begins to thicken. At 13 Ma after CAI formation, the temperature at the base of the mantle drops below $T_{\phi_{\mathrm{C}}}$ and the CMB boundary layer begins to thicken. As the stagnant lid and CMB boundary layer thicken, F_{CMB} decreases and the first epoch of magnetic field generation ends ~170 Ma after CAI formation. At ~260 Ma after CAI formation, the combined CMB boundary layer and stagnant lid thickness reaches the thickness of the mantle, so mantle convection stops (Figure 2.6). Immediately after the cessation of mantle convection, there is a shallower temperature gradient across the portion of the mantle that was the CMB boundary compared to the portion of the mantle that was the stagnant lid (Figure A.8). As a single conductive gradient is established throughout the whole mantle, the conductive temperature gradient at the CMB increases and the temperature gradient near the surface decreases. As a result, F_{CMB} increases and the dynamo restarts at ~280 Ma after CAI formation. Core solidification starts at ~370 Ma, which provides an additional source of buoyancy for dynamo generation. As solidification proceeds the liquid core sulfur content increases and the core reaches the FeS eutectic at ~550 Ma. This reduces the buoyancy to drive the dynamo, causing Re_{m} to become subcritical and the dynamo shuts off. The core solidifies completely by ~770 Ma.

	My model	Previous model	Reference	Reason
Peak mantle temperature /K	1525 at 1.2 Ma	1620 at 1.2 Ma	a	New viscosity model, lower ϕ_C
Mantle hotter than the core until /Ma	1.7	9	a	Inclusion of ^{60}Fe
Core thermal stratification eroded /Ma	2.0	40	a	Inclusion of ^{60}Fe
End of mantle convection/Ma	260	56	a	Mantle convection model
First dynamo onset /Ma	2.0	-	a	Inclusion of ^{60}Fe
	1.4	5.4	b	
First dynamo cessation /Ma	170	-	a	Mantle convection model
	150	17	b	

Table 2.3: Differences between key aspects of planetesimal thermal evolution between my model and previous models, and a reason for each difference. My model run is for a 500 km radius planetesimal accreted at 0.8 Ma after CAI formation with ^{60}Fe/^{56}Fe $=10^{-8}$. The Case 1 run from Dodds et al. (2021) (a) is used for comparison. Dynamo generation is compared with both Case 1 from Dodds et al. (2021) and the single accretion event model from Bryson et al. (2019a) (b), because thermal stratification prevented dynamo generation in Dodds et al. (2021). A model run for a 400 km radius planetesimal accreted at 0.5 Ma after CAI formation was used to compare with the Bryson et al. (2019a) model. All times are Ma after CAI formation and are given to a precision of 0.1 Ma from 1–10 Ma, 1 Ma for 10–100 Ma and 10 Ma for >100 Ma. ϕ_C is the critical melt fraction.

2.3.1 Inclusion of ^{60}Fe

Previous models neglected the role of radiogenic heating by ^{60}Fe in the core because it only led to a ~10 K difference in peak core temperature over the lifetime of the planetesimal (Henke et al., 2013). Although this temperature difference is small compared to the overall core temperature, it is significant compared to the temperature difference across the CMB ($\sim 1-5$ K). Radiogenic heating by ^{60}Fe is therefore important at early times in the thermal evolution. Indeed, radiogenic heating from ^{60}Fe can increase the core temperature above the temperature at the base of the mantle, causing the core's thermal stratification to be removed far more rapidly (see Table 2.3) than in previous models (Dodds et al., 2021). As a result, the inclusion of ^{60}Fe can lead to an earlier onset of dynamo generation (by ~4 Ma compared to Bryson et al., 2019a) or an early epoch of dynamo generation that was not observed for an instantaneously accreting body in the model presented by Dodds et al. (2021). Because it will cause more heat to be produced, the effect of ^{60}Fe on dynamo timing and strength will be even more significant for the upper estimates of primordial ^{60}Fe/^{56}Fe.

2.3.2 Mantle convection criterion

Mantle convection and the first epoch of dynamo generation lasts an order of magnitude longer in my model than previous models (Table 2.3) due to my chosen criteria for the cessation of mantle convection. In previous models, solid-state convection immediately ceased when the Rayleigh number dropped below the critical Rayleigh number, Ra_c, for the first time (Sterenborg and Crowley, 2012; Bryson et al., 2019a; Dodds et al., 2021). This previous cessation criterion resulted in mantle convection ceasing early, at a time when the combined boundary layer thicknesses were less than half the mantle thickness, the CMB boundary layer was very thin, and the deep mantle was isothermal (the mantle adiabatic gradient is negligible). This isothermal profile resulted in a pause in cooling at the CMB until conductive cooling from the top of the mantle reached the CMB. I have mitigated this artefact in my model by assuming the cessation of convection occurs when the combined stagnant lid and CMB boundary layer thickness equals the mantle thickness. This better represents the gradual cessation of convection, because the convecting domain gradually shrinks in size until the entire domain is conductive (Figure 2.6). This criterion has been used to calculate cessation of convection by many planetary thermal evolution studies (e.g., Grott et al., 2011; Morschhauser et al., 2011) and predicts similar thermal evolutions to equivalent 2D and 3D numerical simulations (Tosi et al., 2013). I assume a conductive profile in the CMB boundary layer, such that upon the cessation of mantle convection there is already a conductive temperature gradient at the base of the mantle. This ensures there is mantle and core cooling via conduction the moment convection ceases. The gradual thickening of the CMB boundary layer is reflected in the slow decrease in F_{CMB} and dynamo field strength in Figures 2.7 and 2.8 and lack of spike in F_{CMB} at cessation of convection compared to Bryson et al. (2019a). The conductive gradient in the CMB boundary layer enables a second epoch of dynamo generation to begin before the onset of core solidification, because the conductive temperature gradient at the CMB is large enough to produce supercritical Re_{m}.

2.3.3 Magnetic field generation with time

Planetesimal magnetic field generation can be split into four regimes (Figure 2.8). In Regime 1, radiogenic heating from ^{60}Fe is strong and the mantle is above ϕ_{C}, such that the CMB boundary layer is thin and F_{CMB} is high. The peak magnetic field strength ($16\,\mu$T for my example run) for the whole thermal evolution is reached at the onset of dynamo generation, when the temperature gradient across the CMB is largest due to heating by ^{60}Fe. Magnetic field strength decreases as the CMB boundary layer thickens (see Figures 2.6 and 2.8). Regime 1 ends ~13 Ma after CAI formation when the temperature at the base of the mantle drops below T_{ϕ_C}. There is a downward spike in magnetic field strength at this time, because the CMB boundary layer thickness increases rapidly (see Figure A.4 and A.7) and the same temperature difference is accommodated across a larger distance, which decreases F_{CMB}. At the beginning of Regime 2, as the mantle continues to cool, the core-mantle temperature difference initially increases more rapidly than the CMB boundary layer thickness, which temporarily increases F_{CMB} and the magnetic field strength. F_{CMB} and magnetic field strength then decline as the CMB boundary layer thickening outweighs the change in core-mantle temperature difference. Regime 3 occurs after the mantle has stopped convecting. The conductive temperature gradient at the CMB steepens (Figure A.8), which increases F_{CMB} enough to restart the dynamo. Magnetic field strength increases with time up to 8 μT, because the temperature gradient in the deep mantle increases as the mantle cools. Once core solidification begins, this provides an additional source of buoyancy to drive the dynamo (Regime 4) and the field strength is approximately constant at 13μT until the core reaches the eutectic composition. Once the core reaches this composition there is insufficient buoyancy flux to drive the dynamo.

The field strengths and transition times between these regimes will change with chosen planetesimal parameters. For lower core sulfur contents, core solidification will start earlier and the compositionally driven regime (Regime 4) may overlap with preceding regimes (Figure 2.10). Smaller planetesimals will cool more quickly, so will have a compressed magnetic field generation history. The transition between Regimes 1 and 2 is partially due to the jump in viscosity. These two regimes may become one with a smooth decrease in field strength with time if viscosity parametrisations are improved in the future.

2.3.3.1 Compositional vs thermal dynamos

In my model, the primary difference between compositional and thermal dynamos is the release of gravitational potential energy in the liquid region of the core, which increases the buoyancy flux to drive the dynamo. As a result, thermo-compositional dynamos generate stronger magnetic fields than thermal dynamos at the same point in planetesimal thermal evolution (orange/grey vs yellow lines in Figure 2.10). For a 500 km body at the thermo-compositional field strength peak, the magnetic field is 1.7 times stronger than the thermal dynamo alone at the same period of dynamo

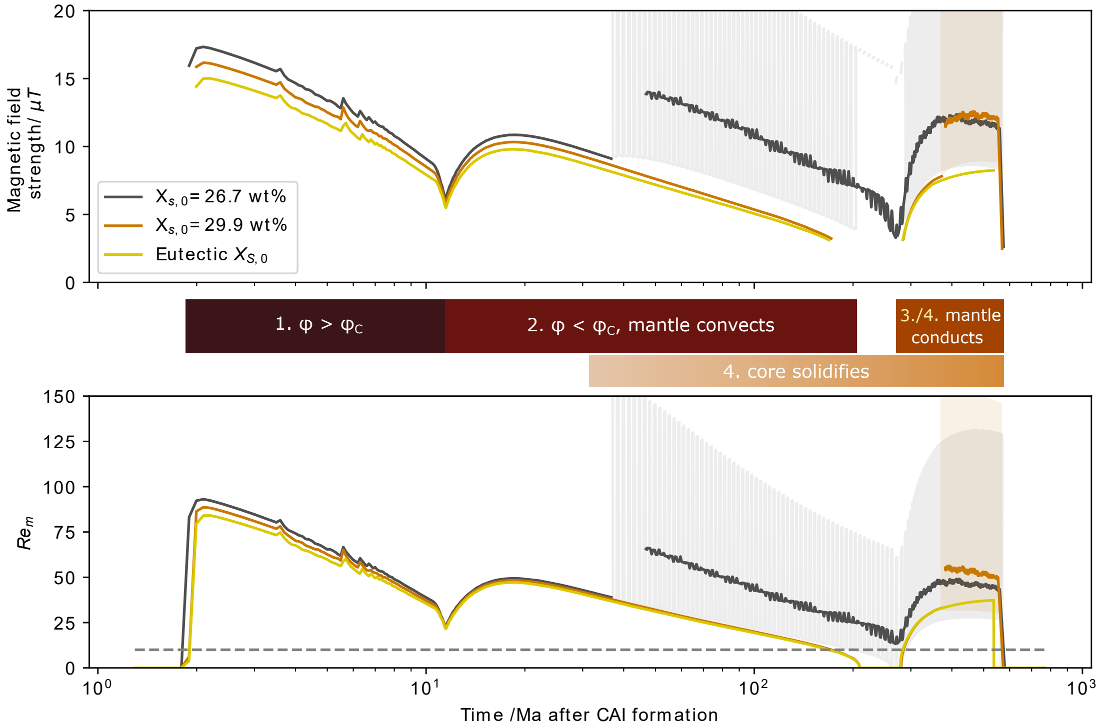

Figure 2.10: Magnetic field strength and Re_m with time for 500 km planetesimals with $^{60}\mathrm{Fe}/^{56}\mathrm{Fe} = 10^{-8}$ and initial core sulfur contents, $X_{\mathrm{S},0}$, from 26.7–33 wt%. Due to the discrete nature of the model, the magnetic field strength and Re_m oscillate during core solidification. This oscillating output is shown by the faded traces and the rolling average over 200 output steps (20 Ma) is shown in bold. The small gap between the purely thermally driven dynamo and the average values for the thermo-compositional dynamo is due to the lag in the rolling average. The dynamo generation regimes are the same as in Figure 2.8. As $X_{\mathrm{S},0}$ decreases, the core liquidus temperature increases and the onset of core solidification moves to earlier times. Compositional buoyancy leads to up to a 70% increase in magnetic field strength. Core solidification is not required to produce a second epoch of dynamo generation.

generation and the compositional buoyancy flux is ∼6 times higher than the thermal buoyancy flux (Figure 2.8). However, the absolute difference in magnetic field strength between mechanisms (∼7 μT) would require small measurement uncertainties to be detected in the paleomagnetic record and would be degenerate with the time the magnetisation was recorded. For instance, in Regime 3, both field strengths decrease with time so a later generated thermo-compositional field could have the same strength as a thermally generated one earlier in the same regime.

Although the onset of core solidification may not have a resolvable affect on field strength, it can have a strong effect on the timing of dynamo generation. For $X_{\mathrm{S,0}}$ =26.7 wt%, the increase in buoyancy flux due to core solidification is enough to prevent cessation of the dynamo when mantle convection ceases and there is no gap in dynamo generation.

My model now predicts the first epoch (epoch denotes a continuous period of dynamo generation compared to regimes, which demarcate the different mantle/core states during dynamo generation) of thermal dynamo generation can last up to 170 Ma after CAI formation for 500 km radius planetesimals (Figure 2.8). The dynamo restarts in 500 km radius planetesimals with $X_{\mathrm{S,0}} = 29.85$ wt% and 33 wt% at ∼ 280 Ma after CAI formation prior to the onset of core solidification (Figure 2.10). As such, core solidification is not required for a second epoch of dynamo generation. Core solidification does not prolong the life of the dynamo, but strengthens the resulting magnetic field and narrows the gap between generation epochs. The restart of the dynamo prior to core solidifcation predicted by my model suggests that core solidification may not be required to explain younger magnetic remanences (e.g., Nichols et al., 2021; Maurel et al., 2021, >65 Ma after CAI formation based on current evidence). This could resolve the problem of finding an inward solidification mechanism which can drive compositional convection rather than stably stratifying the core (Dodds et al., 2025), because the later meteorite paleomagnetic remanences could have been generated by a purely thermal dynamo.

2.3.3.2 Magnetic field strengths

The magnetic field generation scaling laws I use enable me to predict both Re_{m} and dipolar, surface magnetic field strengths for the entire planetesimal thermal evolution. These magnetic field strengths can be compared to the paleomagnetic record to determine a range of possible parameters for a given meteorite parent body (see Chapter 3). I have determined that a MAC scaling law for magnetic field strength is appropriate for planetesimal cores (Section 2.2.6.2,Table A.1). Previous planetesimal thermal evolution models were uncertain which core force balance and scaling law was appropriate for planetesimals, so did not predict magnetic field strengths (Bryson et al., 2019a; Dodds et al., 2021) or used multiple scaling laws (Sterenborg and Crowley, 2012). Additionally, I have developed a parametrised model for inward core solidification, which enables me to calculate a combined thermal and compositional buoyancy flux (Equation 2.36) and use the same convective velocity and magnetic field scaling laws before and during core solidification. This means a full internally-generated magnetic field history for a given planetesimal can be predicted without having to assume a single buoyancy source at a given time. This is important for trying to understand time-resolved magnetic field generation records for a specific body, such as the Main Group pallasites (Tarduno et al., 2012; Bryson et al., 2015; Nichols et al., 2021) and the IIE irons (Maurel et al., 2021), for which magnetic field strengths were previously predicted only during outward solidification with a conductive mantle. The magnetic histories of these meteorite parent bodies will be explored in Chapter 5.

2.4 Accretion and differentiation assumptions

2.4.1 Accretion timescale and partial differentiation

I do not consider the effects of gradual accretion because there are a range of possible accretion growth laws (Neumann et al., 2012) and the most appropriate law for planetesimals may depend on the initial conditions of dynamical simulations (Weidenschilling, 2019). Prolonged accretion over $\mathcal{O}(0.1\,\mathrm{Ma})$ could erode core thermal stratification by the later addition of cool material to the top of the core, which can bring forward the onset of the dynamo relative to the instantaneous accretion case (Dodds et al., 2021). However, my model includes heating by ^{60}Fe in the core, which can rapidly remove thermal stratification and will counter the effect of prolonged accretion on core thermal structure.

Accretion over even longer timescales ($\mathcal{O}(1\,\mathrm{Ma})$) following an exponential accretion law can lead to partial differentiation, smaller planetesimal cores, and weaker dynamos (Dodds et al., 2021). Partial differentiation could be included in the model in the future by adding regolith with lower conductivity to the top of the planetesimal and introducing a variable ratio of core to planetesimal radii, $\frac{r_c}{R}$. This could lead to a weaker dynamo with shorter duration for a given planetesimal radius compared to the results in this chapter due to reduced core and mantle size. These extensions will be important for applying the model to partially differentiated bodies that preserve a thick chondritic layer and have been proposed to have generated a magnetic field, such as the CV and H chondrites (Elkins-Tanton et al., 2011; Bryson et al., 2019b).

2.4.2 Compaction, sintering and regolith

My model does not include variations in planetesimal thermal conductivity between accretion and differentiation due to compaction and sintering. The planetesimal sinters at 700 K (Yomogida and Matsui, 1984) and rapidly reaches the thermal properties assumed in this model. For a 500 km planetesimal the inner 496 km is below 700 K only for the first 0.12 Ma after accretion and the last node sinters 0.5 Ma after accretion, so a lower thermal conductivity prior to sintering has a negligible effect on heat transport over the 10–500 Ma timescales for dynamo generation. I have neglected any unsintered regolith because this layer is so thin (< 500 m). This may result in a very slight over-estimate of the surface heat flux and planetesimal cooling rate.

2.4.3 Water

Following other models of differentiated planetesimals (Neumann et al., 2018; Sturtz et al., 2022b; Monnereau et al., 2023), my model does not include the thermal effects of water prior to differentiation. I adopted this approach because radiogenic heating is strong enough that the thermal contributions of melting ice, hydrating, and dehydrating silicates has a minimal effect on the differentiation time. Additionally, the early accreted planetesimals considered here rapidly reach temperatures above the silicate dehydration temperature (1223 K; Lichtenberg et al., 2019a), and after differentiation planetesimals retain very little water (Peterson et al., 2023; Newcombe et al., 2023). The effect of water on planetesimal evolution will be discussed further in Chapter 4.

2.4.4 Differentiation mechanism

My model for differentiation must enable planetesimals to form a core in which a dynamo can be generated. In order for the planetesimal to differentiate, the material which will form the core, assumed to be Fe-FeS, must be able to move to the centre of the body. There are at least two possible differentiation mechanisms: percolation, where Fe-FeS melt, which has a lower solidus than silicates, moves along grain boundaries in a solid, silicate matrix; and rain-out, where more dense molten Fe-FeS falls through less dense silicate melt to the planetesimal centre. Percolation requires an interconnected network of melt. Metal melts have large dihedral angles (110°; Néri et al., 2020) and need high volume fractions to form this interconnected network (up to 20-25%; Néri et al., 2020). These high volume fractions would require high planetesimal metal contents, which would result in unrealistically large core radii. Only 12.5 vol% metal is required to form a core that has a radius that is 50% the radius of the planetesimal (Dodds et al., 2021) and cores predicted to form from chondritic compositions have core radii that are 30–50% of the planetesimal radius (Bercovici et al., 2022). However, the need for an inter-connected network of metal for percolation could be removed by shear deformation due to solid-state convection (Rushmer et al., 2000), crack formation (Keil and Wilson, 1993) or silicate melting (Wilson et al., 2008).

Estimates of the percolation velocity, assuming Darcy flow, are linearly dependent on the permeability of the planetesimal matrix, for which model values vary by six orders of magnitude from $10^{-8}\mathrm{m}^2$ (Fu and Elkins-Tanton, 2014) to $10^{-14}\mathrm{m}^2$ (Neumann et al., 2012). As a result, the time taken to differentiate via this mechanism is very uncertain ($\mathcal{O}(10–10^6)$ years, see Appendix A.5.1). Differentiation via rain out occurs rapidly in comparison to a model timestep, $\mathcal{O}(10^2)$ years for 1 mm radius droplets, once $\phi = \phi_C$ (i.e., once the silicate portion of the body has a liquid viscosity). Therefore, in this model I adopt differentiation via rain out when $\phi = \phi_C$, because the mechanics are simpler and any Fe-FeS that has not already reached the centre via percolation will move there rapidly once $\phi = \phi_C$.

2.4.4.1 Minimum core sulfur content

My model assumes differentiation occurs at the critical melt fraction and that the core of the planetesimal is completely molten at the point of differentiation, which limits the range of initial core sulfur contents I can model. For the core material to be completely molten at differentiation requires the differentiation temperature to be greater than or equal to the Fe-FeS liquidus. The liquidus temperature is a function of core sulfur content and core pressure (Equation 2.29), while the differentiation temperature is assumed to be equal to the temperature of ϕ_C, which depends on the mantle solidus (Section 2.5.1) and the choice of ϕ_C. Experiments (0.2; Scott and Kohlstedt, 2006) and previous planetesimal thermal evolution models (0.5; e.g., Bryson et al., 2019a) provide a possible range of ϕ_C.

Previous studies of planetesimal dynamo generation were not limited in their value of $X_{S,0}$, because they used the linear liquidus approximation (Neufeld et al., 2019; Nichols et al., 2021), which has lower liquidus temperatures for $X_{S,0}$ in the range 0–10 wt% compared to the Buono and Walker (2011) liquidus (Figure A.9). Prior studies

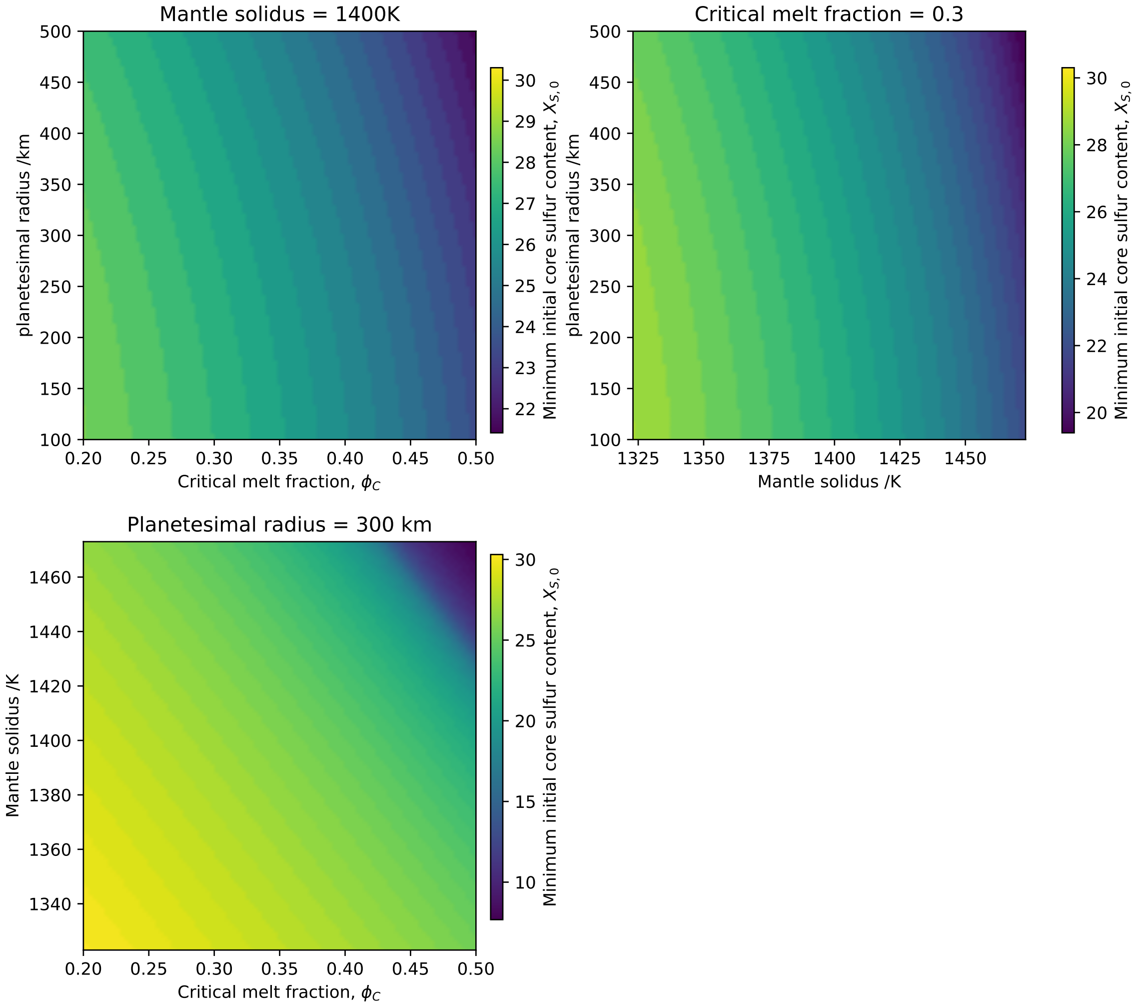

Figure 2.11: Minimum initial core sulfur content, $X_{\mathrm{S},0}$, in my model as a function of: planetesimal radius, which controls core pressure (top left, top right); critical melt fraction, which controls the temperature at differentiation (top left, bottom left); and mantle solidus, which controls the temperature at differentiation (top right, bottom left). The lowest radii, lowest critical melt fractions and lowest mantle solidus temperatures have the highest minimum $X_{\mathrm{S},0}$. The minimum and maximum values on the colour scale vary between subplots, in order to highlight the effect of each parameter. Variations in mantle solidus temperature combined with variations in critical melt fraction produce the largest spread in $X_{\mathrm{S},0}$.

of planetesimal differentiation via percolation predicted differentiation of sulfur-poor bodies, because they only considered heat transfer via conduction not convection, which allows for higher maximum planetesimal temperatures (Neumann et al., 2012).

For the mantle solidus used in this model (1400 K), the minimum $X_{\mathrm{S,0}}$ varies from 22.2–28.3 wt% (Figure 2.11), which is higher than the sulfur contents in iron meteorites (0–17 wt%; Kruijer et al., 2014). If the mantle solidus in the model is raised to 1473 K (Fu and Elkins-Tanton, 2014), the minimum $X_{\mathrm{S,0}}$ varies from 6.9–25.9 wt% (Figure 2.11). However, it is unclear if this is the most appropriate solidus value and the lower values in this range require extremal values of planetesimal size (500 km) and critical melt fraction (0.5). Planetesimals could have initially been sulfur rich and lost their sulfur by later processes, such as immiscible fluid separation in the core (e.g., Bercovici et al., 2022) or volatile loss (e.g., Hirschmann et al., 2021). Bodies differentiating from CI, CM, LL, CO, CV, and CK chondritic starting compositions are predicted to have $X_{\mathrm{S}} \geq 22\%$ (Bercovici et al., 2022), which is in line with the minimum $X_{\mathrm{S,0}}$ in the model. Further research is needed to constrain the mantle solidus and critical melt fraction and to explore these additional processes occuring during or immediately after differentiation.

As a first estimate, sulfur-poor bodies would have an earlier onset and longer duration of compositional convection than those modelled here, because the core liquidus temperature is higher and more core solidification is required before the bulk liquid core sulfur content reaches the eutectic. In addition, decreasing $X_{\mathrm{S,0}}$ lowers the density difference between the solidified iron and the bulk liquid core, which could decrease buoyancy flux and magnetic field strength at the beginning of core solidification.

2.5 Mantle assumptions

2.5.1 Silicate solidus and liquidus

The silicate solidus, $T_{\mathrm{m,s}}$, and liquidus, $T_{\mathrm{m,l}}$, depend on pressure and composition (Hirschmann, 2000). Meteorite melting experiments suggest the silicate solidus lies between 1323-1423 K and the liquidus is ∼400 K hotter than the solidus (Agee et al., 1995; McCoy et al., 1999). Previous planetesimal models have used values for the mantle solidus between 1400–1473 K (Hevey and Sanders, 2006; Elkins-Tanton et al., 2011; Fu and Elkins-Tanton, 2014; Kaminski et al., 2020; Bryson et al., 2019a; Dodds et al., 2021) based on differing degrees of rounding of these experimental results in

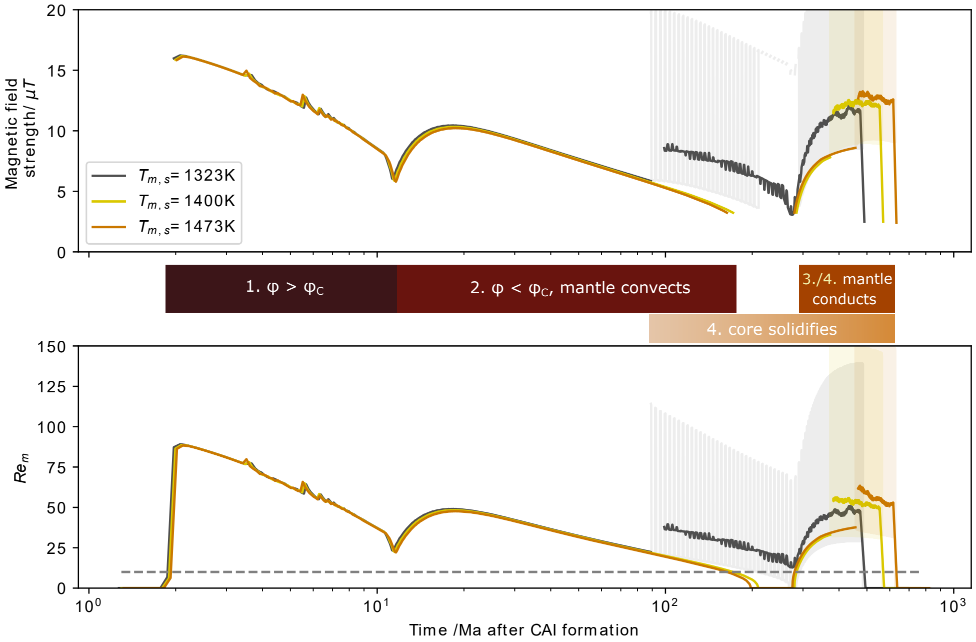

Figure 2.12: Magnetic field strength and Re_m with time for 500 km planetesimals with $^{60}\mathrm{Fe}/^{56}\mathrm{Fe} = 10^{-8}$, $X_{\mathrm{S},0}$=29.85 wt% and three different mantle solidus temperatures. In all scenarios, the mantle liquidus temperature is 400 K above the solidus temperature. Due to the discrete nature of the model, the magnetic field strength and Re_m oscillate during core solidification. This oscillating output is shown by the faded traces and the rolling average over 200 output steps (20 Ma) is shown in bold. The spikes in F_CMB prior to 13 Ma is due to the discretisation of the stagnant lid. The small gap between the purely thermally driven dynamo and the average values for the thermo-compositional dynamo is due to the lag in the rolling average. The dynamo generation regimes are the same as in Figure 2.8. Mantle solidus temperatures do not affect thermal dynamo generation, but lower solidus temperatures bring forward the onset and completion of core solidification, because less cooling is required to reach the core liquidus. This earlier onset of core solidification can provide additional buoyancy and prevent a gap in dynamo generation at the cessation of convection.

°C. For consistency with the studies of Bryson et al. (2019a) and Dodds et al. (2021), I have chosen to use a mantle solidus and liquidus of 1400 K and 1800 K, respectively.

Increasing the silicate solidus and liquidus temperature increases the temperature of the critical melt fraction and peak planetesimal temperature. Increasing the silicate solidus has little effect on thermal dynamo generation (Figure 2.12), but will delay compositional dynamo generation, because a higher silicate solidus temperature requires more cooling before the core reaches the Fe-FeS liquidus, for the same initial core sulfur content. In contrast, decreasing the silicate solidus lowers the planetesimal peak temperature, which means less cooling is required to reach the core solidus. This can bring forward the onset of core solidification, for a given initial core sulfur content, to before the cessation of mantle convection. In this scenario, the additional buoyancy provided by core solidification could power the dynamo when mantle convection ceases and prevent a gap in dynamo generation. The choice of mantle solidus will determine the range of $X_{\mathrm{S},0}$ over which early onset of core solidification is possible.

2.5.2 Silicate melt migration

Silicate melt migration could lead to formation of high silicate melt fraction layers rather than global planetesimal (pre-differentiation) or mantle (post-differentiation) melting due to the preferential partitioning of ^{26}Al into melt (e.g., Neumann et al., 2014). Depending on the buoyancy of the silicate melt, these melt-rich layers could form at the surface (H, LL, or EH chondrite starting compositions) or at the CMB (CM or CV chondrite starting compositions; Fu and Elkins-Tanton, 2014). In both scenarios, the strong radiogenic heating in these melt-rich layers would delay the onset of dynamo generation. A surface melt-rich layer would be hotter than the rest of the interior delaying the cooling of the lower mantle and the core until the melt-rich layer had cooled to the temperature of the lower mantle. A melt-rich layer at the CMB would experience higher radiogenic heating per unit mass than the homogeneous mantle presented in this chapter. As a result, this melt-rich layer would transfer more heat to the core and increase core thermal stratification at early times, delaying the onset of the dynamo. In both scenarios, the onset of dynamo generation could still be brought forward by the presence of ^{60}Fe in the core, which raises the core temperature relative to the mantle. Melt migration would also inhibit mantle convection because most of the mantle would be melt-poor and have high viscosity. This could lead to a single epoch of dynamo generation because there would be no transition from mantle convection to conduction and no resulting pause in dynamo generation.

Melt migration is significant if the timescale for percolation of silicate melt through the solid matrix is shorter than the timescale for radiogenic heating (Lichtenberg et al., 2019b; Monnereau et al., 2023). However, the timescale for melt migration varies by seven orders of magnitude between studies (Moskovitz and Gaidos, 2011; Neumann et al., 2012; Monnereau et al., 2023) due to different assumptions about silicate grain growth and matrix permeability. Therefore, the importance of melt migration in planetesimal differentiation is heavily debated. Due to the uncertainties in melt migration timescale, I have neglected melt migration in this model. For bodies that accrete $< 1.1\,\mathrm{Ma}$ after CAI formation, the radiogenic heating timescale is short enough to neglect melt migration (Monnereau et al., 2023). Based on the differentiation ages of iron meteorites, it is likely that most differentiated planetesimals accreted within this time (Spitzer et al., 2021).

2.5.3 Compositional homogeneity

I do not specify a mantle composition and assume the mantle is compositionally homogeneous. A compositionally distinct, cumulate layer could form at the base of the mantle when it is convecting above the critical melt fraction (Sturtz et al., 2022b). This could thicken the conductive boundary layer at the base of the mantle, decreasing F_{CMB} and reducing dynamo strength. However, formation of this cumulate is very sensitive to crystal size and also depends on mantle composition (Sturtz et al., 2022b). Because these parameters are uncertain, it is unclear how widespread cumulate formation will be among planetesimals and I have not included it in my model.

2.6 Core solidification model

In order to calculate a full planetesimal thermal history, I had to balance detail in my core solidification model with ease of implementation. Since there is such large uncertainty in the mechanism of core solidification, I did not want to adopt an unreasonable level of specificity in my core solidification model. I chose to focus on two key changes to dynamo generation that will result from core solidification: decrease in convective lengthscale; and change in density difference due to changing composition of bulk liquid core during solidification. The assumptions within my core solidification model are discussed below.

2.6.1 Convective lengthscale

For a planetesimal core solidifying inwards, either a stably stratified, partially solid layer may remain at shallow depths in the core, (e.g. iron snow Rückriemen et al., 2015; Davies and Pommier, 2018) or a portion of material may delaminate and fall to the centre of the planetesimal forming a passively growing inner core (e.g., Scheinberg et al., 2016; Neufeld et al., 2019). The m_{frac} parameter allows me to adjust my model between these two endmembers: no passively growing inner core ($m_{\mathrm{frac}}= 0$); and all material immediately falling to the centre to form an inner core ($m_{\mathrm{frac}}= 1$). This gives me a first estimate to the effect of core solidification for the most ($m_{\mathrm{frac}}= 1$) and least ($m_{\mathrm{frac}}= 0$) rapid changes in geometric lengthscale. In reality, the convective lengthscale is some fraction of the geometric lengthscale (Davidson, 2013; Aubert et al., 2017), which could increase the magnetic field strength and decrease Re_{m} (Figure A.5). However, the value of this fraction for planetesimal cores is uncertain, so I approximate the convective lengthscale as equal to the geometric lengthscale. This may overestimate dynamo duration and underestimate magnetic field strength. The endmember with the passively growing inner core was used in Figures 2.8 and 2.10, because this is the minimum estimate of geometric lengthscale and will give a minimum estimate of Re_{m}. Core solidification with a passively growing inner core has a slightly stronger magnetic field strength and lower Re_{m} than core solidification where solid without an inner core (Figure 2.9). However, magnetic field strength and Re_{m} both scale weakly with convective lengthscale (see Figure A.10), so these changes are minimal.

For both scenarios, the amount of material solidified is parametrised by the inward motion of a solidification frontat r_i; the buoyancy flux is calculated at this position. For $m_{\mathrm{frac}}= 0$, the radius of the base of the solidified outer layer, r_1 is equal to the position of the solidification front ($r_1 = r_i$). For $m_{\mathrm{frac}}= 1$, there is no outer shell ($r_1 = r_{\mathrm{c}}$) and all the material is at the centre. In this case, r_i differs from r_1 by a maximum of 6% (Figure A.11) before the core reaches the eutectic. Therefore, evaluating the buoyancy flux at r_i rather than r_{c} for $m_{\mathrm{frac}}= 1$ introduces a minimal effect.

2.6.2 Density difference

During core solidification, the density difference between the solidified, pure iron phase and the Fe-FeS liquid drives convection. The density difference between the solid and liquid varies as the core solidifies and the sulfur content of the liquid core increases. The adiabatic gradient in planetesimal cores is probably too shallow for solidified iron to remelt as it falls towards the centre of the planetesimal (Dodds et al., 2025). Therefore, I assume the bulk liquid core becomes more sulfur rich as the core solidifies and the driving density difference is between solidified iron and the bulk Fe-FeS liquid. Assuming perfect partitioning of sulfur into the liquid portion of the core (Goldstein et al., 2009) may overestimate the density difference available to drive the dynamo. I use the same density difference formalism in both solidification endmembers, because this estimate is the correct order of magnitude for the density difference even if it may differ between solidification modes.

My variable density difference is up to seven times larger than in previous models (see Figure A.12) which assumed a constant fractional density difference ($\frac{\Delta\rho}{\rho_c}$ of 5% based on Earth values, eg. Nimmo, 2007; Bryson et al., 2015, 2019a; Nichols et al., 2021). This previous value underestimated the density difference due to the higher pressure and lower core sulfur content in the Earth's core compared to planetesimal cores. My variable density difference increases the density difference available to drive a dynamo.

My model does not consider the density difference resulting from super-eutectic ($X_{S,0} > 33\,\mathrm{wt\%}$) core solidification as a mechanism for driving the dynamo. This is for two reasons. First, there is minimal evidence for super-eutectic planetesimal cores in the meteorite record. For instance, there are no iron meteorites with super-eutectic compositions (Hilton et al., 2022) and only parent bodies formed from CM chondrite and CI chondrite compositions potentially could have formed super-eutectic cores (Bercovici et al., 2022). Second, the density and liquidus of super-eutectic Fe-FeS is very poorly constrained (Rückriemen et al., 2018). As a result, it is unclear whether crystallisation of super-eutectic Fe-FeS can drive a compositional dynamo.

2.6.3 Comparison with iron snow

The m_{frac}= 0 endmember is an approximation to iron snow solidification, and uses a simplified description of the energetics and solid fraction in the snow zone. The full energetics of the iron snow system is complex (Rückriemen et al., 2015; Davies and Pommier, 2018) and the dynamics of iron snow solidification, including nucleation and bursts of solidification (Huguet et al., 2023), are still poorly understood and difficult to incorporate into a numerical model. My simplified model aims to capture the key aspects of this complicated solidification mechanism for dynamo generation. Additonally, my simplications enable easy transition between core solidification endmembers using a single parameter, m_{frac}.

One key approximation in my model compared to the iron snow system is the treatment of the solid fraction in the snow layer. In a full iron snow model, stable stratification is formed at the top of the core by a slurry layer, with a very low, almost constant solid fraction (Davies and Pommier, 2018), whereas in my model this stable stratification is formed by a layer of pure, solid iron. This solid iron layer still captures the decrease in the lengthscale of convection with the downward growth of the snow layer.

Another key approximation in my model is in the energetics; specifically, the treatment of gravitational potential energy in the solid and the release of latent heat for driving the dynamo. Since my snow layer is a pure solid, I neglect release of gravitational potential energy in the snow zone and only consider release of gravitational potential energy in the liquid portion of the core, when calculating the buoyancy flux (Equation 2.36). Neglecting the gravitational potential energy release in the snow region is reasonable, because gravitational potential energy release in the liquid dominates (Davies and Pommier, 2018). Energetically, this is the same as the growth of a solid inner core, but adapted for inward core solidification (Gubbins et al., 2003; Nimmo, 2007). My model includes the release of latent heat due to core solidification, but not absorption of latent heat by remelting of falling snow. In an iron snow system, these two latent heat contributions almost balance (Davies and Pommier, 2018), so could be neglected altogether. However, the adiabatic gradient in planetesimal cores may not be steep enough for iron snow to remelt (Dodds et al., 2025). Therefore, I have omitted latent heat absorption during remelting but included latent heat release during solidification. This enables a single parameter, m_{frac}, to capture variation between core solidification endmembers. The contribution of latent heat release during solidification is an order of magnitude smaller than the other contributions to core energetics during solidification (Figure 2.7), so including it has a minimal effect on core solidification.

2.7 Outlook

My model includes several physical and chemical features that have been neglected or simplified in previous models. For instance, my planetesimal thermal evolution model is the first to model sub-eutectic core solidification of a mantled planetesimal that also includes mantle convection. Calculating a unified buoyancy flux also enables me to use the same scaling laws for Re_{m} and magnetic field strength throughout the thermal evolution, and allows thermal and compositional convection to occur simultaneously. Additionally, radiogenic heating from ^{60}Fe has been added to the core thermal structure. I also chose to adjust the mantle convection parametrisation to model the gradual cessation of convection and boundary-layer thicknesses applicable to systems with surface cooling and internal heating. I have implemented more physically realistic values in the mantle viscosity function and added extra pieces to the viscosity function to capture the full range of viscosity behaviour as a function of temperature. The stagnant lid scaling laws have also been implemented, such that they respond to changes in mantle viscosity. This will enable future studies to choose viscosity parameters that are most applicable for a planetesimal of a given size and composition. The other parameters in the model are fully adjustable, which enables future studies of the effects of a given parameter as well as application to specific meteorite parent bodies to enable interpretation of the meteorite paleomagnetic record. In Chapter 3, I systematically vary mantle viscosity, primordial ^{60}Fe/^{56}Fe, initial core sulfur content and planetesimal size to gain a deeper understanding of these parameters on dynamo generation and the implications of my model for the meteorite paleomagnetic record.

There are two key refinements that could be made to the model. First, the mechanism of planetesimal differentiation and initial core sulfur contents must be reconciled. Whether planetesimal cores can either form with initially low sulfur contents or lose their sulfur later and the consequences of these factors for the onset of core solidification and dynamo generation require further study. Second, possible mechanisms of inward core solidification in mantled planetesimals and the implications of this on dynamo generation should be explored in more detail. Additional improvements to the model could be made by including partial differentiation and crust formation.

2.8 Conclusions

Planetesimals formed during the first few Ma after Solar System formation and many were accreted into the terrestrial planets. Thermal evolution and dynamo generation models can provide insight into the interior structures and thermal histories of these planetesimals. However, previous models have focused on either early or late epochs of dynamo generation, limiting their ability to predict a complete magnetic field history. My model focuses on the description of mantle convection and the parametrisation for sub-eutectic core solidification to provide a unified, more versatile model for planetesimal thermal evolution and dynamo generation. Specific enhancements include:

- Radiogenic heating from ^{60}Fe in the core.
- A mantle viscosity model that is self-consistent with the mantle convection parametrisation and can be adjusted to investigate the effect of mantle viscosity.
- Stagnant lid and CMB boundary layer parametrisations consistent with boundary heat fluxes and internal heating.
- Cessation of convection when the combined stagnant lid and CMB boundary layer thickness is greater than the mantle thickness.
- A parametrised model for sub-eutectic core solidification with a unified thermal and compositional buoyancy flux to drive magnetic field generation.
- Calculation of magnetic field strength during epochs of dynamo generation.

The key results of these changes implemented in my model are demonstrated by an example of the magnetic history generated for a 500 km radius planetesimal. Compared to previous models I find that:

- Core thermal stratification is eroded more rapidly.
- Mantle convection and the first epoch of dynamo generation lasts longer.
- Core solidification marginally increases dipole field strength, but exerts a much stronger control on dynamo duration by providing an additional buoyancy source after the cessation of mantle convection.
- The second epoch of dynamo generation is not triggered by core solidification.

My model can predict a complete magnetic field generation history for a planetesimal with magnetic field strengths for both compositional and thermal dynamos. It therefore serves as a powerful tool for understanding the general controls on planetesimal dynamo generation (Chapters 3 and 4), as well as recovering constraints on the properties of meteorite parent bodies from their paleomagnetic records (Chapter 5). In the next chapter, I will use this model to investigate the effect of mantle viscosity, core composition and planetesimal radius on dynamo generation and re-evaluate previous interpretations of the meteorite paleomagnetic record.

Chapter 3

Early and elongated epochs of planetesimal dynamo generation

3.1 Introduction

The meteorite paleomagnetic record provides a unique insight into the evolution of planetesimals and the protoplanetary disk. Meteorite magnetic remanences that record dynamo fields indicate that some planetesimals met the criteria for dynamo generation during their thermal history. Thermal evolution and dynamo generation models can be used to constrain the properties of meteorite parent bodies from these magnetisations (e.g., Nichols et al., 2021; Dodds et al., 2021; Maurel et al., 2021). Meanwhile, magnetic records of the nebula field provide constraints on the lifetime of the protoplanetary disk and movement of material within it (e.g., Borlina et al., 2022; Bryson et al., 2020b). The sources of meteorite magnetisations must be correctly identified to obtain these insights, and for post-accretionary magnetic remanences, this relies on results from thermal evolution and dynamo generation models (e.g., Sterenborg and Crowley, 2012; Bryson et al., 2019a; Dodds et al., 2021). Refinements to these models presented in Chapter 2 allow the previous interpretations of the meteorite paleomagnetic record to be re-evaluated here.

Previous thermal evolution models (e.g., Sterenborg and Crowley, 2012; Bryson et al., 2019a; Dodds et al., 2021) that successfully generate dynamos predict several events in the thermal evolution:

1. Following instantaneous accretion or during gradual accretion, planetesimals are heated by ^{26}Al decay, causing the body to differentiate into a metallic core and silicate mantle.

2. Following differentiation, ^{26}Al partitions into the silicate mantle. After further heating, the melt fraction in the mantle is high enough to initiate mantle convection. The core is heated by the mantle from above and develops a stable thermal stratification that prevents the onset of a dynamo.

3. Once the mantle cools below the temperature at the CMB, the core thermal stratification is removed and the CMB heat flux becomes superadiabatic. Core convection triggers the onset of thermal dynamo generation.

4. As the mantle cools, it becomes more viscous until mantle convection ceases. The cessation of mantle convection leads to a sharp decrease in CMB heat flux and core convection drops below the critical value, terminating the dynamo.

5. Eventually the core cools below its solidus temperature and begins to solidify, which can lead to a compositional dynamo and a second epoch of dynamo generation.

6. Once the core has fully solidified, dynamo generation is no longer possible.

These previous models predict two epochs of dynamo generation: an early thermal dynamo with a delayed onset due to core thermal stratification, and a second later compositional dynamo during core solidification. This has led to remanences <5 Ma after CAI formation being interpreted as a record of a nebula field due to the delay in start time of thermal dynamos (Bryson et al., 2019a, 2020a; Fu et al., 2021). Meanwhile, remanences that were acquired after the dissipation of the nebula field, ∼4–5 Ma after CAI formation (Weiss et al., 2021), are thought to originate from planetesimal dynamos. Paleomagnetic remanences 5–30 Ma after CAI formation have been interpreted as thermal dynamos (Bryson et al., 2019a; Dodds et al., 2021), while those >65 Ma after CAI formation have been interpreted as evidence of a solidifying core (Maurel et al., 2020, 2021). For meteorites with slow cooling rates without radiometric ages for remanence acquisition, the onset of the second epoch of dynamo generation due to core crystallisation was used to constrain meteorite depths, remanence ages and parent body parameters (Tarduno et al., 2012; Bryson et al., 2015; Nichols et al., 2016, 2021).

As discussed in Chapter 2, previous models made several assumptions that limited their ability to predict the full magnetic history of a body. They neglected heating from ^{60}Fe in the core; did not fully combine thermal and compositional dynamo generation, mantle convection, and sub-eutectic core solidification; and did not investigate the effect of mantle viscosity on dynamo generation. An example run from my model that reassessed these assumptions has already demonstrated two key differences in dynamo generation compared to previous models (Section 2.3). Inclusion of ^{60}Fe brings forward the onset of thermal dynamo generation and a second epoch of dynamo generation can begin before the onset of core solidification. These differences could affect previous interpretations of the meteorite record, but are currently based on a single combination of planetesimal parameter values. In this chapter, I model dynamo histories for a full range of realistic values for mantle viscosity, ^{60}Fe abundance, initial core sulfur content and planetesimal size. This sheds light on the controls on planetesimal dynamo generation and enables re-interpretation of the meteorite paleomagnetic record.

3.2 Methods

This chapter uses the 1D, spherically symmetric planetesimal thermal evolution and dynamo generation model from Chapter 2 to predict the timings of dynamo generation in planetesimals with a radius up to 500 km. This model builds on the previous planetesimal thermal evolution models of Sterenborg and Crowley (2012), Bryson et al. (2019a) and Dodds et al. (2021) by including radiogenic heating from ^{60}Fe in the core, an adjustable mantle viscosity law, and updated stagnant lid and CMB boundary layer parametrisations that better reflect mantle conditions. The model includes both convection and conduction in the mantle and models magnetic field generation by sub-eutectic core solidification.

3.2.1 Thermal evolution model

All model runs begin at 0.8 Ma after CAI formation with instantaneous accretion of the planetesimal at 200 K. The body heats up due to radiogenic heating of ^{26}Al and the Fe-FeS and silicate phases melt until the silicate reaches its critical melt fraction, ϕ_C. At this point, differentiation is assumed to take place instantaneously, as the molten, dense Fe-FeS sinks through the rheologically weak silicates to the centre. The model then consists of two coupled reservoirs: the Fe-FeS core and the silicate mantle. Sulfur is the only light element considered in the core. The surface temperature is held constant at 200 K throughout the simulation.

In the mantle, heat is transported either by conduction or convection. Mantle convection is assumed to occur in the stagnant lid regime with an isothermal, convective layer between conductive boundary layers at the CMB and the surface. These boundary layers thicken as the mantle cools and convection ceases once the combined CMB and surface boundary layer thicknesses reach the total mantle thickness. The crust is part of the conductive boundary layer at the surface and is not modelled explicitly (Chapter 2). As a result, my model assumes crustal heat transport is purely conductive and neglects advective heat transport, e.g. heat pipes (Moore and Webb, 2013). The temperature at the CMB is calculated by assuming continuity of heat flux across the boundary.

The core also transports heat by conduction or convection. For the core to convect, either the CMB heat flux, F_{CMB}, must be superadiabatic or the core must be undergoing sub-eutectic solidification. During inward core solidification, the density difference between the more dense, solidified pure iron and the less dense Fe-FeS liquid drives core convection, as the solidifed iron sinks to the centre of the core. When the core is convecting, the combined thermal and compositional buoyancy flux can be used to calculate a magnetic field strength (Chapter 2). Once the eutectic composition is reached, core solidification no longer generates a compositional buoyancy flux. Combining buoyancy flux contributions enables the thermal and compositional drivers of convection to be considered simultaneously. The model ends once the whole core has solidified and dynamo generation is no longer possible.

3.2.1.1 Dynamo generation

The vigour of convection in the liquid part of the core is characterised by the magnetic Reynolds number, Re_m, which must be supercritical for the core flow to be strong enough to generate a magnetic field. The analytical estimate of the critical value is 10, while from empirical simulations this value ranges from 40–100 (Stevenson, 2003; Aubert et al., 2009). I use a critical Re_{m} of 10 in line with previous work (Bryson et al., 2019a; Dodds et al., 2021). However, the proportions of model runs with $10 \leq \mathrm{Re}_{\mathrm{m}} < 40$, $40 \leq \mathrm{Re}_{\mathrm{m}} < 100$, and $Re_m \geq 100$ are also investigated.

For compositional dynamo generation, I use the $m_{\mathrm{frac}} = 1$ core solidification endmember from Chapter 2, because this provides a lower estimate of Re_{m} and a more conservative time for when the dynamo will be on. The maximum difference in Re_{m} between endmembers for a given lengthscale is 16% (Chapter 2) so the choice of endmember does not have a large effect on the trends observed in this chapter.

3.2.2 Parameter variation

Models were run for a range of mantle viscosities, planetesimal radii, initial core sulfur contents, and $^{60}\mathrm{Fe}/^{56}\mathrm{Fe}$ ratios in the accreted material (Table 3.1).

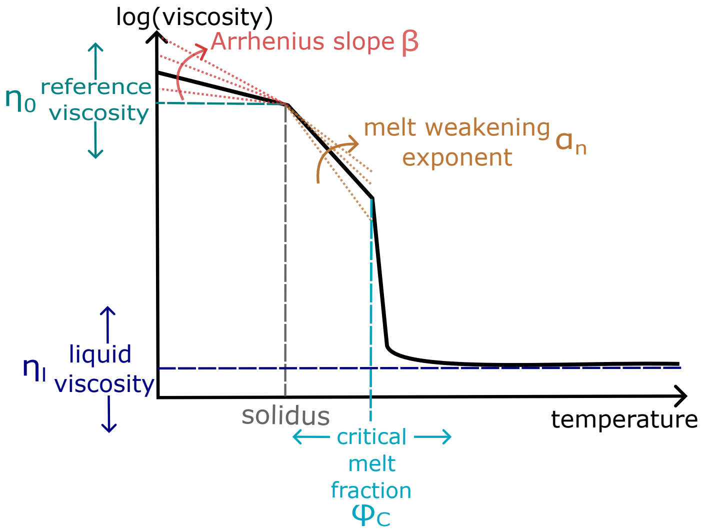

Figure 3.1: Illustration of the parameters varied in the mantle viscosity model. Reference viscosity, η_0=10^{15}–10^{24} Pas, is the viscosity at the mantle solidus. Liquid viscosity, η_l=1–100 Pas, is the viscosity when the mantle is fully molten. Critical melt fraction, ϕ_C =0.2–0.5, is the melt fraction for which all crystals become surrounded by melt, the material disaggregates and becomes rheologically weak. Arrhenius slope, β=0.01–0.035 K^{-1}, determines the rate of decrease in viscosity with increasing temperature. Melt weakening exponent, α_n=25–40, determines the additional rate of decrease in viscosity with increasing temperature due to melting.

The temperature dependence of mantle viscosity is defined piece-wise (Figure 3.1) by five control parameters. Below the solidus, the viscosity has an Arrhenius temperature dependence with slope β, which is proportional to the activation energy for viscous deformation. At the solidus, the mantle has a reference viscosity, η_0. Above the solidus, melt weakens the material and the viscosity decreases with a steeper Arrhenius dependence, quantified by the melt weakening exponent, α_n (Hirth and Kohlstedt, 2003). At the critical melt fraction, ϕ_C, there is enough melt to completely surround any remaining solid phases and the material disaggregates with a rapid drop in viscosity. Beyond ϕ_C, the viscosity tends to a constant liquid viscosity, η_l, following the Krieger-Dougherty relation (Sturtz et al., 2022b) as the melt fraction tends to one.

Each parameter was varied independently while the others were held constant at the median value of their range, except ϕ_C where the constant value was the experimental upper bound. The justifications for each parameter range are detailed in the following subsections.

3.2.2.1 Reference viscosity, η_0

The reference viscosity, η_0, ranges from 10^{15}–10^{24} Pas. The lower bound is based on experimental measurements extrapolated to a range of mantle grain sizes (Scott and Kohlstedt, 2006), while the upper bound is set by extrapolating reference viscosities used in models of Ganymede (Rückriemen et al., 2018) to planetesimal mid-mantle pressures (see Appendix B.2.1). Due to the uncertainty in extrapolating from experimental to planetesimal conditions and the uncertainty in mantle grain sizes, the lower range of values from 10^{15}–10^{18} Pas are less likely to occur in planetesimals, but are included for completeness.

3.2.2.2 Critical melt fraction, ϕ_{C}

Experiments suggest the critical melt fraction, ϕ_{C}, is between 0.2–0.3 (Scott and Kohlstedt, 2006). However thermal evolution models of planetesimals both for dynamo generation (Sterenborg and Crowley, 2012; Bryson et al., 2019a; Dodds et al., 2021) and differentiation (e.g., Lichtenberg et al., 2019b; Monnereau et al., 2023) use a value of $\phi_{\mathrm{C}} = 0.5$. Although it is unclear if $\phi_{\mathrm{C}} = 0.5$ is physically reasonable, I adopted the range $\phi_{\mathrm{C}} = 0.2$–0.5 to enable comparison with previous models and encapsulate experimental observations.

3.2.2.3 Arrhenius slope, β

The Arrhenius slope in the viscosity law, β, is typically defined as $\frac{E}{RT_{\mathrm{ref}}^2}$, where E is the activation energy, $R = 8.31\,\mathrm{J\,mol^{-1}\,K^{-1}}$ is the gas constant, and T_{ref} is a reference temperature — often taken to be the temperature at which the reference viscosity is measured. Experimentally measured activation energies for a range of silicate mantle compositions and strain rates range from 240–$570\,\mathrm{kJ\,mol^{-1}}$ (Karato and Wu, 1993; Hirth and Kohlstedt, 2003). For a reference temperature of the mantle solidus (1400 K), this corresponds to β=0.015–$0.035\,\mathrm{K^{-1}}$. Dodds et al. (2021) used $\beta = 0.01\,\mathrm{K^{-1}}$, so to enable comparison with previous thermal evolution models, I explore $\beta = 0.01$–$0.035\,\mathrm{K^{-1}}$.

3.2.2.4 Melt weakening exponent, α_{n}

The melt weakening exponent, α_{n}, depends on whether deformation occurs by diffusion creep ($\alpha_{\mathrm{n}} = 25$–30) or dislocation creep ($\alpha_{\mathrm{n}} = 30$–45) (Hirth and Kohlstedt, 2003). To cover both deformation modes I consider values from 25–45.

3.2.2.5 Liquid viscosity, η_l

The liquid viscosity, η_l, is determined by mantle composition and can range from 1–100 Pas across the compositions of all volcanic rocks commonly encountered on Earth (Giordano et al., 2008). Increasing silica content increases viscosity and increasing volatile content decreases viscosity (Lesher and Spera, 2015).

3.2.2.6 Initial core sulfur content, $X_{\mathrm{S},0}$

The initial core sulfur content, $X_{\mathrm{S},0}$, ranges from the minimum Fe-FeS sulfur content for which the metal phase will be fully molten before differentiation to the eutectic composition (33 wt% for $T_{\mathrm{s,Fe}} = 1260\,\mathrm{K}$ for R=300 km). The Fe-FeS liquidus temperature is pressure dependent so the minimum Fe-FeS changes with planetesimal radius.

3.2.2.7 Primordial ^{60}Fe/^{56}Fe

Estimates on the primordial ^{60}Fe/^{56}Fe vary by almost three orders of magnitude from 10^{-9} (Fang et al., 2025) to 6×10^{-7} (e.g., Cook et al., 2021, see Appendix B.1 for more details). However, previous thermal evolution and dynamo models neglected the presence of ^{60}Fe in the core. Therefore, the model was run for five values of ^{60}Fe/^{56}Fe $= [0, 1 \times 10^{-9}, 1 \times 10^{-8}, 1 \times 10^{-7}, 6 \times 10^{-7}]$ to cover the full range of possible values and to compare with previous models.

3.2.2.8 Planetesimal radius, r

Models were run for planetesimal radii between 100–500 km. The lower limit is set by previous estimates for the minimum radius for compositional dynamo generation (Nimmo, 2009). The upper limit corresponds approximately to the radius of Ceres, the largest known asteroid today.

3.3 Results

3.3.1 Constant radius

Firstly, I ran models with a constant radius of 300 km to identify the impact of other parameters on thermal evolution and dynamo generation. The lowest mantle reference viscosity, η_0, and lowest initial core sulfur content, $X_{\mathrm{S},0}$, result in a single epoch of dynamo generation, and a single value in each of η_0, ϕ_C, and α_n result in three epochs of dynamo generation (see Appendix B.2.3). Otherwise, all other parameter

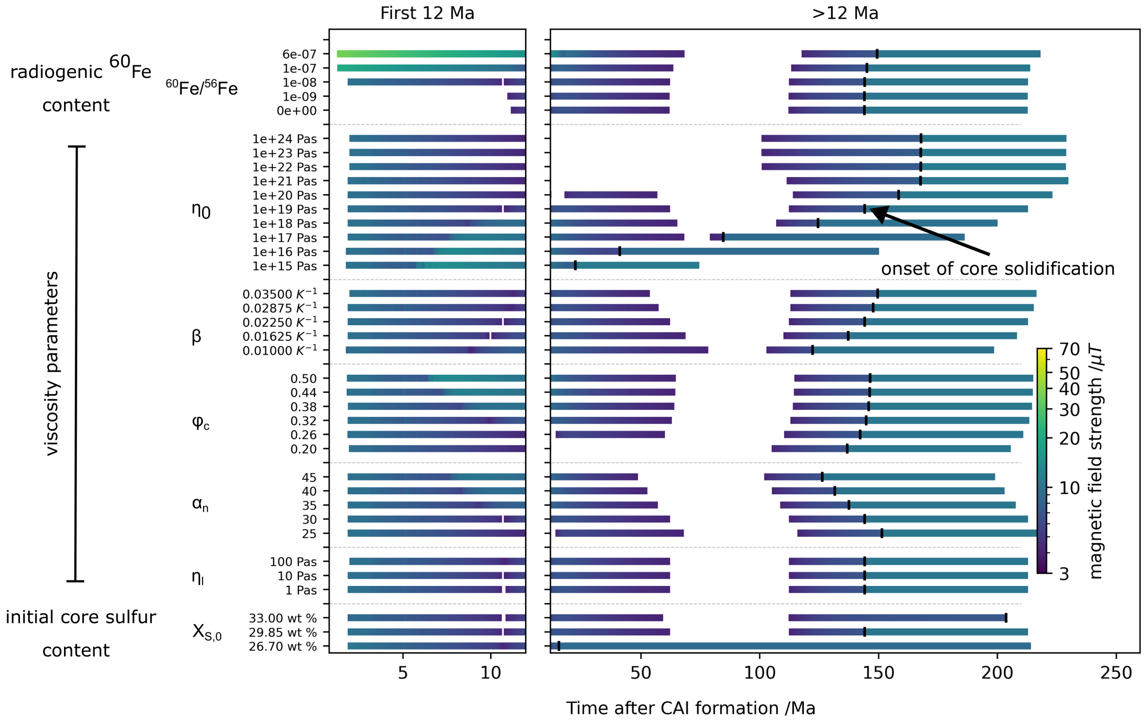

Figure 3.2: Dynamo timings for a 300 km radius planetesimal for a range of initial ^{60}Fe/^{56}Fe, mantle viscosities, and core compositions. Filled bars indicate periods when a dynamo is active and the colour of the bar indicates dipole magnetic field strength at the surface. The small, vertical, black line on each bar indicates the onset of core solidification in each model run. Magnetic field strengths between the onset of core solidification and the end of dynamo generation are averages for this time interval to remove oscillations in field strength due to the discretisation of the model (Chapter 2). The thin, vertical, white lines in some runs are < 0.5 Ma breaks in dynamo generation due to a rapid increase in viscosity at ϕ_C. These lines are artefacts of my viscosity and stagnant lid parametrisation and should not be interpreted. For each parameter, the model was run across the range of values in Table 3.1, while all other parameters are held at a constant median value (except ϕ_C where the constant value was the experimental upper bound). The constant parameter values were: $\eta_0 = 10^{19}$ Pas, $\beta = 0.0225\,\mathrm{K}^{-1}$, $\alpha_n = 30$, $\phi_C = 0.3$, $\eta_l = 10$ Pas, $^{60}\mathrm{Fe}/^{56}\mathrm{Fe} = 10^{-8}$, $X_{S,0} = 29.85$ wt%. See Figures 3.6–3.9 for identical figures for 100–500 km radius planetesimals.

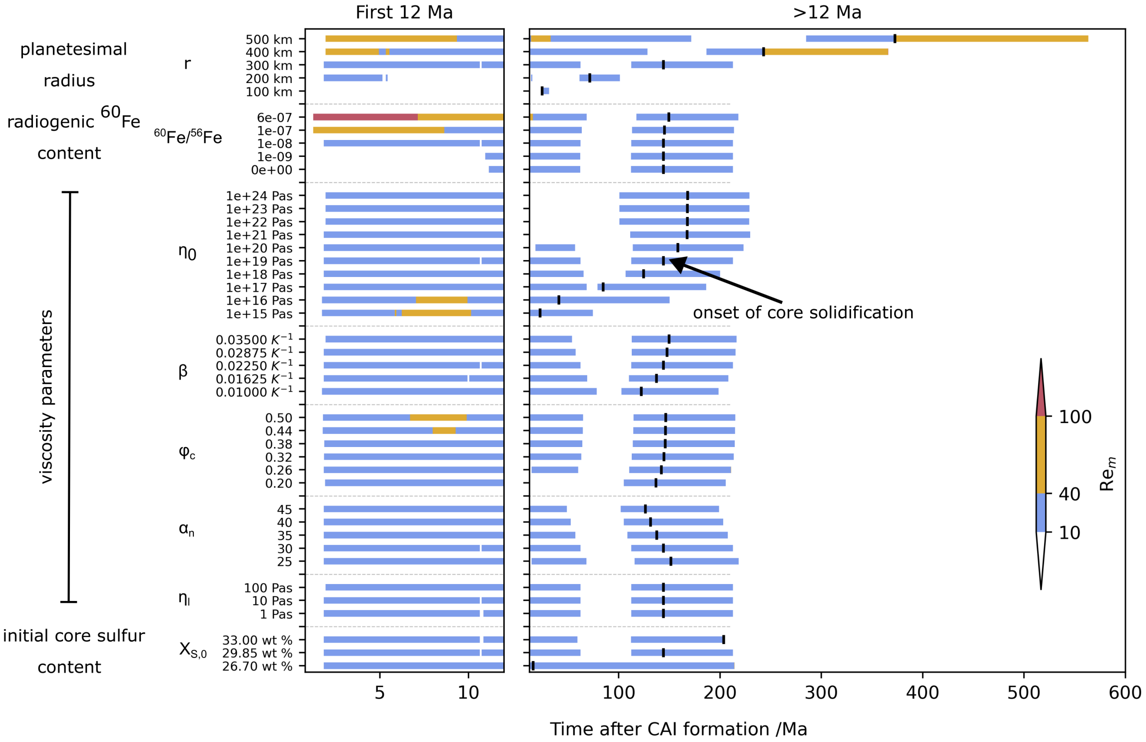

Figure 3.3: Magnetic Reynolds number (Re_m) as a function of time for a range of initial ^{60}Fe/^{56}Fe, mantle viscosities, core compositions, and planetesimal radii. Filled bars indicate periods when the dynamo is on and the colour of the bars indicates the magnetic Reynolds number. Subcritical values (< 10) are not shown. Supercritical values are categorised according to the range of possible criticality limits: 10–40, 40–100 and > 100 (Christensen and Aubert, 2006; Stevenson, 2003). The small, vertical, black line on each bar indicates the onset of core solidification in each model run. Magnetic Reynolds numbers between the onset of core solidification and the end of dynamo generation are averages for this time interval to remove oscillations in Re_m due to the discretisation of the model (Chapter 2). The thin, vertical, white lines in some runs are < 0.5 Ma breaks in dynamo generation due to a rapid increase in viscosity at ϕ_C. These lines are artefacts of my viscosity and stagnant lid parametrisation and should not be interpreted. For each parameter, the model was run across the range of values in Table 3.1, while all other parameters were held at a constant median value (except ϕ_C where the constant value was the experimental upper bound). The range of values for radius are shown explicitly. The constant parameters values are: $r = 300\,\mathrm{km}$, $\eta_0 = 10^{19}\,\mathrm{Pas}$, $\beta = 0.0225\,\mathrm{K}^{-1}$, $\alpha_\mathrm{n} = 30$, $\phi_\mathrm{C} = 0.3$, $\eta_\mathrm{l} = 10\,\mathrm{Pas}$, $^{60}\mathrm{Fe}/^{56}\mathrm{Fe} = 10^{-8}$, $X_{\mathrm{S},0} = 29.85\,\mathrm{wt}\%$.

Symbol	Meaning	Range of values	Constant value	Reference
η_0	Reference viscosity	10^{15}–10^{24} Pas	10^{19} Pas	a, b
ϕ_C	Critical melt fraction	0.2–0.5	0.3	a, c
β	Arrhenius slope	0.01–0.035 K^{-1}	0.0225 K^{-1}	a, d, e
α_n	Melt weakening exponent	25–45	30	f
η_l	Liquid viscosity	1, 10, 100 Pas	10 Pas	g
$X_{\mathrm{S},0}$	Initial core sulfur content	26.7–33 wt%	29.85 wt%	
$^{60}\mathrm{Fe}/^{56}\mathrm{Fe}$	$^{60}\mathrm{Fe}/^{56}\mathrm{Fe}$ in accreting material	0, 10^{-9}, 10^{-8}, 10^{-7}, 6×10^{-7}	10^{-8}	h, i, j, k
r	Planetesimal radius	100–500 km	300 km	c

Table 3.1: Values for variable and constant parameters in simulations as described in Section 3.2.2. The upper five parameters occur in the viscosity law. The range on $X_{\mathrm{S},0}$ is for a 300 km radius planetesimal. For [500, 400, 200, 100] km radius planetesimals the minimum and median $X_{\mathrm{S},0}$ were [25.9, 26.3, 27.1, 27.1] wt% and [29.45, 29.65, 30.05, 30.05] wt% respectively. The constant values are median values in their range, except ϕ_C where the constant value was the experimental upper bound. η_l and $^{60}\mathrm{Fe}/^{56}\mathrm{Fe}$ vary over several orders of magnitude, so the explored input values are stated explicitly and the constant value was the median from this list of values. (a) Scott and Kohlstedt (2006), (b) Rückriemen et al. (2018), (c) Bryson et al. (2019a), (d) Karato and Wu (1993), (e) Dodds et al. (2021), (f) Hirth and Kohlstedt (2003), (g) Giordano et al. (2008), (h) Tang and Dauphas (2012), (i) Cook et al. (2021), (j) Kodolányi et al. (2022a), (k) Kodolányi et al. (2022b).

combinations produce two periods of dynamo generation (Figure 3.2). Across these two dynamo generation periods, I observe two distinctive trends in magnetic field strength: (i) the first dynamo generation period can have two peaks in magnetic field strength (ii) in the second dynamo generation period, magnetic field strength increases with time towards a peak value during core solidification. The first peak in the first epoch of dynamo generation corresponds to the onset of dynamo generation and the second peak occurs when the base of the mantle first cools below the critical melt fraction (Chapter 2). The peak in field strength at the beginning of the first epoch of dynamo generation is always the strongest because radiogenic heating by ^{60}Fe increases CMB heat flux (F_CMB). For all runs with multiple field generation periods, the final dynamo generation period begins before the onset of core solidification. This is due to the delayed steepening of the mantle conductive gradient at the CMB after the cessation of mantle convection, which increases F_CMB (Chapter 2). Reference viscosity has the strongest effect on the duration of the gap in dynamo generation and $^{60}\mathrm{Fe}/^{56}\mathrm{Fe}$ has the strongest influence on the resulting magnetic field strength. Despite the range in dynamo durations and strengths, most Re_m values fall between 10–40 (Figure 3.3).

3.3.1.1 Effect of ^{60}Fe

Increasing ^{60}Fe/^{56}Fe brings forward the onset of the dynamo to 1–2 Ma after CAI formation and increases peak field strength and Re_{m} in the first epoch of dynamo generation. The onset of the dynamo is earlier for increased ^{60}Fe because increased heating either erodes core thermal stratification more rapidly or prevents its formation altogether, which brings forward the time that F_{CMB} becomes superadiabatic. Radiogenic heating by ^{60}Fe also increases the temperature of the core and the temperature difference relative to the mantle, which increases F_{CMB} and the strength of the dynamo. Model runs with $^{60}\mathrm{Fe}/^{56}\mathrm{Fe} \geq 10^{-7}$ had peak field strengths in the first period of dynamo generation 2–3 times higher than runs with $^{60}\mathrm{Fe}/^{56}\mathrm{Fe} = 10^{-8}$. This extra heat is removed from the core by an elevated F_{CMB} during the first period of dynamo generation. As such, by the second epoch of dynamo generation the peak field strengths, Re_{m}, and the onset of core solidification are similar across all values of ^{60}Fe/^{56}Fe. There are similar onset times and field strengths for the first dynamo generation period for $^{60}\mathrm{Fe}/^{56}\mathrm{Fe} =0$ and $^{60}\mathrm{Fe}/^{56}\mathrm{Fe} = 10^{-9}$. This similarity suggests that when $^{60}\mathrm{Fe}/^{56}\mathrm{Fe} \leq 10^{-9}$ the effect of ^{60}Fe can be neglected. The onset times vary little across variations in other parameters indicating ^{60}Fe/^{56}Fe is the dominant control on onset time for the first period of dynamo generation.

3.3.1.2 Effect of viscosity

The reference viscosity, η_0, has the strongest effect on the duration of the first period of dynamo generation and the following gap. Above 10^{21} Pas, the first period of dynamo generation ends after 13–14 Ma and is followed by a gap of > 80 Ma in dynamo generation. This results from the rapid thickening of the surface stagnant lid, which shuts off convection earlier for the highest reference viscosities. In contrast, below 10^{16} Pas, there is only one epoch of dynamo generation, because the mantle viscosity is sufficiently low that mantle convection does not cease before core solidification. The second peak in magnetic field strength in the first epoch of dynamo generation widens and increases in strength with decreasing reference viscosity, because the thinner boundary layer at the CMB raises F_{CMB}. An elevated F_{CMB} increases the rate at which the core cools, which brings forward the onset of core solidification and the end of dynamo generation.

The viscosity parameters have very little effect on the supercriticality of Re_{m}. Only the lowest η_0 and highest values of ϕ_{C} increase Re_{m} in the first 12 Ma (Figure

3.3). However, the highest value $\phi_{\mathrm{C}} = 0.5$ has been adopted in previous thermal evolution models, despite not being supported by experimental data for basaltic melts (Scott and Kohlstedt, 2006). The elevated Re_{m} for this value may have resulted in overestimates of field strength and dynamo duration in previous work. The lowest values of η_0 ($< 10^{18}\,\mathrm{Pas}$) are less applicable, because of the uncertainty in extrapolating from laboratory to planetesimal grain sizes (see Appendix B.2.1). As such, the very rapid core cooling and elevated Re_{m} observed in models with $\eta_0 \leq 10^{16}\,\mathrm{Pas}$ is unlikely to occur in planetesimals.

3.3.1.3 Effect of $X_{\mathrm{S},0}$

Intial core sulfur content, $X_{\mathrm{S},0}$, has a strong effect on the timing of core solidification, because increasing $X_{\mathrm{S},0}$ lowers the liquidus temperature of the core and more cooling is required to reach this temperature. The lowest $X_{\mathrm{S},0}$ removes the gap in dynamo generation, because the early onset of core solidification provides additional compositional buoyancy flux to drive the dynamo even when mantle convection ceases.

3.3.2 Variable radius

To identify the impact of planetesimal radius on thermal evolution and dynamo generation I ran models with varying radii and other variables held constant (Table 3.1). Core radius was assumed to be half the planetesimal radius. Planetesimal radius has the strongest effect on dynamo timing, duration, and width of the gap in dynamo generation (Figure 3.4). Larger planetesimals cool more slowly so mantle convection ceases later, which prolongs the first epoch of dynamo generation. Larger core size increases the lengthscale of convection; this raises the Re_{m} value for a given F_{CMB}, which further prolongs dynamo generation. Larger core size also increases magnetic field strengths (Figures 3.6–3.9). The increase in magnetic field strength is most pronounced at the onset of the first epoch of dynamo generation when the highest values of $^{60}\mathrm{Fe}/^{56}\mathrm{Fe}$ are considered. Bodies with radius of 100 km only generate magnetic fields after the onset of core solidification (Figure 3.6) except for the highest values of $^{60}\mathrm{Fe}/^{56}\mathrm{Fe}$. Increasing planetesimal radius from 100 km to 500 km increases the end time of dynamo generation from ~30 to ~600 Ma (Figure 3.4, 3.6–3.9). The gap in dynamo generation moves later (~20–200 Ma) and increases in duration (~20–270 Ma) for increasing planetesimal radius. For each body size, the timings of the dynamo generation periods are consistent across variations in the other parameters (Figure 3.4). An exception is η_0 (Figure 3.5), where values $< 10^{16}\,\mathrm{Pas}$ do not produce

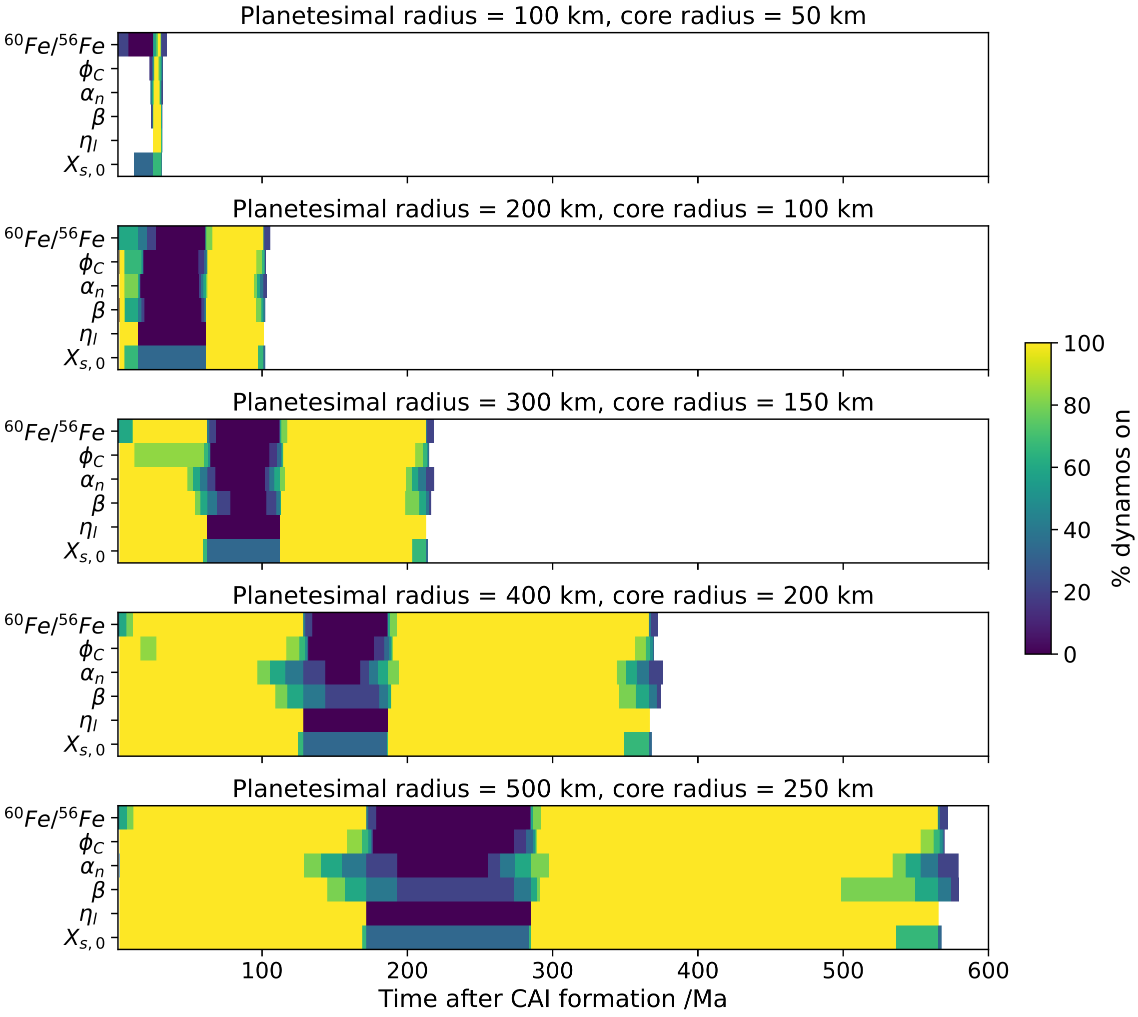

Figure 3.4: Percentage of active dynamos across the range of possible values for initial ^{60}Fe/^{56}Fe, mantle viscosities, and core compositions for planetesimals ranging from 100-500 km in radius. In an individual panel, model runs are grouped in horizontal blocks by parameter. Yellow indicates that all dynamos are on at a given time irrespective of the value of a parameter, dark blue indicates no dynamos are on at a given time irrespective of the value of a parameter. Light blue to green regions indicate a dynamo is on for a subset of values of that parameter. White space indicates times after the last period of dynamo generation and the end of the simulation. The constant parameters values are: $\eta_0 = 10^{19}\,\text{Pas}$, $\beta = 0.0225\,\text{K}^{-1}$, $\alpha_\text{n} = 30$, $\phi_\text{C} = 0.3$, $\eta_\text{l} = 10\,\text{Pas}$, $^{60}\text{Fe}/^{56}\text{Fe} = 10^{-8}$ and the range for each parameter is given in Table 3.1. η_0 causes a wide variation in dynamo timings, so is shown separately in Figure 3.5.

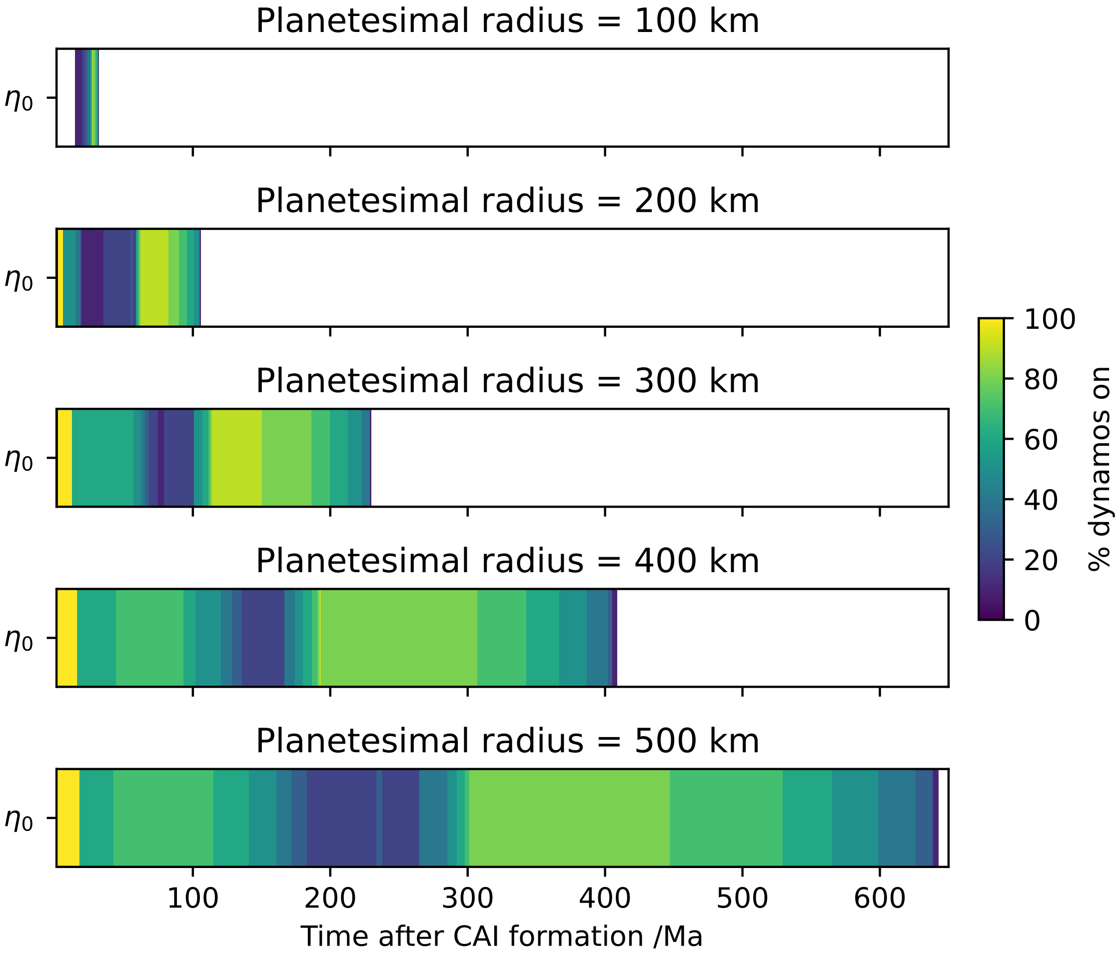

Figure 3.5: Percentage of active dynamos across the range of possible values for reference viscosity, η_0, for planetesimals ranging from 100–500 km in radius. Core radius is half the planetesimal radius. Yellow indicates that all dynamos are on at a given time irrespective of the value of η_0, dark blue indicates no dynamos are on at a given time irrespective of the value of η_0. Light blue to green regions indicate a dynamo is on for a subset of values of η_0. White space indicates times after the last period of dynamo generation and the end of the simulation. The vertical axis is equivalent to one horizontal block in Figure 3.4 and has no physical meaning. The constant parameter values are: $\beta = 0.0225\,\mathrm{K}^{-1}$, $\alpha_\mathrm{n} = 30$, $\phi_\mathrm{C} = 0.3$, $\eta_\mathrm{l} = 10\,\mathrm{Pas}$, $^{60}\mathrm{Fe}/^{56}\mathrm{Fe} = 10^{-8}$, $X_{\mathrm{S},0}$ =[29.45, 29.65, 29.85, 30.05, 30.05] wt% for [500, 400, 300, 200, 100] km radius planetesimals. The range for η_0 is given in Table 3.1.

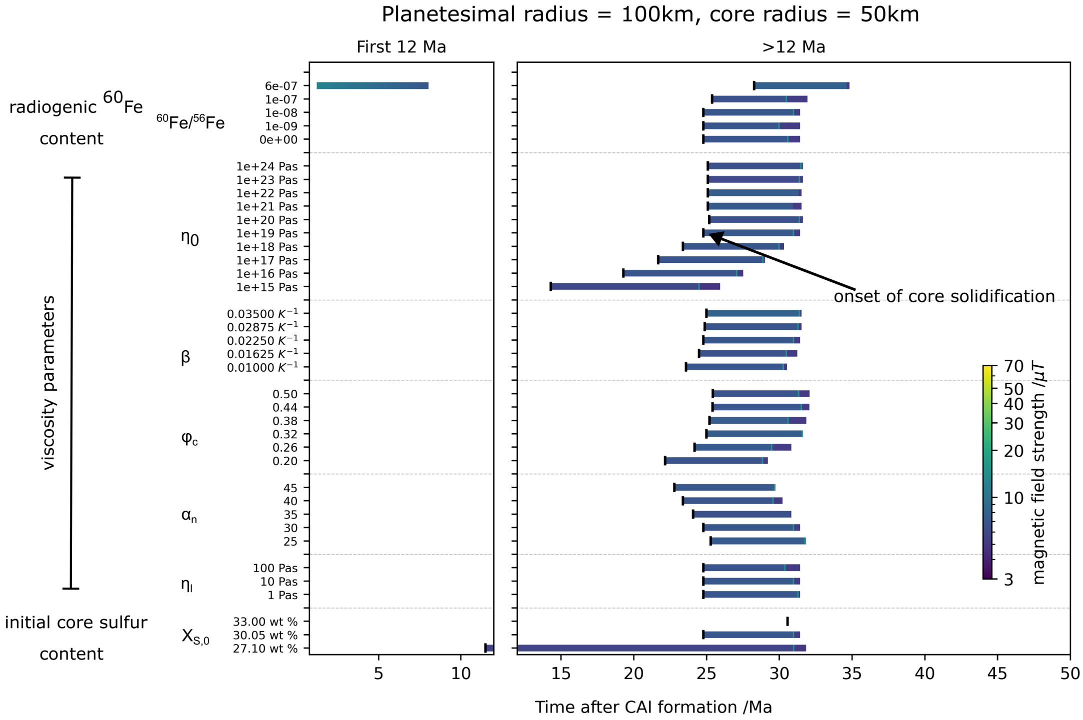

Figure 3.6: Same as Figure 3.2 but for a 100 km radius planetesimal. The colour scale is set based on the maximum and minimum field strengths across Figures 3.6–3.9.

a gap in dynamo generation. However, there is still a trend of increasing dynamo duration with radius for η_0.

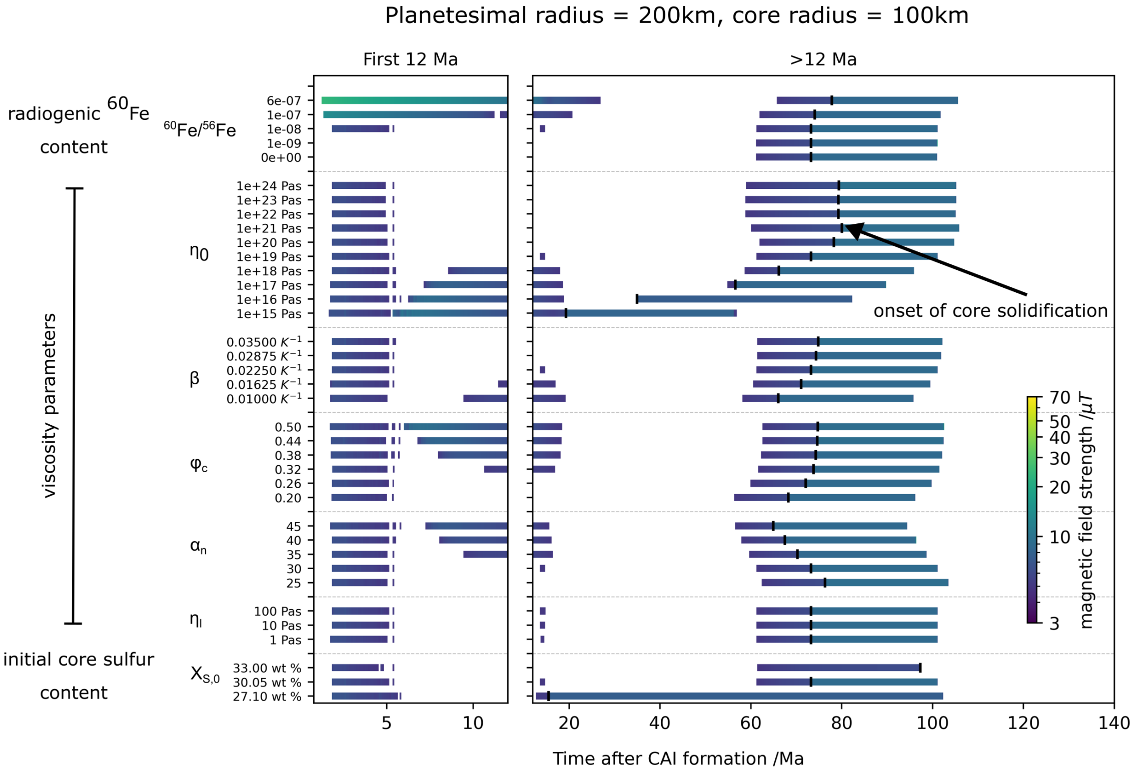

Figure 3.7: Same as Figure 3.2 but for a 200 km radius planetesimal. The colour scale is set based on the maximum and minimum field strengths across Figures 3.6–3.9.

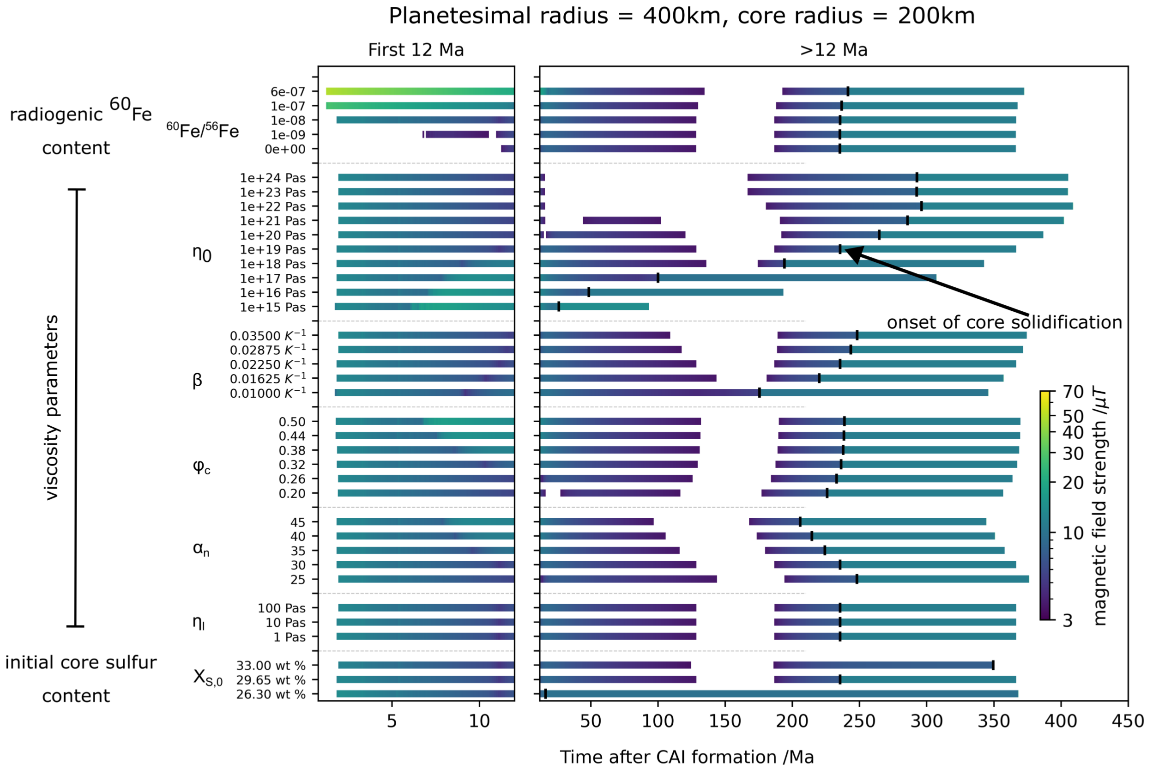

Figure 3.8: Same as Figure 3.2 but for a 400 km radius planetesimal. The colour scale is set based on the maximum and minimum field strengths across Figures 3.6–3.9.

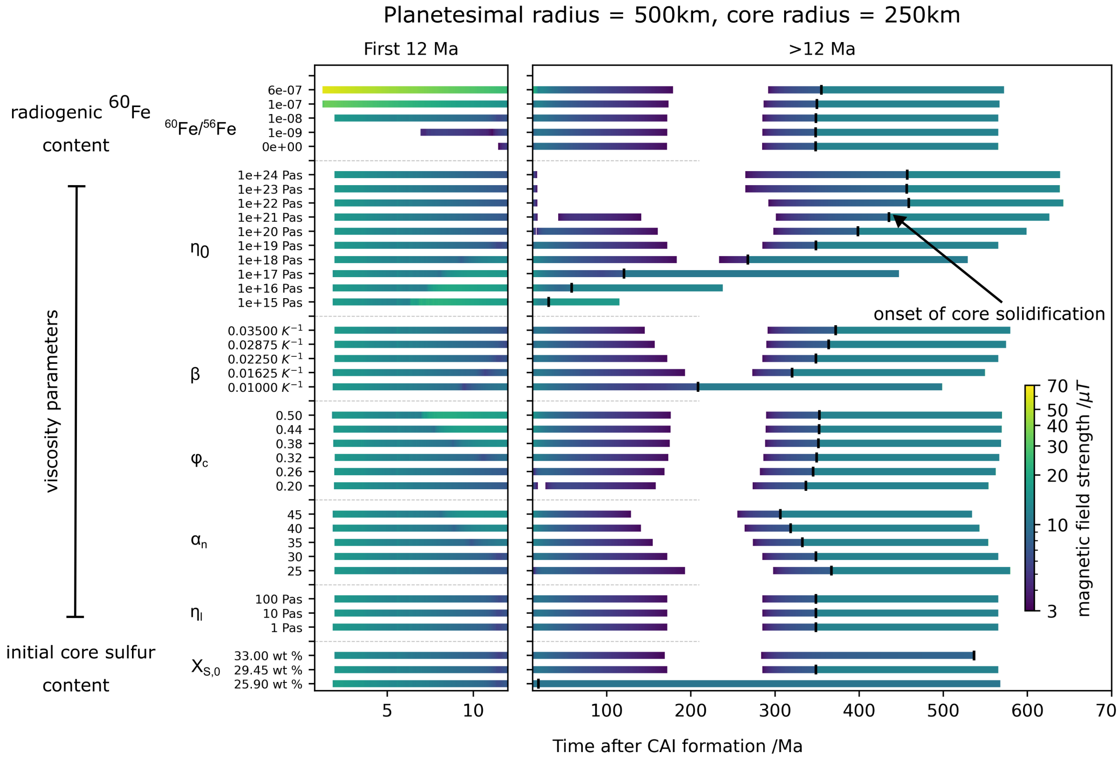

Figure 3.9: Same as Figure 3.2 but for a 500 km radius planetesimal. The colour scale is set based on the maximum and minimum field strengths across Figures 3.6–3.9.

3.4 Discussion

3.4.1 Reevaluating the paleomagnetic record

The purpose of my model is to determine the origins (nebula field, thermal dynamo, or compositional dynamo) of magnetisations in the meteorite paleomagnetic record. Overall, my model results suggest two key interpretations of the paleomagnetic record should be revisited. First, the earliest recorded magnetisations (<5 Ma after CAI formation), previously attributed to the nebula field, could have been dynamo generated. This is due to inclusion of $^{60}\text{Fe}/^{56}\text{Fe} \geq 10^{-8}$ in my model bringing forward the onset of thermal dynamos to 1–2 Ma after CAI formation, which allows for thermal dynamo generation prior to the dissipation of the nebula field (Figure 3.10). Second, late magnetic remanences, previously ascribed to the second epoch of dynamo generation during core solidification, may not have been in the second epoch and do not require core solidification, but could instead be produced by a thermal dynamo. My model predicts an elongated first epoch of dynamo generation lasting until 20–200 Ma after CAI formation (depending on radius) rather than until 9–34 Ma after CAI formation as suggested by previous models (Dodds et al., 2021). Additionally, in my model, the second epoch of dynamo generation begins before the onset of core solidification. The meteorite paleomagnetic record in light of my new model results is reassessed in detail below.

3.4.1.1 Paleomagnetic records of the nebula field

Unidirectional magnetisation within chondrules, but non-unidirectional magnetisation between chondrules in a meteorite is only possible if the chondrules acquired their remanence prior to accretion onto the meteorite parent body. The nebula field is the only source of a pre-accretionary magnetisation, therefore non-unidirectional chondrule magnetisations provide conclusive evidence that a paleointensity can be attributed to the nebula field. Non-unidirectional measurements of chondrules from CO (Borlina et al., 2021), LL3 (Fu et al., 2014b) and CR chondrites (Fu et al., 2020) are interpreted as evidence for the nebula field ∼1.7–4 Ma after CAI formation with paleointensities up to $\sim 150\,\mu\text{T}$ (Figure 3.10). Bulk meteorite magnetisations from parent bodies that were too small to generate a dynamo can also be attributed to the nebula field (e.g. Erg Chech 002; Neumann et al., 2023; Maurel and Gattacceca, 2024).

Null remanences could indicate the dissipation of the nebula field, but there are two other possible interpretations, which must be excluded first. Firstly, a meteorite

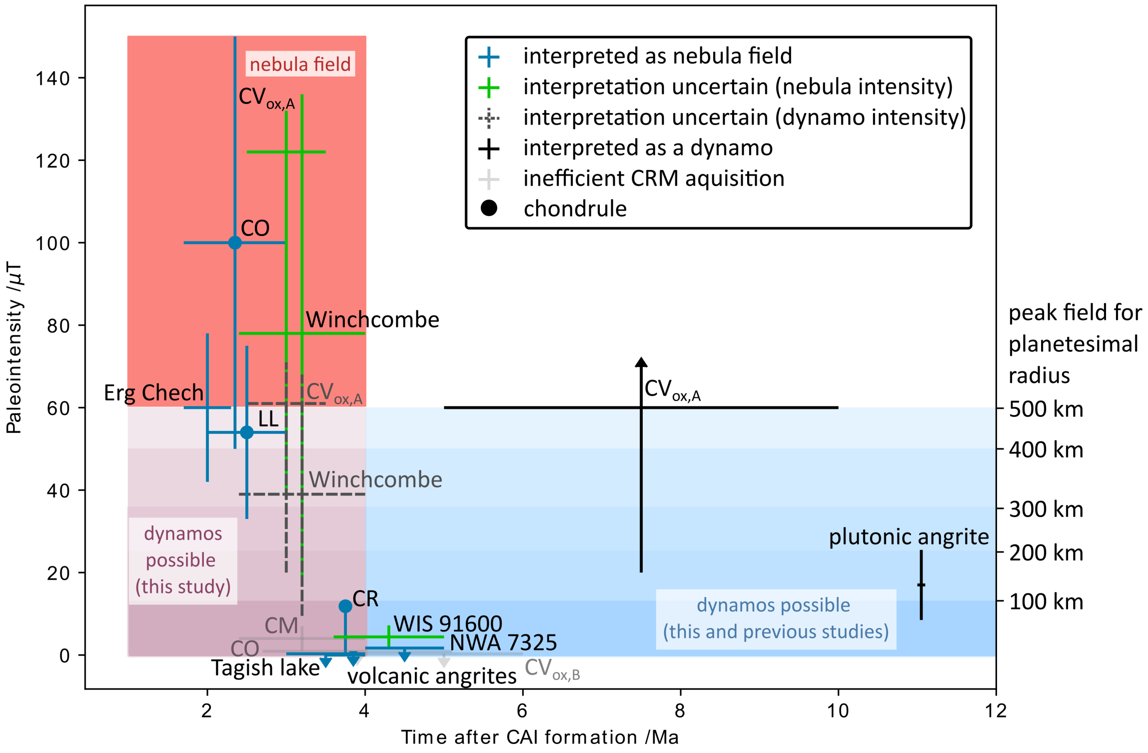

Figure 3.10: A summary of meteorite paleointensities for the first 12 Ma after CAI formation. Meteorites for which the cause of magnetisation is interpreted as a nebula field (or lack of) are plotted in blue. Meteorites for which the cause of magnetisation has been interpreted as a dynamo field are plotted in black. Meteorites which could have a nebula or dynamo origin are plotted in green for their possible nebula field paleointensities. The dashed grey lines indicate the paleointensities of Winchcombe (Bryson et al., 2023) and Allende (Fu et al., 2021) if the factor of two correction for the nebula field is not applied. Faded grey points correspond to null or low paleointensities, which may be due to formation of magnetite by pseudomorphic replacement which cannot record a chemical remanent magnetisation (CRM) (Bryson et al., 2023). The blue circles indicate pre-accretionary remanences from chondrules. The IVA irons have not been included, because they were generated by a solidifying, unmantled core (Bryson et al., 2017). The R chondrites have too large an age uncertainty and the CV chondrules are too altered to provide useful constraints, so neither are shown (Cournède et al., 2020; Shah et al., 2017). Intensity bars with arrows indicate values with a upper/lower limit (the cap) and for the CV$_{ox,A}$ the best guess is the intersection with the time error bar. My new model brings forward the onset of dynamo generation (pink box) relative to previous models (blue box). The graduated shading in the blue and pink regions indicates the maximum paleointensity for a given planetesimal radius (shown by ticks on the right hand vertical axis). The orange box indicates the duration of the nebula field, which may be 1 Ma longer than shown here if the angrite age is recalculated based on Piralla et al. (2023). This would further increase the overlap between dynamo and nebula fields. Data and references for this table are given in Tables B.2 and B.3.

parent body may have formed in a distal part of the Solar System where the field was weak (e.g., Tagish Lake; Bryson et al., 2020b). Secondly, the magnetic minerals may not have formed in a way that allowed them to record a remanence. Many carbonaceous (CC) chondrites record magnetisation in magnetite, which formed during aqueous alteration. If the magnetite formed by pseudomorphic replacement of FeNi metal rather than precipitation, it may not have recorded a new remanence during this process (Bryson et al., 2023). This could explain the null remanence in CV chondrite Kaba (Gattacceca et al., 2016) and the upper limit on paleointensity of $0.9\,\mu$T from the matrix of CO chondrites (Borlina et al., 2022). For the volcanic angrites both these interpretations can be excluded. They formed in the inner Solar System, erupted ~3.8–3.9 Ma after CAI formation[1] and cooled quickly forming magnetite that should have recorded any magnetic fields present (Wang et al., 2017). Therefore, a null remanence in the angrites suggests the nebula field in the inner Solar System dissipated 3.8–3.9 Ma after CAI formation (Wang et al., 2017). The recovered paleointensity of $< 0.6\,\mu$T from ungrouped achondrite NWA 7325 at ~4–5 Ma after CAI formation (Weiss et al., 2017) further supports the nebula field in the inner Solar System having dissipated by this time.

3.4.1.2 Ambiguous paleomagnetic records: nebula or dynamo fields?

Interpretation of bulk chondrite paleomagnetic remanences (i.e. not individual chondrule measurements) from the first 5 Ma after CAI formation is complicated because these meteorites could sample the outer layer of a partially differentiated planetesimal (Carporzen et al., 2011; Elkins-Tanton et al., 2011; Weiss and Elkins-Tanton, 2013). In this case, a chondritic meteorite could record a paleomagnetic remanence from a dynamo generated in the core of their partially differentiated parent body rather than the nebula field. The feasibility of this scenario rests on the timing of planetesimal dynamos, evidence for partially differentiated meteorite parent bodies, and the value of primordial ^{60}Fe/^{56}Fe. My model demonstrates that a parent body with ^{60}Fe/^{56}Fe $\geq 10^{-8}$ would have an early onset of a thermal dynamo before the dissipation of the nebula field. Thermally metamorphosed chondritic meteorites could have been heated purely radiogenically on a parent body that partially differentiated. The interpretation of bulk remanences in the CM and CV chondrites and WIS 91600 (green points in Figure 3.10) is less clear than previously, in light of the possibility they record an early dynamo. The ages of the R chondrites are too poorly constrained (0–20 Ma

---

[1] These ages were originally reported as absolute Pb-Pb ages and may be shifted to 4.8–4.9 Ma after CAI formation based on reevaluation of the anchor for Pb-Pb (Piralla et al., 2023).

after CAI formation, Cournède et al., 2020) for the origin of their remanence to be discussed.

The CM chondrites and WIS 91600 recorded a magnetic field 2–4 Ma after CAI formation (Cournede et al., 2015; Bryson et al., 2023) and likely 3.6–5 Ma after CAI formation (Bryson et al., 2020a), respectively. The timing of these remanences is consistent with either a nebula field or dynamo origin. For example, a 500 km radius planetesimal with ^{60}Fe/^{56}Fe = 1–6$\times10^{-7}$ and other constant parameters from Table 3.1 produces intensities that match those recovered from Winchcombe (Figure B.6). However, lack of evidence for prolonged thermal metamorphism in the CM chondrites and WIS 91600 (Suttle et al., 2021; Bryson et al., 2020a) argues against partially differentiated parent bodies for these meteorites; unless they sample the topmost, coolest layer of such a body. Further numerical modelling of partially differentiated bodies combining gradual accretion and ^{60}Fe are required to determine whether a dynamo in a partially differentiated body or the nebula field is the source of these remanences.

The CV chondrites are thermally metamorphosed (Carporzen et al., 2011; Elkins-Tanton et al., 2011; Gattacceca et al., 2016) and have a complex paleomagnetic record. CV chondrules have been modified by impacts, heating and aqueous alteration and have a non-unidirectional magnetisation within an individual chondrule, so their remanence cannot be attributed to the nebula field (Fu et al., 2014a; Shah et al., 2017). Allende records a magnetisation in the iron sulfides in the matrix from 2.5–3.5 Ma after CAI formation (Fu et al., 2021), and has a bulk remanance dated to 5–40 Ma after CAI formation (Carporzen et al., 2011; Elkins-Tanton et al., 2011). The CV chondrite Kaba has a null remanence from aqueous alteration at 4–6 Ma after CAI formation, but a $\sim3\,\mu$T remanence from prolonged metamorphism tens of Ma after CAI formation (Gattacceca et al., 2016). The later (>5 Ma after CAI formation) CV chondrite remanences, combined with evidence for thermal metamorphism, suggest the CV chondrite parent body was partially differentiated and generated a dynamo (Elkins-Tanton et al., 2011; Gattacceca et al., 2016). Previously, Kaba's null remanance, recorded during aqueous alteration, was used as evidence for the dissipation of the nebula field before the onset of the dynamo on the CV chondrite parent body. This supported a nebula origin for the earliest Allende remanence (2.5–3.5 Ma after CAI formation Fu et al., 2021). However, Kaba's magnetite may have been unable to acquire a remanance during formation (Bryson et al., 2023), so this null remanance may not indicate an absence of a magnetic field on the CV parent body at 4–6 Ma after CAI formation. Altogether, the altered interpretation of Kaba's null remanence, thermal metamorphism of the CV chondrite parent body and the early dynamo onset predicted by my models suggests the earliest remanence on Allende could be due to the early onset of a thermal dynamo.

Intensity of remanence Next, I assess whether paleointensity can be used to determine if a remanence has a dynamo or nebula field origin. As shown in Figure 3.10, the maximum nebula intensities inferred from paleomagnetic measurements are stronger than the maximum intensities predicted by my dynamo model. However, the nebula intensities estimated from Winchcombe (CM chondrite, Bryson et al., 2023) and Allende (CV chondrite, Fu et al., 2021) were calculated from the paleointensities recorded by these meteorites by multiplying by a factor of two to account for rotation of the parent body during prolonged remanence acquisition. If these paleointensities were produced by dynamo fields this correction would not be required, because the magnetic field is co-rotating with the planetesimal. Removing this correction decreases their paleointensities so they are within the range of field strengths predicted by my dynamo models (dashed lines on Figure 3.10). My upper limits on dynamo field strengths ($> 30\,\mu$T) are for the largest planetesimals with highest values of ^{60}Fe at early times ($< 3\,$Ma after CAI formation). Most parameter combinations predict weaker dynamo strengths $< 3\,$Ma after CAI formation (10–30 μT, Figure 3.2 and 3.6–3.9). A combination of approaches would be required to determine if measured paleointensities, even without the factor of two amplification, are too strong to be dynamo generated. The uncertainty on the paleointensity measurements could be reduced, and parent body size and ^{60}Fe/^{56}Fe could be independently constrained, e.g. by thermal models and isotopic measurements. Regardless of improved measurements, the difficulty in converting from field strengths acquired by thermal remanent magnetisation in the laboratory to those acquired by chemical remanent magnetisation on the parent body (factors of 2–5; Weiss and Tikoo, 2014; Maurel and Gattacceca, 2023) and uncertainties in the ratio of dipole field at the CMB to the internal dynamo field from dynamo scaling laws (0.06–0.1 for Earth; Davies et al., 2022) may mean that the uncertainties of measured and predicted paleointensities overlap. Overall, current recovered paleointensities and modelled field intensities cannot be used to distinguish between a dynamo or nebula field.

The possibility of the earlier onset of a thermal dynamo due to ^{60}Fe reduces the number of meteorite paleomagnetic studies that provide compelling evidence for the nebula field in the outer Solar System, because the bulk remanences in CM and CV chondrites may not record nebula fields. This should be considered when using this data to discuss differences in field strength and protoplanetary disk dispersal time between the inner and outer Solar System (Weiss et al., 2021; Borlina et al., 2022). Paleomagnetic measurements of individual, pristine chondrules are vital to understand the nebula field, because their non-unidirectionality can indicate conclusively if a remanence is preaccretionary (Fu et al., 2014b, 2020; Borlina et al., 2021).

3.4.1.3 Paleomagnetic records of planetesimal core crystallisation

My results argue that late remanences ($> 65\,\mathrm{Ma}$ after CAI formation based on the current meteorite record) do not require the presence of a solidifying core. The first epoch of dynamo generation can last until 20–200 Ma after CAI formation (depending on radius) rather than until 9–34 Ma after CAI formation suggested by previous models (Dodds et al., 2021). Additionally, my improved core solidification model reveals the second epoch of dynamo generation can begin prior to the onset of core solidification. As a result, the source of buoyancy to drive a dynamo cannot be assumed purely based on timing of a magnetic remanence. For extremes of some parameter values (low η_0 and $X_{\mathrm{S},0}$), onset of solidification is early and most of dynamo generation is powered by a combination of thermal and compositional buoyancy. Previous studies of the Main Group pallasites (Bryson et al., 2015; Nichols et al., 2021) and IIE irons (Maurel et al., 2020) have used the onset of a late-stage dynamo as an indicator for the start of core solidification. This assumption has been used to constrain planetesimal radius, core size, thermal history, and core composition. My model highlights that the beginning of a second epoch of dynamo is unlikely to be coincident with the beginning of core solidification for any initial core sulfur content, and therefore these studies should be re-evaluated (Chapter 5).

3.4.1.4 Paleomagnetic constraints on primordial $^{60}\mathrm{Fe}/^{56}\mathrm{Fe}$

The null paleointensities in the volcanic angrites and NWA 7325 at 3.8–5 Ma after CAI formation (Wang et al., 2017; Weiss et al., 2017) contradicts the early onset of a dynamo in bodies with $^{60}\mathrm{Fe}/^{56}\mathrm{Fe} \geq 10^{-8}$ predicted by this model. Magnetic remanences in the plutonic angrite, Angra dos Reis at 11 Ma after CAI formation (Wang et al., 2017), indicate the angrite parent body was differentiated and did generate a dynamo later in its history. Explanations, such as parent body size, gradual accretion, or $^{60}\mathrm{Fe}$ fractionation are unlikely to cause this delay in dynamo onset (see Appendix B.3). Another explanation could be $^{60}\mathrm{Fe}/^{56}\mathrm{Fe}$ was $\leq 10^{-9}$ in the formation region of the angrites such that the time taken to erode core thermal stratification led to a delay in dynamo generation (Bryson et al., 2019a; Dodds et al., 2021). Tang and Dauphas (2012) measured values of $^{60}\mathrm{Fe}/^{56}\mathrm{Fe} = 0.9 \pm 0.5 \times 10^{-8}$ in the angrites. Additionally, values of $^{60}\mathrm{Fe}/^{56}\mathrm{Fe}$ from silicates in non-carbonaceous (NC) chondrules are within error of zero ($0.8 \pm 1.0 \times 10^{-7}$; Kodolányi et al., 2022a). For a 300 km radius body accreted at 0.8 Ma after CAI formation, $^{60}\mathrm{Fe}/^{56}\mathrm{Fe} < 1.75 \times 10^{-9}$ results in a dynamo onset time consistent with the angrite data (see Figure 3.11). This limit lies within the lower bounds of these NC $^{60}\mathrm{Fe}/^{56}\mathrm{Fe}$ values. Current measurements from the CC IID and IVB irons ($6 \pm 2 \times 10^{-7}$; Cook et al., 2021) and CC chondrule silicates ($4 \pm 2 \times 10^{-7}$ Kodolányi et al., 2022a) have large uncertainties (see Appendix B.1), but neither are within error of $^{60}\mathrm{Fe}/^{56}\mathrm{Fe} < 10^{-8}$. This suggests there could be heterogeneity in $^{60}\mathrm{Fe}/^{56}\mathrm{Fe}$ between the CC and NC reservoirs (Cook et al., 2021; Kodolányi et al., 2022a). Measurement of a paleomagnetic remanence in a CC achondrite between the age of the volcanic and plutonic angrites could inform this discussion. If such a CC achondrite has a null paleomagnetic remanence, this could provide evidence for $^{60}\mathrm{Fe}/^{56}\mathrm{Fe} < 10^{-8}$ throughout the Solar System and constrain the timing of the dissipation of the nebula field in the outer Solar System. If this CC achondrite is found to have acquired a remanence at a similar time to null remanence acquisition in the volcanic angrites (i.e., when the nebula field has dissipated), this could provide evidence for early dynamo onset and heterogeneity in $^{60}\mathrm{Fe}/^{56}\mathrm{Fe}$ in the early Solar System.

3.4.2 Viscosity parameters in future planetesimal thermal evolution models

Mantle critical melt fraction, ϕ_{C}, is a crucial parameter in thermal evolution models. It determines planetesimal peak temperature and melt fraction (see Appendix B.2.2), and defines the threshold for magma ocean formation and convection in some models (e.g., Sturtz et al., 2022a; Neumann et al., 2023). A range of values of ϕ_{C}, including lower values in line with experimental data (Scott and Kohlstedt, 2006) should be used in future models. For models of specific parent bodies, this will affect the extent of the magma ocean and the inferred initial location of a meteorite (e.g. Erg Chech 002; Sturtz et al., 2022a). In two-phase flow models for planetesimal differentiation (e.g., Lichtenberg et al., 2019b; Monnereau et al., 2023), reducing ϕ_{C} and planetesimal peak temperature may alter the Fe-FeS compositions that can be molten, which will affect initial core composition. Additionally, reducing the melt threshold for magma ocean onset in differentiation models may decrease the time available for processes such as differentiation via percolation.

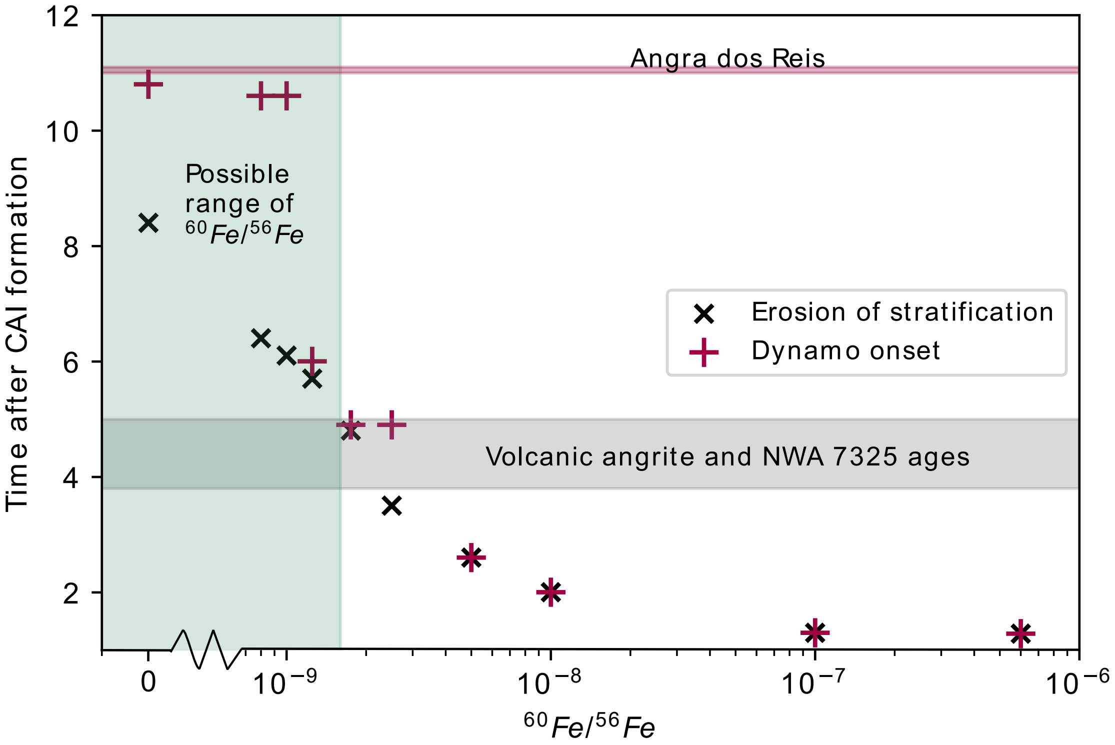

Figure 3.11: Primordial ^{60}Fe/^{56}Fe required to match the paleomagnetic record of the angrites and NWA 7325. The light green box indicates the range ^{60}Fe/^{56}Fe for which the angrite dynamo starts after the formation of the volcanic angrites and NWA 7325 (grey box), but before the formation of Angra dos Reis (pink box). For the 300 km radius body modelled here, $^{60}\mathrm{Fe}/^{56}\mathrm{Fe} < 1.75 \times 10^{-9}$ is required to explain these observations. This is a first estimate, which may change with accretion time, body size, and differentiation processes. For $^{60}\mathrm{Fe}/^{56}\mathrm{Fe} < 10^{-8}$, the time taken for erosion of stratification increases linearly because heating to remove the stratification is weaker. There is a lag between dynamo onset time and removal of stratification for $^{60}\mathrm{Fe}/^{56}\mathrm{Fe} < 1 \times 10^{-9}$, because the lack of heating increases the time taken to remove stratification as well as reducing F_{CMB}. Therefore, even once stratification is removed F_{CMB} may not be high enough to immediately start the dynamo.

The value of mantle reference viscosity, η_0, has a strong effect on planetesimal cooling rate. Future models should test multiple values in the extrapolated range of η_0 when attempting to constrain a parent body thermal history from meteorite isotope data (e.g., Bryson et al., 2019b; Neumann et al., 2023). Future models could attempt to constrain values for planetesimal η_0 (and other viscosity parameters) based on parent body composition, water content, and observed gaps in the paleomagnetic record.

3.4.3 Validity

This work only explored variations within one parameter at a time, while all other parameters were held at their median values (except ϕ_C where the constant value was the experimental upper bound). Using endmember values for multiple parameters simultaneously may result in an even wider range of dynamo generation times (explored in Chapter 5). Varying a single parameter enables the effect of each parameter to be understood and the dominant factors in dynamo generation timing to be isolated. As demonstrated in Figure 3.4, even across variations in parameters other than radius, there are large portions of time where the planetesimal dynamo is consistently active. Therefore, even if multiple parameters are varied, the trends in timing with radius predicted here are likely to hold true.

I used a critical magnetic Reynolds number (Re_m) of 10 to calculate the dynamo timings in this chapter. This is the lowest possible critical value from stability analysis, but numerical simulations for the geodynamo find an empirical critical Re_m of 40–100 (Christensen and Aubert, 2006; Stevenson, 2003). The empirical critical Re_m depends on the simulation set-up, such as boundary conditions and inner to outer core ratio, which will differ between planetesimals and the Earth. Figure 3.3 indicates the times for which the Re_m is greater than each of these critical values. Very few runs reach $Re_m > 40$ and only one run for the highest $^{60}Fe/^{56}Fe$ reaches $Re_m > 100$. Furthermore, none of the runs achieve $Re_m > 40$ at 100–200 Ma after CAI formation, where there is paleomagnetic evidence for dynamo generation. Since these higher critical values predict planetesimal dynamo histories that are inconsistent with the paleomagnetic record, I chose to apply $Re_m > 10$ as the criterion for planetesimal dynamo generation.

Also, I assumed that the core radius was half of the planetesimal radius. This is the upper bound of predicted core sizes for cores formed from chondritic starting material (30–50% Bercovici et al., 2022). However, this core fraction is smaller than that predicted for planetesimals that had their mantles stripped by impacts (e.g. the

IVA parent body, asteroid (16) Psyche; Yang et al., 2007; Elkins-Tanton et al., 2020). I chose a 50% core radius fraction as a median of these two scenarios. The effect of core radius on dynamo generation will be explored in Chapter 4.

3.5 Conclusions

Using the refined planetesimal thermal evolution model presented in Chapter 2, I explored the effects of ^{60}Fe, mantle viscosity, initial core sulfur content, and planetesimal radius on planetesimal dynamo generation. My results suggest there is a wider range in dynamo timings and durations than previously predicted. The meteorite paleomagnetic record therefore cannot be split into three distinct epochs of magnetic field generation (nebula field, thermal dynamos, and compositional dynamos) and the implications of some paleomagnetic remanences should be re-evaluated.

- Inclusion of ^{60}Fe/^{56}Fe $\geq 10^{-8}$ in the core can bring forward the onset of thermal dynamos to 1–2 Ma after CAI formation, extending the time at which the first planetesimal dynamos were possible. Therefore, some meteorite remanences recorded prior to 5 Ma after CAI formation could have a thermal dynamo origin rather than a nebula field origin. As a result, individual, pristine chondrules are crucial to understand the nebula field, because their non-unidirectionality can indicate conclusively that a remanence is preaccretionary.

- Null paleomagnetic remanences in the angrites contradict the early onset of thermal dynamos caused by ^{60}Fe. This could provide evidence for heterogeneous ^{60}Fe/^{56}Fe in the early Solar System. Paleomagnetic measurements of an old (<10 Ma after CAI formation) carbonaceous achondrite could help inform this.

- Increasing planetesimal radius (from 100 km to 500 km) greatly increases the start time of the gap in planetesimal dynamo generation (20 to 200 Ma after CAI formation) and final end of dynamo duration (40 to 640 Ma after CAI formation).

- The paleomagnetic record does not reflect early thermal dynamos and later compositional dynamos during core solidification, as previously interpreted. Variation in initial core sulfur content and mantle reference viscosity can produce early thermo-compositional dynamos. For most parameter combinations, there is a second thermal dynamo period prior to the onset of core solidification.

- Late magnetic remanences (>65 Ma post CAI formation based on the current record) do not require a solidifying core. As a result, the planetesimal radii, core sizes, thermal histories, and core compositions of the Main Group pallasites and IIE irons will be re-evaluated in Chapter 5.

- A range of planetesinal radii, mantle reference viscosities, and initial ^{60}Fe/^{56}Fe ratios should be explored when attempting to constrain parent body properties based on a meteorite paleomagnetic remanence.

This chapter has focused on interpreting the meteorite paleomagnetic record in terms of magnetic field generation mechanisms. In the next chapter, I will shift to interpreting the record in terms of planetesimal water content and oxidation state. I will suggest priorities for future measurements that will enlarge this paleomagnetic record and enable it to shed light on the differences between NC and CC differentiated planetesimals.

Chapter 4

Differences in thermal and magnetic histories between NC and CC differentiated planetesimals

4.1 Introduction

Planetesimals formed in two isotopically distinct reservoirs: non-carbonaceous (NC) in the inner Solar System and carbonaceous (CC) in the outer Solar System (Warren, 2011; Bermingham et al., 2020; Kruijer et al., 2020). Whether there were other, non-isotopic contrasts between differentiated planetesimals in these two reservoirs, for example in their internal structures, water contents, and formation times, is an area of active research (e.g., Newcombe et al., 2023; Grewal et al., 2024; Hellmann et al., 2024; Spitzer et al., 2025). Possible differences between NC and CC differentiated planetesimals are linked to local conditions in the protoplanetary disk during their formation (Grewal et al., 2024). Therefore, determining the differences between NC and CC differentiated planetesimals will improve our understanding of protoplanetary disk evolution and planetesimal formation.

While CC planetesimals likely formed in the water-rich region beyond the water condensation line (Drążkowska and Dullemond, 2018; Lichtenberg et al., 2021; Izidoro et al., 2022; Morbidelli et al., 2022), there are two hypotheses for the formation conditions of NC planetesimals. In the first hypothesis, NC and CC planetesimals formed contemporaneously at different condensation lines with different water contents and oxidation states (Izidoro et al., 2022; Morbidelli et al., 2022). NC planetesimals would have formed dry and reduced just outside the silicate sublimation line, while CC planetesimals would have formed wet and oxidised beyond the water condensation line. In the second hypothesis, NC and CC planetesimals formed sequentially just outside the water condensation line with the same oxidation state and water content (Drążkowska and Dullemond, 2018; Lichtenberg et al., 2021). In this scenario, NC planetesimals formed early (0.2–0.5 Ma after CAI formation), while the protoplanetary disk was dominated by viscous heating and the water condensation line was migrating outwards to 15 au (Lichtenberg et al., 2021). CC planetesimals formed later (0.7–4 Ma after CAI formation), once the disk became dominated by stellar irradiation and the water condensation line began migrating inwards to 3 au (Lichtenberg et al., 2021).

Previous studies have tested these two hypotheses using planetesimal accretion times (Spitzer et al., 2021; Hellmann et al., 2024; Spitzer et al., 2025), iron meteorite oxidation states (Rubin, 2018; Hilton et al., 2022; Grewal et al., 2024), and mantle water contents (Newcombe et al., 2023; Rider-Stokes et al., 2024). However, these studies reach conflicting conclusions (e.g., Rubin, 2018; Grewal et al., 2024) or are limited by instrument sensitivity (Newcombe et al., 2023). Meteorite paleomagnetism combined with dynamo generation modelling could provide a new method to explore the differences between the formation conditions of NC and CC planetesimals due to the precise criteria for dynamo generation. To generate a magnetic field, a planetesimal must have a molten, metallic core in which sufficiently vigorous flow is being driven. In planetesimals, this flow can be driven by thermal and/or compositional convection. Thermal convection is driven by density differences induced by rapid core cooling (superadiabatic core-mantle boundary heat fluxes). Compositional convection is driven by density differences due to core solidification. Possible differences in water content and oxidation state between NC and CC planetesimals could affect dynamo generation in three key ways. Firstly, bodies with higher water contents will be more oxidised and so will form smaller cores during differentiation (Spitzer et al., 2021; Grewal et al., 2024; Spitzer et al., 2025). Secondly, more water-rich bodies will have a lower mantle viscosity and mantle solidus (Hirth and Kohlstedt, 1996; Katz et al., 2003; Keller et al., 2017), which will affect the mantle, and hence core, cooling rate. Third, a higher fraction of water ice in the undifferentiated body could delay differentiation by lowering the overall abundance of radiogenic ^{26}Al within the body (Spitzer et al., 2021) because ^{26}Al is only present in the silicate phase. In this chapter, I will explore the effects of these differences on planetesimal thermal evolution and dynamo generation. This will determine the extent to which meteorite paleomagnetism and thermochronometers can shed light on differences in internal structure and water content between NC and CC, differentiated planetesimals.

In contrast to the dry planetesimal evolution considered in previous chapters, a water-rich planetesimal that fully differentiates will undergo the following additional stages in its thermal evolution (Fu and Elkins-Tanton, 2014; Castillo-Rogez and Young, 2017; Fu et al., 2017; Monteux et al., 2018; Lichtenberg et al., 2021; Trinh et al., 2023):

1. At ~273 K, ice melts and water-rock differentiation occurs. Water can react with the rock and form hydrated silicates.
2. Melted water escapes by porous flow or through fracturing of silicate by pressurised super-heated water vapour.
3. At ~1200 K, hydrated silicate phases break down and their water escapes. A small amount of water could be retained in nominally anhydrous minerals (NAMs).
4. At ~1260 K, Fe-FeS begins to melt. Fe-FeS could begin to percolate down towards the centre of the planetesimal to form a core.
5. At ~1200–1400 K, depending on silicate water content, silicates begin to melt and at the silicate critical melt fraction, core formation occurs via rain-out.

Depending on its accretion time and resulting concentration of radiogenic ^{26}Al, a planetesimal's thermal evolution may stall at one of these stages and the body may not fully differentiate. For example, chondrites only reached the first stage and retain hydrated minerals formed during aqueous alteration (Monteux et al., 2018). The deep interiors of icy bodies, such as Ceres (Castillo-Rogez and McCord, 2010) and Europa (Trinh et al., 2023) may have reached the third stage, while their surfaces remained cold enough to retain substantial amounts of ice. Thermal evolution models of chondrites and icy bodies (Castillo-Rogez and McCord, 2010; Monteux et al., 2018; Ma et al., 2022) include the thermal effects of ice melting and silicate (de)hydration, because these are the dominant processes within their evolution. In contrast, stages 1–3 represent a small fraction of the total thermal evolution of metal-silicate differentiated bodies. Therefore, modelling approaches for these bodies often neglect the thermal effects of water and assume no water is retained on the planetesimal after hydrated silicate phases break down (Lichtenberg et al., 2019a, 2021; Neumann et al., 2024). Spitzer et al. (2021) did include the effect of water on ^{26}Al abundances prior to planetesimal differentiation, but did not account for water loss during stages 1–3 as the planetesimal heated up. In this study, I begin planetesimal thermal evolution at the point of differentiation and do not explicitly model steps 1–3. Instead, I explore the thermal effects of water on the delay between accretion and differentiation by varying the differentiation time (see Sections 4.2.1,4.3.1.3). Unlike previous studies, I include the effect of water retained in NAMs on the thermal evolution (100-1000s ppm; Fu et al., 2017). The effect of water in NAMs has not been considered in thermal evolution models for planetesimals, but has been for planets (e.g. Mars; Sandu and Kiefer, 2012).

I use a thermal evolution and dynamo generation model adapted from Chapter 2 to explore possible differences in thermal evolution and dynamo generation between NC and CC differentiated planetesimals. In Section 4.2, I describe the modifications to the model presented in Chapter 2 for variable water content and justify the range input parameter values. In Section 4.3, I first explore the individual effects of core size, water content and differentiation time on dynamo generation. I then compare the thermal evolution and dynamo generation of two planetesimal endmembers: dry and reduced; and wet and oxidised. I compare these endmembers to the meteorite paleomagnetic record in Section 4.4 and discuss the implications for the formation history of NC planetesimals. I also suggest future paleomagnetic studies that will reveal differences between NC and CC planetesimals and their formation mechanisms. I conclude in Section 4.5.

4.2 Methods

I used a modified version of the model outlined in Chapter 2 to explore the differences in thermal and dynamo histories between two hypothetical planetesimal compositions: ‘wet’ and ‘dry’. Dry planetesimals accreted without water ice in a reduced environment, while wet planetesimals accreted with water ice in a more oxidised environment. These contrasting formation histories result in two key differences between planetesimals with these compositions: their core size, and mantle water content in NAMs. These are incorporated into the model by varying the fractional core radius, mantle solidus and liquidus, and mantle viscosity. I explored parameter space for 300 km radius planetesimals where fractional core radius, water content, and differentiation time were varied individually while other parameters were set to their dry values (Table 4.1). I also ran endmember models for ‘wet’ and ‘dry’ 100–500 km radius planetesimals, where mantle water content, fractional core radius, and the slope of the viscosity law were set to wet or dry values. (Table 4.2).

4.2.1 Accretion and differentiation

Unlike in Chapter 2, the model begins at the point of differentiation and neglects water-rock interactions prior to metal-silicate differentiation, such as water-rock differentiation and silicate (de)hydration (Fu and Elkins-Tanton, 2014; Castillo-Rogez and Young, 2017; Trinh et al., 2023). These processes will affect the time between accretion and differentiation, but the differentiation criteria (reaching the temperature of critical melt fraction) determines the conditions for the subsequent thermal evolution and dynamo generation, which are of primary interest here. Additionally, the time between accretion and differentiation is very short (0.5–4 Ma) in comparison to the time between differentiation and complete core solidification ($> 100\,\mathrm{Ma}$) due to the strength of radiogenic heating (Kruijer et al., 2020; Spitzer et al., 2021). This approach is similar to Neumann et al. (2024), who neglect the thermal effect of water prior to differentiation for planetesimals that form cores.

The mean $^{182}\mathrm{Hf}/^{182}\mathrm{W}$ differentiation age of the NC grouped irons ($2.2 \pm 0.5\,\mathrm{Ma}$ after CAI formation) is older than that of the CC grouped irons ($3.0 \pm 0.4\,\mathrm{Ma}$ after CAI formation; Hellmann et al., 2024). However, iron meteorites from both reservoirs span a range of differentiation ages from 0.5–4.5 Ma after CAI formation (Spitzer et al., 2021; Hellmann et al., 2024; Spitzer et al., 2025). Therefore, I explored this full range of differentiation times for both the wet and dry planetesimal endmembers. This range of differentiation times also serves as a proxy for the unknown time delay between accretion and differentiation.

4.2.2 Fractional core radius

Fractional core radius, $\frac{r_c}{r}$, decreases with increasing planetesimal oxidation state (Hilton et al., 2022; Grewal et al., 2024). In the parameter space exploration of $\frac{r_c}{r}$, I ran models for $\frac{r_c}{r}$=0.1–0.9 to investigate the widest possible range of fractional core radii. For the endmember models, I used estimates for planetesimal fractional core radii from measurements of highly siderophile element concentrations in iron meteorites (Hilton et al., 2022). The average core mass fraction and core sulfur contents for NC (more reduced) and CC (more oxidised) iron meteorites from Hilton et al. (2022) give fractional core radii of 0.4 and 0.5, respectively (Table C.1). These averages neglect iron meteorites that experienced significant volatile loss (IIIAB, IIIF, IVA, IVB; Goldstein et al., 2009). The NC fractional core radius will be used in the dry planetesimal endmember, while the CC value will be used for the wet endmember. I used the values from Hilton et al. (2022) rather than those from Grewal et al.

(2024) that do not find a difference between CC and NC irons to test the influence of core size on paleomagnetic and isotope thermochronometer observations.

4.2.3 Water content

Hydrated silicate minerals are unstable at the high temperatures (∼1600 K) reached by differentiated planetesimals (Lichtenberg et al., 2019a; Trinh et al., 2023) and liquid water will have rapidly escaped as the planetesimal heated up (Fu and Elkins-Tanton, 2014). Therefore, I assume the only water retained in the planetesimal is in small quantities in NAMs. The quantity of this water, X_w, can be estimated from measurements of water in NAMs in meteorites (Peterson et al., 2023; Newcombe et al., 2023; Rider-Stokes et al., 2024; Harries et al., 2023). Petrological evidence suggests that the meteorites in which NAMs have been measured crystallised from a melt (Newcombe et al., 2023). Therefore, these measurements can be combined with the degree of melting on the parent body and water solid-melt partition coefficients to find the original water concentration in NAMs on the parent body (Newcombe et al., 2023). Using this method, Rider-Stokes et al. (2024) find water concentrations of 519–1089 ppm wt based on olivine partitioning or 85–110 ppm wt based on clinopyroxene partitioning in the angrites. For five different meteorite parent bodies, Newcombe et al. (2023) find a range of parent body water contents from 2.5–700 ppm wt, although they note that these values are upper limits and the real values could be up to two orders of magnitude lower, because the measurements were at the detection limit. The assumed partition coefficients have a large impact on the results and it is unclear for planetesimal pressures which values are most appropriate and in which minerals water is most compatible (Newcombe et al., 2023; Rider-Stokes et al., 2024). I adopted the 0–700 pm wt (X_w =0–0.07 wt%) values from Newcombe et al. (2023), because these values account for water partitioning into multiple minerals unlike the values suggested by Rider-Stokes et al. (2024) who consider water partitioning entirely into olivine or entirely into clinopyroxene. To contrast the most extreme possibilities of water loss and retention, my endmember runs used the largest and smallest values in this range. The concentration of water in NAMs is assumed to be constant throughout a model run, because the timescale for volatile loss through the planetesimal surface after differentiation is long (10^5–10^{11} years, see Section 4.4.3.2). I explore whether paleomagnetism provides a complementary method for constraining parent body water contents in the inner and outer Solar System by using a range of planetesimal water contents.

4.2.3.1 Effect on mantle solidus and liquidus

To capture the effect of water on mantle melting, I replaced the constant, dry solidus and liquidus values in Chapter 2 with the parametrisation presented by Katz et al. (2003) for the hydrated mantle solidus, $T_{\mathrm{m,s}}$ and liquidus, $T_{\mathrm{m,l}}$ converted to K,

$$T_{\mathrm{m,s}} = A_1 + A_2 P + A_3 P^2 - \Delta T(X_{\mathrm{w}}), \tag{4.1}$$

and

$$T_{\mathrm{m,l}} = C_1 + C_2 P + C_3 P^2 - \Delta T(X_{\mathrm{w}}). \tag{4.2}$$

P is the pressure in GPa, $A_1 = 1358.7\,\mathrm{K}$, $A_2 = 132.9$ KGPa^{-1}, $A_3 = -5.1$ KGPa^{-2}, $C_1 = 2053\,\mathrm{K}$, $C_2 = 45$ KGPa^{-1}, $C_3 = -2.0$ KGPa^{-2}. $\Delta T(X_{\mathrm{w}})$ is the temperature reduction for a water fraction, X_{w}, in wt% in the melt,

$$\Delta T(X_{\mathrm{w}}) = K \left(\frac{X_{\mathrm{w}}}{D_{\mathrm{w,K}} + F(1 - D_{\mathrm{w,K}})} \right)^{\gamma}, \tag{4.3}$$

where $D_{\mathrm{w,K}} = 0.01$ is the bulk distribution coefficient of water between the solid and melt for this solidus parametrisation, F is the melt fraction, and $K = 43\,\mathrm{K\,wt\,\%}^{-\gamma}$, and $\gamma = 0.75$ are constants (Katz et al., 2003). I assume the melt remains homogeneously mixed with the solid (Section 2.5.2) so the degree of melting and melt fraction are equivalent ($F = 0$ at the solidus and $F = 1$ at the liquidus).

4.2.3.2 Effect on viscosity

The mantle viscosity is inversely proportional to the water content of the solid phase, C_H^{sol} (Hirth and Kohlstedt, 1996) and the constant prefactor in the viscosity law is an order of magnitude higher than for dry silicate (A_0; Keller et al., 2017). Therefore, in the wet planetesimals the first two pieces in the viscosity law (Equation 2.1a and 2.1b) are multiplied by a factor of $\frac{10}{C_H^{\mathrm{sol}}}$. For a partially molten system, the water content of the solid phase depends on the melt fraction, ϕ, and the partition coefficient of water between the solid and the melt, $D_{\mathrm{w}} = \frac{C_H^{\mathrm{sol}}}{C_H^{\mathrm{melt}}}$.

$$C_H^{\mathrm{sol}} = C_H^{\mathrm{tot}} \left(1 - \phi + \frac{\phi}{D_{\mathrm{w}}} \right)^{-1}. \tag{4.4}$$

$C_H^{\mathrm{tot}} = 2 \times 10^4 X_{\mathrm{w}} \frac{M_{\mathrm{min}}}{M_{H_2O}}$ is the total water content of the system in units of number of H atoms per million Si atoms, X_{w} is the water concentration in wt %, and M_{min} and M_{H_2O} are the molar mass of the chosen mineral and water, respectively. In this model, I use the molar mass for KLB-1 peridotite ($M_{\mathrm{min}} = 55.1$), which is a close natural

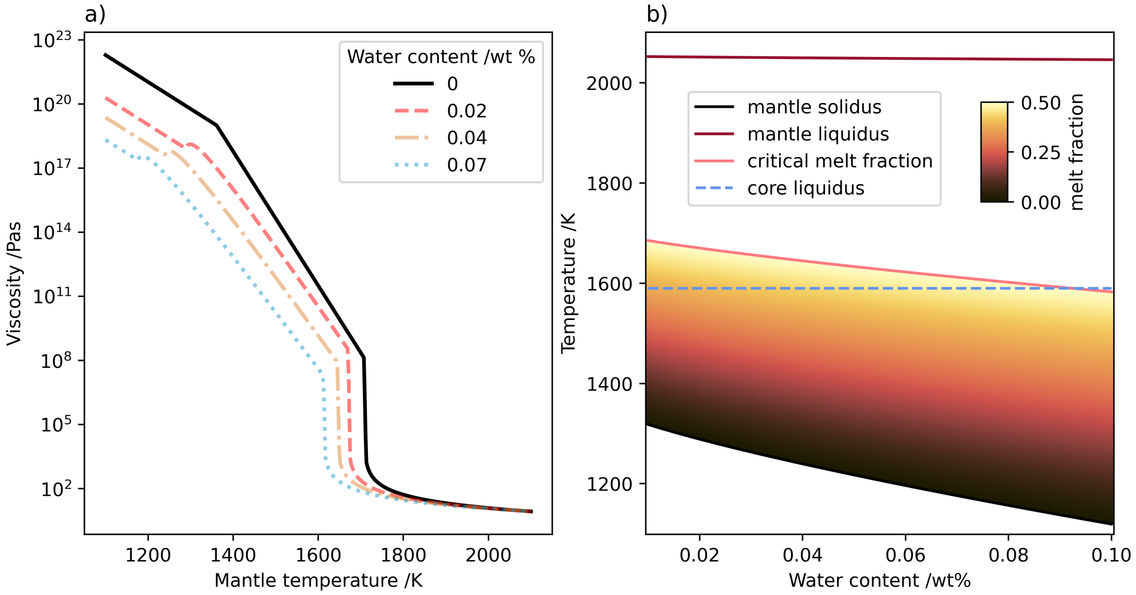

Figure 4.1: a) Viscosity profiles for a range of water contents assuming $\eta_{0,dry} = 10^{19}$ Pas, $D_\mathrm{w} = 6 \times 10^{-3}$ and a KLB1 peridotite composition. Below the solidus, wet materials have lower viscosities. At the solidus, wet materials have a slight increase in viscosity, because the water begins to move into the melt and the viscosity of the solid phase increases. The viscosity then decreases due to the increasing melt fraction with increasing temperature. b) Mantle solidus, $T_\mathrm{m,s}$, liquidus, $T_\mathrm{m,l}$, and temperature of the critical melt fraction, T_{ϕ_C}, as a function of water content based on the solidus and liquidus parametrisation from Katz et al. (2003). The critical melt fraction is assumed to be 0.5. The core liquidus, $T_\mathrm{c,l}$, is for a 300 km radius planetesimal with 23 wt% sulfur in its core.

analogue to upper mantle compositions (Davis et al., 2009) and matches the mantle composition in Katz et al. (2003). I adopt the partition coefficient for peridotite at 1 GPa, $D_{\mathrm{w}} = 0.006$ from Hirschmann et al. (2009). Although this partition coefficient is for pressures 2-3 times higher than in planetesimal mantles, the pressure dependence of the partition coefficient is weak (Hirschmann et al., 2009). Note, the value of this partition coefficient is different to the partition coefficient used to calculate the effect of water on the mantle solidus and liquidus ($D_{\mathrm{w,K}}$, Equation 4.3). For the mantle solidus, I use the same value $D_{\mathrm{w,K}} = 0.01$ as in Katz et al. (2003), because the constants in Equations 4.1–4.3 have been calibrated against experimental data using this value. Water reduces viscosity, so for any given temperature, the viscosity of a wet planetesimal will be less than or equal to that of a dry planetesimal. For my chosen constants, the $\frac{10}{C_H^{\mathrm{sol}}}$ modification to the viscosity law reduces viscosity for water contents ≥ 0.0136 wt% (Appendix C.1). Therefore, I will explore water contents from 0.02–0.07 wt% and water contents below this will be considered effectively dry.

The Arrhenius slope, $\beta = \frac{E}{RT_{\mathrm{m,s}}^2}$ is sensitive to changes in mantle solidus and activation energy, E, due to the addition of water. For pure olivine, the activation energy for dislocation creep rises from $440 \pm 10\,\mathrm{kJmol^{-1}}$ in anhydrous conditions to $506 \pm 16\,\mathrm{kJmol^{-1}}$ in hydrous conditions (Zhao et al., 2009, 2018). Therefore, I assume $\beta = 0.029\,\mathrm{K^{-1}}$ and $\beta = 0.044\,\mathrm{K^{-1}}$ for the wet and dry planetesimal endmembers, respectively. Although we assume the planetesimal has a peridotite composition, flow laws and activation energies for pure olivine are a good approximation to olivine-pyroxene aggregates (Bystricky et al., 2024). A parameter space exploration for β was carried out in Chapter 3 so is not repeated here. My chosen Arrhenius slope is slightly above the maximum value explored in Chapter 3, but given the value is the same order of magnitude, the effect on dynamo generation does not differ qualitatively from Chapter 3.

The other parameters in the viscosity law are minimally affected by water. There is no difference within experimental error in the melt weakening exponent between hydrous and anhydrous conditions (Mei et al., 2002), and liquid viscosity requires two orders of magnitude more water for an appreciable change in viscosity (Lesher and Spera, 2015). Therefore, I will use the constant values from Chapter 3 for both these parameters in both the wet and dry planetesimals.

4.2.4 Initial core sulfur content

I chose my initial core sulfur contents based on the range of values I can model (Chapter 2) and the sulfur contents of iron meteorites, which are fragments of planetesimal

Parameter	Symbol	Range	Notes
Fractional core radius	$\frac{r_c}{r}$	0.1–0.9	Section 4.2.2
Water content in NAMs	X_w	0,0.02–0.07 wt%	Newcombe et al. (2023) Section 4.2.3.2
Differentiation time	t_diff	0.5–4.5 Ma after CAI formation	Hellmann et al. (2024)
Initial core sulfur content	$X_{\mathrm{S},0}$	23–33 wt%	Section 4.2.4

Table 4.1: Range of values for parameter space exploration. Values without references were chosen in this study.

cores. CC iron meteorites have lower sulfur contents (2–13 wt%) than NC iron meteorites (15–19 wt%; Hilton et al., 2022; Zhang et al., 2022, 2024), but the exact sulfur content depends on assumptions about melt trapping during fractional crystallisation (Hirschmann et al., 2021). These estimates suggest that more oxidising conditions (CC reservoir) produce lower initial core sulfur contents. However, chemical models for core formation from chondritic material suggests that the sulfur content of the planetesimal prior to differentiation influences core sulfur content more than planetesimal's oxidation state (Bercovici et al., 2022). Furthermore, sulfur degassing during differentiation (Hirschmann et al., 2021) and immiscibility within planetesimal cores (Hilton et al., 2019; Bercovici et al., 2022; Bromiley et al., 2024) can alter core sulfur contents compared to the values expected from their bulk compositions. Due to the complexity of relating initial core sulfur content to oxidation state, I treat the initial core sulfur contents of the oxidised (wet) and reduced (dry) planetesimals as a free parameter. In my model, the minimum initial core sulfur content is the lowest sulfur content that can be molten at differentiation (Section 2.4.4.1). The differentiation temperature is set by the temperature of the critical melt fraction. For a planetesimal with a solidus (and hence critical melt fraction) lowered by the presence of 0.07 wt% water, the lowest possible initial core sulfur content is 23 wt%, which is larger than the estimated core composition from all iron meteorites. Therefore, I use this minimum value in both endmembers models to be as close to the meteorite values as possible. Additionally, I run a separate set of endmember models for 300 km radius planetesimal with a range of initial core sulfur contents from 23–33 wt% to determine whether coupling a change in core sulfur content to oxidation state and water content affects the dynamo. The effect of initial core sulfur content as a single parameter has already been explored in Chapter 3.

Parameter	Symbol	Dry	Wet	Reference
Water content in NAMs / wt%	X_{w}	0	0.07	Newcombe et al. (2023)
Mantle solidus / K	$T_{\mathrm{m,s}}$	1361	1176	Katz et al. (2003)
Mantle liquidus / K	$T_{\mathrm{m,l}}$	2053	2048	Katz et al. (2003)
Core radius fraction	$\frac{r_{\mathrm{c}}}{r}$	0.5	0.4	Hilton et al. (2022)
Arrhenius slope / K^{-1}	β	0.029	0.044	Zhao et al. (2009) Zhao et al. (2018)

Table 4.2: Parameter values for wet and dry planetesimal endmembers. Values that are the same between endmembers are given in Table 4.3. The mantle solidus and liquidus are calculated using X_{w} and Equations 4.1 and 4.2. Example values for a 300 km radius planetesimal are given here for illustration.

Parameter	Symbol	Value	Notes
Initial core sulfur content	$X_{\mathrm{S},0}$	23 wt%	Value in model range closest to meteorite values
Differentiation time	t_{diff}	2 Ma after CAI formation	Hellmann et al. (2024)
Critical melt fraction	ϕ_C	0.5	Maximal to allow widest range of $X_{\mathrm{S},0}$, Chapter 2

Table 4.3: Constant parameters between simulations. Any parameters not stated are the same as those in Table 2.1 and the constant values in Table 3.1 Values for parameters that also appear in Table 4.1 indicate the values used in the endmember runs.

4.3 Results

4.3.1 Parameter space exploration

4.3.1.1 Fractional core radius

Magnetic field strength at the surface depends on the inverse cube of the distance from the CMB. Therefore, a larger fractional core radius, $\frac{r_c}{r}$, strongly increases dynamo strength as measured at the surface (Figure 4.2), because the distance from the CMB to the surface is reduced. There is a non-monotonic trend in dynamo duration (Figure 4.2) due to the competing effects of increased core convective lengthscale and earlier cessation of mantle convection with increasing $\frac{r_c}{r}$. At low values of $\frac{r_c}{r}$ (≤ 0.6 for 100 km radius, ≤ 0.3 for 300 km radius, ≤ 0.2 for 500 km radius), the small core size limits dynamo duration. Smaller cores have smaller convective lengthscales ($\approx r_c$, Section 2.6.1), which decreases the magnetic Reynolds number for a given heat flux (Figure 4.3). This reduces the time for which the magnetic Reynolds number is supercritical and a dynamo can be generated. As a result, planetesimals with the smallest values of $\frac{r_c}{r}$ do not generate a dynamo. The absolute size of the core also contributes to this effect — for smaller planetesimals the minimum $\frac{r_c}{r}$ for a dynamo is larger (≥ 0.5 for 100 km radius, Figure 4.2). For intermediate values of $\frac{r_c}{r}$ (≈ 0.4 for 300 km radius, 0.3–0.4 for 500 km radius) there is a gap in dynamo generation around the cessation of mantle convection, when the CMB heat flux is reduced. For high values of $\frac{r_c}{r}$ (≥ 0.5 for 300-500 km radius, ≥ 0.7 for 100 km radius), dynamo duration is limited by the mantle thickness rather than core convective lengthscale. Convection ceases earlier in thinner mantles, because less cooling is required before the convective boundary layer thickness is equal to the mantle thickness (Figure 4.3). Once mantle convection ceases, the shorter distance for conduction between the CMB and the surface in thinner mantles increases the rate of core cooling. This results in the core reaching the eutectic composition earlier, shutting off compositional convection and the dynamo (Figure 4.3).

4.3.1.2 Water content

Increasing water content delays the cessation of convection, brings forward the onset of core solidification and decreases dynamo duration (Figure 4.4). Magnetic field strength is very similar for all water contents. Mantle convection ceases later for higher water contents because the mantle viscosity is lower at any given temperature, so the stagnant lid thickens more slowly (Figure 4.5). Core solidification begins earlier

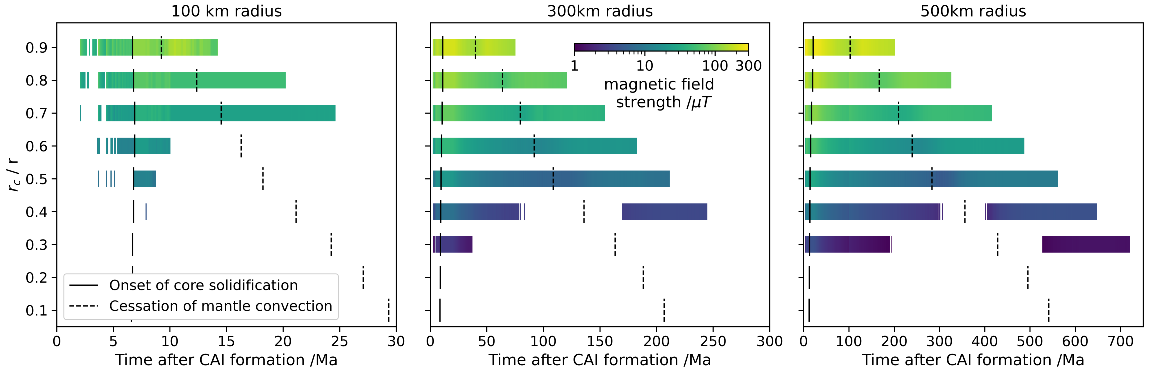

Figure 4.2: Dynamo strength and duration as a function of fractional core radius, $\frac{r_c}{r}$, for 100 km, 300 km and 500 km radius planetesimals. All other parameters match the ‘dry’ column in Table 4.2. Filled bars indicate periods when a dynamo is active and the colour of the bar indicates dipole magnetic field strength at the surface. The black, vertical lines indicate the onset of core solidification (solid) and the cessation of mantle convection (dashed).

for increased water contents because the planetesimal differentiation temperature (the temperature of the critical melt fraction) is closer to the core liquidus (Figure 4.1b). The mantle, and hence the core, cools more rapidly because the mantle effective specific heat capacity (Equation 2.15) is lowered by the addition of water. Faster core cooling truncates the dynamo because it increases the rate of core solidification and brings forward the time when the core reaches the eutectic composition and compositional convection ends.

4.3.1.3 Differentiation time

Differentiation time has minimal effect on dynamo generation (Figure 4.6). Post-differentiation thermal evolution depends on the peak temperature of the mantle and mantle cooling rate. The temperature of differentiation is determined by the temperature of the critical melt fraction and so is independent of differentiation time. Differentiation time alters the abundance of radiogenic ^{26}Al remaining after differentiation and its possible heating effect. However, due to the short half-life of ^{26}Al, radiogenic heating cannot delay mantle cooling beyond ~5 Ma after CAI formation (Figure 2.7, Chapter 2). Overall, planetesimal dynamo generation cannot be used to infer differences in differentiation time (and by extension accretion time) resulting from differing water contents and oxidation states.

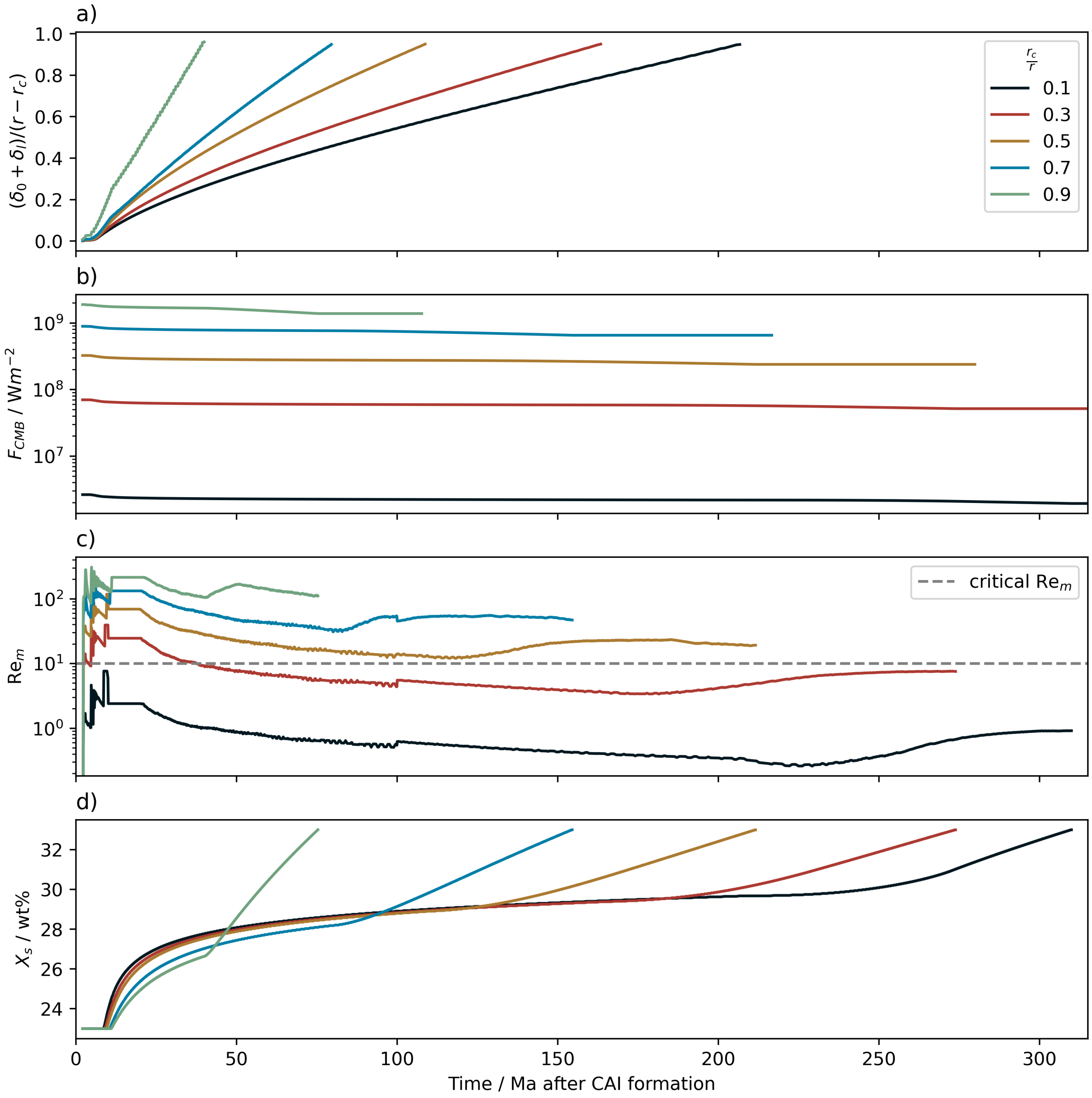

Figure 4.3: a) Total convective boundary layer thickness as a fraction of mantle thickness, $(\delta_0+\delta_l)/(r-r_c)$, b) CMB heat flux, F_{CMB}, c) magnetic Reynolds number, Re_m, and d) core sulfur content, X_{S}, as a function of time for a 300 km radius planetesimal with a range of fractional core radii, $\frac{r_c}{r}$. Time evolution of each parameter in each panel is truncated a) when mantle convection ceases, b) when the core completely solidifies, c) and d) when the core reaches the eutectic composition. The time the final core reaches the eutectic composition sets the upper limit on the horizontal axis range.

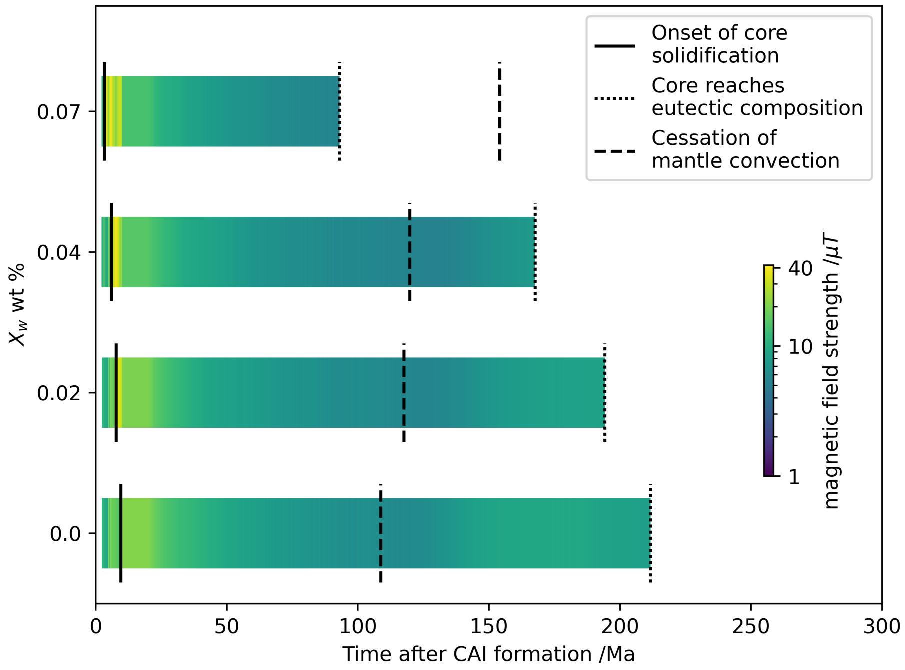

Figure 4.4: Dynamo strength and duration as a function of water content in nominally anhydrous minerals, X_{w}, for a 300 km radius planetesimal. All other parameters match the 'dry' column in Table 4.2. The black, vertical lines indicate the onset of core solidification (solid), when the core reaches the eutectic composition (dotted) and the cessation of mantle convection (dashed).

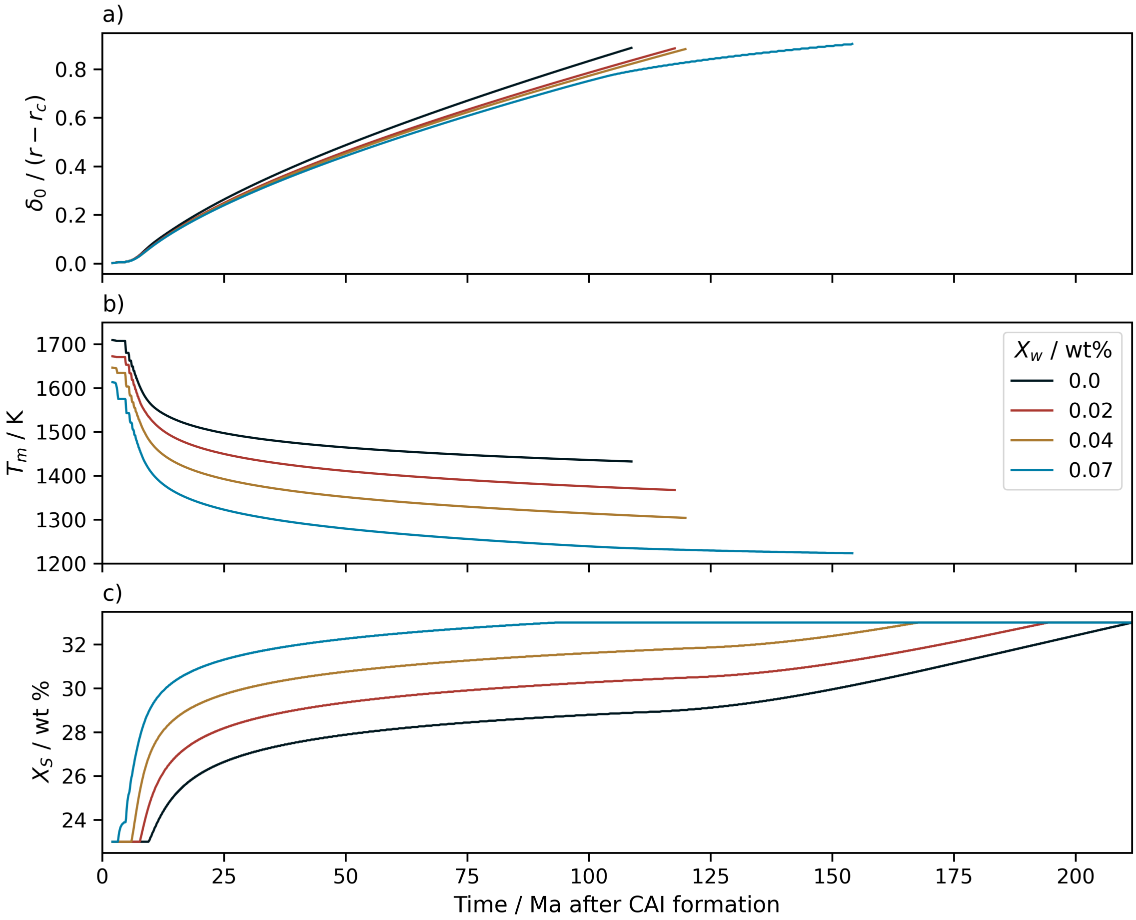

Figure 4.5: a) Stagnant lid thickness as a fraction of mantle thickness, $\delta_0/(r - r_\mathrm{c})$, b) convective mantle temperature, T_m, and c) core sulfur content, X_S, as a function of time for a 300 km radius planetesimal with a range of water contents in nominally anhydrous minerals, X_w. Stagnant lid thickness and mantle convective temperature are plotted until the cessation of convection.

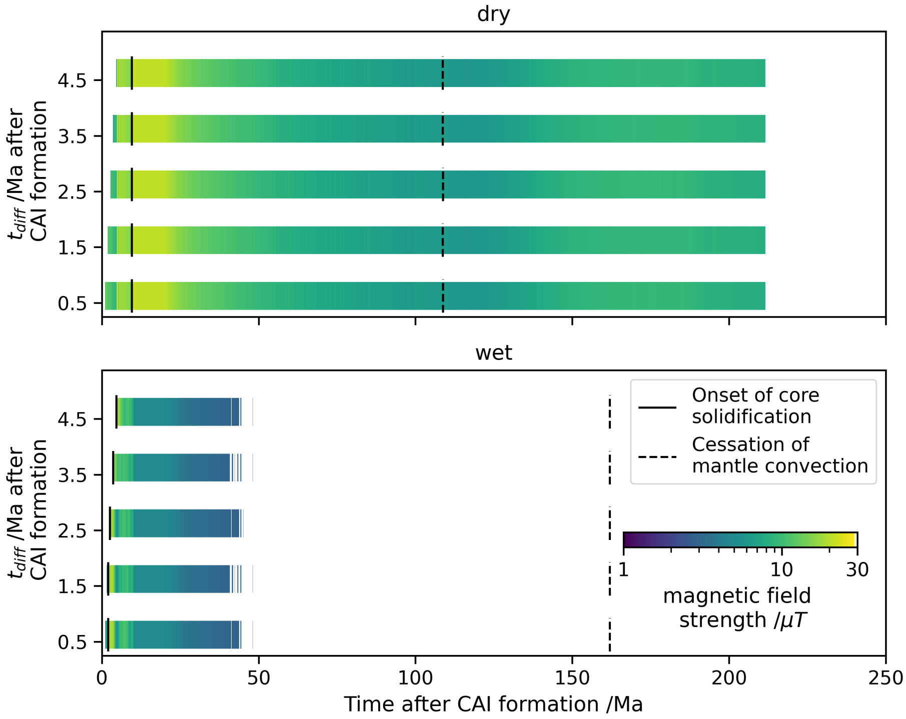

Figure 4.6: Dynamo strength and duration for 300 km radius dry (upper panel) and wet (lower panel) planetesimals for a range of differentiation times. The black, vertical lines indicate the onset of core solidification (solid) and the cessation of mantle convection (dashed).

4.3.2 Wet vs dry planetesimals

Wet and dry planetesimals have contrasting paleomagnetic histories. Wet planetesimals have shorter and weaker fields than dry ones (Figure 4.7). No wet planetesimal generates a field more than ~200 Ma after CAI formation and none generate a field intensity $> 5\,\mu$T beyond 50 Ma after CAI formation. In contrast, when dry planetesimals dynamos are active the magnetic field strength is always $> 5\,\mu$T. The weaker field strengths in wet planetesimals are due to the smaller $\frac{r_c}{r}$, resulting in a larger distance from the core to the surface. Together, the smaller $\frac{r_c}{r}$ and increased water content shorten the dynamo by increasing the flux required for a supercritical magnetic Reynolds number and bringing forward when the core reaches the eutectic composition, respectively.

Varying initial core sulfur content, $X_{\mathrm{S},0}$, does not remove the contrast between wet and dry planetesimals (Figure 4.8). Increasing $X_{\mathrm{S},0}$ from 23–31 wt%, slightly increases dynamo duration in wet planetesimals (Figure 4.8) because the size of the liquid inner core decreases more slowly as the core cools (Equation 2.27), which results in a more gradual reduction in the magnetic Reynolds number. When starting at the eutectic composition (33 wt%), the lack of compositional convection shortens the duration of the dynamo. Increasing $X_{\mathrm{S},0}$ in dry planetesimals can lead to a gap in dynamo generation when mantle convection ceases because core solidification has not yet begun and there is no compositional buoyancy to drive the dynamo. However, regardless of $X_{\mathrm{S},0}$, all wet, 500 km radius planetesimal dynamos are weaker than $5\,\mu$T beyond ~ 65 Ma after CAI formation. In contrast, all active dry planetesimals dynamos are stronger than $5\,\mu$T beyond these times, irrespective of $X_{\mathrm{S},0}$.

Planetesimal size has a stronger effect on the time at which a thermochronometer cools through its closure temperature than whether the planetesimal is wet or dry (Figure 4.9) because the temperature ranges recorded by thermochronometers are only reached in the conductive portion of the planetesimal (Figure 4.10; 350–1200 K; Henke et al., 2012; Bryson et al., 2019b). The timescale for conductive cooling is proportional to the square of the length over which heat is conducted and inversely proportional to the thermal diffusivity. My model assumes the same thermal diffusivity for wet and dry planetesimals. Therefore, mantle thickness, which depends on planetesimal size, controls the cooling timescale and the age recorded by thermochronometers. As a result, thermochronometers cannot be used to distinguish wet and dry planetesimal histories.

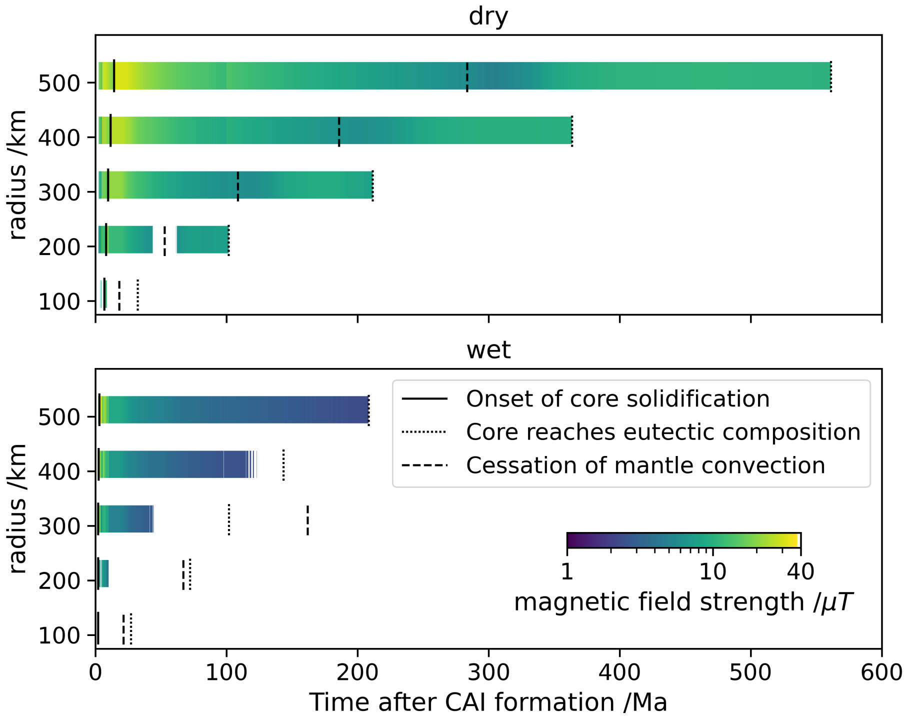

Figure 4.7: Dynamo strength and duration for wet and dry planetesimals with radii from 100–500 km. Parameters which differ between the two panels are given in Table 4.2. In both panels, planetesimals differentiate at 2 Ma after CAI formation, have a critical melt fraction of 0.5 and an initial core sulfur content of 23 wt%. The black, vertical lines indicate the onset of core solidification (solid), when the core reaches the eutectic composition (dotted), and the cessation of mantle convection (dashed).

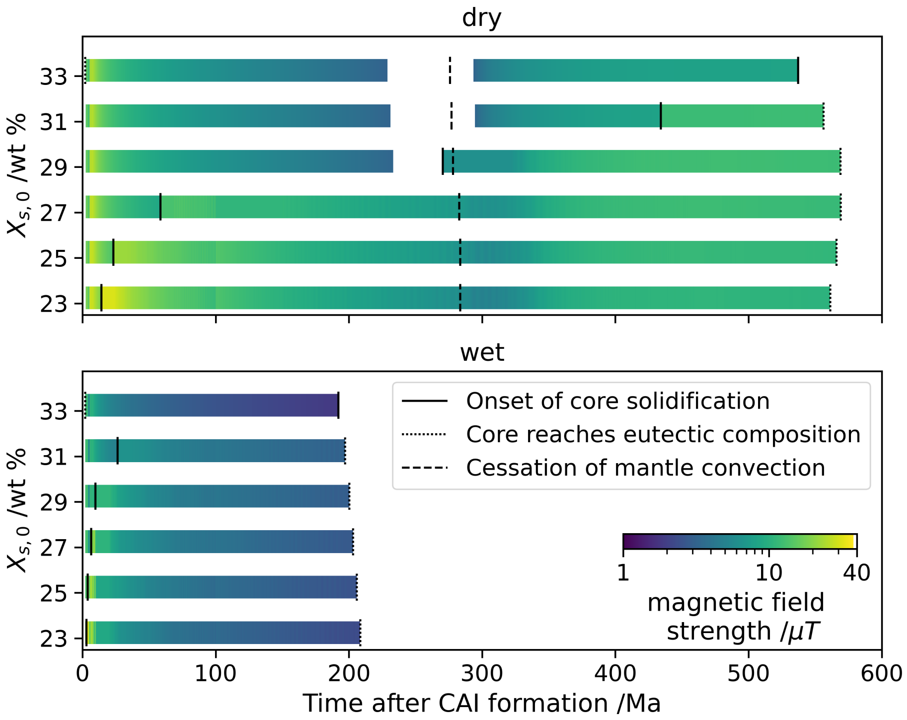

Figure 4.8: Dynamo strength and duration for 300 km radius dry (upper panel) and wet (lower panel) planetesimals as a function of initial core sulfur content, $X_{\mathrm{S},0}$. Parameters which differ between the the upper and lower panels are given in Table 4.2. The minimum initial core sulfur content on the vertical axis is set by the peak temperature at differentiation. The black vertical lines indicate the onset of core solidification (solid), when the core reaches the eutectic composition (dotted), and the cessation of mantle convection (dashed).

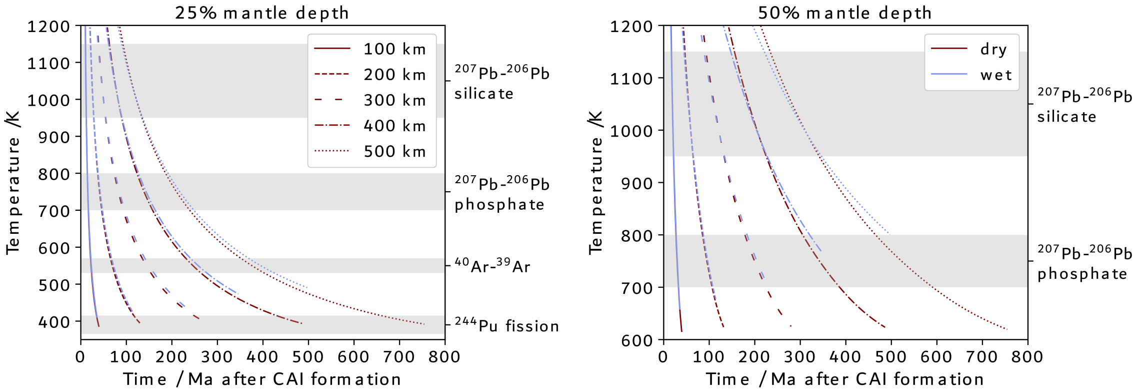

Figure 4.9: Mantle temperature at 25% (left) and 50% (right) mantle depth as a function of time for the planetesimals in Figure 4.7. Grey shaded boxes indicate the closure temperature range of example thermochronometers that have previously been used to trace planetesimal thermal histories (Bryson et al., 2019b). The right panel has a smaller temperature range, because the deeper mantle cools less before the core solidifies.

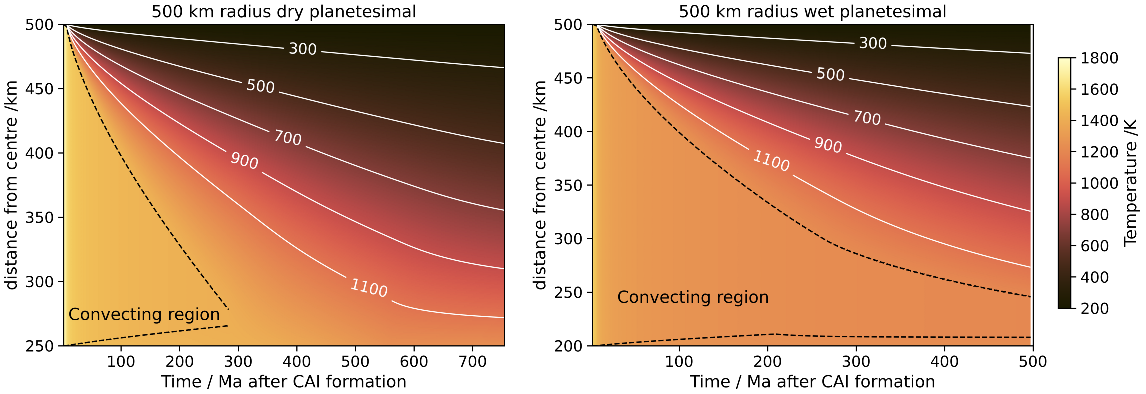

Figure 4.10: Interior temperature profiles for 500 km radius dry (left panel) and wet (right panel) planetesimal. The region enclosed by the black dashed lines is convecting. The temperature contours span the range of thermochronometer closure temperatures in Figure 4.9 and are all located in the conductive portion of the planetesimal. The horizontal axis limit is set by the solidification of the planetesimal core. The right panel has a larger vertical axis range because the wet planetesimal has a smaller core. This panel also has a smaller horizontal axis range because the mantle cools more rapidly, so the core solidifies earlier.

4.4 Discussion

Wet and dry planetesimals have distinct magnetic histories. Wet planetesimals generate weak magnetic fields for a short period of time due to their smaller core radius fractions and less viscous, more rapidly cooling mantles. In contrast, dry planetesimals generate strong magnetic fields for long periods due to their large core radius fractions and more viscous, slower cooling mantles. Isotopic thermochronometers are not sensitive to the differences between wet and dry planetesimals but are key indicators of planetesimal size.

4.4.1 Implications for differentiated NC planetesimals

Wet planetesimals do not produce dynamos with surface magnetic field strengths $> 5\,\mu$T beyond ~50 Ma after CAI formation, irrespective of size (Figure 4.7) and initial core sulfur content (Figure 4.8). Therefore, paleointensity data from after 50 Ma after CAI formation is the best test for the water content and oxidation state of planetesimals. Only paleointensity data from NC meteorites is available in this time range (Figure 4.11). The H and L/LL chondrites are thought to originate from outer, chondritic layers of partially differentiated planetesimals (Bryson et al., 2019b; Shah et al., 2017), while the IIE irons and Main Group pallasites are both stony irons and formed at some depth within the mantle of their parent bodies (Maurel et al., 2021; Nichols et al., 2021). Dry planetesimals of all sizes (Figure 4.11) produce surface magnetic fields that match the paleointensities recorded by the H and L/LL chondrites. In contrast, no wet planetesimals produce surface magnetic fields that match the L/LL chondrite paleointensity and only overlap with the lower bound on the H chondrite paleointensity. For dry planetesimals, formation at a 50% depth or shallower on 300–500 km radius planetesimals can explain the IIE iron and Main Group pallasite paleointensities. For wet planetesimals, no mantle depths $\leq$ 50% or planetesimal radii $\leq$ 500 km can reproduce the strongest Main Group pallasite paleointensity and only 500 km radius planetesimals can generate fields that span the same time period as the paleomagnetic data.

Overall, a very limited parameter space for wet planetesimals can only explain a fraction of the paleointensity data for NC meteorites, while a wide range of dry planetesimal parameters can explain all the paleointensity data for NC meteorites. This suggests the dry planetesimal endmember is a closer representation of NC, differentiated planetesimals. The core size of the dry endmember ($\frac{r_c}{r}$ =0.5) is consistent with estimates of core sizes and oxidation states for NC iron parent bodies (Table C.1; Hilton et al., 2022; Grewal et al., 2024)). The water content of the dry endmember indicates NC planetesimals either formed without water or their water was lost very efficiently during differentiation. NC iron meteorites are more oxidised than nebula gas suggesting water was present in the NC reservoir during their formation (Grewal et al., 2024), supporting subsequent efficient water loss. The hypothesis of efficient degassing aligns with previous studies (Newcombe et al., 2023; Grewal and Manilal, 2025). The low water contents required by the paleomagnetic data are incompatible with the uppermost limits on NC achondrite water contents (Rider-Stokes et al., 2024; Newcombe et al., 2023). This strengthens the argument that the partition coefficients used to calculate parent body water contents might not apply in planetesimal conditions or that the true NC achondrite water contents are below SIMS detection limits (Newcombe et al., 2023). However, if the NC differentiated planetesimals accreted with similar compositions to surviving NC chondrites, they may have accreted very little water ($<$ 3 wt%) due to their low proportion of matrix ($\approx$ 15 vol.% Alexander, 2019b). In contrast, CC chondrites had higher matrix fraction (30–100 vol.%) and could have contained more water ($\approx$3–30 wt% Alexander, 2019a).

4.4.2 Key future paleomagnetic measurements

Wet and dry planetesimals have stark differences in vigour and duration of dynamo generation, whereas isotope thermochronometers are dominated by differences in parent body size. Therefore, meteorite paleomagnetic measurements could be key to shed light on differences in water content and oxidation state between the NC and CC reservoirs. Below, I discuss the key paleomagnetic measurements that should be made to best utilise these possible differences in dynamo histories.

4.4.2.1 Carbonaceous achondrites

Carbonaceous planetesimals formed beyond the water condensation line, so originate from a more oxidising environment and should have accreted some water (Alexander, 2019a; Spitzer et al., 2021). Therefore, comparison between CC achondrite paleomagnetic measurements and the wet planetesimal models can reveal the extent of water loss on differentiated planetesimals and variations in their oxidation state. There is currently no paleointensity data for CC achondrites for discriminating between wet and dry planetesimals (Chapter 3). However, recently discovered ungrouped CC achondrites (Bogdanovski and Lugmair, 2004; Sanborn et al., 2019; Hyde et al., 2022; Rider-Stokes et al., 2025) are promising targets for these measurements. If paleomagnetic measurements of a magnetite-bearing, CC achondrite in the key time range ($> 50\,\mathrm{Ma}$ after CAI formation) find a paleointensity $> 5\,\mu\mathrm{T}$, this would indicate the dry planetesimal endmember is also a good match for CC differentiated bodies. This would imply CC planetesimals also degassed efficiently during differentiation and their oxidation states were similar to NC planetesimals. If a paleointensity $< 5\,\mu\mathrm{T}$ is measured and the parent body was large enough to generate a dynamo ($>200\,\mathrm{km}$), this would indicate the wet planetesimal endmember is a good match for CC differentiated planetesimals. This would imply that planetesimals can retain some water during differentiation and CC planetesimals formed smaller cores than NC planetesimals. This would support the idea that there was more water in the CC reservoir than in the NC reservoir. Overall, paleomagnetic measurements of a magnetite-bearing CC achondrite from $> 50\,\mathrm{Ma}$ after CAI formation could provide a key piece of evidence for understanding the volatile content and oxidation state of the NC and CC reservoirs.

4.4.2.2 Paleointensity estimates

Meteorite paleointensity depends on proximity to the core, which is a function of planetesimal radius, planetesimal core radius fraction and a meteorite's depth within the mantle. Different size planetesimals have similar magnitude field strengths for the same core radius fraction (Figure 4.2). Therefore, if uncertainties on paleointensity measurements could be reduced and meteorite depths within the mantle could be constrained (see Chapter 5), paleointensity could be a signature of planetesimal core fraction and hence oxidation state. In particular, an improved understanding of how cloudy zones (the paleomagnetic recorders in the pallasites and IIE irons) acquire their remanent magnetisations is key (Einsle et al., 2018; Maurel et al., 2019; Devienne et al., 2024). Further magneto-hydrodynamic simulations with parameters appropriate for planetesimal core soldification are also required to reduce uncertainties on the paleointensities predicted by numerical models. These refinements to paleointensity measurements could help us understand differences in oxidation state between the NC and CC reservoirs and the difference in oxidation state between the NC reservoir and nebula gas (Rider-Stokes et al., 2024; Grewal et al., 2024). This could reveal the trigger for planetesimal formation in the two reservoirs and determine the quantity of water-rich material which must have been present in the inner Solar System during formation of the NC iron parent bodies.

4.4.3 Model assumptions

4.4.3.1 Initial core sulfur content

Initial core sulfur content, $X_{\mathrm{S},0}$, does not drive the main differences in dynamo generation between wet and dry planetesimals. Therefore, the unknown $X_{\mathrm{S},0}$ value of wet and dry planetesimals (Section 4.2.4) does not preclude predictions of the dynamo histories of these bodies. For dry planetesimals with $X_{\mathrm{S},0} \geq 29\,\mathrm{wt\%}$, a gap in dynamo generation (Figure 4.8) could lead to degeneracy in null measurements in this time period between wet and dry planetesimals. Multiple magnetic measurements from a single meteorite group where non-zero paleointensities follow null paleointensities, like those for the Main Group pallasites (Nichols et al., 2021), could resolve this degeneracy. Regardless, iron meteorite compositions suggest these high $X_{\mathrm{S},0}$ values are unlikely to occur in meteorite parent bodies (Section 4.2.4). Instead $X_{\mathrm{S},0}$ is likely to be at the bottom of or below the range explored here, although how lower sulfur content cores differentiate is uncertain (Section 2.4.4.1). These low sulfur contents

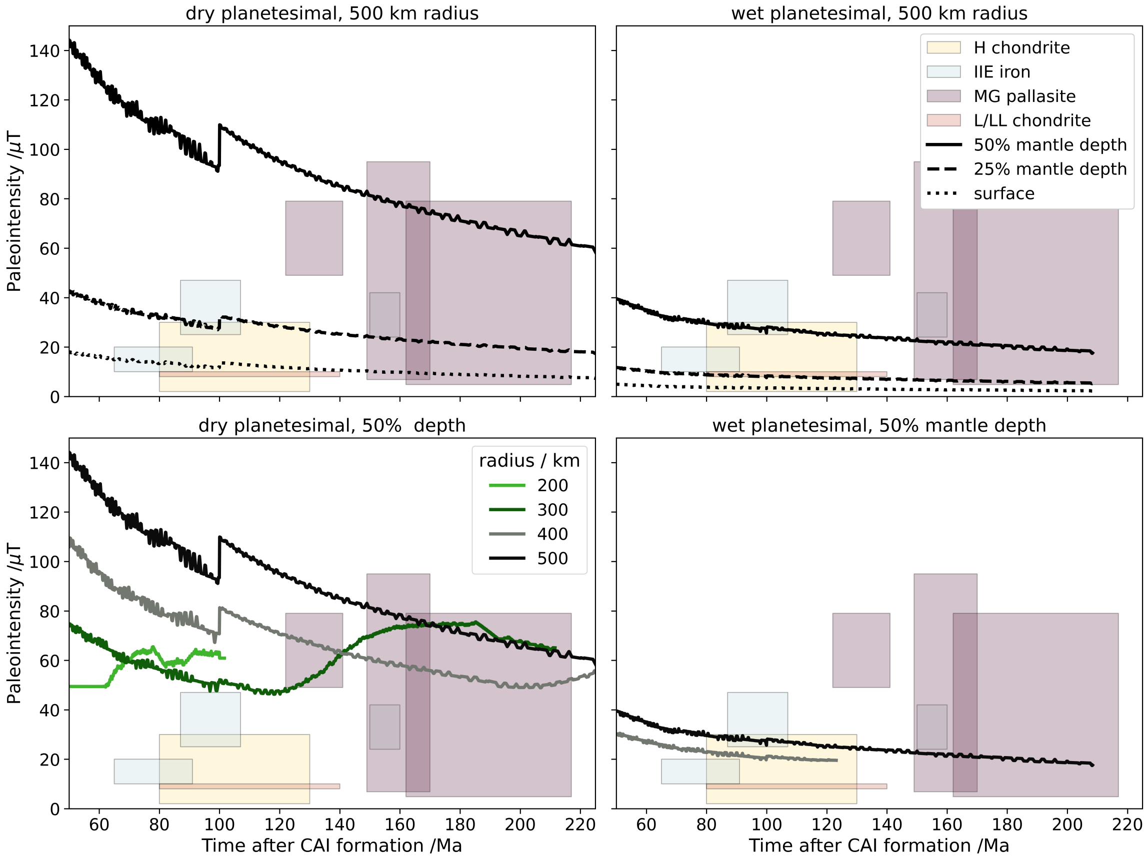

Figure 4.11: Paleointensity data (coloured boxes) from 50–220 Ma after CAI formation (Shah et al., 2017; Bryson et al., 2019b; Nichols et al., 2021; Maurel et al., 2021) overlaid by magnetic field strengths for a range of wet and dry planetesimal sizes and depths (lines). In the upper panels, the data is overlaid by magnetic field strengths for 500 km radius dry (left) and wet (right) planetesimals. For each planetesimal type, three traces are given corresponding to three possible formation depths of each meteorite within the planetesimal mantle. In the lower panels, the data is overlaid by magnetic field strengths at 50% mantle depth for 100–500 km radius dry (left) and wet (right) planetesimals. Radii not shown in the lower panels do not generate a magnetic field in this time interval. Each coloured box represents an individual meteorite and the size of the box indicates the uncertainty on the paleointensity and timing. Darker regions are where multiple measurements overlap. Only the non-null paleointensity data from this time period is plotted. The uncertainty on the final two MG pallasite data points (Imilac and Esquel) is large, because for these meteorites the angle between the primordial field and remanent field is unknown (Nichols et al., 2021). Additional uncertainties on MG pallasite, H chondrite and IIE iron data due to magnetostatic interactions and induced fields are difficult to quantify (see Maurel et al., 2021, for discussion) and have not been included. The uncertainties on these measurements will be discussed further in Chapter 5.

would not have a gap in dynamo generation preventing this possible degeneracy in null measurements.

4.4.3.2 Progressive dehydration of nominally anhydrous minerals

I assume the water content in the planetesimal mantle remains constant during the thermal evolution and that negligible water degasses to the surface. The validity of this assumption depends on the timescale for water loss from the surface in comparison to the time over which water will be transported within the planetesimal interior (i.e. the duration of mantle convection). For bodies convecting in the stagnant-lid regime, water enriched melt will rapidly be brought to the base of the stagnant lid ($\mathcal{O}(10\,\text{years})$; Miyazaki and Korenaga, 2022). However, for water to escape from the planetesimal, this melt must be able to reach the surface. The concentrations of water in NAMs are too low for volatile exsolution to drive eruption; instead melt transport is driven by buoyancy of melt relative to the crust (Fu and Elkins-Tanton, 2014). Melt density increases with oxidation state and melts with CM- and CV-like compositions are more dense than their overlying crusts (Fu and Elkins-Tanton, 2014). This inhibits melt migration through the crust and degassing from the surface. Therefore, melts on our wet planetesimals are likely to be too dense to reach the surface.

In the scenario where the melt is buoyant (e.g. H- and LL-like compositions), the time taken to remove all volatiles from the mantle can be estimated by

$$\tau_{\text{dry}} = \frac{X_{\text{w}} M_{\text{mantle}}}{\dot{w}}, \tag{4.5}$$

where $\dot{w}$ is the rate of water loss from the surface, X_{w} is the water concentration in the mantle in ppm wt and M_{mantle} is the mantle mass. The rate of water loss depends on the proportion of the planetesimal's surface through which melt can escape, X_{SA}, the percolation velocity through the crust, u_{perc}, the melt density, ρ_{melt}, and the water content of the melt, $X_{\text{w,melt}}$,

$$\dot{w} = 4\pi r^2 X_{\text{SA}} u_{\text{perc}} \rho_{\text{melt}} X_{\text{w,melt}}. \tag{4.6}$$

The percolation velocity can be calculated from Darcy's law

$$u_{\text{perc}} = \frac{K(\phi)\Delta\rho g}{\eta_{\text{melt}}}, \tag{4.7}$$

where $K(\phi)$ is the permeability, $\Delta\rho = \rho_{\text{crust}} - \rho_{\text{melt}}$, g is the gravitational field strength at the surface, and η_{melt} is the melt viscosity. The water content of the melt can be

Parameter	Estimate	Notes
$K(\phi)$	10^{-11}m^2	Chapter 2
g	0.5ms^{-2}	Chapter 2
η_{melt}	100 Pas	Chapter 3
$\Delta\rho$	500 kgm^{-3}	Fu and Elkins-Tanton (2014)
ϕ	0.5	maximum melt fraction
X_{SA}	0.1	assumption
$\frac{r_{\mathrm{c}}}{r}$	0.5	Chapter 2
r	200 km	assumption

Table 4.4: Parameter values used to estimate timescale for volatile loss from planetesimals.

related to that of the mantle using the partition coefficient D_{w}. For a small partition coefficient ($D_{\mathrm{w}} = 10^{-3}$)

$$X_{\mathrm{w}} = \phi X_{\mathrm{w,melt}}, \tag{4.8}$$

where ϕ is the melt fraction. Combining Equations 4.5–4.8, and assuming the melt and the mantle have the same density, Equation 4.5 simplifies to

$$\tau_{\mathrm{dry}} = \frac{1}{3}\frac{r\phi}{X_{\mathrm{SA}} u_{\mathrm{perc}}}\left[1 - \left(\frac{r_{\mathrm{c}}}{r}\right)^3\right]. \tag{4.9}$$

For the values assumed in Table 4.4, water will be completely lost after 4×10^8 years, which is longer than the duration of convection in any of our model runs. However, this timescale estimate depends strongly on our assumed permeability and surface coverage of volcanism. Estimates of planetesimal permeability vary from $10^{-8} - 10^{-14}$m^2 (Chapter 2), which leads to a range in τ_{dry} of $10^5 - 10^{11}$ years. Additionally, more conservative estimates of surface volcanism could further increase these timescales by one or two orders of magnitude. For the lower estimates of these timescales, planetesimals may lose significant water during mantle convection. However, this could still be inhibited by the melt density relative to the crust. Therefore, it is reasonable to assume a constant water content in the mantle.

4.4.3.3 Solidus parametrisation

The dry solidus description from Katz et al. (2003) has a larger temperature difference between the solidus and liquidus compared to Chapters 2 and 3. This larger difference raises the temperature of the critical melt fraction and enables lower $X_{\mathrm{S,0}}$ values to be run in the model (4.44 wt% compared to 22.63 wt% for dry, 300 km radius planetesimals with critical melt fractions equal to 0.3). Other than the initial core

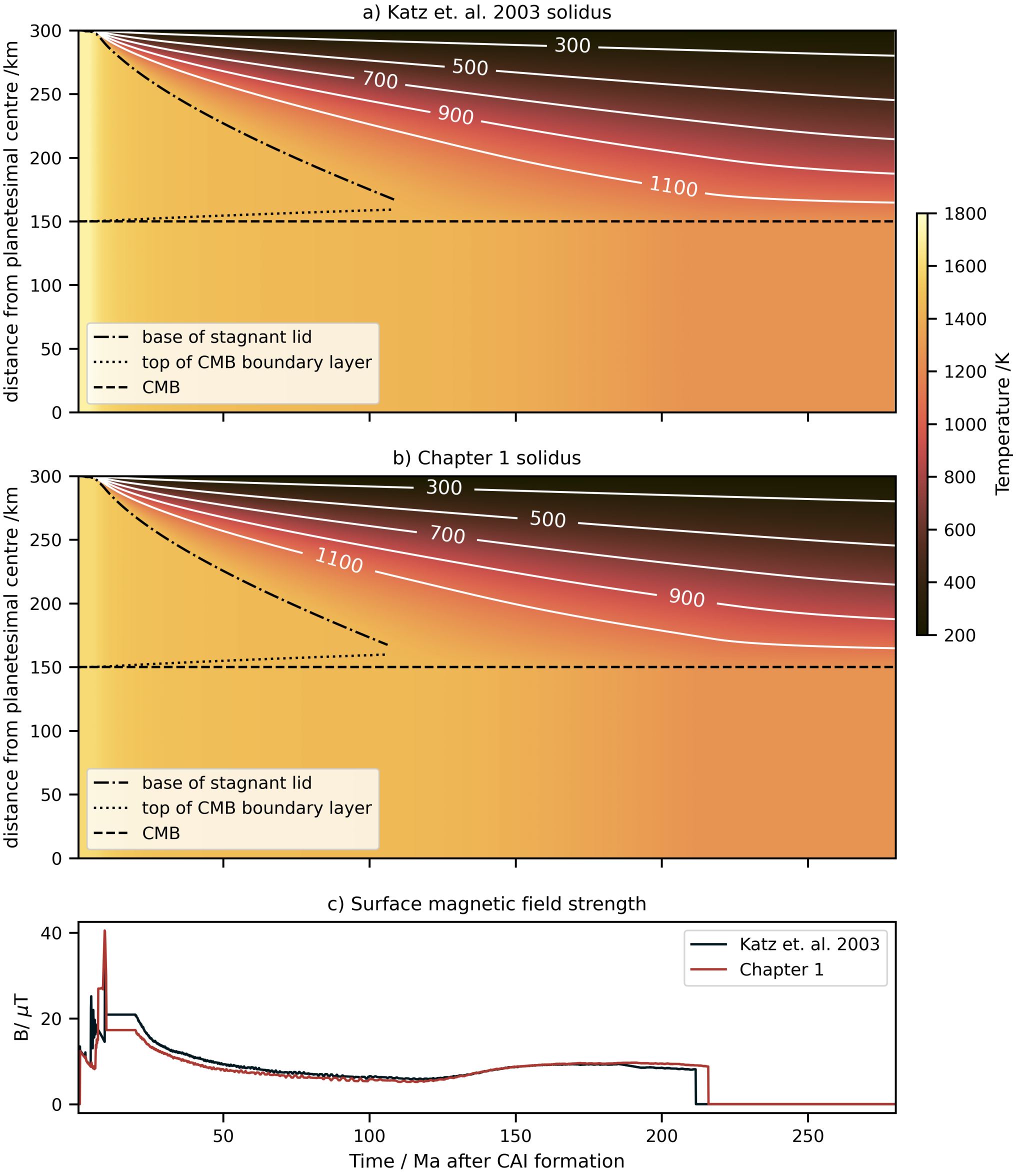

Figure 4.12: Thermal evolution of two identical, 300 km radius, dry planetesimals using a) the Katz et al. (2003) solidus and b) the Chapter 2 solidus. The peak temperature is higher for the Katz et al. (2003) solidus, but otherwise the thermal evolutions are very similar. c) magnetic field strength, B, as a function of time for the Katz et al. (2003) solidus parametrisation (black trace) and the constant values used in Chapter 2 (brown trace). The spike in the brown trace at early times comes from the earlier onset of core solidification due to the lower differentiation temperature.

sulfur content, the solidus parametrisation has minimal effect on the timing of thermal evolution. Identical, 300 km radius, dry planetesimals with differing solidii have $< 5\%$ difference in their times for the cessation of mantle convection, dynamo generation, and core solidification. The magnetic field evolution for the two dry solidii are very similar (Figure 4.12).

The iron concentration of silicate minerals strongly affects their solidii (Kiefer et al., 2015). This results in a ~ 40 K difference in dry solidus temperature between the parametrisation of Katz et al. (2003) for mantle peridotite (Mg#90; Davis et al., 2009), and that of Chapter 2 based on CC chondrite Allende (Mg#69; Agee et al., 1995). Iron contents in planetesimal mantles will be lower than those in chondrites due to movement of iron to the core during differentiation. Therefore, the composition assumed in Katz et al. (2003) is more appropriate for the iron content in differentiated planetesimals. I neglect differences in dry solidus temperature between the wet and dry planetesimal endmembers due to changing core fraction because addition of 0.07 wt% water lowers the solidus more (185 K) than the addition of iron (≤ 40 K depending on composition).

Silicate mineralogy also affects the solidus, because different minerals have different partition coefficients for water (Rider-Stokes et al., 2024). I adopt the parametrisation of Katz et al. (2003), because it enables easy quantification of the effect of mantle water content on the solidus. While the trend in solidus depression with increasing water content will be similar in planetesimal mantles, the exact temperature differences may vary due to mineralogical differences between mantle peridotite and planetesimal mantles, and mantle heterogeneity.

4.4.3.4 Other light elements in planetesimal cores

Other elements that could also be present in planetesimal cores include O, C, and Si (Pommier et al., 2020; Bromiley, 2023). However, appropriate abundances for the wet and dry endmembers are hard to constrain because oxygen fugacity, planetesimal bulk composition, differentiation mechanism, and fluid immiscibility all affect core light element composition (Poirier, 1994; Rubie et al., 2015; Bromiley, 2023; Bromiley et al., 2024). Additionally, the thermal conductivity and density of iron alloys containing multiple light elements is poorly constrained, particularly at planetesimal core pressures (Pommier et al., 2020). Therefore, it would not be insightful to include O, C, and Si in my thermal evolution and dynamo generation model due to the large uncertainties in their abundance and effect on core properties.

4.5 Conclusions

The early Solar System consisted of two distinct reservoirs of planetesimals: non-carbonaceous (NC) planetesimals in the inner Solar System and carbonaceous (CC) planetesimals in the outer Solar System. Although these reservoirs are isotopically distinct, the differences in water content and oxidation state between differentiated planetesimals in these two reservoirs are debated. I used the planetesimal thermal evolution and dynamo generation model of Chapter 2 to determine whether meteorite paleomagnetism or thermochronometry could reveal differences in water content and oxidation state between NC and CC differentiated planetesimals. The model was modified to include the effect of water content on the mantle viscosity and mantle solidus. I ran models for a range of water contents and core sizes, as well as end-member models to predict differences in dynamo histories between 'wet' and 'dry' planetesimals. The effects on thermal evolution and dynamo generation are:

- Increasing water content decreases the mantle solidus. This decreases the planetesimal differentiation temperature, shortening the dynamo, because less cooling is required to reach the core eutectic temperature.
- Increasing water content decreases mantle viscosity. This enhances mantle cooling and delays the cessation of mantle convection. This cools the core more rapidly, shortening the dynamo.
- Decreasing the fractional core radius results in weaker surface magnetic field strengths because magnetic field strength follows an inverse cube law and the distance from the CMB to the surface is larger.
- Dynamo duration has a non-monotonic dependence on fractional core radius. The magnetic Reynolds number in the smallest cores is subcritical and there is no dynamo generation. In contrast, in the largest cores the corresponding thin mantles cool very rapidly reducing the time for which CMB heat flux is high enough to drive a dynamo.
- Wet, more oxidised planetesimals generate shorter, weaker fields than dry, more reduced planetesimals. No wet planetesimals generate fields $> 5\,\mu\text{T}$ more than $\sim 50\,\text{Ma}$ after CAI formation, irrespective of size. In contrast, all dry planetesimals with radii $\geq 200\,\text{km}$ generate fields $> 5\,\mu\text{T}$ beyond this time and up to $\sim 600\,\text{Ma}$ after CAI formation.

- The closure temperatures for isotopic thermochronometers occur in the conductive portion of the mantle, so are determined by the mantle thickness. As a result, meteorite isotopic thermochronometer measurements cannot reveal planetesimal water content. However, they are key to explore planetesimal radius, which is challenging to glean from paleomagnetic measurements.

The stark differences between wet and dry planetesimal endmembers demonstrates planetesimal dynamo generation can constrain the water content and core size of planetesimals. NC paleomagnetic data is consistent with NC planetesimals with cores $\frac{r_c}{r} \sim 0.5$ that formed either without water or degassed all their water rapidly during differentiation. This supports previous arguments that measurements of water in NC achondrites have been limited by the detection threshold of the equipment, rather than reflecting actual meteorite water content. This conclusion will be tested further in Chapter 5 using the time-resolved paleomagnetic histories of the parent bodies of the Main Group pallasites and IIE iron meteorites. Paleomagnetic measurements of CC achondrites dated to > 50 Ma after CAI formation are crucial to reveal whether efficient degassing of differentiated planetesimals was prevalent throughout the Solar System and how strongly planetesimal core sizes are affected by their pre-differentiation water contents. Reducing errors on paleointensity measurements, particularly from cloudy zones, will enable meteorite paleomagnetism to shed light on planetesimal core sizes. These measurements will clarify differences between NC and CC differentiated planetesimals, enabling us to better understand the evolution of the protoplanetary disk and the formation of planetesimals.

Chapter 5

Refined internal structures of the Main Group pallasite and IIE iron meteorite parent bodies from paleomagnetism

5.1 Introduction

The earliest accreting planetesimals contained sufficient ^{26}Al to melt and differentiate, forming metallic cores and rocky mantles. However, some meteorites contain both metal and silicate suggesting some planetesimals experienced either incomplete differentiation or later mixing between core and mantle material. One example is the IIE iron meteorites that contain both chondritic and achondritic silicate inclusions, suggesting they originate from a partially differentiated parent body (Ruzicka, 2014). Another example is the pallasite meteorites that consist of achondritic silicates surrounded by an Fe-Ni matrix (Wasson and Choi, 2003). Pallasites have been proposed to form either at the core-mantle boundary (CMB, e.g. Scott, 1977a,b; Wasson and Choi, 2003), or through impacts between differentiated planetesimals (e.g., Tarduno et al., 2012; Walte et al., 2020; Kruijer et al., 2022), or through eruption of metallic material from the core into the mantle (Johnson et al., 2020a). Meteorite paleomagnetism can help to reveal the properties of these meteorite parent bodies, and shed light on their formation in several ways. Firstly, a non-zero paleomagnetic remanence indicates the parent body had a core (e.g., Carporzen et al., 2011; Elkins-Tanton et al., 2011; Weiss and Elkins-Tanton, 2013; Maurel et al., 2019). Secondly, a non-zero remanance strong enough to be a dynamo also indicates a meteorite cooled sufficiently to record a magnetic field while one was being generated. This precludes the formation of a meteorite at the core-mantle boundary, where temperatures would have been far above the blocking temperature when the dynamo was being generated (Tarduno et al., 2012). Thirdly, a time-resolved paleomagnetic record combined with meteorite cooling rates can trace the thermal evolution of a planetesimal's interior. This can constrain the size of the parent body, its core size, and the timing of core crystallisation (e.g., Bryson et al., 2015; Maurel et al., 2021; Nichols et al., 2021).

Paleomagnetic measurements have been performed on two carriers within these meteorites: single crystal paleointensity analysis on olivine crystals containing taenite inclusions in the Main Group pallasites (Tarduno et al., 2012; Nichols et al., 2021); and X-ray photoemission electron microscopy (XPEEM) on cloudy zones within meteorite metal in both the Main Group pallasites and IIE irons (Bryson et al., 2015; Nichols et al., 2016; Maurel et al., 2020; Nichols et al., 2021; Maurel et al., 2021). Cloudy zones are Fe-Ni microstructures that form within meteorite metal by spinodal decomposition below 623 K in slow cooled meteorites ($< 10,000\,\mathrm{K Ma^{-1}}$; Maurel et al., 2019). As the cloudy zone cools through 593 K (its blocking temperature), it records a chemical transformation remanent magnetisation (CTRM) that is stable for billions of years (Einsle et al., 2018). A time-resolved paleomagnetic record can be obtained by measuring several meteorites with different cooling rates from a single parent body. The slower the cooling rate, the deeper within the body the meteorite originated, and so the later it cooled through its blocking temperature and acquired a remanence. Two cooling rates can be obtained from the metal alloys in each meteorite. Firstly, cooling rates can be obtained between 875–975 K, when the Widmanstätten pattern formed. Metallographic cooling rates can be calculated at this temperature from the shape of the Ni composition profile across kamacite bands (Yang et al., 2010). Alternatively, cooling rates can be calculated using empirical correlations between cloudy zone island size and metallographic cooling rates (Yang et al., 2010). Secondly, cooling rates can be determined at 623 K, when the cloudy zone first formed, by combining the size of an island within the cloudy zone with thermodynamic models of cloudy zone formation (Maurel et al., 2019).

Five Main Group pallasites, the predominant group of pallasites originating in the inner Solar System from the same parent body (Greenwood et al., 2006), have been paleomagnetically measured. Marjalahti and Brenham cooled through the cloudy zone blocking temperature first and have null magnetic remanences consistent with the absence of a dynamo field (Nichols et al., 2016; Maurel et al., 2019). Springwater (Nichols et al., 2021), Imilac and Esquel (Tarduno et al., 2012; Bryson et al., 2015) acquired their remanences later and all record non-zero paleointensities, arguing that a dynamo field was present at this time. Conductive cooling models have been used to estimate the depth and timing of remanence acquisition by finding depths that matched metallographic cooling rates and calculating when these depths cooled through their blocking temperature (Tarduno et al., 2012; Bryson et al., 2015; Nichols et al., 2016; Murphy Quinlan et al., 2021). All these models assumed the magnetic fields recorded in the meteorites were generated only by compositional convection from core solidification. Once the core began to solidify, an outward solidification model was used to estimate the duration of dynamo generation. Using a similar model, Nichols et al. (2021) explored a wider range of planetesimal radii, core radius fractions, and initial core sulfur contents for the Main Group pallasite parent body and were the first to compare these model runs to all five meteorites. They also included a maximum energy approach to estimate possible magnetic field strengths during inward core solidification. They concluded that the Main Group pallasite parent body had a large core and thin mantle (core radius $\gtrapprox 70\%$ of the total parent body radius) and was 180–360 km in radius.

All three IIE irons that have been paleomagnetically measured record non-zero paleointensities (Colomera, Techado and Miles; Maurel et al., 2020, 2021). Planetesimal thermal evolution and dynamo generation models were used to determine the depth of each meteorite in their parent body and possible planetesimal sizes and core radius fractions. Unlike the models for the Main Group pallasites, these models included mantle convection and conduction and considered the duration of eutectic core solidification as a proxy for dynamo generation rather than explicitly modelling dynamo generation during core solidification. These models suggest the IIE iron parent body had a radius $\geq$220 km and was partially differentiated with a core radius fraction $\geq 19\%$.

Previous models for the Main Group pallasites and IIE irons both assumed that their meteorites record magnetic fields generated during core solidification. However, in Chapter 3, I demonstrated that dynamos > 65 Ma after CAI formation may not require core solidification and instead could have been generated by thermal convection. Additionally, variations in mantle viscosity parameters and planetesimal size can lead to longer dynamo durations than previously thought. These conclusions result from three key refinements in the planetesimal thermal evolution and dynamo generation model presented in Chapter 2 compared to previous models. Firstly, this model includes both mantle convection and conduction. Secondly, this model describes inward core solidification, which is more likely to occur in planetesimals than outward solidification due to the low pressure at their CMB compared to planets (Williams, 2009; Dodds et al., 2025). Thirdly, this model describes magnetic field generation using a combined thermal and compositional buoyancy flux, which means both thermal and compositional convection can be considered simultaneously as possible drivers for the dynamo. In this chapter, I will use this refined thermal evolution and dynamo generation model to explore possible thermal and dynamo histories of the Main Group pallasites and IIE irons. I will compare my model outputs to metallographic cooling rates and the paleomagnetic record to re-evaluate the depths and timings of remanence acquisition. Additionally, I will determine the likely core and overall sizes of these meteorite parent bodies, and the implications for the formation of these unusual meteorites. Altogether, this study will determine the extent to which time-resolved paleomagnetic observations can constrain the properties of meteorite parent bodies.

5.2 Methods

I calculated possible parent body thermal and magnetic histories using the thermal evolution and dynamo generation model presented in Chapter 2. I also included the amended mantle viscosity and mantle solidus from Chapter 4 that account for non-zero mantle water contents in nominally anhydrous minerals. I explored planetesimal parameter space in two stages: broad and sparse, to consider all possible combinations of parameters; then, narrow and dense, to consider combinations of key parameters (Section 5.2.4). I compared the planetesimal history for each parameter combination with measured cooling rates and paleomagnetic remanences of meteorites from each parent body to see if it was consistent with the meteorite record (see Sections 5.2.1 and 5.2.3). I collated planetesimal parameter combinations that produced histories consistent with the meteorite record to determine the distribution of possible parent body parameters. I also used the consistent model runs to predict the distribution of possible meteorite depths within each parent body and the distribution of possible remanence acquisition times in the Main Group pallasites.

5.2.1 IIE iron constraints

For the IIE irons, three meteorites (Colomera, Techado, Miles) have been measured paleomagnetically (Maurel et al., 2020, 2021) and can be used to determine properties of the IIE parent body. Three sets of experimental measurements on these meteorites provide constraints on the history of the IIE parent body (Table 5.1). Firstly, all three meteorites record a paleomagnetic remanence, indicating the planetesimal generated a dynamo field as the cloudy zone in each meteorite cooled through 593 K (Maurel et al., 2020, 2021). Secondly, the thermodynamics of cloudy zone formation provides an estimate of each meteorite's cooling rate at 623 K (Maurel et al., 2019, 2020, 2021). Finally, the closure temperature of ^{40}Ar/^{39}Ar system in 0.1–1 mm feldspars overlaps with the cloudy zone blocking temperature (603 ± 70 K Bogard et al., 2000; Cassata et al., 2011), so ^{40}Ar/^{39}Ar ages give the time of remanence acquisition. I compared these constraints to thousands of planetesimal thermal and magnetic histories to determine whether each one was consistent with the observed history of the IIE irons. I also used these constraints to calculate possible depths of each meteorite within the parent body. I applied these constraints in the following steps:

1. Check that the dynamo is active for some fraction, or all, of the ^{40}Ar/^{39}Ar age range for each meteorite.
2. Find the depth range on the 593 K contour (temperature of remanence acquisition) for each meteorite's ^{40}Ar/^{39}Ar age (Figure 5.1). The upper and lower age limits correspond to upper and lower depth limits, respectively.
3. Find the cooling rate for the median of each meteorite depth range at 623 K (the temperature of cloudy zone formation).
4. Check that the model cooling rate at 623 K lies within the uncertainty of the experimental cooling rate.
5. Check the model relative paleointensity lies within the range of the measured relative paleointensity. Calculation of the relative paleointensities is described in Section 5.2.2 below.

All three meteorites must satisfy the criteria at every step for a parameter combination to be a possible fit to the IIE parent body.

	Techado	Colomera	Miles
^{40}Ar/^{39}Ar age[1] / Ma after CAI formation	78 ± 13	97 ± 10	159 ± 9
Cooling rate at 623 K[2,3] / KMa^{-1}	4.6 ± 1.9	2.5 ± 1.4	3.8 ± 2.6
Paleointensity[2,3] / μT	36 ± 11	15 ± 5	33 ± 9
Relative paleointensity	1.0 ± 0.4	0.42 ± 0.18	0.92 ± 0.38

Table 5.1: Experimental constraints on parent body histories for the IIE irons. [1]Bogard et al. (2000), [2]Maurel et al. (2020),[3]Maurel et al. (2021). Calculation of relative paleointensities is discussed in Section 5.2.2.

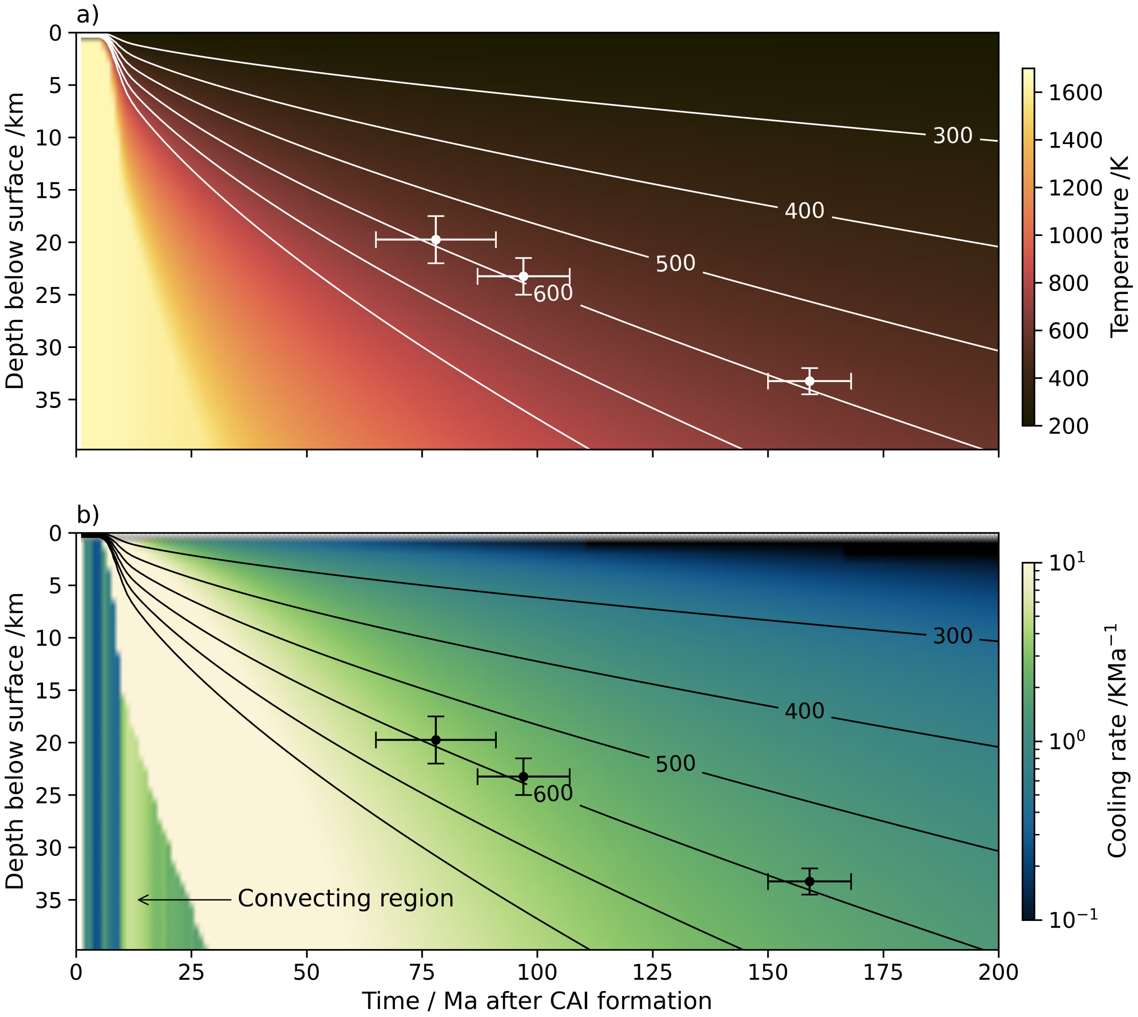

Figure 5.1: a) Example temperature and b) cooling rate profile used for comparison with the thermal history of the IIE irons. temperature contours are shown on both panels. From left to right the black points and error bars correspond to the radiometric ages and calculated depths for Techado, Colomera and Miles. The convecting region has an isothermal interior and a vertically uniform cooling rate. The profile shown is for a 500 km radius planetesimal with 250 km radius core and all other parameters are the modal IIE values in Table 5.4.

5.2.2 Relative paleointensity values

Induced fields in kamacite and interactions between cloudy zones could amplify or reduce, respectively, the recorded paleointensity compared to the primordial field (Maurel et al., 2020, 2021). However, these effects are likely to be similar across cloudy zones. Therefore, while the absolute paleointensity values from a meteorite may not be accurate, the relative paleointensities of different meteorites from the same body can provide insight into the change in magnetic field strength over time. To utilise this information, I compared the relative paleointensities of each meteorite with the relative paleointensities from the model at the time the meteorite recorded the remanence. I calculated the relative paleointensity of a given meteorite, $B^{\text{exp}}_{\text{rel},i}$ by dividing the measured paleointensity, B_i, by the maximum of the measured mean paleointensity values within a meteorite group, $\max\limits_{i\in n}(B_i)$,

$$B^{\text{exp}}_{\text{rel},i} = \frac{B_i}{\max\limits_{i\in n}(B_i)}. \tag{5.1}$$

Errors on experimental relative paleointensities were calculated by propagating the errors on the measured paleointensities. The relative paleointensities for the model outputs are calculated as follows:

1. Find the paleointensity at the upper time bound, B_i^{max}, and lower time bound, B_i^{min}, for a given meteorite.
2. Find the average of these pairs of values. $B_i^{\text{av}} = (B_i^{\text{min}} + B_i^{\text{max}})/2$
3. Divide all average values by the maximum average value $B^{\text{model}}_{\text{rel},i} = B_i^{\text{av}}/\max\limits_{i\in n}(B_i^{\text{av}})$.

Using relative paleointensities also accounts for uncertainties in the model paleointensities due to choice of convective lengthscale in the dynamo scaling laws and the core solidification parametrisation (Chapter 2). Both these uncertainties could lead to over- or under-estimation of paleointensity by a constant multiplicative factor. Normalising the paleointensities accounts for this factor and emphasises relative changes in paleointensity with time rather than absolute values.

5.2.3 Main Group pallasite constraints

Paleointensity estimates have been recovered for five Main Group pallasites (Majalahti, Brenham, Springwater, Imilac and Esquel; Tarduno et al., 2012; Bryson et al., 2015; Nichols et al., 2016, 2021). The paleomagnetic remanences recorded in the cloudy zone in Marjalahti and Brenham are consistent with zero, while Springwater, Imilac, and Esquel have non-zero remanences (Maurel et al., 2019; Nichols et al., 2021). Marjalahti and Brenham are older and originated from shallower depths on the parent body than Springwater, Imilac and Esquel, because their cooling rates are faster (Nichols et al., 2021). Therefore, the Main Group pallasite parent body must have experienced an inactive dynamo followed by an active dynamo. Whether the dynamo is active when the cloudy zone in each meteorite recorded its remanence provides one constraint on the dynamo generation history of the Main Group pallasites (Nichols et al., 2021). Unlike the IIE irons, there are currently no radiometric ages for remanence acquisition in the Main Group pallasites due to a lack of suitable mineralogy (e.g. feldspars). Instead, the time of remanence acquisition is inferred from the time from thermal modelling at which a meteorite's original depth on the parent body cooled through the cloudy zone's blocking temperature (593 K; Einsle et al., 2018). The original depth of each meteorite is inferred from the cooling rate at the kamacite nucleation temperature (875–975 K, Yang et al., 2010, Table 5.2) and the cooling rate at the onset of cloudy zone formation (623 K, Maurel et al., 2019, Table 5.2). The kamacite nucleation temperature depends on several factors including bulk Ni content in the metal and nucleation mechanism (Yang and Goldstein, 2005), so I use the middle value in the range of nucleation temperatures for the Main Group pallasites (925 K; Yang et al., 2010). The model depth must have cooling rates consistent with the experimental measurements at both 925 K and 623 K. If no depths are consistent with both cooling rates or the planetesimal does not cool below the required temperature before the end of core solidification, then a given parameter combination cannot describe the Main Group pallasite parent body and thus is rejected.

I apply the above constraints to each planetesimal thermal and dynamo history in the following steps to determine if a parameter combination is a possible fit to the experimental observations for the Main Group pallasite parent body.

1. Check that a period of dynamo generation follows a period without dynamo generation. In the models, this corresponds to a gap between two periods of dynamo generation (Chapter 3).

2. Find the range of depths on the 925 K contour which match the Yang et al. (2010) cooling rates for each meteorite.

3. Check that some depths within each meteorite depth range also match the cooling rates at 623 K from Maurel et al. (2019). Refine the depth range for

each meteorite so both high and low temperature cooling rates lie within their required range.

4. Check that the dynamo is active/inactive as required when each meteorite depth range reaches 593 K. If the dynamo turns on or off within a depth range, reduce the depth range to depths where the dynamo behaves as required.

The cooling rates and dynamo behaviour for all model meteorite depths must match the observed cooling rates and paleomagnetic record to be consistent with that of the Main Group pallasites. Unlike for IIE irons, I do not compare the relative paleointensities between the model and experimental values, because there is large uncertainty on the paleointensities of Imilac and Esquel. There is a large discrepancy between single olivine crystal paleointensities (Tarduno et al., 2012) and cloudy zone paleointensities (Bryson et al., 2015; Nichols et al., 2021). Additionally, these meteorites' paleomagnetic remanences were measured using a single XPEEM orientation. Therefore, the angle between the primordial field and the recorded field is unknown. When accounting for the uncertainty in field direction, the 95% confidence value is an order of magnitude larger than the measured paleointensity (Nichols et al., 2021). Marjalahti and Brenham were also measured using a single XPEEM orientation but their measured values lie below the 95% confidence value for a null measurement based on models of cloudy zone remanence acquisition (Maurel et al., 2019), and the 95% confidence values based on uncertainties in orientation are too weak to be dynamo generated (Nichols et al., 2021).

	Marjalahti	Brenham	Springwater	Imilac	Esquel
Cooling rate at 925 K[1] /KMa^{-1}	7.6 ± 0.6	6.2 ± 0.9	5.1 ± 0.7	4.3 ± 0.3	3.3 ± 0.6
Cooling rate at 623 K[2] /KMa^{-1}	2.9 ± 1.5	2.5 ± 1.4	1.7 ± 1.2	1.2 ± 0.7	0.9 ± 0.5
Dynamo behaviour[3]	Off	Off	On	On	On

Table 5.2: Experimental constraints on parent body histories for the Main Group pallasites. [1]Yang et al. (2010), [2]Maurel et al. (2019),[3]Nichols et al. (2021). Dynamo behaviour is limited to whether the dynamo is on or off due to the uncertainty in the paleointensity measurements of Imilac and Esquel (Nichols et al., 2021).

5.2.4 Parameter variation

I explored possible parent body properties in two stages. In stage 1, I ran models over all possible combinations of parameter values for a limited number of values of each parameter (90,000 model runs, Section 5.2.4.1). I used this to determine which parameter values are most likely to produce planetesimal histories consistent with that of a given meteorite group. In this stage, I also explored correlations between parameters that produce consistent planetesimal histories. In the stage 2, I performed a more detailed parameter space exploration for the parameters of the most interest for understanding the IIE and Main Group pallasite parent bodies: radius, fractional core radius, mantle water content, and initial core sulfur content (82 runs, Section 5.2.4.2).

5.2.4.1 Stage 1 — Broad parameter variation

Due to the large number of parameters, I used a limited range of values for each parameter to enable the number of runs across all parameter combinations to be computationally feasible (Table 5.3). I held radiogenic ^{60}Fe abundance and differentiation time constant, because they only affect the first 5 Ma of dynamo generation (Chapter 3 and 4) well before the IIE or Main Group pallasites could have recorded a remanence. I held liquid viscosity constant, because it has no effect on the timing of dynamo generation (Chapter 3). Small planetesimals (≤ 100 km radius) were not considered, because they are too small to produce the long-lived dynamo generation required (Chapter 3). The range in initial core sulfur contents was chosen to enable a consistent range across all water contents, critical melt fractions and planetesimal sizes. Due to the large change in the temperature of the critical melt fraction with these three parameters, the resulting range of initial core sulfur contents is narrow (28.7–32 wt%). A wider range of sulfur contents was explored in the more detailed parameter variation (stage 2, Table 5.4). The range of reference viscosities, critical melt fractions, and melt-weakening exponents was taken from Chapter 3. The upper limit on the Arrhenius slope was taken from Chapter 4 because this value exceeds the maximum value in Chapter 3. The range of water contents in nominally anhydrous minerals was also taken from Chapter 4.

5.2.4.2 Stage 2 — Key parameter variation

In this stage, I focussed on the key parameters for understanding the possible formation mechanism of the IIE irons and Main Group pallasites and the interior structures of their parent bodies. I performed a more detailed parameter space exploration of planetesimal radius, core radius fraction, mantle water content in nominally anhydrous minerals (NAMs), and initial core sulfur content. All other parameters were held at their modal values from the broad parameter space exploration (Figures 5.2,

Parameter	Symbol	Range of values
Radius /km	r	200, 300, 400, 500
Core radius fraction	$\frac{r_c}{r}$	0.1, 0.3, 0.5, 0.7, 0.9
Critical melt fraction	ϕ_C	0.3, 0.4, 0.5
Reference viscosity /Pas	η_0	10^{15}, 10^{17} , 10^{19} , 10^{21}, 10^{23}
Arrhenius slope /K^{-1}	β	0.01, 0.02, 0.03, 0.04, 0.05
Melt weakening exponent	α_n	25, 30, 35, 40, 45
Initial core sulfur content /wt%	$X_{\mathrm{S},0}$	28.7, 30.35, 32
Water content in NAMs /wt%	X_w	0, 0.2, 0.4, 0.7

Table 5.3: Parameter values for exploration of all possible parameter combinations explored in stage 1. Ranges on parameter values are from Chapter 3 and Chapter 4 or are described in the text. Liquid viscosity, $^{60}\mathrm{Fe}/^{56}\mathrm{Fe}$, and differentiation time were held constant at 100 Pas, 10^{-8} and 1 Ma after CAI formation, respectively. The X_w values are the same as in Chapter 4. NAMs = nominally anhydrous minerals.

5.3 and Table 5.4). Planetesimal radius and core radius fraction both influence mantle thickness and therefore mantle cooling rate. This strongly influences whether a given planetesimal history is consistent with the meteorite record. Therefore, these two parameters were varied together over the ranges in Table 5.4. Mantle water content in NAMs and core fractional radius could both reflect the formation conditions of these meteorite parent bodies (Chapter 4). As a result, I varied these two parameters together to determine whether each meteorite parent body was more consistent with the wet or dry planetesimal endmembers discussed in Chapter 4. Finally, initial core sulfur content will strongly affect the onset time of core solidification and whether these meteorite paleomagnetic records are signatures of core solidification as previously suggested. To explore the range of possible initial core sulfur contents, I varied initial core sulfur content while all other parameters were held constant at their modal values.

Constant parameters			
Parameter	Symbol	IIE mode	Pallasite mode
Radius /km	r	500	400
Core radius fraction	$\frac{r_\mathrm{c}}{r}$	0.5	0.5
Initial core sulfur content /wt%	$X_{\mathrm{S},0}$	28.7	32
Water content in NAMs /wt%	X_w	0	0
Critical melt fraction	ϕ_C	0.4	0.3
Reference viscosity /Pas	η_0	10^{21}	10^{23}
Arrhenius slope /K^{-1}	β	0.03	0.05
Melt weakening exponent	α_n	25	45
Detailed parameter exploration			
		Range of values	Number of values
Radius /km	r	300–500	5
Core radius fraction	$\frac{r_\mathrm{c}}{r}$	0.3–0.7	5
Initial core sulfur content /wt%	$X_{\mathrm{S},0}$	IIE:11–33 PMG:24–33	IIE:12 PMG:10
Water content in NAMs /wt%	X_w	0 – 0.07	7 (exclude 0.01)

Table 5.4: Range of parameters explored in detail in stage 2. All parameter ranges were evenly spaced and included the start and end values given in the table. A series of runs were performed where radius and core radius fraction were varied together and another series were performed where core radius fraction and mantle water content were varied together. Liquid viscosity, ^{60}Fe/^{56}Fe, and differentiation time were held constant at 100 Pas, 10^{-8} and 1 Ma after CAI formation, respectively. The range of initial core sulfur contents for the Main Group pallasites (PMG) is narrower than for the IIE irons, because of the lower modal critical melt fraction and resulting lower differentiation temperature for the Main Group pallasites.

5.3 Results

5.3.1 Broad parameter variation

5.3.1.1 Parent body properties

The constraints on the Main Group pallasite parent body properties are more refined than for the IIE irons with 1% and 15% of parameter combinations being consistent with each parent body history, respectively. This is because there are more paleomagnetically measured Main Group pallasites than IIE irons. Additionally, the inactive dynamo period followed by the active dynamo period observed in the Main Group pallasites that requires models to have a gap in dynamo generation also tightens the constraints on certain parameters, as discussed below.

For both meteorite parent bodies there is a strong preference for certain planetesimal radii (Figure 5.2a and 5.3a) and core radius fractions (Figure 5.2b and 5.3b). The modal radius for the IIE irons is larger than for the Main Group pallasites and the distribution of IIE core radius fractions is skewed to larger values. Overall, the IIE irons have a wider range of possible radii and core radius fractions than for the Main Group pallasites because the paleomagnetic constraint on their parent body history is more relaxed. The IIE irons require a continuous record of dynamo generation from ∼60–170 Ma after CAI formation, which could occur during the second epoch of dynamo generation in a ∼300 km radius planetesimal or in the first epoch of dynamo generation in a ∼500 km radius planetesimal (Chapter 3). In contrast, the Main Group pallasites require models to have a gap in dynamo generation, which requires a match to a specific set of cooling rates during the second epoch of dynamo generation.

The constraints on the viscosity of both bodies are more relaxed. Both the critical melt fraction, ϕ_C, and the melt weakening exponent, α_n, have slight peaks in their distributions, but a narrow range of peak heights (Figure 5.2c, 5.2f, 5.3c and 5.3f). The Arrhenius slope, β, has a very weak peak in the middle of the range for the IIE irons, but is more pronounced and shifted towards the largest values for the Main Group pallasites (Figure 5.2e and 5.3e). Increasing the Arrhenius slope widens the gap in dynamo generation (Chapter 3), which is more favourable for the Main Group pallasites, because it increases the range of times over which the null paleointensity measurements could be matched. Out of the viscosity parameters the reference viscosity, η_0, has the clearest trend (Figure 5.2d and 5.3d), because it has the strongest effect on the timing of dynamo generation (Chapter 3). Higher reference viscosity values $\geq 10^{21}$ Pas are more likely in both bodies, because these values provide the

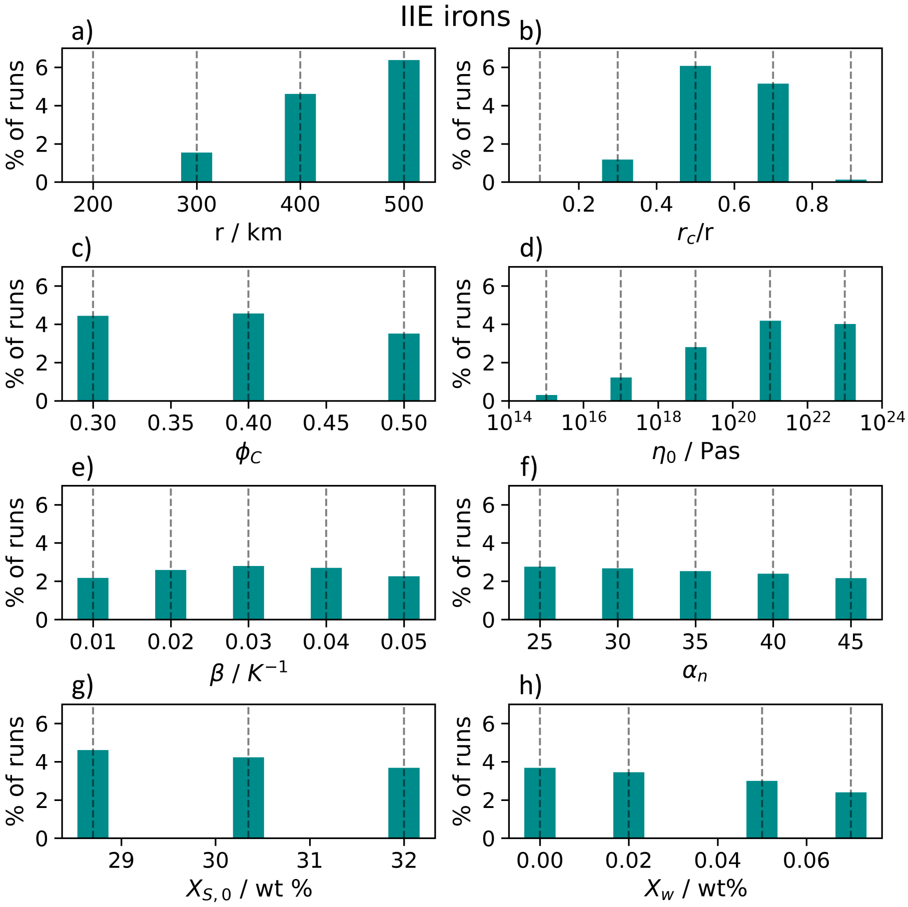

Figure 5.2: Distributions of input parameter values that produce thermal and dynamo histories consistent with the IIE iron meteorite record. The input parameters are planetesimal radius, r, core radius fraction, $\frac{r_c}{r}$, critical melt fraction, ϕ_C, reference viscosity, η_0, Arrhenius slope, β, melt weakening exponent, α_n, initial core sulfur content, $X_{S,0}$, and mantle water content in NAMs, X_w. Bars are discretised to the input values in Table 5.3 and vertical dashed lines indicate the possible values of the input parameters. Bars are missing at $r = 200\,\text{km}$ and $\frac{r_c}{r} = 0.1$, because these parameter values did not produce results consistent with the meteorite record. The y-axis is the ratio of the number runs with that parameter value that were consistent with the meteorite record compared to the total number of explored parameter combinations.

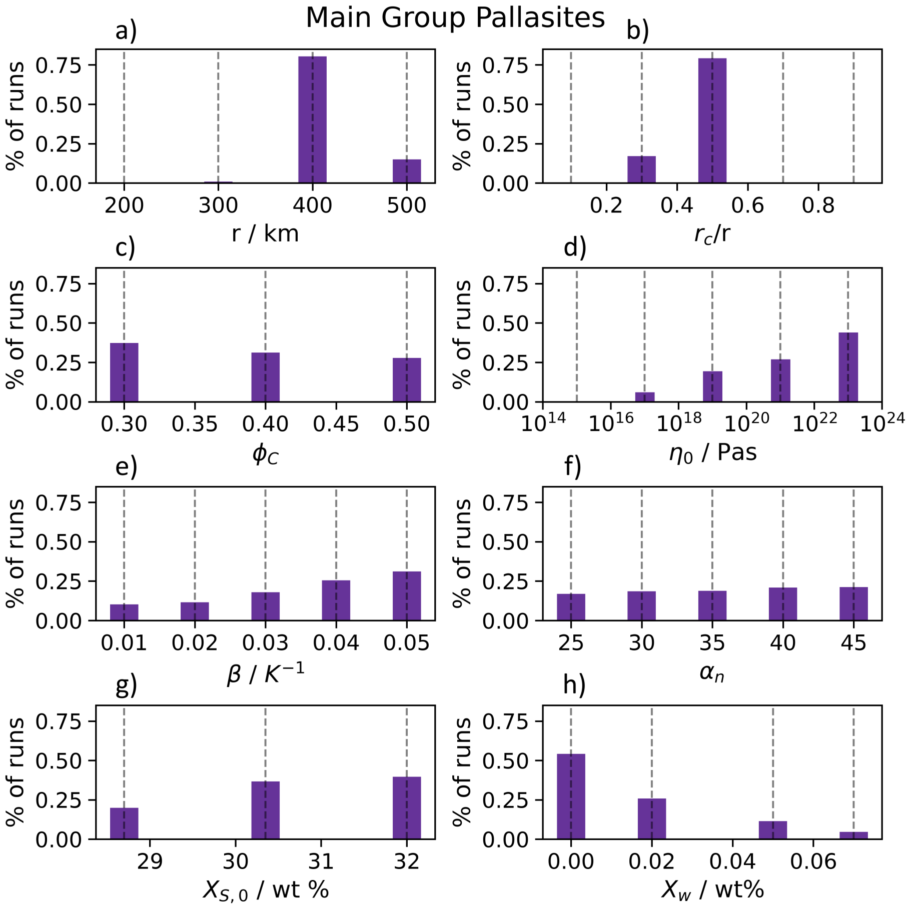

Figure 5.3: Distributions of input parameter values that produce thermal and dynamo histories consistent with the Main Group pallasite meteorite record. The input parameters are planetesimal radius, r, core radius fraction, $\frac{r_c}{r}$, critical melt fraction, ϕ_C, reference viscosity, η_0, Arrhenius slope, β, melt weakening exponent, α_n, initial core sulfur content, $X_{\mathrm{S},0}$, and mantle water content in NAMs, X_w. Bars are discretised to the input values in Table 5.3 and vertical dashed lines indicate the possible values of the input parameters. Bars are missing at $r = 200\,\mathrm{km}$, $\frac{r_c}{r} = 0.1, 0.7, 0.9$ and $\eta_0 = 10^{15}\,\mathrm{Pas}$ because these parameter values did not produce results consistent with the meteorite record. The y-axis is the ratio of the number runs with that parameter value that were consistent with the meteorite record compared to the total number of explored parameter combinations.

sufficiently slow cooling required to sustain dynamo generation for 100s of Ma. Increasing the reference viscosity widens the gap in dynamo generation (Chapter 3), so the largest reference viscosity values are favoured in the Main Group pallasites, while a slightly lower value is favoured in the IIE irons to prevent this gap occurring between ∼60–170 Ma after CAI formation when they acquired their positive remanences.

Constraints on parent body composition are weak. IIE irons slightly favour lower sulfur contents (Figure 5.2g), because this promotes the earlier onset of core solidification, which can prevent a gap in dynamo generation. In contrast, the Main Group pallasite record favours a higher initial core sulfur content to delay core solidification and ensure a gap in dynamo generation (Figure 5.3g). A wider range of initial core sulfur contents is discussed in Section 5.3.2. Both parent bodies favour the absence of water in the mantle (Figure 5.2h and Figure 5.3h), but the preference is stronger in the Main Group pallasites because there must be a gap in dynamo generation, which is more difficult to achieve in bodies with water in their mantles due to the earlier onset of core solidification prior to the cessation of an early thermal dynamo (Chapter 4). In the IIE irons, the long duration of dynamo generation favours the low initial water contents.

For the IIE irons, there are no strong correlations between input parameters in model runs consistent with the meteorite record (Figure 5.4). For the Main Group pallasites, the correlations between fractional core radius, $\frac{r_c}{r}$, and planetesimal radius, r, and between each of these parameters and reference viscosity, η_0, and Arrhenius slope, β, are slightly stronger. However, these are spurious correlations due to the presence of only two possible values for each parameter, which inflates the influence of the less frequent parameter value when calculating the correlation coefficient. Overall, the absence of strong correlations between parameters in both bodies mean it is reasonable to vary one parameter at a time to understand possible parent body properties in more detail (Section 5.2.4.2 and Section 5.3.2).

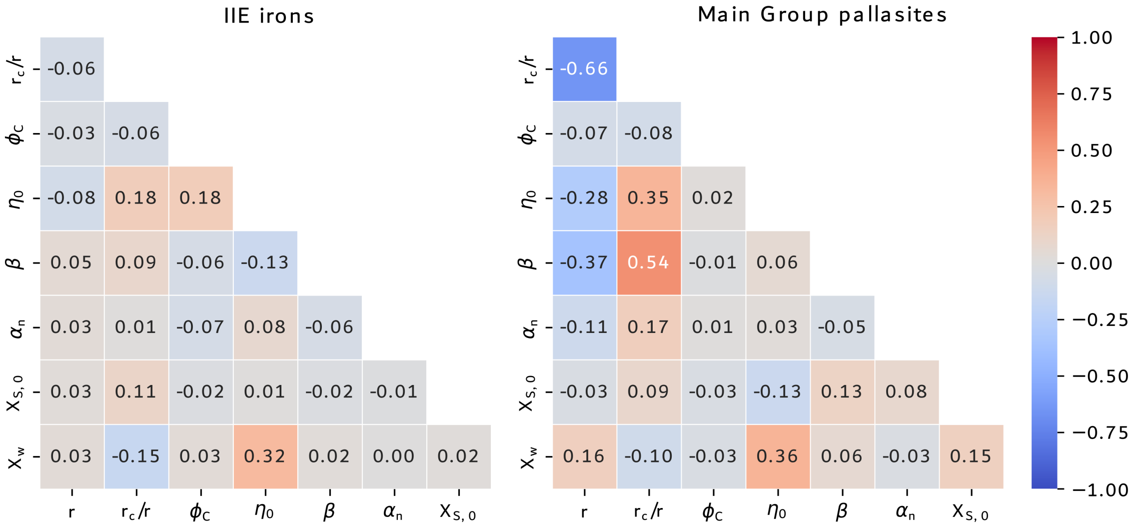

Figure 5.4: Spearman's rank correlation coefficients between input parameters for runs that produce planetesimal histories consistent with the IIE iron (left) and Main Group pallasite (right) meteorite record. Input parameters are planetesimal radius, r, core fractional radius, $\frac{r_c}{r}$, critical melt fraction, ϕ_C, reference viscosity, η_0, Arrhenius slope, β, melt-weakening exponent, α_n, initial core sulfur content, $X_{S,0}$, and water content in nominally anhydrous minerals, X_w.

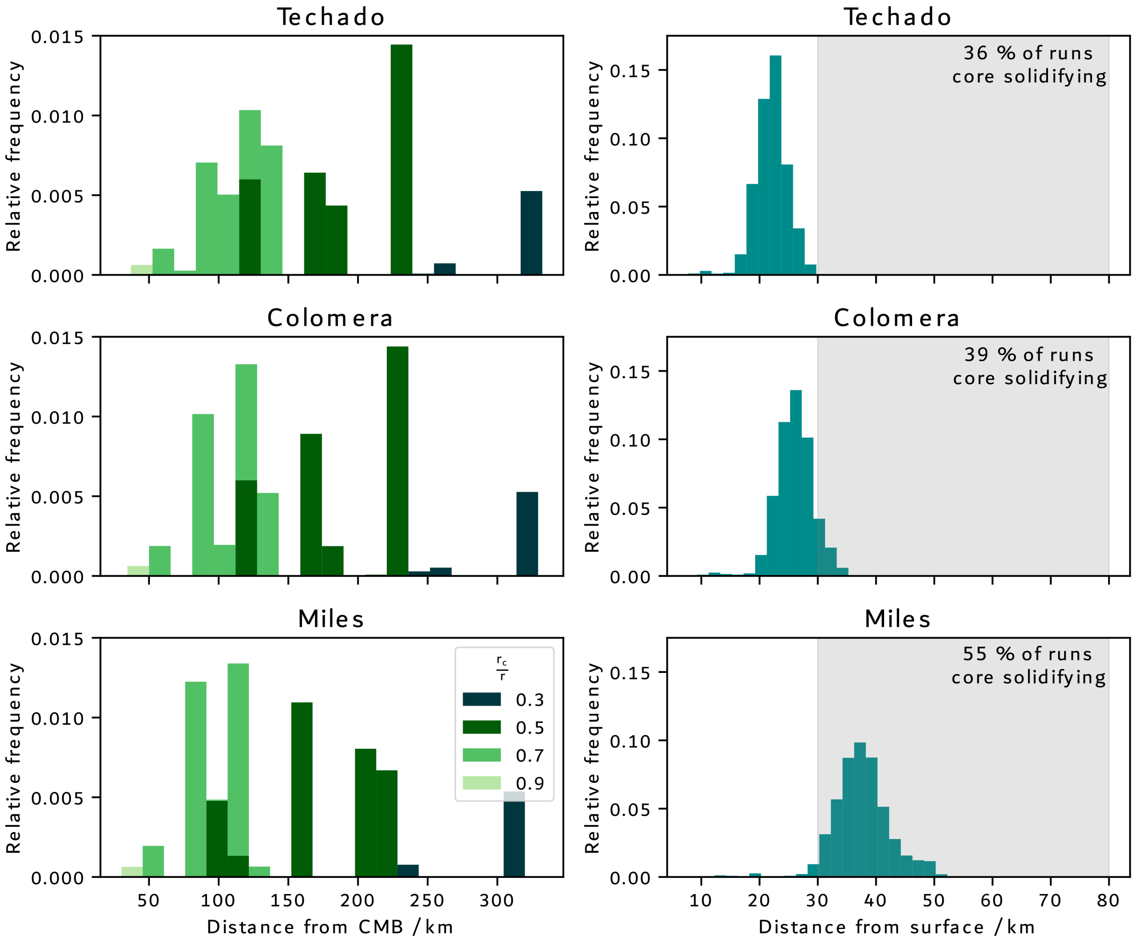

Figure 5.5: Distribution of meteorite origin locations for the IIE irons displayed as distance from the CMB (left) and distance from the surface (right). The average of the upper and lower bounds on depth for each model run were used to construct the distribution. Each row is for a different meteorite. The y-axis displays the relative frequency. The mean and standard deviation for each depth and time distribution is given in Table 5.5. The gaps in the middle of the distribution of distances from the CMB are arbitrary and are due to the discretisation of planetesimal radius and core radius fraction. Grey boxes indicate the depth range predicted by Maurel et al. (2021), which was given for all three meteorites together rather than each individual meteorite. The percentage of successful runs in which the core is solidifying is given in the right column.

5.3.1.2 Timing and depth of remanence acquisition

Core solidification is no longer required to generate the paleomagnetic remanences in the IIE irons and Main Group pallasites (Figures 5.5 and 5.6). For the IIE irons, only Miles recorded in a remanence during core solidification in more than 50% of model runs. For the Main Group pallasites, the the percentage of model runs for

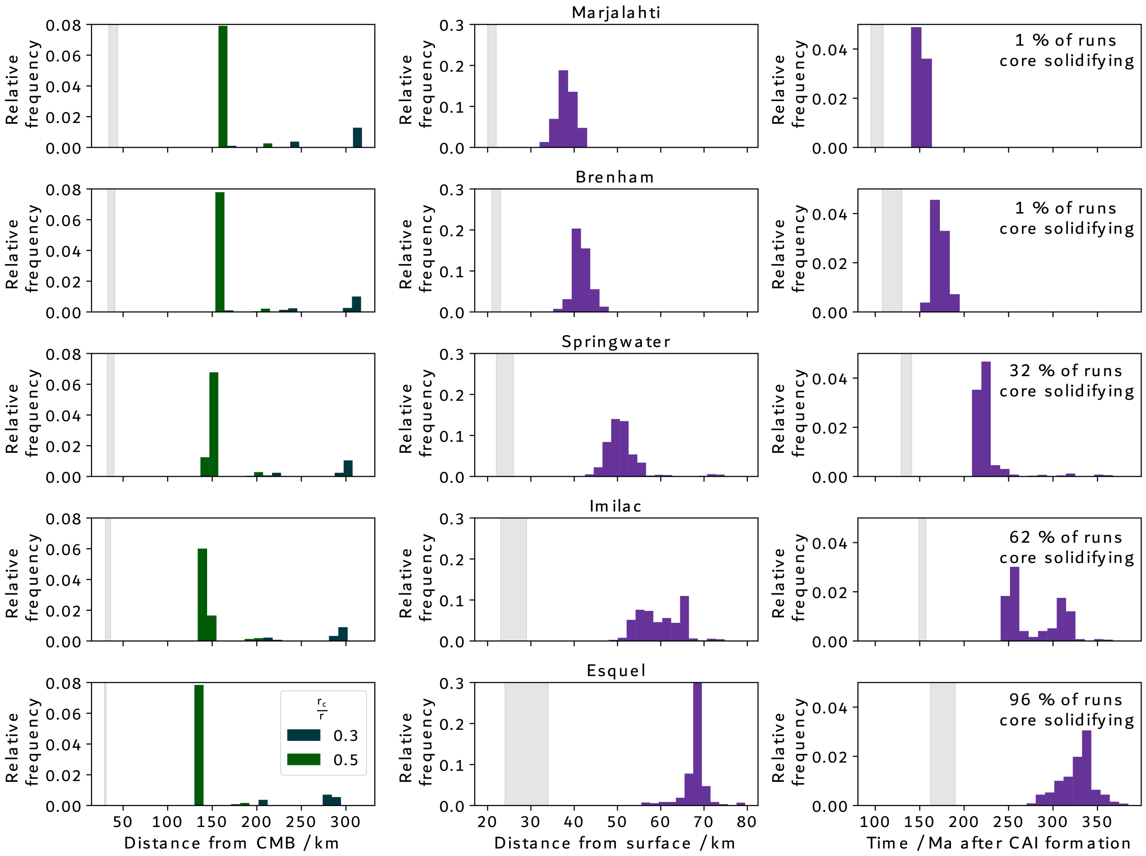

Figure 5.6: Distribution of meteorite origin locations (left two columns) and time of remanence acquisition (right) for the Main Group pallasites. Origin locations are displayed as distance from the CMB (left) and distance from the surface (middle). The average of the upper and lower bounds on depth and time for each model run were used to construct the distribution. Each row is for a different meteorite. The y-axis displays the relative frequency. The grey boxes indicate the corresponding values for meteorite depth and time of remanence acquisition for models using inward core solidification from Nichols et al. (2021). The mean and standard deviation for each depth and time distribution is given in Table 5.6. The percentage of successful runs in which the core is solidifying is given in the top right corner.

which a remanence is generated by a solidifying core increases for younger meteorites. This percentage of model runs increases from 1% for Marjalahti and Brenham to 96% for Esquel, so it is very likely core solidification began sometime between these groups of meteorites recording their remanences (i.e. between ∼170–270 Ma after CAI formation). The absolute uncertainty on the model ages of remanence acquisition for the Main Group pallasites (Table 5.6) is the same order of magnitude as for the ^{40}Ar/^{39}Ar ages of remanence acquisition in the IIE irons.

When meteorite cooling rates and paleomagnetic remanences are recorded, the

Meteorite	Distance from the surface /km	Distance from the CMB / km	Fraction of sucessful runs with remanence recorded during core solidification
Techado	22 ± 3	170 ± 70	0.35
Colomera	26 ± 3	160 ± 70	0.39
Miles	40 ± 5	150 ± 70	0.55

Table 5.5: Mean distance from the surface and distance from the CMB for the IIE irons from the broad parameter space exploration (Figure 5.5). Errors are one standard deviation on the mean.

surrounding mantle is transferring heat by conduction due to the low, subsolidus mantle temperatures at which these processes occur. As a result, the distribution of distances of a meteorite from the surface is tightly clumped, because the cooling rate is controlled by the conductive lengthscale (distance from the surface). In contrast, there is large variability in the distance above the core-mantle boundary (CMB), because the rate of heat transfer into the conductive lid from the convective interior is independent of thickness of the convecting mantle after ^{26}Al has decayed (Chapter 2). Therefore, the distance from a meteorite to the CMB has little effect on its measured cooling rate. The IIE irons have a wider range of possible distances from the CMB compared to the Main Group pallasites because they have a wider range of possible parent body radii and core radius fractions (Figure 5.2). Most Main Group pallasite distances from the CMB are for the dominant radius (400 km) and core radius fraction ($\frac{r_c}{r} = 0.5$). The small peak at $\sim$ 300 km from the CMB are for the small number of runs at the smallest core radius fraction ($\frac{r_c}{r} = 0.3$) and the largest parent body sizes ($r = 500$ km). Gaps in the distribution of possible distances from the CMB in Figures 5.5 and 5.6 are due to the spacing of planetesimal radius and core fractional radius values input into the model.

5.3.2 Key parameter variation

5.3.2.1 Possible interior structures

For the Main Group pallasites, for a given planetesimal radius the range of possible fractional core sizes is very small (left panel, Figure 5.7). This small range of options is in agreement with the narrow distribution of planetesimal radii and fractional core sizes in Figure 5.3. This tight relationship between fractional core radius and planetesimal radius is due to the requirement to have a gap in dynamo generation and match required cooling rates at two temperatures. If the core radius fraction

Meteorite	Distance from the surface /km	Distance from the CMB / km	Time of remanence acquisition / Ma after CAI formation	Fraction of sucessful runs with remanence recorded during core solidification
Marjalahti	38 ± 2	180 ± 50	152 ± 4	0.01
Brenham	42 ± 2	180 ± 50	172 ± 7	0.01
Springwater	51 ± 4	170 ± 50	230 ± 20	0.32
Imilac	60 ± 5	160 ± 50	280 ± 30	0.62
Esquel	68 ± 3	160 ± 50	330 ± 20	0.96

Table 5.6: Mean distance from the surface, distance from the CMB and time of remanence acquisition for the Main Group pallasites from the broad parameter space exploration (Figure 5.6). Errors are one standard deviation on the mean.

is too large, the mantle will cool very quickly, so there will not be a gap in dynamo generation and the cooling rates will exceed those measured in meteorites. Conversely, if the core radius fraction is too small, the core is too small for the second epoch of dynamo generation to start before the onset of core solidification and the gap in dynamo generation is too large to explain the meteorite record.

For the IIE irons, a broader range of planetesimal radii and fractional core radius combinations can explain the parent body's thermal and paleomagnetic history (right panel, Figure 5.7). This is consistent with the wider ranges of these parameters in the broad parameter investigation (Figure 5.2). The broader range of IIE iron parameters is due to the smaller number of paleomagnetically measured IIE irons and no requirement for a gap in dynamo generation.

The range of combinations in Figure 5.7 is not exhaustive. Some planetesimal radii and core radius fractions present in the full parameter exploration (Figures 5.2 and 5.3) are absent in the more detailed parameter exploration (Figure 5.7). This results from all other parameters being held at their modal values in the more detailed parameter exploration, preventing changes in other parameters compensating for changes in fractional core radius or planetesimal radius. Figure 5.7 only indicates that combinations of fractional core radius and planetesimal radius are possible, not that they are probable because variations in other parameters are not accounted for.

5.3.2.2 Parent body water content and oxidation state

There is no relation between water content in NAMs, X_{w}, and fractional core radius, $\frac{r_{\mathrm{c}}}{r}$, for either the IIE irons or the Main Group pallasites (Figure 5.8). All water

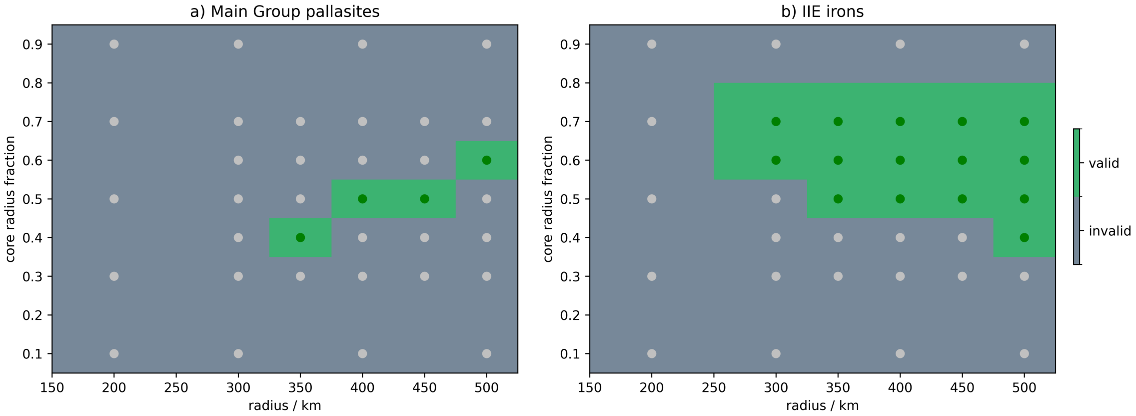

Figure 5.7: Possible combinations of planetesimal radius and core radius fraction for a) the Main Group pallasites and b) the IIE irons. All other parameters were held constant at the modal values in Table 5.4. Green dots indicate planetesimal histories consistent with the meteorite record while grey dots indicate histories inconsistent with the model record. Parameter space was explored more sparsely on the edges of the regime diagram in the initial broad, parameter sweep (Section 5.2.4.1), and was explored in more detail in the second, narrower parameter sweep (Section 5.2.4.2).

contents in NAMs are possible, but as shown in Figures 5.2 and 5.6, the high water contents are highly unlikely. The possible fractional core radii are the same as in Figure 5.7 for each parent body. For the IIE irons, increasing the water content in NAMs lowers the mantle viscosity; this extends the range of fractional core radii in two ways. Firstly, lowering mantle viscosity increases the rate of mantle cooling, which increases the CMB heat flux. This can drive a dynamo in smaller cores, which lowers the possible fractional core radius to 0.3 for $X_\mathrm{w} \geq 0.04\,\mathrm{wt\%}$. Secondly, lower mantle viscosity also delays the cessation of mantle convection, increasing the duration of the first epoch of dynamo generation and enabling larger core sizes ($X_\mathrm{w} = 0.07\,\mathrm{wt\%}$ and $\frac{r_\mathrm{c}}{r} = 0.9$).

5.3.2.3 Initial core sulfur contents

The initial core sulfur content for the Main Group pallasites is restricted to 27–33 wt%, because the Main Group pallasites require a gap in dynamo generation (Figure 5.9). If the core has a sufficiently low initial core sulfur content, it will reach the liquidus and begin solidifying before the end of the first epoch of dynamo generation. The additional buoyancy from core solidification can sustain the dynamo after a decrease in CMB heat flux following the cessation of mantle convection and prevent a gap in dynamo generation (Chapter 2). The IIE irons can have lower initial core sulfur contents (15–33 wt%), because they do not require a gap in dynamo generation. For

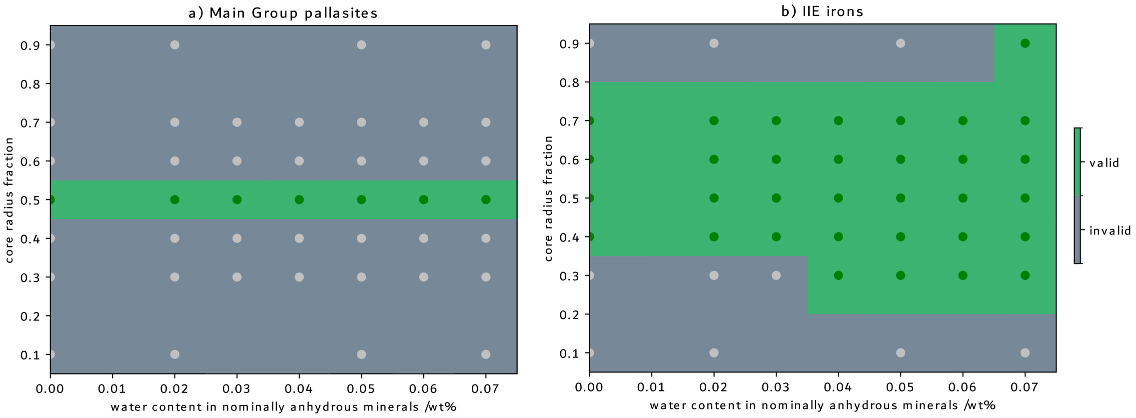

Figure 5.8: Possible combinations of mantle water content in nominally anhydrous minerals (NAMs) and core radius fraction for a) the Main Group pallasites and b) the IIE irons. All other parameters were held constant at the modal values in Table 5.4. Green dots indicate planetesimal histories consistent with the meteorite record while grey dots indicate histories inconsistent with the model record. Parameter space was explored more sparsely on the edges of the regime diagram in the initial broad, parameter sweep (Section 5.2.4.1), and was explored in more detail in the second, narrower parameter sweep (Section 5.2.4.2).

these meteorites, the mantle cooling rate criterion restricts the initial core sulfur contents to $\geq 15\,\mathrm{wt\%}$.

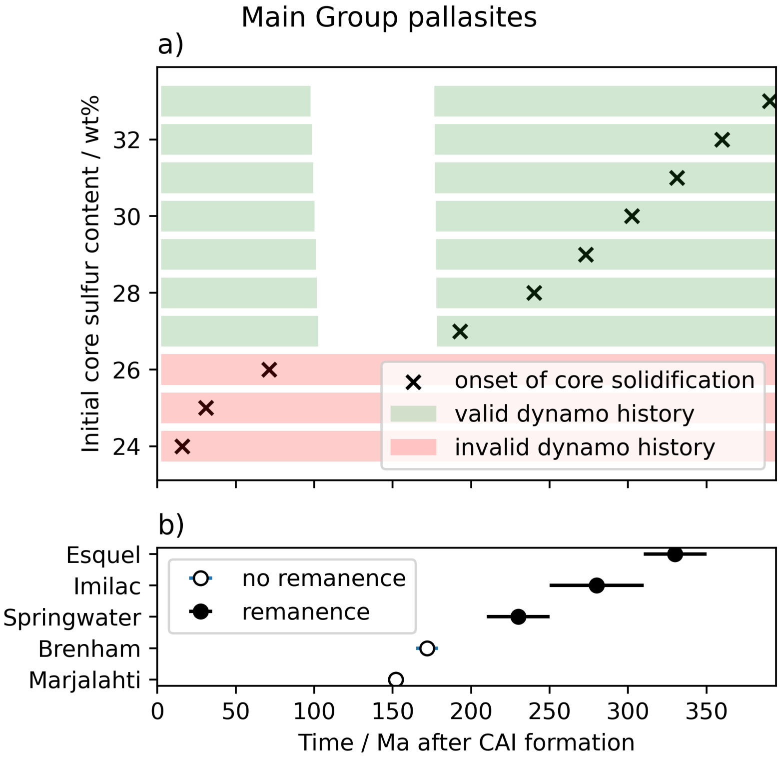

Figure 5.9: a) Dynamo duration as a function of initial core sulfur content for the modal parameters for the Main Group pallasites. Black crosses indicate the onset of core solidification. Green bars indicate planetesimal dynamo histories that are consistent with the meteorite record, while red are those which are inconsistent. b) Mean time of remanence acquisition for each meteorite from Table 5.6, error bars correspond to one standard deviation. The horizontal axis limit is set by the latest time for the onset of core solidification.

5.4 Discussion

Unlike suggestions from previous models, I find that core solidification is not required to generate the paleomagnetic remanences observed in the IIE irons and Main Group pallasites. Both these meteorite parent bodies were likely large (400–500 km radius) with intermediate core sizes (core radius 50% of total radius) and no water in their mantles. Main Group pallasites need higher initial core sulfur contents (> 26 wt%) than the IIE irons (> 15 wt%), because they require models with a gap in dynamo generation.

5.4.1 Constraints on planetesimal properties

The properties of the Main Group pallasites ($< 1\%$ of parameter combinations successful) are more constrained than those of the IIE irons (15% of parameter combinations successful), because there are more meteorites to compare against and their paleomagnetic record has a period without dynamo generation (recorded by two meteorites) followed by a period with dynamo generation (recorded by three meteorites). Models must have a pause in dynamo generation to recreate these paleomagnetic observations. The gap in dynamo generation is a key discriminant, because it requires a precise set of mantle cooling conditions, core sizes, and core compositions for dynamo generation to pause and then restart before the meteorites cool through their blocking temperature. The Main Group pallasites and IIE irons have equal numbers of conditions to apply to each meteorite. Remanence acquisition has been radiometrically dated for the IIE irons, but not for the Main Group pallasites; while the cooling rates at kamacite nucleation have been determined for the Main Group pallasites, but not for the IIE irons. Therefore, knowing the time of remanence acquisition does not provide tighter constraints on the IIE irons.

Together, meteorite paleomagnetism and cooling rates tightly constrain the depth below the surface and the timing of remanence acquisition. The standard deviation on these values is small (2–13%, Tables 5.5 and 5.6) despite the variation in input parameters (Figures 5.2 and 5.3). The distance of each meteorite from the CMB is only constrained to within an order of magnitude, because this distance does not affect the meteorite cooling rate. However, an order of magnitude is still sufficient to determine that meteorites originate from far closer to the surface than the CMB in both parent bodies.

The possible combinations of core radius fraction and planetesimal radius are very restricted for the Main Group pallasites (Figure 5.3 and Figure 5.7a). There are more possible combinations for the IIE irons (Figure 5.7b) but the relative frequency of core radius fractions peaks at intermediate values and planetesimal radius peaks at the largest values (Figure 5.2). Overall, paleomagnetism and meteorite cooling rates can provide insight into the interior structures of these parent bodies, by narrowing the range of possible interior structures to large bodies with similar thickness cores and mantles. Paleomagnetic and cooling-rate measurements of more meteorites or finding a gap in dynamo generation in the IIE irons would help narrow these constraints further (see Section 5.4.6).

Planetesimal viscosity parameters are poorly constrained apart from reference viscosity, which is likely to be high ($\geq 10^{21}$ Pas). This is consistent with the weak effect of all viscosity parameters apart from reference viscosity on dynamo generation (Chapter 3). For the Main Group pallasites, lower bounds on initial core sulfur content can be constrained by the requirement for a gap in dynamo generation. Different initial core sulfur contents could also affect planetesimal magnetic histories by increasing magnetic field strength after the onset of core solidification (Figure 2.10). But if all meteorite remanences are recorded after the onset of core solidification, this increase will not be visible in the relative paleointensity values. The uncertainty on experimental relative paleointensity values may also be larger than a change in model relative paleointensities due to the onset of core solidification. A planetesimal's thermal history is not sensitive to initial core sulfur content because it has a limited effect on mantle cooling rates. This reduces the number of constraints on initial core sulfur content.

5.4.2 Water content of differentiated inner Solar System planetesimals

Both the Main Group pallasites and IIE irons are isotopically non-carbonaceous (NC), meaning they originated in the inner Solar System (Warren, 2011; Rubin, 2018). Therefore, their mantle water contents and fractional core sizes could provide insight into the amount of water present in the NC reservoir when these planetesimals formed and how much water is retained in the mantle during differentiation. I explored differences in the magnetic histories of hypothetical, wet, oxidised and dry, reduced planetesimal endmembers in Chapter 4. In this chapter, I investigated likely water contents and core sizes for two specific meteorite parent bodies while allowing variation in all other input parameters. All mantle water contents are possible for the IIE irons and Main Group pallasites and there is no link between fractional core radius, a measure of oxidation state, and water content (Figure 5.8). However, this narrow parameter exploration only demonstrates possible water content and core size combinations rather than their likelihood. It is most likely that both parent bodies contained no water in their mantles (Figures 5.2 and 5.3). 56% and 29% of successful runs for the Main Group pallasites and IIE irons, respectively, are for planetesimals with completely dry mantles. The predominance of dry mantles is lower for the IIE irons compared to the Main Group pallasites, because of the lack of a gap in dynamo generation. For both bodies the most likely core radius is 50% of the planetesimal radius. This core radius fraction agrees with estimates of core sizes of NC iron meteorite parent bodies (Hilton et al., 2022; Grewal et al., 2024). The likely combination of dry mantles and core radius fraction equal to 0.5 is consistent with the dry planetesimal endmember in Chapter 4. These core sizes suggest some water must have been present in the inner Solar System when these planetesimals accreted, in order to increase their oxidation state relative to nebula gas and form these intermediate size cores (Grewal et al., 2024). The combination of these intermediate core sizes and dry mantles suggests that any water in these planetesimals was degassed very efficiently during differentiation. This agrees with the conclusions in Chapter 4 and with previous measurements of water in nominally anhydrous minerals in meteorites (Newcombe et al., 2023). The agreement between the likely water contents and core sizes of NC planetesimals inferred from these thermal and dynamo generation models and experimental measurements of these properties demonstrates meteorite paleomagnetism is an alternative technique for constraining these properties of meteorite parent bodies.

5.4.3 Comparison with previous studies

The main difference compared to previous studies is that compositional convection from core solidification is no longer required to generate the paleomagnetic remanences in Main Group pallasites and IIE irons. This difference was expected based on the start of the second epoch of dynamo generation prior to the onset of core solidification in Chapter 3. In this detailed study, I have quantified the fraction of model runs for which compositional convection generates the observed remanences. For the IIE irons, 33%, 39% and 55% of successful model runs find that compositional convection contributes to the dynamo during remanence acquisition for Techado, Colomera and Miles, respectively. For the Main Group pallasites, the percentage of sucessful model runs for which a meteorite's remanence records a dynamo contributed to by compositional convection rises from 32% for Springwater to 62% for Imilac and up to 96% for Esquel. For both parent bodies, the range of possible radii and core radius fractions has changed compared to previous studies (Sections 5.4.3.1 and 5.4.3.2). These differences arise both from relaxing the requirement on core solidification and explicitly modelling thermal and compositional dynamo generation.

5.4.3.1 IIE irons

Two studies previously explored properties of the IIE iron parent body using a thermal model with two-stage accretion, mantle conduction and mantle convection (Maurel et al., 2020, 2021). Their model used the timing of core solidification as a proxy for compositional convection and dynamo generation. For a model run to be successful, core solidification had to be ongoing at the ^{40}Ar/^{39}Ar ages of each meteorite. Therefore, the minimum core radius fraction and minimum planetesimal radius were set by the size above which a core would be partially molten at these times, rather than whether these cores were able to generate a dynamo. As a result, their minimum values of core radius fraction (13% for 450 km radius, 19% for 250 km radius) and planetesimal radius (220 km) were lower than in this chapter because these small planetesimals and cores are partially molten but unable to generate a dynamo at the required time.

Based on the mixture of chondritic and achondritic silicate inclusions within the IIE irons, these meteorites are thought to originate from a partially differentiated parent body (Maurel et al., 2020). Therefore, Maurel et al. (2021) imposed an upper limit on core radius fraction of 0.43, based on the metal content of the H chondrites, which are isotopically similar to the chondritic inclusions in the IIE irons. This limit is lower than the modal (0.5) and maximum (0.9) core radius fractions consistent with the meteorite paleomagnetic record. A core radius fraction closer to the modal value could be achieved if the parent body's initial composition was slightly more metal-rich than H chondrites and the body almost completely differentiated. Depending on initial and final accretion time, it is possible for 80–90% of a partially differentiated planetesimal's radius to be fully differentiated (Dodds et al., 2021). To achieve core radius fractions larger than 0.5 requires a fraction of the mantle to be removed by impacts (Asphaug and Reufer, 2014), which is unlikely given the evidence for a chondritic layer at the surface of the IIE parent body. Therefore, core radius fractions of > 0.5 are very unlikely for the IIE parent body despite being consistent with the paleomagnetic record.

5.4.3.2 Main Group pallasites

Nichols et al. (2021) performed the most recent and broadest exploration of possible parent body properties for the Main Group pallasites and was the first study to include paleomagnetic constraints from all five measured meteorites. Nichols et al. (2021) used a thermal evolution and dynamo generation model that included mantle conduction and dynamo generation by core solidification. For outward core solidification, compositional convection was modelled explicitly, while for inward solidification the duration of core solidification was taken as a proxy for dynamo generation. Dynamo generation by thermal convection was not included in the model.

My upper limit on planetesimal radius is larger than Nichols et al. (2021) ($\leq$ 500 km compared to $\leq$360 km, respectively). In Nichols et al. (2021) the upper limit was determined by the maximum radius for which core solidification would begin before Springwater acquired its paleomagnetic remanence. In my model, Springwater's paleomagnetic remanance could record thermal dynamo generation, which allows parent body radii as large as 500 km. Similar to the IIE irons, the lower limit on planetesimal size is larger than previous studies (300 km rather than 200 km; Tarduno et al., 2012; Bryson et al., 2015; Nichols et al., 2021), because these bodies are too small to generate a dynamo when the Main Group pallasites acquired their remanence (Chapter 3).

I demonstrate the Main Group pallasite parent body was likely large (400 km radius) with approximately equal core and mantle thicknesses. In contrast, Nichols et al. (2021) suggested the parent body had a large core ($>$ 200 km radius) and a thin mantle ($<$ 70 km) to produce the strong single crystal olivine paleointensities measured by Tarduno et al. (2012). At a minimum, this corresponds to a core radius fraction of 74%, which exceeds the upper limit on core radius fraction that produces planetesimal histories consistent with the paleomagnetic record in this chapter. These thin-mantled bodies have cooling rates that are too fast and have gaps in dynamo generation that are too wide for the time predicted by the model between Brenham and Springwater acquiring their remanences. The larger mantles (larger parent body radii and smaller core radius fractions) predicted in this chapter increase the depths of the Main Group pallasites and their time of remanence acquisition (Figure 5.6). These larger mantles cool more slowly and so for a given temperature the same cooling rates are reached at deeper mantle depths at later times.

The lower limit on initial core sulfur contents is higher in this paper compared to Nichols et al. (2021), because my model includes the initial epoch of thermal dynamo generation and convective cooling. If the initial core sulfur content is too low, core solidification begins before the cessation of the first epoch of dynamo generation and prevents the gap in dynamo generation required to explain the Main Group pallasite paleomagnetic record.

5.4.4 Formation of the Main Group pallasites

There are two dominant hypotheses for the formation of the Main Group pallasites: ferrovolcanism (Johnson et al., 2020a), and injection of one planetesimal core into another's mantle during an impact (e.g., Yang et al., 2010; Tarduno et al., 2012; Walte et al., 2020; Kruijer et al., 2022). In ferrovolcanism, pockets of sulfur-rich melt within the core become pressurised during core solidification and erupt into the overlying mantle (Johnson et al., 2020a). There are two reasons this is an unlikely formation mechanism for the Main Group pallasites based on the results in this chapter. Firstly, only 1% of successful model runs predicted that core solidification had begun by the time Marjalahti and Brenham cooled through their blocking temperature, which means these pallasites had to form prior to core solidification and possible ferrovolcanism (Table 5.6). Secondly, pallasites formed $> 100\,\mathrm{km}$ from the core mantle boundary. This exceeds the maximum height of a ferrovolcanic intrusion on a planetesimal with modal properties of the Main Group pallasite parent body by over a factor of two (Appendix D.1).

Instead, the paleomagnetic record supports an impact origin for the Main Group pallasites, based on the proximity of the meteorites to the surface ($\leq 80\,\mathrm{km}$ depth). This aligns with multiple strands of evidence that support an impact origin for the Main Group pallasites: isotope disequilibrium between metal and olivine (Windmill et al., 2022; Bennett et al., 2022); comparison between high strain rate deformation experiments and textures within the meteorites (Walte et al., 2020; Walte and Golabek, 2022; Walte et al., 2023); similarities in ^{182}W and Mo isotopes between Main Group pallasites and IIIAB irons suggesting metal was injected from the IIIAB iron parent body (Kruijer et al., 2022); and agreement between thermal modelling of small impact intrusions into the mantle and the observed range of cooling rates (Murphy Quinlan et al., 2023).

Previously, it has been suggested that the Main Group pallasite parent body could be similar to asteroid (16) Psyche (Elkins-Tanton et al., 2020; Johnson et al., 2020a; Walte et al., 2020; Nichols et al., 2021). For initial core sulfur contents consistent with the Main Group pallasite paleomagnetic record ($> 26\,\mathrm{wt\%}$), Psyche's core radius fraction would have to be ≥ 0.9 to be consistent with Psyche's bulk density (Courville et al., 2025). This is much larger than the upper limit on core radius fraction for the

Main Group pallasites suggesting the interior structure of the Main Group pallasite parent body is different to asteroid (16) Psyche.

5.4.5 Limitations

My thermal evolution and dynamo generation model does not include impacts, gradual accretion, or partial differentiation. Impacts probably played significant roles in the formation of the IIE irons (Ruzicka, 2014; Maurel et al., 2020) and Main Group pallasites (e.g., Walte et al., 2020; Kruijer et al., 2022; Murphy Quinlan et al., 2023) and could have affected the post-impact thermal evolution by excavating material from the mantle or depositing regolith on the surface (e.g., Bryson et al., 2015; Walte et al., 2020). However, recent modelling of metal-olivine intrusions within a silicate mantle suggests the range of cooling rates in the Main Group pallasites can be explained by impacts intruding small amounts of material locally without disrupting the mantle's overall thermal structure (Murphy Quinlan et al., 2023). Therefore, it is not necessary to include the thermal effects of impacts when modelling the entire mantle's evolution. Gradual accretion and partial differentiation likely also played a role in the evolution of the IIE irons parent body due to the presence of achondritic and chondritic silicate inclusions within these meteorites (Maurel et al., 2020). These processes also have been suggested to occur in the Main Group pallasite parent body (Walte et al., 2023). As discussed in Chapter 2, neglecting porous, undifferentiated material close to the surface could slightly overestimate surface cooling rates, but should not change the large-scale dynamo behaviour. Partial differentiation can lead to smaller cores, which I have accounted for by exploring a range of core radius fractions.

The range of initial core sulfur contents in the broad parameter space exploration was very narrow (28.7–32 wt%), because the lowest value must be compatible with a broad range of planetesimal sizes, core radius fractions, and water contents in NAMs. This modelling constraint limits our understanding of the relationship between initial core sulfur content and other planetesimal parameters when predicting a consistent planetesimal history for a given meteorite group. In future, an intermediate parameter space exploration could be performed for a smaller range of plantesimal sizes ($r \geq 300\,\mathrm{km}$), core radius fractions ($\frac{r_\mathrm{c}}{r}$ =0.4–0.6) and water contents ($X_\mathrm{w} \leq 0.02\,\mathrm{wt\%}$) but a wider range of initial core sulfur contents.

5.4.6 Future work

For the Main Group pallasites, the key missing experimental constraint is thermochronology. There is no feldspar in the Main Group pallasites (Wasson and Choi, 2003). Therefore, the feldspar ^{40}Ar/^{39}Ar system used to date remanence acquisition in the IIE irons (Bogard et al., 2000) cannot be applied to the Main Group pallasites. ^{53}Mn/^{53}Cr dating has been performed on minor chromite phases (closure temperature $\approx$1300 K) for Brenham but not the other meteorites that have been paleomagnetically measured (Windmill et al., 2022). Relative paleointensity could be another additional constraint for the Main Group pallasites. Improving XPEEM measurements on Marjalahti, Brenham, Imilac, and Esquel from one to three rotations would remove the uncertainty on the direction between the primordial field and the recorded field, reducing the uncertainty on paleointensity and enabling relative paleointensity to be used as a constraint. Paleomagnetic measurements of the Glorieta Mountain and Finmarken meteorites would provide additional time points in the Main Group pallasites paleomagnetic history. Glorieta Mountain has a slower cooling rate (2.5 ± 0.3 K/Ma at 925 K; Yang et al., 2010) and hence deeper formation depth and later remanence acquisition time than Esquel. Therefore, this meteorite could record the end of the dynamo, which would constrain the parent body size. Finmarken has a much faster cooling rate (18.7 ± 1.2 K/Ma at 925 K; Yang et al., 2010), shallower formation depth, and earlier time of remanence acquisition than Marjalahti. As a result, this meteorite could record the first epoch of dynamo generation on the parent body and help determine the width of the gap in dynamo generation. As well as measuring these meteorites paleomagnetically, their cooling rates at 623 K could be calculated using the cloudy zone formation model of Maurel et al. (2019) and their published cloudy zone island sizes (Yang et al., 2010).

For the IIE irons, measuring Ni concentration profiles across kamacite lamellae to calculate cooling rates at kamacite nucleation (925 K) would give another experimental constraint on each meteorite. Unfortunately, there are currently no good candidates for additional paleomagnetic measurements. Out of the IIE irons with measured ^{40}Ar/^{39}Ar ages, Weekeroo Station formed at the same time as Techado, so would not provide additional information; while the ages of Watson and Netschaëvo were reset by an event > 800 Ma after CAI formation (Bogard et al., 2000). Therefore, the first step should be to measure ^{40}Ar/^{39}Ar ages for more IIE irons. Once these ages are obtained, any meteorites younger than Miles should be the first target for paleomagnetic analysis to try find the cessation of dynamo generation.

As well as narrowing constraints on these individual parent bodies, paleomagnetic measurements should be carried out on similar meteorites from different parent bodies. Measurements of the Eagle Station pallasites, which originated from the outer Solar System (Clayton and Mayeda, 1996; Greenwood et al., 2017), could reveal differences in dynamo generation between the inner and outer Solar System. The Sombrerete meteorite formed in a similar way to the IIE irons, but on a different parent body (Bogard et al., 2000). This meteorite cooled through its blocking temperature at 26 Ma after CAI formation, so is likely to record a dynamo if its parent body was large enough to generate one. A paleomagnetic remanence in this meteorite would strengthen the evidence for IIE-like parent bodies having substantial cores. Cloudy zones in two IAB iron meteorites, Toluca and Odessa, have null paleomagnetic remanences (Nichols et al., 2018). Paleomagnetic measurements of two faster cooled IAB irons, Pitts and Carlton (Goldstein et al., 2014), could reveal an earlier period of dynamo generation or confirm that this parent body was too small to generate a dynamo as suggested by Nichols et al. (2018).

5.5 Conclusions

Meteorite paleomagnetism has been used to determine the parent body properties and formation histories of the IIE irons and Main Group pallasites. Previously, these measurements have demonstrated the presence of a core on the IIE parent body and help disprove a possible core-mantle boundary origin of the Main Group pallasites. Combined with cooling rate measurements, paleomagnetic measurements have also been used to constrain the parent body radii, core sizes, and timing of core crystallisation. However, these parent body properties had previously been constrained by assuming the magnetic fields recorded by these meteorites were generated by core solidification. In Chapter 3, I demonstrated that these remanences could record a second epoch of thermal dynamo generation prior to the onset of core solidification. In this chapter, I explored the consequences of this result for the formation histories and parent body properties of the IIE irons and Main Group pallasites.

I used the planetesimal thermal evolution and dynamo generation model of Chapter 2 to calculate planetesimal thermal and dynamo histories over a wide range of input parameters. Then, I compared model outputs to paleomagnetic data, metallographic cooling rates and radiometric ages to determine possible values of parent body properties, including planetesimal size, core radius, and mantle viscosity. I also estimated each meteorite's formation depth (and timing of remanence acquisition for the Main Group pallasites). This has revealed the following insights about these two parent bodies:

- Core solidification is no longer a requirement for producing any of the observed paleomagnetic remanences. The percentage of successful model runs which predicted that an individual meteorite recorded a remanence generated by core solidification varies between 35–55% and 32–96% for the IIE irons and Main Group pallasites, respectively.
- The Main Group pallasite and IIE iron parent bodies were likely large ($\geq$400 km radius) with approximately equal core and mantle thicknesses.
- The Main Group pallasite parent body had a high initial core sulfur content (>26 wt%) in order to produce a gap in dynamo generation, whereas for the IIE iron parent body initial core sulfur contents could have been as low as 15 wt%.
- The possible combinations of planetesimal radius and core radius fraction are very limited for the Main Group pallasites because of the gap in dynamo generation in their paleomagnetic record.
- The Main Group pallasites formed $\leq$ 80 km below the surface and $\gtrsim$150 km from the CMB. This suggests these meteorites formed by impacts rather than ferrovolcanism.
- The paleomagnetic records of the Main Group pallasites and the IIE irons support efficient degassing of water during planetesimal differentiation and are consistent with their formation in the NC reservoir.

Despite removing the requirement for core crystallisation, meteorite paleomagnetism can shed light on the parent body properties of both these meteorite groups. Both meteorite parent bodies were large, with roughly equal core and mantle thicknesses, long-lived dynamo generation, and extended core crystallisation. Overall, combining meteorite paleomagnetism with thermal evolution and dynamo generation models can provide valuable insights into the long-term evolution of differentiated planetesimals and metal-silicate mixing on these bodies.

Chapter 6

Conclusions

I have developed a refined planetesimal thermal evolution and dynamo generation model that includes: a new description of core solidification; a more realistic description of mantle viscosity and mantle convection; and a unified description of dynamo generation by thermal and compositional convection (Chapter 2). My model can predict a complete magnetic field generation history for a planetesimal for a wide range of planetesimal parameters. In the subsequent chapters, I utilised this model to answer the four questions outlined in Chapter 1, and described below.

6.1 Key questions

What are the effects of mantle heat transfer and core composition on planetesimal dynamo generation? In Chapter 3, I explored the effect of mantle viscosity, core ^{60}Fe abundance, initial core sulfur content, and planetesimal size on dynamo generation. Variations in the mantle viscosity law, particularly changes in reference viscosity, lead to a wide range in dynamo generation timings. If the mantle has a low viscosity, mantle convection is very vigorous and the transition from mantle convection to mantle conduction is delayed. Vigorous and prolonged mantle convection rapidly cools the core, bringing forward the onset of core solidification and shortening the duration of the dynamo. In contrast, if the mantle is very viscous, the mantle transitions from convection to conduction earlier. This brings forward the temporary decrease in CMB heat flux caused by the cessation of mantle convection, widening the gap between the two epochs of dynamo generation. Increasing core ^{60}Fe abundance brings forward the onset of thermal dynamo generation, because it provides a heat source in the core to erode core thermal stratification. Decreasing initial core sulfur content raises the core liquidus and brings forward the onset of core solidification. This can prevent a gap in dynamo generation.

Are previous interpretations of the meteorite paleomagnetic record still valid when mantle viscosity, core composition and compositional dynamo generation are properly accounted for? The thermal evolution and dynamo generation model developed in Chapter 2 and the parameter space exploration presented in Chapter 3 reveal three key changes in behaviour that affect the interpretations of the meteorite record presented in current literature. Firstly, inclusion of ^{60}Fe in the core brings forward the onset of thermal dynamo generation, such that dynamo-generated fields overlap with the existence of the nebula field. The early onset of thermal dynamos casts doubt on the origin of bulk remanences <5 Ma after CAI formation and means that non-unidirectional remanences in pristine chondrules are the most reliable recorders of the nebula field. Secondly, variations in planetesimal radius and mantle viscosity increase the duration of the first epoch of dynamo generation compared to previous models. Thirdly, the second epoch of dynamo generation can begin before the onset of core solidification. Altogether, there is a wider range in dynamo timings and durations than previously predicted and the meteorite paleomagnetic record therefore cannot be split into three distinct epochs of magnetic field generation (i.e., nebula field, thermal dynamos, and compositional dynamos). The change in timing of thermal and compositional dynamo generation mean that paleomagnetic remanences >65 Ma after CAI formation are not necessarily signatures of solidifying planetesimal cores and the properties of parent bodies based on this assumption need to be re-evaluated (see Chapter 5).

Could meteorite paleomagnetism reveal differences in water content and oxidation state between NC and CC planetesimals? Depending on the distribution of water in the early Solar System and the trigger for planetesimal formation, NC and CC differentiated planetesimals could have formed with different mantle water contents and core sizes. In Chapter 4, I explored differences in dynamo generation arising from differences in formation conditions using two endmembers: wet and oxidised (possibly CC-like), and dry and reduced (possibly NC-like). I found that wet, oxidised planetesimals generate shorter and weaker fields than dry, reduced planetesimals due to their lower mantle solidii and smaller core sizes. So, the NC and CC paleomagnetic records could differ considerably if NC and CC planetesimals formed in different conditions and retained different amounts of water during differentiation. The starkest contrast in dynamo behaviour between endmembers, regardless of size, occurs >50 Ma after CAI formation. Therefore, paleomagnetic remanences from this time period would provide the most insight about differences between these planetesimal populations. Only measurements from NC meteorites have been made in this time window, but these results demonstrate that measurements of relatively young CC achondrites should be a priority. Existing NC paleomagnetic remanences >50 Ma after CAI formation are consistent with the magnetic field histories of the dry, reduced endmember. This suggests NC planetesimals degassed water efficiently during differentiation and have reasonably large cores.

What can a time-resolved paleomagnetic record tell us about the size, structure, and composition of a meteorite parent body? In Chapter 5, I demonstrated that time-resolved paleomagnetic records can shed light on the internal structures of meteorite parent bodies and the formation of stony-iron meteorites. The meteorite paleomagnetic remanences and metallographic cooling rates recovered for the Main Group pallasites and IIE irons can constrain properties of their parent bodies. For both meteorite groups, their time-resolved records tell us these parent bodies were likely large planetesimals (400–500 km in radius) with approximately equal mantle and cores thicknesses. These records also suggest both parent bodies retained very little water after differentiation based on their ability to generate a long-lived dynamo. These meteorites are predicted to form at shallow depths, far from the CMB, on both parent bodies. As a result, these meteorites more likely originate from impacts rather than ferrovolcanism. Comparison between the Main Group pallasite and IIE iron records indicate that a gap in dynamo generation is key for tightly constraining the mantle viscosity and initial core sulfur content.

6.2 Future Work

6.2.1 Suggested meteorite paleomagnetic measurements

The conclusions of my thesis allow me to suggest targets for future paleomagnetic measurements that could deepen our understanding of the following topics:

- **Heterogeneity of ^{60}Fe/^{56}Fe in the early Solar System.** The delayed dynamo onset in the angrite paleomagnetic record suggests low abundances of ^{60}Fe (^{60}Fe/^{56}Fe $\leq 10^{-9}$) in the NC reservoir. Measurement of CC achondrites that could have recorded a remanence 5–10 Ma after CAI formation (e.g., NWA 2976 and NWA 6704; Bouvier et al., 2011; Sanborn et al., 2019) could test whether the abundance of ^{60}Fe was similar in the CC reservoir. If these ancient CC achondrites were from parent bodies large enough to generate a dynamo but are unmagnetised, then this would argue for homogenous ^{60}Fe/^{56}Fe throughout the Solar System. If these ancient CC achondrites do record a paleomagnetic remanence, then this would imply the abundance of ^{60}Fe in the CC reservoir was higher than in the NC reservoir.

- **Differences between NC and CC differentiated planetesimals.** There are currently no paleomagnetic measurements on young (>50 Ma after CAI formation) CC achondrites to compare to the endmember models in Chapter 4. Work is ongoing to measure the Eagle Station pallasites (Fish pers. comm.). These meteorites are the CC analogues of the Main Group pallasites, and would enable direct comparison between similar NC and CC planetesimals. There are no grouped CC rocky achondrites (Krot et al., 2014), but the large number of ungrouped CC rocky achondrites provides an opportunity to survey a wide range of meteorite parent bodies (Spitzer et al., 2025). If these meteorites have strong paleointensities, this would suggest that CC differentiated planetesimals formed in similar conditions to NC differentiated planetesimals, resulting in similar size cores, and that all differentiated planetesimals retained little water in their mantles. If these meteorites have weak paleointensities, then it would imply that CC planetesimals formed in more oxidising conditions than NC planetesimals, resulting in smaller cores, and retained more water during differentiation.
- **Properties of the Main Group pallasite parent body** There are two promising meteorites for further improving our constraints on the Main Group pallasite parent body. Finmarken is a very rapidly cooled Main Group pallasite and could record the first epoch of dynamo generation. Determining the duration of the gap in dynamo generation would improve our estimates of mantle viscosity, which could be applied in all thermal evolution models for planetesimals. Glorieta Mountain is a very slowly cooled Main Group pallasite and could record the end of the dynamo. Knowing the dynamo end time would narrow the range of possible parent body sizes.

6.2.2 Further improvements to thermal evolution and dynamo generation models

The model developed in this thesis focussed on refining the description of mantle convection and compositional dynamo generation. Therefore, the descriptions of gradual accretion and partial differentiation included in previous models were omitted (see discussion in Chapter 2). In the future, this model could be extended to include these processes, which would enable more accurate modelling of partially differentiated planetesimals. This would be useful for applying the refined descriptions of mantle convection and dynamo generation to the paleomagnetic histories of the H and L/LL chondrites (Shah et al., 2017; Bryson et al., 2019b). Additionally, it would allow dynamo generation on partially differentiated parent bodies to be explored as a source of bulk chondritic remanences from $< 5\,\mathrm{Ma}$ after CAI formation that are no longer guaranteed to record the nebula field (e.g., CM chondrites Cournede et al., 2015; Bryson et al., 2023).

No thermal evolution and dynamo generation models have included the effects of impacts, despite their likely influence on the histories of dynamo generating bodies (Elkins-Tanton et al., 2011; Sterenborg and Crowley, 2012; Bryson et al., 2019a; Dodds et al., 2021). Instead, separate impact modelling has been done alongside thermal evolution models (Maurel et al., 2020; Murphy Quinlan et al., 2023; Cambioni et al., 2024). However, thermal disturbances from impacts could directly influence dynamo generation. Impacts could strip the outer layers of a planetesimal and enhance mantle cooling, or could inject material into the mantle and add a heat source. It would be instructive to implement simple descriptions of these processes within a thermal evolution model to explore their effects on dynamo generation. Results from hydrodynamic impact simulations could be used to estimate the initial conditions to input into these models.

6.2.3 Poorly understood processes in planetesimal evolution

Planetesimal core solidification and differentiation are challenging processes to understand and have big implications for planetesimal thermal evolution and dynamo generation. The direction and mechanism of planetesimal core solidification determines whether compositional dynamo generation is possible (Scheinberg et al., 2016; Dodds et al., 2025). The direction of planetesimal core solidification depends strongly on the core's thermal expansivity and the pressure dependence of the liquidus, both of which are poorly constrained (Dodds et al., 2025; Williams, 2025). Therefore, more research into the properties of metal alloys at pressures and temperatures appropriate for planetesimals is needed. In this thesis, I developed a general parametrisation for core solidification, because the exact solidification mechanism is unknown. Analogue tank experiments could shed light on possible solidification mechanisms (e.g., Dodds, 2022). Mathematical descriptions of fluid behaviour observed in these experiments could be incorporated into thermal evolution models to explore its ability to drive a dynamo.

Planetesimal differentiation creates a planetesimal's core and sets the conditions for subsequent thermal evolution. It is currently unclear how differentiation affects initial core composition. In the differentiation via rain-out model adopted in this thesis, the sulfur contents of metal alloys that can be melted during differentiation are higher than the sulfur contents of iron meteorites. This results from the onset of convection limiting planetesimal peak temperatures (Section 2.4.4.1). Extremal planetesimal mantle parameters (a high critical melt fraction and a low mantle solidus) must be assumed to differentiate Fe-FeS compositions that match the most sulfur-poor iron meteorites (Section 4.4.3.3). Models for differentiation via percolation (Neumann et al., 2012; Lichtenberg et al., 2019b; Monnereau et al., 2023) are not limited in their initial core sulfur contents because they neglect convection below the critical melt fraction, so can reach higher temperatures. More research is needed to clarify the significance of convection during differentiation and whether it truly limits planetesimal peak temperatures and initial core sulfur contents. For example, models for differentiation via percolation could be adapted to allow for the onset of convection at lower melt fractions. Other differentiation mechanisms, such as differentiation via compaction (Néri et al., 2021), could also be explored. Better constraining initial core sulfur contents will improve our understanding of the timing of core solidification and compositional dynamo generation.

It is also uncertain whether material be removed from the core after differentiation, altering core composition. Both fluid immiscibility (Bercovici et al., 2022; Bromiley et al., 2024) and eruptions of core material into the mantle due to excess pressure during core solidification (ferrovolcanism; Abrahams and Nimmo, 2019; Johnson et al., 2020b; Courville et al., 2025) have been hypothesised to remove light elements from planetesimal cores. Depending on the volume of material removed, both processes could rapidly lower the core sulfur content, accelerating core solidification and shortening the duration of a compositional dynamo. Two-phase dynamical models of these processes could be developed and combined with existing geochemical models (e.g., Chabot and Drake, 2000; Corgne et al., 2008; Bromiley et al., 2024) to quantify the rate at which material is removed from the core. Upcoming observations of the metal-rich asteroid (16) Psyche could also enhance our understanding of ferrovolcanism (Elkins-Tanton et al., 2020; Dibb et al., 2024). Psyche's high density suggests it could be a differentiated body with a large core radius fraction and there appear to be iron sulfide patches on Psyche's surface. Spacecraft observations will help determine whether these patches originated in the core, possibly providing the first planetesimal-scale evidence for ferrovolcanism.

6.3 Summary

Studies of magnetic fields provide unique insights into the thermal history and composition of rocky bodies in the Solar System. In this thesis, I wrote and employed a refined thermal evolution and dynamo generation model to re-interpret the meteorite paleomagnetic record and shed light on the interior structures and evolution of differentiated planetesimals, and the composition of the protoplanetary disk. The combination of numerical modelling and meteorite paleomagnetic and thermal history measurements can provide a wealth of information about large-scale Solar System processes and individual meteorite parent bodies. Current measurements constrain the duration of the nebula field and the formation mechanisms of stony-iron meteorites, while future measurements could shed light on differences in water content and ^{60}Fe abundance between the inner and outer Solar System. Overall, this thesis has deepened our understanding of the evolution of planetary building blocks and demonstrated the potential of meteorite paleomagnetism combined with thermal modelling to reveal further insights about the protoplanetary disk in which they formed.

Appendix A

Supplementary Information for Chapter 2

A.1 Mantle boundary layer parametrisations

The boundary layer thicknesses in my model were chosen to ensure they are self consistent with the mode of mantle heating (conduction vs convection), the chosen rheology, and adjust as the constants in the viscosity law change. In order to fulfil these requirements, the scaling laws I use have been derived from 2D and 3D simulations (Thiriet et al., 2019; Deschamps and Vilella, 2021).

A.1.1 Theoretical background

A stagnant lid system occurs where there is a viscosity contrast $> 10^4$ between the surface and the convecting interior (Solomatov, 1995; Deschamps and Vilella, 2021). In this system, there is a fully convective, isothermal interior with temperature T_{m}, surface temperature T_{s}, and an approximately linear temperature gradient across a stagnant lid, δ_0, with temperature difference $\Delta T = T_{\mathrm{m}} - T_{\mathrm{s}}$ (Figure A.1). The lid is so thick and the viscosity contrast is so large that only the layer at the base of the lid, with thickness δ_{eff}, is mobile with an effective temperature difference across this layer of ΔT_{eff} (assuming a linear temperature profile through the lid). The lid is assumed to become too viscous to participate in convection after a factor of e increase in viscosity, which sets the ratios of lengthscales of the mobile and stagnant layers (Solomatov, 1995).

$$\frac{\delta_{\mathrm{eff}}}{\delta_0} = \frac{1}{f_{\mathrm{rh}}} = -\frac{\eta(T_{\mathrm{m}})}{(d\eta/dT)(T_{\mathrm{m}})\Delta T}, \tag{A.1}$$

where η is the viscosity. $1/f_{\mathrm{rh}}$ parametrises the proportion of ΔT which controls convection ($\Delta T_{\mathrm{eff}} = \frac{\Delta T}{f_{\mathrm{rh}}}$; Michaut and Neufeld, 2022).

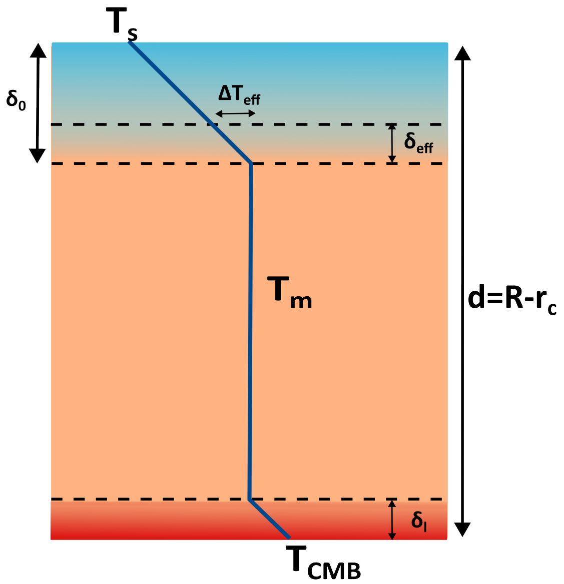

Figure A.1: Schematic of a stagnant lid convecting system. The blue line indicates the temperature profile in the interior and temperature increases to the right. δ_0 and δ_l are the stagnant lid and CMB boundary layer thicknesses, respectively. δ_{eff} is the mobile portion of the stagnant lid.

Analytical derivations of stagnant lid thickness are based on the stability of the boundary layer (Howard, 1966). They calculate δ_{eff} for which the mobile layer's Rayleigh number becomes supercritical and the mobile layer becomes convectively unstable. This is then related to δ_0 using Equation A.1. The thickness of the overall stagnant lid is directly related to the change in viscosity with temperature and choice of constants in the viscosity law (Equation 2.1). The stagnant lid parametrisation must be consistent with choice of viscosity law and adjust to changes in viscosity parameters. Additionally, scaling laws based on this analysis must be appropriate for the relevant heating modes and boundary conditions.

A.1.2 Stagnant lid thickness

Stagnant lid scaling laws can be obtained analytically using the approach outlined above (e.g., Solomatov, 1995) or empirically from 2D or 3D numerical models (e.g., Deschamps and Vilella, 2021). The chosen scaling law should match the boundary conditions (heat flux and tractions on the top and bottom boundaries), rheology (e.g. isoviscous, exponential viscosity), and presence/absence of internal heating. Parametrisations for systems with purely internal heating, or purely basal heating are well established (Ferrick and Korenaga, 2023). However, planetesimals have internal heating (from radioactive decay), variable heat flux on the top (surface) and bottom (CMB) boundaries, and temperature dependent viscosity, which is more complicated to parametrise (Ferrick and Korenaga, 2023). Previous planetesimal models have employed variations of the stagnant lid scaling from Solomatov (1995) for a system with fixed top and bottom boundary temperatures, Newtonian viscosity, and no internal heating. Here, I have chosen to use the empirical stagnant lid scaling from Deschamps and Vilella (2021) because it has been derived for mixed heating (basal and surface heat fluxes and internal heating) and a temperature dependent viscosity, and is therefore closer to the mantle convection conditions in planetesimals. The functional form from Deschamps and Vilella (2021), which is expressed as $\delta_0 \propto d f_{\mathrm{rh}}^{1.21} Ra^{-0.27}$ is similar to the analytical boundary layer form $\delta_0 \propto d f_{\mathrm{rh}}^{\frac{4}{3}} Ra^{-\frac{1}{3}}$, but with slight adjustments to the exponents and derivation of constants of proportionality from numerical simulations.

Recently, Ferrick and Korenaga (2023) have developed an analytical scaling law for mixed heating systems with constants determined from numerical simulations. Their new, more complicated scaling laws agree well with numerical simulations and previous scaling laws based on boundary layer stability analysis. Since they conclude previous boundary layer stability scaling laws for convection with mixed heating are valid, I have chosen to utilise the approach of Deschamps and Vilella (2021) because it is simpler to implement.

A.1.2.1 Location of the mobile boundary layer

The formalism described above is one of two methods for describing stagnant lid growth. The first, adopted in my model, describes the growth of the entire lid using a scaling law and the mobile boundary layer at the base of the lid is included in the lid thickness. Models which use this approach include Solomatov (1995); Nimmo and Stevenson (2000); Deschamps and Vilella (2021) and Dodds et al. (2021). The second approach is to use a scaling law to determine the mobile boundary layer thickness and energy conservation at the base of the lithosphere to determine overall lid thickness (e.g., Spohn, 1991; Grott and Breuer, 2008; Michaut and Neufeld, 2022). The second approach allows for processes in the lid, such as crust production to be resolved (e.g., Morschhauser et al., 2011). However, crustal processes are below the resolution of my model so for simplicity I adopt the first formalism. In both formalisms, the heat flux out of the convecting region is determined by the temperature gradient at the boundary between the convecting interior and conductive boundary layer (full lid or mobile boundary layer). Therefore, for stagnant lids of similar thicknesses, the two formalisms should give similar results. Differences in overall lid thickness at a given time for the same initial conditions for the two formalisms has not been studied but could be explored in future work.

A.1.3 Nusselt number and cessation criterion

An additional justification for my convection cessation criterion comes from considering the Nusselt number, Nu, which is the ratio of convective to conductive heat flux out of a convecting system. These heat fluxes can be approximated using the temperature difference across the mantle and the lengthscale for the temperature change in the two scenarios to give the following expression

$$Nu = \frac{F_{\mathrm{conv}}}{F_{\mathrm{cond}}} \approx \frac{\frac{k_{\mathrm{m}}\Delta T}{\delta_l+\delta_0}}{\frac{k_{\mathrm{m}}\Delta T}{R-r_{\mathrm{c}}}} = \frac{R-r_{\mathrm{c}}}{\delta_l+\delta_0}. \tag{A.2}$$

When the combined CMB boundary layer thickness and stagnant lid thickness, $\delta_l+\delta_0$, is equal to the mantle thickness, $R-r_{\mathrm{c}}$, then $Nu=1$. The Nusselt number can also be written in terms of the Rayleigh number $Nu \sim \left(\frac{Ra}{Ra_c}\right)^n$ where n is a constant. Therefore, $Nu = 1$ implies $Ra = Ra_c$ and the system is marginally stable. Using boundary layer thicknesses gives a different time for cessation of convection than the criterion $Ra < Ra_c$ because Equation A.2 is an approximation.

A.2 Increase in ^{26}Al in the mantle during differentiation

Upon differentiation, all the iron in the planetesimal is assumed to go into the core and all the aluminium is assumed to stay in the mantle. The asteroid's initial sulfur content is assumed to partition between the core and mantle to give the desired core sulfur content, X_{S}, but the initial sulfur content of the body is not prescribed and the sulfur content of the mantle and undifferentiated body are not tracked. These assumptions can then be used to calculate the new iron and aluminium abundances of the core and mantle, respectively. The core is assumed to be purely iron and sulfur, so the abundance of iron in the core in wt % is given by

$$X_{\mathrm{Fe,c}} = 100 - X_{\mathrm{S}}, \tag{A.3}$$

where X_{S} is the core sulfur content in wt %, which is specified at the beginning of the model. All aluminium is assumed to remain in the mantle, so by mass conservation the abundance of aluminium in the mantle is given by

$$X_{\mathrm{Al,m}} = \frac{\rho_{\mathrm{ch}} V}{\rho_{\mathrm{m}} V_{\mathrm{m}}} X_{\mathrm{Al,ch}} = \frac{\rho_{\mathrm{ch}} R^3}{\rho_{\mathrm{m}}(R^3 - r_{\mathrm{c}}^3)} X_{\mathrm{Al,ch}} \tag{A.4}$$

A.3 Core

A.3.1 Derivation of core buoyancy flux equation

From equations A8 and A14 in Buffett et al. (1996), an approximation for the dissipation in the core is

$$\Phi = \frac{\alpha_{\mathrm{c}} Q^*_{\mathrm{CMB}}}{c_{p,c}} [\psi(r_{\mathrm{c}}) - \bar{\psi}] + 4\pi r_i^2 \frac{\mathrm{d}r_i}{\mathrm{d}t} \left(\Delta\rho + \frac{\alpha_{\mathrm{c}} \rho_{\mathrm{c}} L_{\mathrm{c}}}{c_{p,c}} \right) [\bar{\psi} - \psi(r_i)], \tag{A.5}$$

where $Q^*_{\mathrm{CMB}} = Q_{\mathrm{CMB}} - Q_{\mathrm{ad}}$ is the difference between the total CMB heat flux and adiabatic flux; ψ is the gravitational potential evaluated at the CMB or solidification front, $r = r_i$; and $\bar{\psi}$ is the mass-averaged gravitational potential in the liquid portion of the core. During core solidification, the region above the solidification front is solid and does not contribute entropy to drive the dynamo. Therefore, I calculate the first term in Equation A.5 at the top of the liquid inner core (dynamo region), $r = r_i$. Before core solidification, $r_i = r_{\mathrm{c}}$. This simplifies the change in gravitational potential and the dissipation in the core becomes

$$\Phi = (F_{\mathrm{T}} + F_{\mathrm{c}})\Delta\psi = \left[\frac{\alpha_{\mathrm{c}} Q^*_{r_i}}{c_{p,c}} - 4\pi r_i^2 \frac{\mathrm{d}r_i}{\mathrm{d}t} \left(\Delta\rho + \frac{\alpha_{\mathrm{c}} \rho_{\mathrm{c}} L_{\mathrm{c}}}{c_{p,c}} \right) \right] (\psi(r_i) - \bar{\psi}), \tag{A.6}$$

where $Q^*_{r_i} = Q_{r_i} - Q_{\mathrm{ad}}$ is the superadiabatic heat flux at the boundary between the solid outer and liquid inner core and F_{T} and F_{c} are the thermal and compositional buoyancy fluxes, respectively (Rückriemen et al., 2015). The combined buoyancy flux, $Q_b = F_{\mathrm{T}} + F_{\mathrm{c}}$ is inside Equation A.6. Using $Q^*_{r_i} = 4\pi r_i^2 (F_{r_i} - F_{\mathrm{ad}}) = (-k_{\mathrm{c}} \frac{\mathrm{d}T}{\mathrm{d}r}\big|_{r_i} - \frac{\alpha_{\mathrm{c}} g(r_i) k_{\mathrm{c}}}{c_{p,c}} T(r_i))$ gives

$$Q_b = 4\pi r_i^2 \left[\frac{\alpha_{\mathrm{c}} k_{\mathrm{c}}}{c_{p,c}} \left(-\frac{\mathrm{d}T}{\mathrm{d}r}\bigg|_{r_i} - \frac{\alpha_{\mathrm{c}} g(r_i)}{c_{p,c}} T(r_i) \right) - \left(\frac{\alpha_{\mathrm{c}} \rho_{\mathrm{c}} L_{\mathrm{c}}}{c_{p,c}} + \Delta\rho \right) \frac{\mathrm{d}r_i}{\mathrm{d}t} \right]. \tag{A.7}$$

Equation A.5 neglects compositional diffusion and assumes compositional fluxes are mixed evenly into the liquid portion of the core rather than assuming the combination of compositional fluxes and entropy are evenly mixed (Lister, 2003). This well-mixed approximation means the latent heat released at the upper boundary of the dynamo generation region during core solidification can contribute entropy to drive the dynamo. This introduces the same amount of error as the Boussinesq approximation (Lister, 2003), so for my model this approximation is acceptable.

For a constant density core and a solidified outer layer only ($m_{\mathrm{frac}}= 0$), the flux-based Rayleigh number approximation to the convective power used by my model is equivalent to calculating the convective power directly. The convective power, p, is related to the Ohmic dissipation, Φ, by

$$p = \frac{\Phi}{\rho_{\mathrm{c}}\Omega^3 l^2 V}, \tag{A.8}$$

where V is the volume of the convecting region (Aubert et al., 2009). For a constant density core $\psi(r_i) = \frac{r_i g_i}{2}$ and $\bar{\psi} = \frac{3 r_i g_i}{10}$ (denoting the outer convecting boundary by r_i rather than r_o and setting the radius of the inner convecting boundary to 0 in Equation 16 in Aubert et al., 2009). Combining the expressions for $\psi(r_i)$ and $\bar{\psi}$ with Equation A.6,

$$\Phi = \frac{Q_b r_i g_i}{5}. \tag{A.9}$$

Substituting Equation A.9, the volume of the convecting core and $r_i = l$ into Equation A.8 gives

$$\begin{aligned} p &= \frac{g_i r_i Q_b}{5\rho\Omega^3 r_i^2 V} \\ &= \frac{3}{5}\frac{g_i Q_b}{4\pi\rho\Omega^3 l^4} = \gamma Ra_Q, \end{aligned} \tag{A.10}$$

which is equivalent to Equation 2.36.

A.3.2 GPE release during core solidification

During core solidification, the heat across the CMB, Q_{CMB}, is balanced by radiogenic heating, Q_{R}, secular cooling, Q_{S}, latent heat release, Q_{L}, and release of gravitational potential energy, Q_{G},

$$Q_{\mathrm{CMB}} = Q_{\mathrm{R}} + Q_{\mathrm{S}} + Q_{\mathrm{L}} + Q_{\mathrm{G}}. \tag{A.11}$$

Substituting for each term following Nimmo (2007)

$$\begin{aligned} F_{\mathrm{CMB}} A_{\mathrm{CMB}} &= M_{\mathrm{c}} H - M_{\mathrm{c}} c_{p,\mathrm{c}} \frac{dT_{\mathrm{c}}}{dt} - 4\pi r_i^2 \rho_{\mathrm{l}} L \frac{dr_i}{dt} + \frac{8}{3}\pi^2 G \rho_{\mathrm{c}} \Delta\rho r_i^4 \frac{dr_i}{dt} \\ &= M_{\mathrm{c}} H + \left[-M_{\mathrm{c}} c_{p,\mathrm{c}} + \frac{4\pi r_i^2 L_{\mathrm{c}}}{g_{\mathrm{c}} \frac{dT_{\mathrm{l}}}{dP}} + \frac{32}{15}\pi^2 G \frac{\Delta\rho r_i^4}{g_c \frac{dT_{\mathrm{l}}}{dP}} \right] \frac{dT_{\mathrm{c}}}{dt}, \end{aligned} \tag{A.12}$$

where M_{c} is the mass of the core; H is the radiogenic heating from ^{60}Fe; $c_{p,\mathrm{c}}$ is the core specific heat capacity; r_i is the boundary between the solid outer and liquid inner

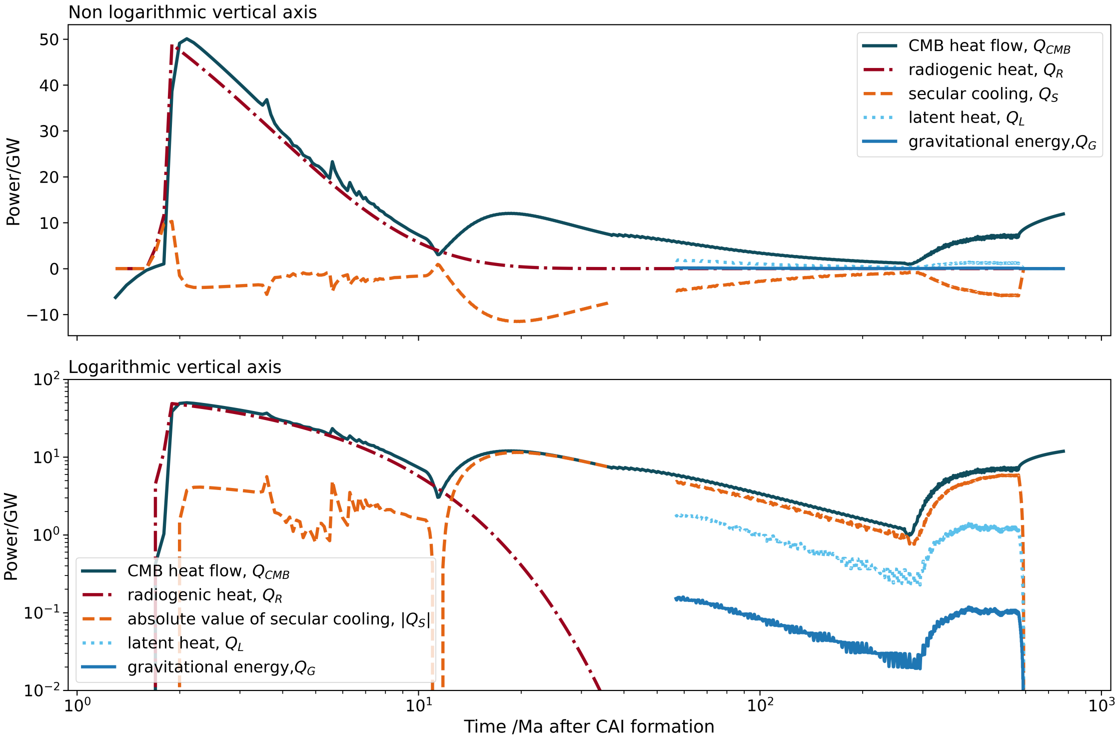

Figure A.2: Power sources in the core for a 500 km radius planetesimal, with a 250 km radius core, accreted at 0.8 Ma after CAI formation with $^{60}\mathrm{Fe}/^{56}\mathrm{Fe} = 10^{-8}$ and $X_{\mathrm{S},0} = 29.85\,\mathrm{wt\%}$. The lower panel shows the same sources as the upper panel, but with a logarithmic vertical axis so that the gravitational contribution, Q_{G}, can be seen. The absolute value of the secular cooling is plotted on the logarithmic axis to enable the values to be log-scaled. Due to the discrete nature of the model, Q_{G}, Q_{L} and Q_{S} oscillate during core solidification and are plotted as a rolling average over 200 output steps (20 Ma). The small gap between the purely thermally driven dynamo and the average values for the thermo-compositional dynamo is due to the lag in the rolling average. The power contribution of gravitational energy release during solidification is two orders of magnitude smaller than other contributions and can be neglected in the thermal evolution of the core.

core; L_{c} is the core's latent heat; g_{c} is the gravitational field strength at the CMB; ρ_{c} is the core density; $\frac{dT_{\mathrm{l}}}{dP}$ is the pressure derivative of the Fe-FeS liquidus; $\Delta\rho$ is the density difference between solidified iron and the liquid inner core; and T_{c} is the core temperature. This can then be rearranged to give an expression for $\frac{dT_{\mathrm{c}}}{dt}$

$$\frac{dT_{\mathrm{c}}}{dt} = \frac{Q_{\mathrm{CMB}} - Q_{\mathrm{R}}}{Q_{\mathrm{ST}} + Q_{\mathrm{LT}} + Q_{\mathrm{GT}}}, \tag{A.13}$$

where Q_{ST} etc. denotes the relevant heat terms divided by $\frac{dT_{\mathrm{c}}}{dT}$. Including Q_{G} in the expression for core cooling during core solidification does not change the core solidification time within the resolution of the model.

A.3.3 Core density

The central pressure in a planetesimal is low enough (2 MPa to 50 MPa) that there is little difference in density compared to ambient pressure (Fig. 10 from Morard et al., 2018), so no correction was made for the pressure difference.

A.3.4 Core liquidus — rebuttal to Williams (2025)

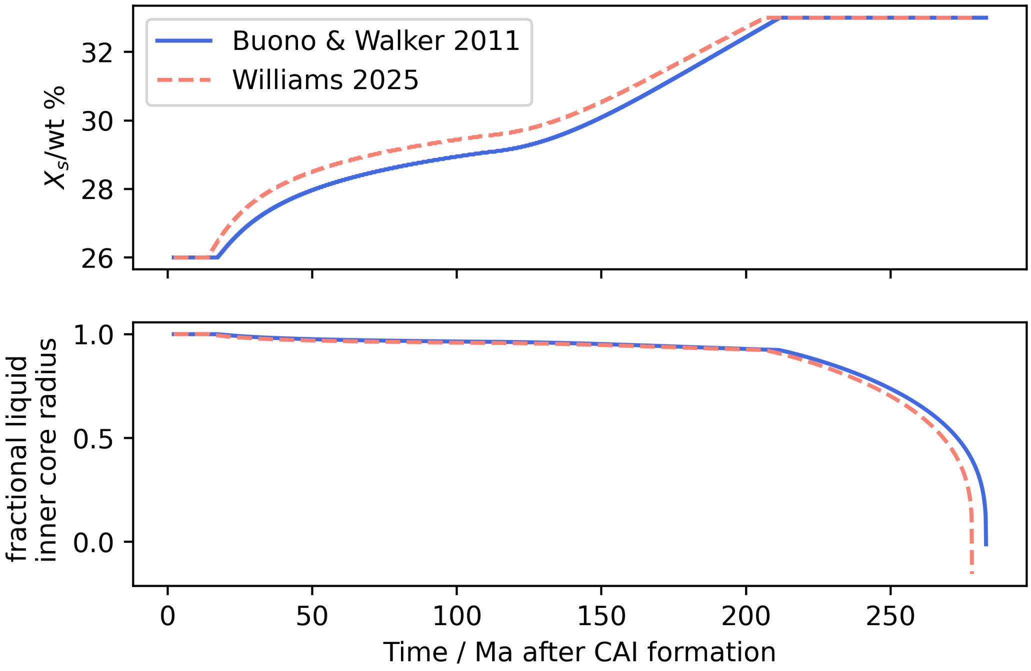

Figure A.3: Core sulfur content and fractional liquid inner core radius as a function of time for two 300 km radius planetesimals with liquidii from either Buono and Walker (2011) or Williams (2025). All other planetesimal parameters are the same as for the example run in Chapter 2.

Williams (2025) focuses on inconsistencies between the slope of the Buono and Walker (2011) liquidus and experimental data for pure iron across a range of pressures. However, my model focusses on cores that contain sulfur. For core sulfur contents > 5 wt%, planetesimal cores solidify top-down for both the Buono and Walker (2011) liquidus and the liquidus slope interpolated from the data in Williams (2025) (Dodds, 2024). Therefore, my assumption of inward solidification is still valid. Using the liquidus interpolated from Williams (2025) (Dodds, pers. comm.) rather than the Buono and Walker (2011) liquidus makes minimal difference to the duration and rate of core solidification (Figure A.3), and the duration of the dynamo. For a 300 km radius planetesimal with all other parameters identical to the example run in Chapter 2, the dynamo ends 2.3% (5 Ma) earlier for the Williams (2025) liquidus and the core solidifies 1.7% earlier (5 Ma).

A.4 Magnetic field generation

Dimensionless number	Symbol	Force balance	Equation	Earth value	Planetesimal value
Ekman number	E	F_ν/F_C	$\frac{\nu}{\Omega l^2}$	10^{-15}	10^{-14}
Rossby number	Ro	F_I/F_C	$\frac{U}{\Omega l}$	10^{-6}	10^{-6}
Buoyancy number	Bu	F_B/F_C	$\frac{\alpha_\mathrm{c}\Delta T' g_\mathrm{c}}{\Omega U}$	10^{-1}	10^{-3}
Dynamic Elsasser number	Λ_d	F_L/F_C	$\frac{B^2}{\rho_\mathrm{c}\mu_0\Omega U l}$	10^{-2}	$10^{-2} - 10^{-3}$
Elsasser number	Λ_t	F_L/F_C	$\frac{B^2}{\rho\mu_0\lambda\Omega}$	10	$1 - 10$

Table A.1: Dimensionless numbers and their values for Earth (Schwaiger et al., 2021) and planetesimals arranged in order of size in planetesimals from smallest to largest. Planetesimal scaling assumes a rotational period of 10 hrs, a core size of 250 km (half the radius of a 500 km planetesimal) and a field strength 0.1–1 times the strength of the Earth. All other quantities are assumed to be the same order of magnitude as Earth. ν is the kinematic viscosity, U is the convective speed, $\Delta T'$ is a temperature perturbation and all other symbols are defined in Chapter 2. The Elsasser number assumes the current density, J, is given by $J = \sigma U B$ and the dynamic Elsasser number assumes $J = \frac{\nabla \times B}{\mu_0}$ and is thought to be a better estimate of the strength of the Lorentz force (Aurnou and King, 2017; Schwaiger et al., 2021). The table indicates that inertial, F_I, and viscous, F_ν, forces are negligible. The Coriolis force, F_C, is slightly larger than the buoyancy force, F_B, and the Lorentz force, F_L. Therefore, a MAC balance is the next most important force balance after the quasi-geostrophic (QG) force balance that dominates in planetary cores (Schwaiger et al., 2021)

A.4.1 Regime 2

When the mantle is convecting $F_\mathrm{CMB} = -k_\mathrm{m}\frac{T_\mathrm{m} - T_\mathrm{CMB}}{\delta_\mathrm{l}}$. When $T < T_{\phi_C}$ (i.e. $T <$ 1520K) there is a jump in lid thickness. This results in a shallower temperature gradient at the CMB (9.59 Ma vs 11.09 Ma, Figure A.4), because the same temperature difference is accommodated across a larger boundary layer. This decreases F_CMB. As the mantle continues to cool, the temperature at the top of the thermal boundary layer drops. This increases the temperature difference across the boundary layer (12.59 to 14.09 Ma, Figure A.4) and increases F_CMB.

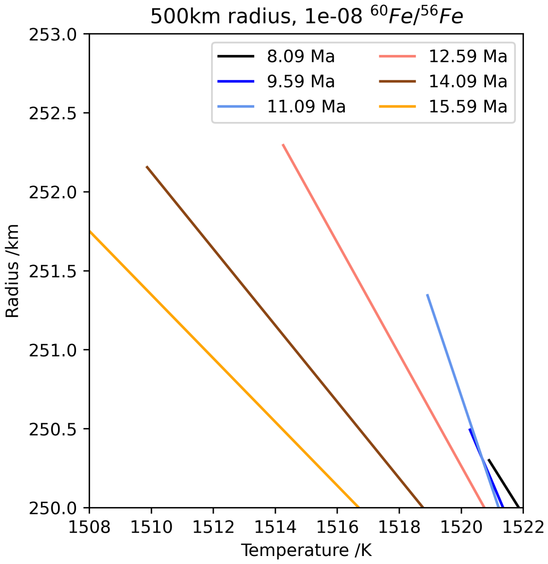

Figure A.4: Temperature profile across the CMB boundary layer, δ_l before (9.59 Ma) and after (11.09 Ma) the basal mantle temperature drops below the temperature of the critical melt fraction. The profiles here are for a 500 km radius planetesimal, with a 250 km core radius accreted at 0.8 Ma after CAI formation with $^{60}\mathrm{Fe}/^{56}\mathrm{Fe} = 10^{-8}$ and $X_{\mathrm{S},0} = 29.85\,\mathrm{wt}\%$.

A.4.2 Convective lengthscale

A possible way to calculate the ratio of the convective lengthscale, l_{conv}, to the geometric lengthscale of the convecting region in the core, l_{geom}, is to use the Rossby number (Davidson, 2013; Aubert et al., 2017)

$$\frac{l_{\mathrm{conv}}}{l_{\mathrm{geom}}} \sim Ro^{\frac{1}{4}}. \tag{A.14}$$

The Rossby number quantifies the ratio between inertial and Coriolis force in the core and is $\approx 10^{-6}$ in planetesimal cores (Table A.1). Therefore, $l_{\mathrm{conv}} \sim 0.03 l_{\mathrm{geom}}$. Using this expression for l_{conv}, in the equations for buoyancy flux, Re_{m}, and magnetic field strength can lead to elevated magnetic field strengths and smaller Re_{m} (Figure A.5). Smaller Re_{m} leads to shorter epochs of dynamo generation, but the second epoch of dynamo generation still starts before the onset of core solidification.

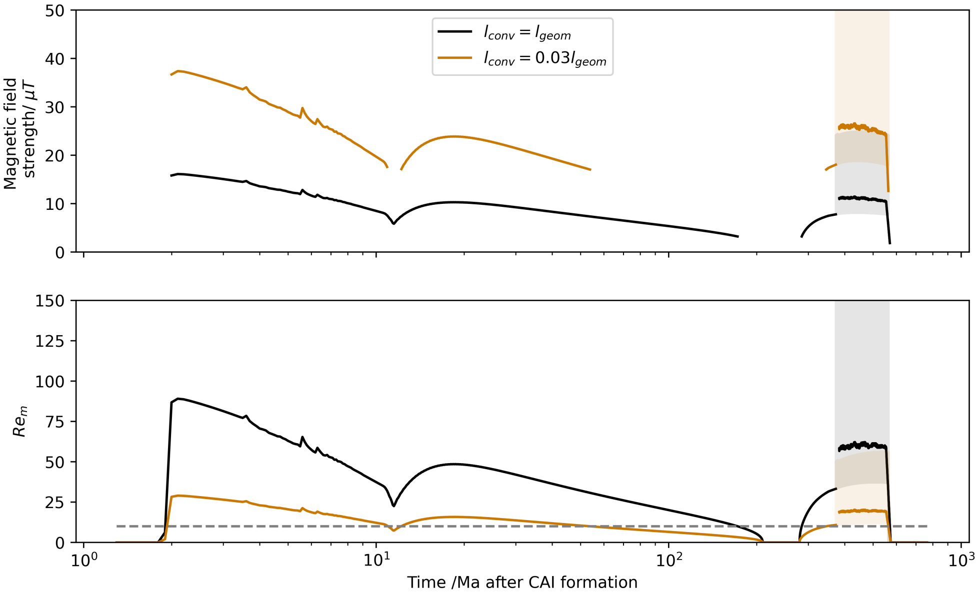

Figure A.5: Magnetic field strength and Re_m with time for 500 km planetesimals with 250 km radius cores, ^{60}Fe/^{56}Fe $=10^{-8}$, $X_{\mathrm{S},0}$=29.85 wt%, assuming either $l_\mathrm{conv} = l_\mathrm{geom}$ or $l_\mathrm{conv} = 0.03 l_\mathrm{geom}$. Due to the discrete nature of the model, the magnetic field strength and Re_m oscillate during core solidification. This oscillating output is shown by the faded traces and the rolling average over 200 output steps (20 Ma) is shown in bold. The spikes in F_CMB prior to 13 Ma are due to the discretisation of the stagnant lid. Using a smaller convective lengthscale increases the magnetic field strength, but decreases Re_m, which leads to shorter epochs of dynamo generation.

A.5 Timescales for differentiation

Here I estimate the timescales for percolation and rain out via Stokes settling. Differentiation via sinking of large iron diapirs (Samuel and Tackley, 2008) has not been included because the timescales are similar to Stokes settling (Neumann et al., 2014). Additionally, diapirism is more pertinent to terrestrial planets, which have rheological boundaries where metal material can accumulate (Samuel and Tackley, 2008). Due to uncertainties in the percolation timescale and the complexity of the percolation mechanism, this work focuses on differentiation via Stokes' settling at $\phi = \phi_{\mathrm{C}}$, which is much more rapid.

A.5.1 Differentiation via percolation

The percolation velocity from Darcy's law is given by

$$\begin{aligned} v &= \frac{K(\phi)\Delta\rho g}{\eta_{\mathrm{c}}} \\ &= 50 \left(\frac{K(\phi)}{10^{-8} m^2}\right) \mathrm{km\,yr}^{-1}, \end{aligned} \tag{A.15}$$

where $\Delta\rho \approx 3000\mathrm{kgm}^{-3}$ is the density difference between molten Fe-FeS and silicate material, $g \approx 0.5\,\mathrm{ms}^{-2}$ is the gravitational field at the surface of a 500 km planetesimal, $\eta_{\mathrm{c}} = 0.01\,\mathrm{Pas}$ is the viscosity of molten iron, and $K(\phi)$ is the permeability of the planetesimal matrix, for which model values vary by six orders of magnitude from $10^{-8}\,\mathrm{m}^2$ (Fu and Elkins-Tanton, 2014) to $10^{-14}\,\mathrm{m}^2$ (Neumann et al., 2012). An upper estimate for the timescale for differentiation can be obtained using $t_{\mathrm{diff}} = \frac{R}{v}$ and the upper limit on planetesimal radius, 500 km. This gives $t_{\mathrm{diff}} = 10 \left(\frac{10^{-8} m^2}{K(\phi)}\right)$ years and differentiation times of 10^{-5}–1 Ma over my permeability range. The literature bounds on differentiation time via percolation are similarly wide from 0.001 Ma (Sahijpal et al., 2007) to 1 Ma (Neumann et al., 2012).

A.5.2 Differentiation via rain-out

The Stokes settling velocity is given by

$$v = \frac{dr}{dt} = -\frac{2\Delta\rho g a^2}{\eta_{\mathrm{m}}} \tag{A.16}$$

where a is the radius of the sinking metal droplet and $\eta_{\mathrm{m}} \approx 10\,Pas$ is the viscosity of the body above ϕ_{C}. Integrating with respect to time gives a settling time of $10^2 \left(\frac{a}{10^{-3}\,\mathrm{m}}\right)^{-2}$ yr for the droplet to fall to 1% of its initial radius ($r_{\mathrm{final}} = 0.01 r_{\mathrm{initial}}$).

The radius of the metal droplets has been estimated as 1 mm based on the size of metal grains in element maps of metal rich chondrites in Krot et al. (2014), but coalescence during melting may be required for metal grains to reach large enough sizes to fall rapidly during rain-out (Néri et al., 2021). Once ϕ_{C} is reached and the silicate phase is rheologically weak, the molten metal will fall rapidly to the centre of the planetesimal and this process can be approximated as instantaneous.

A.6 Numerical Implementation

I use a forward in time, centered in space (FTCS) stencil to calculate the temperature change in the conductive portion of the planetesimal. For a given step the temperature change is calculated by

$$\vec{T}^{i+1} = \vec{T}^{i} + \mathbf{M}\vec{T}^{i}dt \tag{A.17}$$

where $\mathbf{M}$ is the FTCS matrix, $\vec{T}$ is a vector of temperatures with radius in the planetesimal, and ^{i} indicates the i^{th} timestep. For an undifferentiated planetesimal, the whole body has the same thermal diffusivity and $\mathbf{M}$ and $\vec{T}$ are given by

$$\mathbf{M} = \kappa_{ch}\begin{bmatrix} -1 & 1 & & & \\ 1-\frac{dr}{r} & -2 & 1+\frac{dr}{r} & & \\ & \ddots & \ddots & \ddots & \\ & & 1-\frac{dr}{r} & -2 & 1+\frac{dr}{r} \\ & & & & 0 \end{bmatrix} \qquad \vec{T} = \begin{bmatrix} T_{r=0} \\ T_{r=dr} \\ T_{r=2dr} \\ \vdots \\ T_{\mathrm{s}} \end{bmatrix}. \tag{A.18}$$

For the differentiated body, conduction in the core and mantle are calculated separately using $\mathbf{M}_{\mathrm{c}}$ and $\vec{T}_{core}$ in the core

$$\mathbf{M}_{\mathrm{c}} = \kappa_{\mathrm{c}}\begin{bmatrix} -1 & 1 & & & \\ 1-\frac{dr}{r} & -2 & 1+\frac{dr}{r} & & \\ & \ddots & \ddots & \ddots & \\ & & 1-\frac{dr}{r} & -2 & 1+\frac{dr}{r} \\ & & & & 0 \end{bmatrix} \qquad \vec{T}_{core} = \begin{bmatrix} T_{r=0} \\ T_{r=dr} \\ \vdots \\ T_{\mathrm{CMB}} \end{bmatrix} \tag{A.19}$$

and $\mathbf{M}_{\mathrm{m}}$ and $\vec{T}_{\mathrm{mantle}}$ in the mantle

$$\mathbf{M}_{\mathrm{m}} = \kappa_{\mathrm{m}}\begin{bmatrix} 0 & & & & \\ 1-\frac{dr}{r} & -2 & 1+\frac{dr}{r} & & \\ & \ddots & \ddots & \ddots & \\ & & 1-\frac{dr}{r} & -2 & 1+\frac{dr}{r} \\ & & & & 0 \end{bmatrix} \qquad \vec{T}_{mantle} = \begin{bmatrix} T_{\mathrm{CMB}} \\ T_{r_{\mathrm{c}}+dr} \\ \vdots \\ T_{s} \end{bmatrix}. \tag{A.20}$$

The last entry in $\mathbf{M}_\mathrm{c}$ is 0 alongside the first and last entry in $\mathbf{M}_\mathrm{m}$ because the CMB temperature is calculated separately by balancing the core and mantle heat fluxes and the surface temperature is fixed to 200 K. The boundary condition at the top of the core is a fixed temperature boundary condition using the CMB temperature from the previous timestep. This CMB temperature is then updated by balancing the heat fluxes across the CMB. The small timestep ($0.075\tau_{\mathrm{cond,core}}$) ensures consistency between the flux condition and the fixed temperature boundary condition for an individual timestep.

A.6.1 Timestep and gridsize testing

To test the gridsize and timestep, four simulations were run for a 300km body: one using the model gridsize and timestep; one for half the gridsize; one for two thirds the timestep; and one for one third the timestep. Changing the timestep and gridsize results in <1% variation in model outputs, except for the time for beginning of the erosion of core thermal stratification. There is a 0.1 Ma (one output step) difference in the time for beginning of the erosion of core thermal stratification. Core stratification begins to be eroded very early in the thermal evolution (1.6–1.7 Ma after CAI formation). Therefore, this one output step time difference manifests as a large percentage variation, but in absolute terms is not significant. The small variation in model outputs indicates my choice of timestep and gridsize is small enough to not influence my model results.

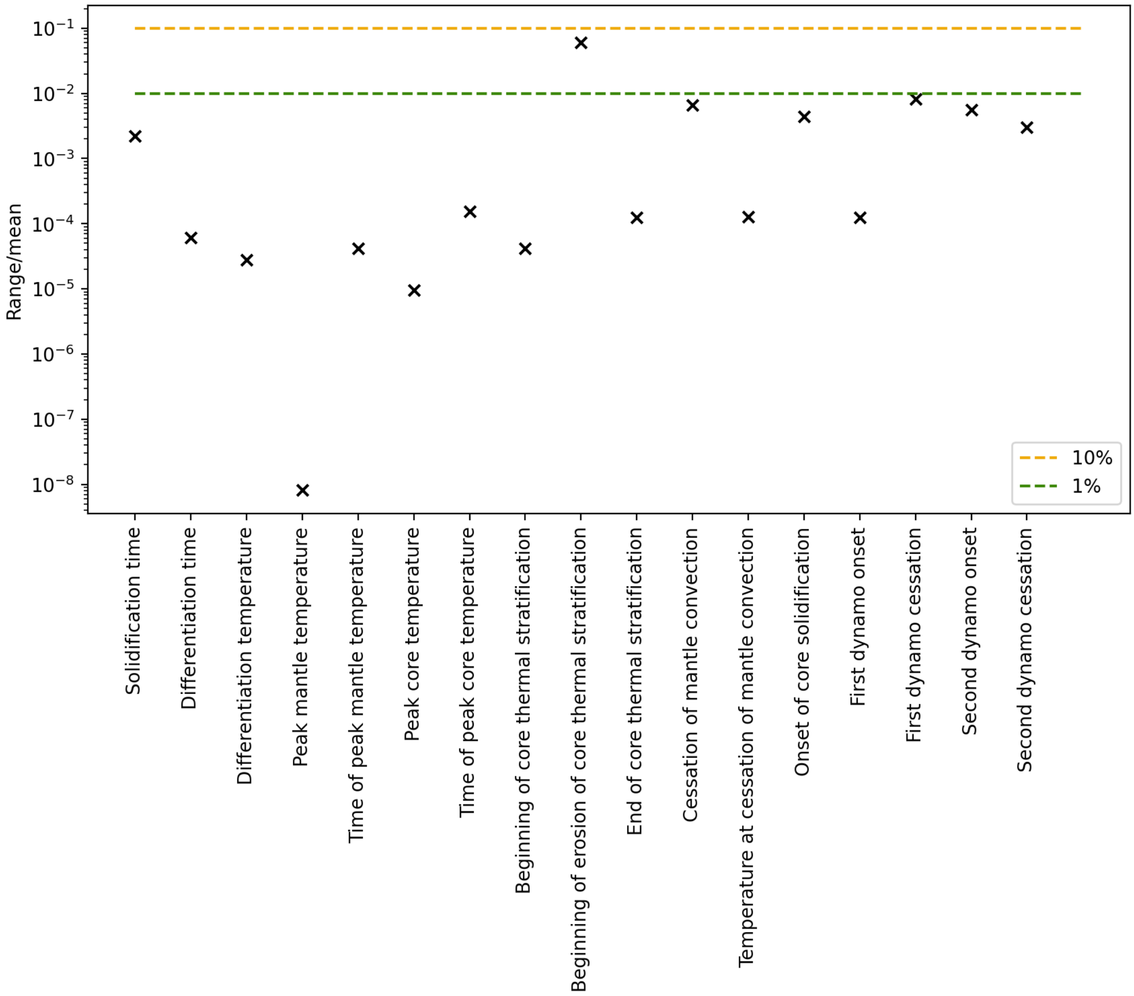

Figure A.6: Variation in temperatures and times of key points in thermal evolution and dynamo generation for changes in gridsize. For each output value, the range in output divided by the mean output value is plotted. Changing the timestep and gridsize results in $< 1\%$ variation in model outputs, except for the time for beginning of the erosion of core thermal stratification. The percentage range in the time for beginning of the erosion of core thermal stratification is larger, because variation by 0.1 Ma (one output step) is a large percentage of the time of this process (1.6–1.7 Ma after CAI formation).

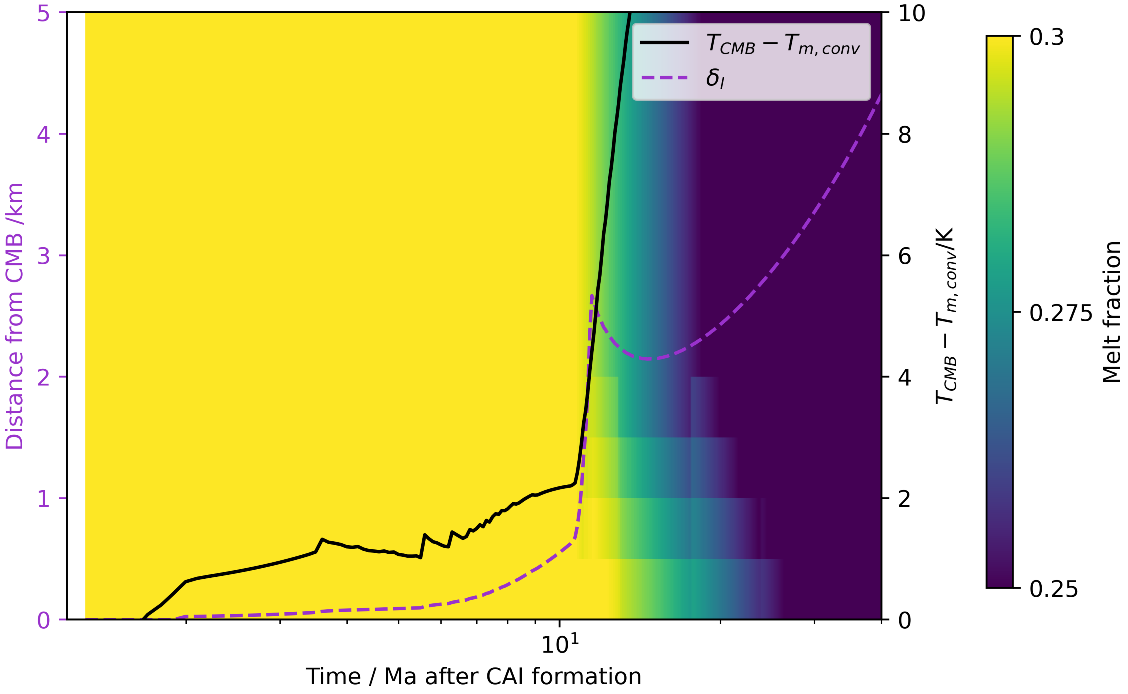

Figure A.7: CMB boundary layer thickness, δ_l, and temperature difference between convective mantle and CMB for the first 40 Ma of the planetesimal thermal evolution. Results are for a 500 km planetesimal, accreted 0.8 Ma after CAI formation with ^{60}Fe/^{56}Fe $=10^{-8}$ (same example run as Figure 6 in Chapter 2). The background colourmap indicates the melt fraction 0–5 km above the CMB (left hand axis). All melt fractions at or above the rheologically critical melt fraction, $\phi_C = 0.3$, are shown in yellow. There is a jump in CMB boundary layer thickness when the melt fraction first drops below the critical melt fraction and the viscosity increases rapidly. This increases the temperature difference between the convecting mantle and CMB.

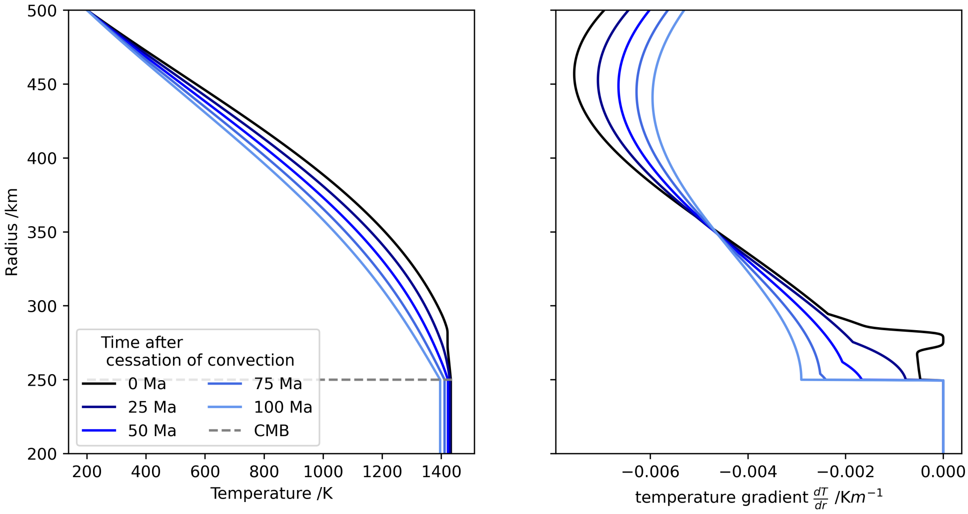

Figure A.8: Planetesimal temperature profiles and temperature gradients following the cessation of convection. The profiles here are for a 500 km radius planetesimal, with a 250 km core radius, accreted at 0.8 Ma after CAI formation with ^{60}Fe/^{56}Fe $=10^{-8}$ and $X_{\mathrm{S},0}$ =29.85 wt%. The grey, dashed line indicates the postion of the CMB. Immediately following the cessation of convection, a small portion of the mantle is isothermal and there is a shallow temperature gradient across the CMB boundary layer. As the mantle cools, a temperature gradient is established throughout the entire mantle and the temperature gradient at the CMB increases.

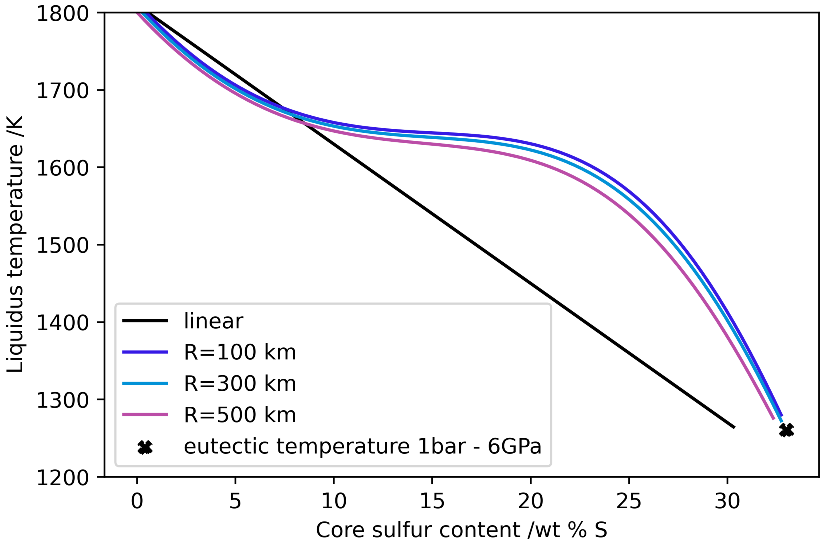

Figure A.9: Comparison between the linear liquidus approximation and the liquidus from Buono and Walker (2011). This liquidus is a function of pressure so liquidi for the range of planetesimal radii appropriate for this model are shown. The liquidus temperatures for core sulfur contents $> 10\,\mathrm{wt\%}$ are higher than temperatures for the linear liquidus approximation. The liquidus gradient is shallow from 10–25 wt% at just above 1600 K. This limits the range of planetesimal initial core sulfur contents to high values $> 25\,\mathrm{wt\%}$ (for a 1400 K mantle solidus), because the maximum possible planetesimal temperatures in my model are ∼1600 K for a critical melt fraction of 0.5.

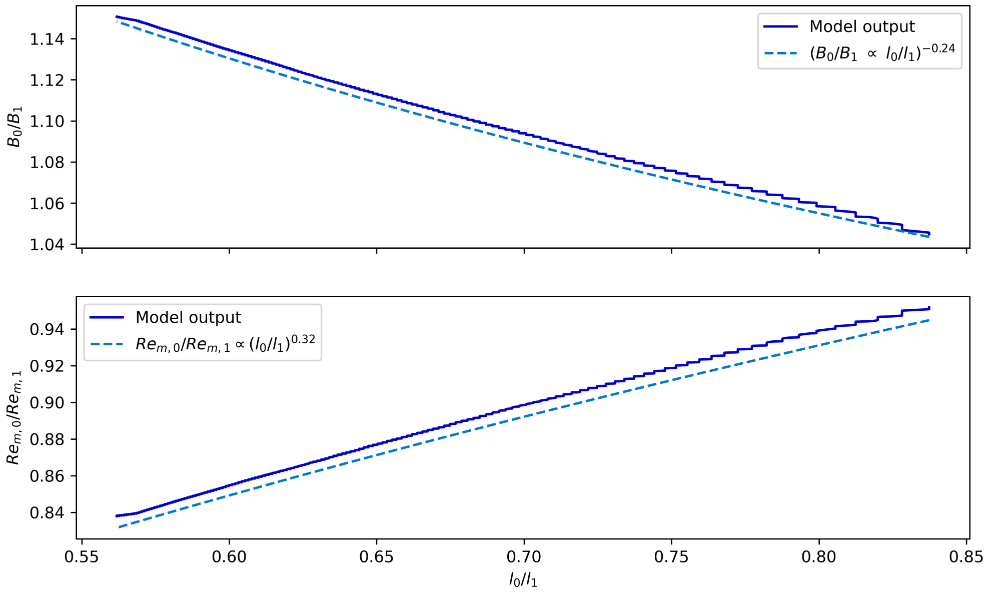

Figure A.10: Ratios of magnetic field strength and Re_{m} for the two endmember models as a function of the ratio of convective lengthscales. Subscripts 0 and 1 indicate the values for the $m_{\mathrm{frac}} = 0$ and $m_{\mathrm{frac}} = 1$ endmembers, respectively. The model output (solid lines) follows the scaling predicted by combining the Equations 2.32, 2.33 and 2.35 for magnetic Reynolds number, convective velocity, and buoyancy flux (dashed lines). Staircasing in the output is due to the discrete nature of my model. The runs shown here are for the same parameters as the example run in Chapter 2. Magnetic field strength and Re_{m} depend weakly on convective lengthscale. $B \propto l^{-0.24}$ and $Re_m \propto l^{0.32}$.

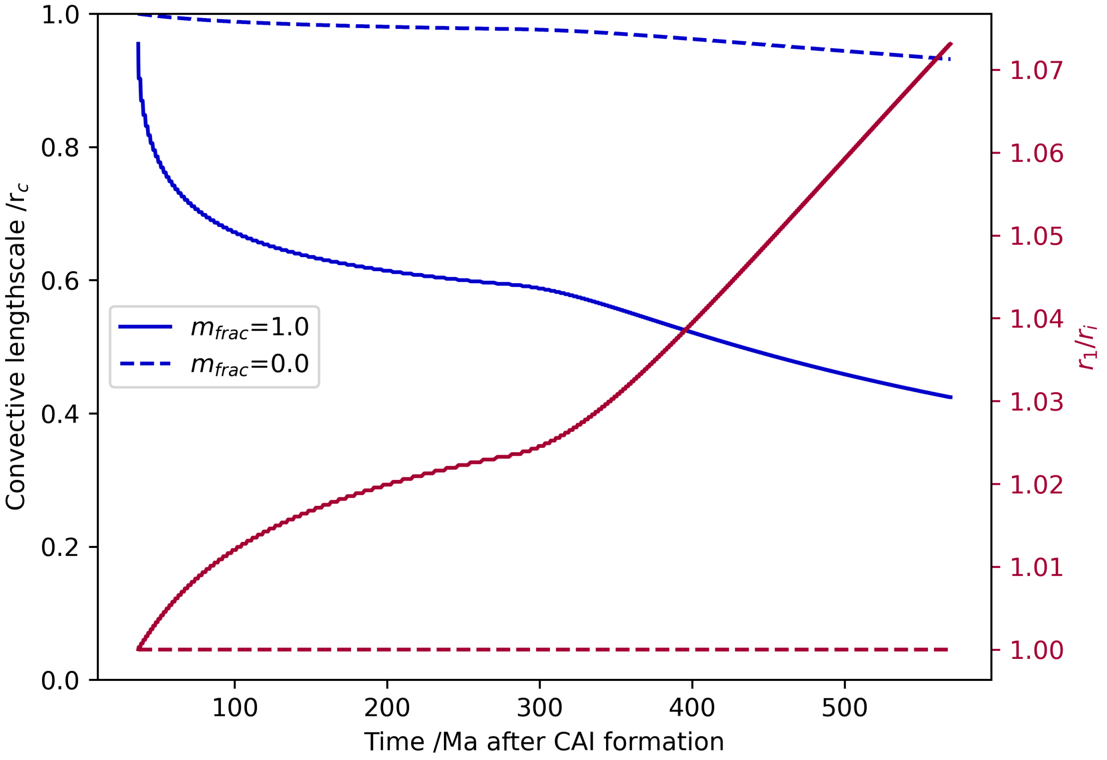

Figure A.11: Convective lengthscale as a function of time for the two endmember solidifcation geometries (dark blue lines). Convective lengthscale decreases more rapidly for $m_{\text{frac}} = 1$. The pink lines indicate the ratio of the radius of the base of the solid outer core, r_1, to the solidification front, r_i. For $m_{\text{frac}} = 1$, the maximum deviation between these positions is less than 6%. The runs shown here are for the same parameters as the example run in Chapter 2, but for $X_{\text{S},0}$ =26.7 wt% in order to investigate the maximum possible change in lengthscale as lower $X_{\text{S},0}$ take longer to reach the eutectic composition.

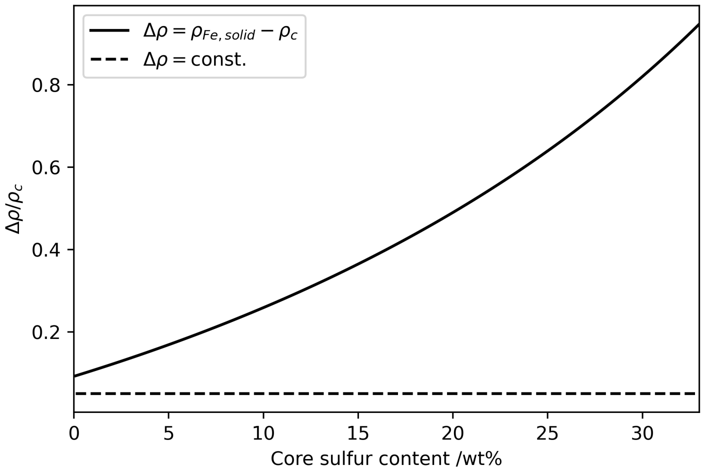

Figure A.12: Density difference driving buoyancy flux in the compositional dynamo. The density difference between solid iron and a liquid inner core increases with increasing sulfur content. The density difference is higher than the previously assumed value of $0.05\rho_c$ for all core sulfur contents.

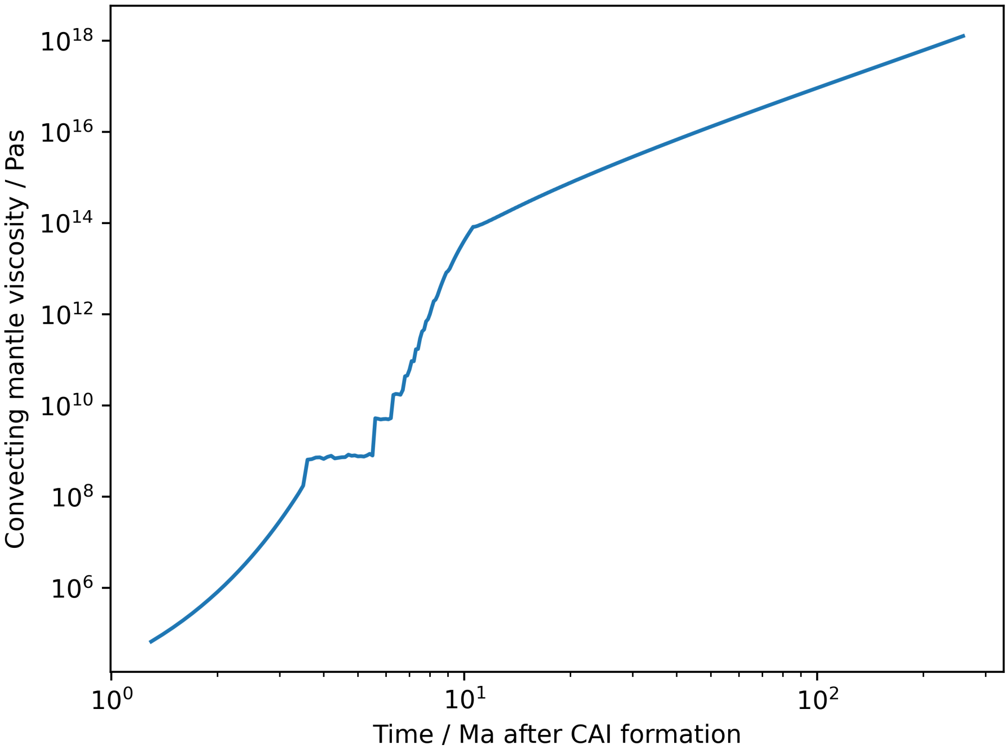

Figure A.13: Viscosity in the isothermal, convecting mantle interior as a function of time for a 500 km planetesimal accreted at 0.8 Ma after CAI formation with ^{60}Fe/^{56}Fe $=10^{-8}$, $X_{\mathrm{S},0}$ =29.85 wt%, $\eta_0 = 10^{19}$ Pas, $\phi_C = 0.3$, $\beta = 0.0225\mathrm{K}^{-1}$, $\alpha_{\mathrm{n}} = 30$, and $\eta_{\mathrm{l}} = 10$ Pas.

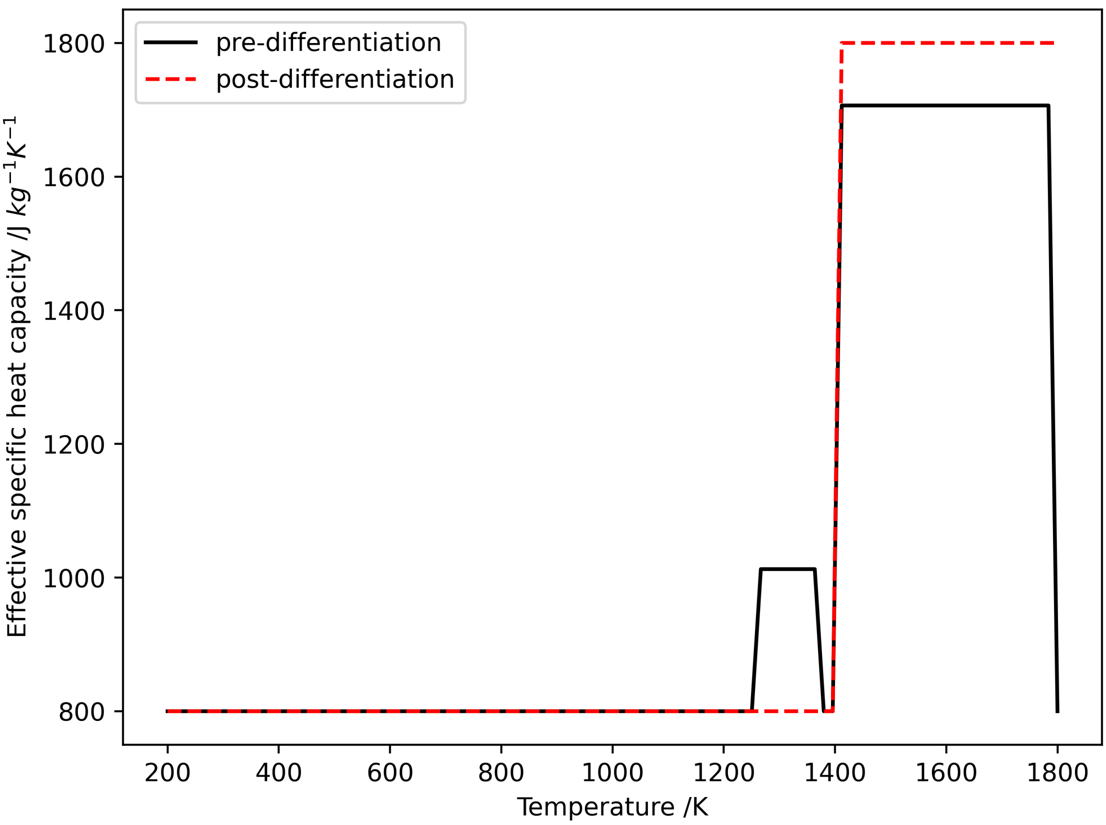

Figure A.14: Chondritic (pre-differentiation) and silicate (post-differentiation) effective specific heat capacity as a function of temperature for $X_{\mathrm{S},0} = 29.85\,\mathrm{wt}\%$. Prior to differentiation, there are two periods of increased specific heat capacity as the Fe-FeS and silicate phases melt. After differentiation, there is one period of increased specific heat capacity when the silicate melts. The post-differentiation increase in effective specific heat capacity is higher, because the material is entirely silicate and does not contain any Fe-FeS volume fraction.

Appendix B

Supplementary Information for Chapter 3

B.1 Range of primordial ^{60}Fe/^{56}Fe

There are several reasons for the range in the primordial ^{60}Fe/^{56}Fe ratio. Firstly, there is up to two orders of magnitude difference in the values of primordial ^{60}Fe/^{56}Fe between bulk analyses and in-situ studies of individual minerals (Kodolányi et al., 2022a,b). Secondly, different meteorite groups or minerals produce different values (e.g. $8.8 \pm 5.2 \times 10^{-9}$ in angrites vs $7.9 \pm 3.7 \times 10^{-7}$ in IID irons; Tang and Dauphas, 2012; Cook et al., 2021). Thirdly, biases in error analysis (Telus et al., 2012) and use of an incorrect reference value for calculating the ^{60}Ni deficit (Kodolányi et al., 2022a) can render measurements inaccurate. Fourthly, measured systems may not be closed (Cook et al., 2021). Finally, uncertainty in the formation time of a sample increases uncertainty when extrapolating back to the ^{60}Fe/^{56}Fe value at CAI formation (e.g. $^{60}\mathrm{Fe}/^{56}\mathrm{Fe} = 4 \times 10^{-8}$–$1.5 \times 10^{-7}$ for a 5 Ma range in ages for troilite formation; Kodolányi et al., 2022b).

B.2 Additional viscosity information

B.2.1 Extrapolation of reference viscosities

Viscosity is temperature, pressure, and grain size dependent. Planetesimal mid-mantle pressures lie above that of lab experiments and below that of planets, therefore extrapolation is required when estimating planetesimal reference viscosities. Laboratory experiments are also on shorter timescales and smaller grain sizes compared to planetary conditions. Therefore, geophysical observations, such as postglacial uplift (Karato and Wu, 1993) are often used to constrain mantle viscosity on Earth. For this reason, the upper range of η_0 in this chapter was extrapolated from planetary values using an Arrhenius law

$$\eta = \eta_0 \mathrm{exp}\left(\frac{E + pV}{RT} - \frac{E + p_{\mathrm{ref}}V}{RT_{\mathrm{ref}}}\right) \tag{B.1}$$

and the Frank-Kamenetskii approximation (Noack and Breuer, 2013)

$$\eta = \eta_0 \mathrm{exp}\left(\frac{E + p_{\mathrm{ref}}V}{RT_{\mathrm{ref}}^2}(T_{\mathrm{ref}} - T) + \frac{V}{RT_{\mathrm{ref}}}(p - p_{\mathrm{ref}})\right). \tag{B.2}$$

In these equations, E and V are the activation energy and volume, p_{ref} and T_{ref} are the reference pressures and temperatures, R is the gas constant, and p and T are the temperatures and pressures being extrapolated to. To estimate planetesimal mid-mantle viscosities (see Table B.1), extrapolations using both laws were performed on reference viscosity values for Ganymede (Rückriemen et al., 2018) using a range in activation volumes from 2×10^{-6}–2×10^{-5} m^{3}mol^{-1} (Hirth and Kohlstedt, 2003) and activation energies from 240–570 kJmol^{-1} (Karato and Wu, 1993; Hirth and Kohlstedt, 2003). Assuming constant density core and mantle, planetesimal mid-mantle pressures range from 2 MPa to 50 MPa for 100–500 km bodies. These extrapolations give a wide range of possible η_0 from 10^{19}–10^{24} Pas due to the large uncertainties in activation volume and activation energy. Equation B.1 and B.2 give values within the same order of magnitude.

η_0 /Pas	p_{ref}/MPa	T_{ref} /K	Extrapolated η_0 /Pas
10^{19}–10^{22}	960	1600	10^{19}–10^{24}

Table B.1: Reference parameters for viscosity extrapolations for Ganymede (Rückriemen et al., 2018). Reference pressure is calculated in the mid-mantle using average values for the Ganymede interior structure model in Rückriemen et al. (2018).

Viscosity has a power law dependence on grain size

$$\eta_1 = \eta_2 \left(\frac{a_1}{a_2}\right)^m, \tag{B.3}$$

where a is the grain size and m a constant exponent (2 for dislocation creep, 3 for diffusion creep; Scott and Kohlstedt, 2006). Grain sizes in planetesimals are likely to be between 10^{-4}–10^{-3}m, based on observations from achondrites (Hutchison, 2004; Lichtenberg et al., 2019b) and grain growth models (Monnereau et al., 2023). Extrapolating to these grain sizes from an experimental value of $\eta_2 = 10^{12.5}$ Pas for

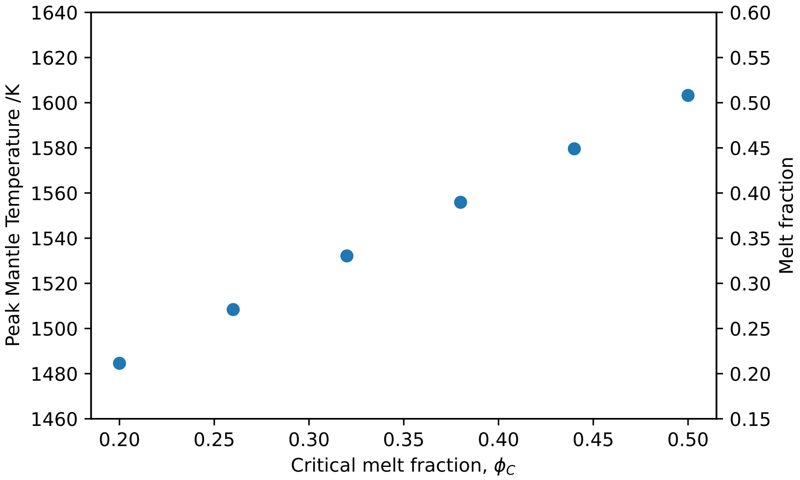

Figure B.1: Peak mantle temperature as a function of critical melt fraction, ϕ_{C}.

$a_2 = 10^{-5}$m in the diffusion creep regime (Scott and Kohlstedt, 2006) gives $\eta_1 = 10^{15}$–10^{18} Pas. For an experimental value of $\eta_2 = 10^{14.5}$ Pas for $a_2 = 5 \times 10^{-5}$m in the dislocation creep regime (Scott and Kohlstedt, 2006) gives $\eta_1 = 10^{15}$–10^{17} Pas. Therefore, $\eta_0 = 10^{15}$ Pas will be used as the minimum value in this work. However, due to the uncertainties in grain size, and differences in lengthscale and stress between experiments and planetesimal interiors, these low η_0 values ($< 10^{18}$ Pas) are less likely to occur in planetesimals.

B.2.2 Effect of ϕ_{C} on peak temperatures

As shown in Figure B.1, peak mantle temperature is close to that of ϕ_{C}, due to the negative feedback loop between mantle temperature and stagnant lid thickness. At ϕ_{C}, an increase in temperature leads to a rapid drop in viscosity and thinning of the stagnant lid. This increases surface heat flux, which reduces mantle temperature, increases the viscosity and thickens the stagnant lid. This means the choice of ϕ_{C} has direct control on the maximum mantle temperature of a planetesimal.

B.2.3 Effect of viscosity on dynamo timing

This section provides further detail on the runs with three epochs of dynamo generation.

B.2.3.1 Critical melt fraction, ϕ_C

Increasing ϕ_{C} lowers the mantle viscosity at peak temperature, which results in a thinner stagnant lid and longer time before the cessation of convection. In all runs, there is a jump in boundary layer thickness and temporary drop in CMB heat flux when the base of the mantle first cools below the critical melt fraction (Figure B.2). The following increase in CMB heat flux is responsible for the second increase in magnetic field strength (Chapter 2).

This jump in CMB boundary layer thickness results in two periods of dynamo generation before the cessation of convection for ϕ_{C} =0.26 and $\eta_0 = 10^{20}$ Pas. In these cases, this jump decreases Re_{m} enough to temporarily switch off the dynamo (Figure B.3 and B.4), but the dynamo restarts after a short period of core cooling. For a more detailed description of CMB boundary layer thickness with time see Chapter 2.

B.2.3.2 Reference viscosity, η_0

For the lowest reference viscosities, η_0, there is no gap in dynamo generation. This is because heat is removed from the core so rapidly, and the mantle has such low viscosity that the core solidifies before the cessation of mantle convection ($\eta_0 = 10^{14}$–10^{15} Pas on Figure B.5).

B.2.3.3 Liquid viscosity, η_{l}

η_{l} has no effect on dynamo timing. This is because the mantle temperature never gets far beyond the critical melt fraction and never reaches the fully liquid viscosity due to efficient feedback between stagnant lid thickness and mantle temperature (Chapter 2).

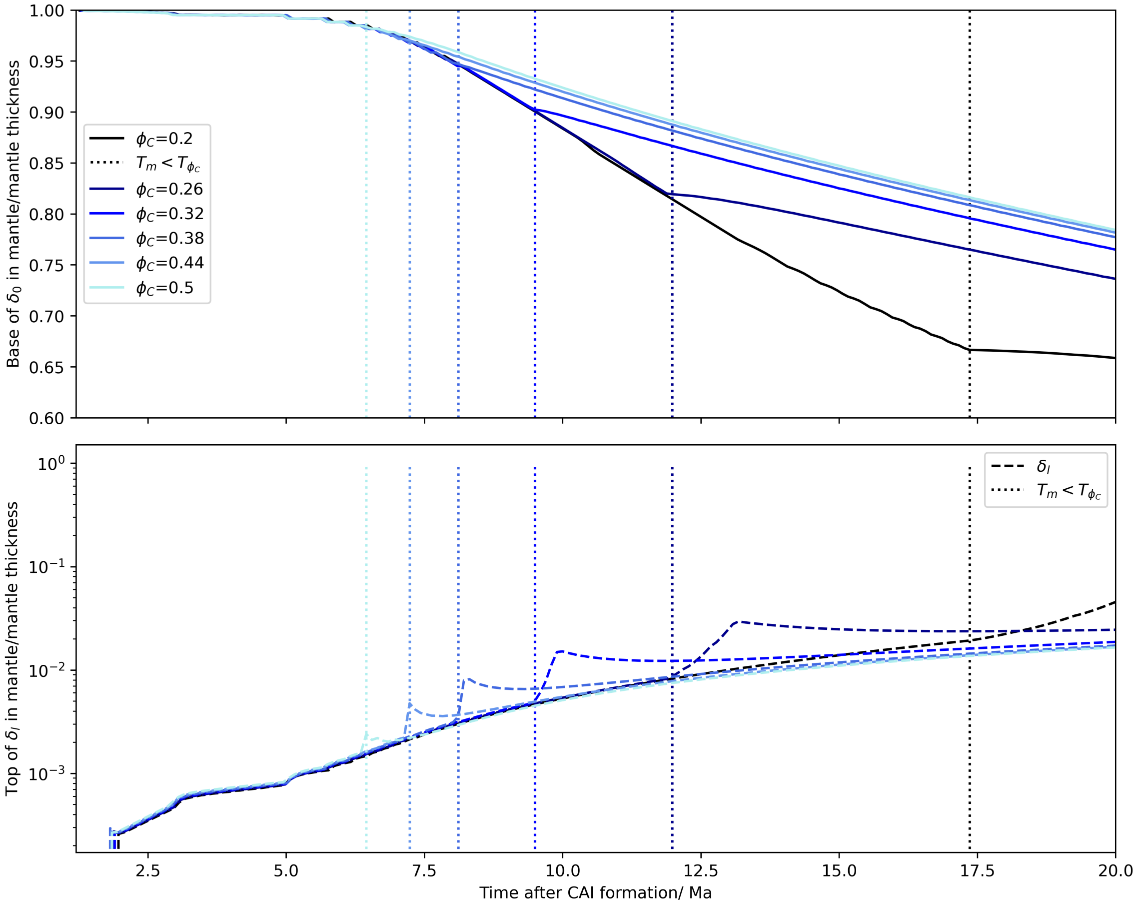

Figure B.2: Stagnant lid thickness, δ_0, (solid) and CMB boundary layer thickness, δ_l, (dashed) as a function of ϕ_{C}. To the right of the vertical dotted lines indicate when the temperature of the convecting mantle drops below the temperature of ϕ_{C}. This coincides with the uptick in boundary layer thickness as viscosity rapidly increases.

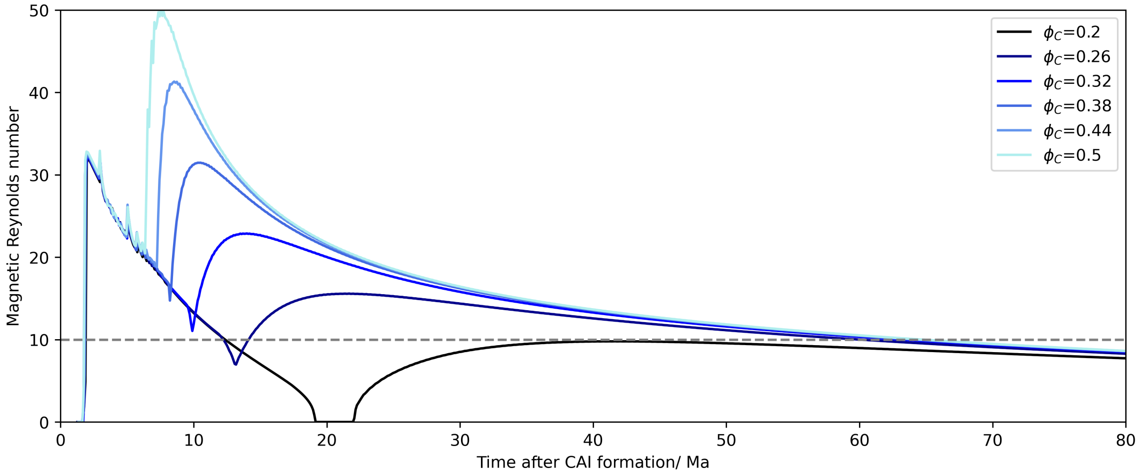

Figure B.3: Magnetic Reynolds number, Re_{m}, as a function of critical melt fraction, ϕ_{C}. The grey, horizontal, dashed line indicates the critical magnetic Reynolds number.

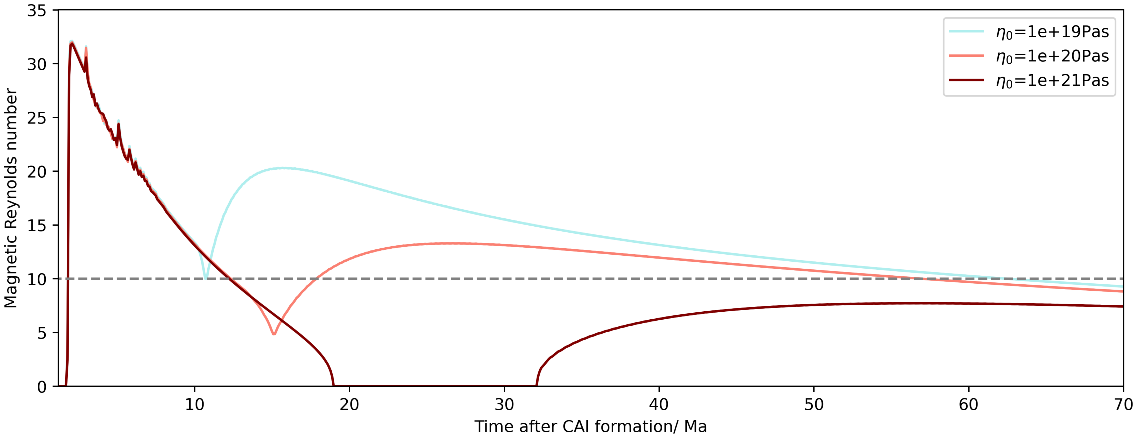

Figure B.4: Magnetic Reynolds number, Re_m, for reference viscosities, η_0, an order of magnitude above and below 10^{20} Pas. The grey, dashed line indicates the critical magnetic Reynolds number.

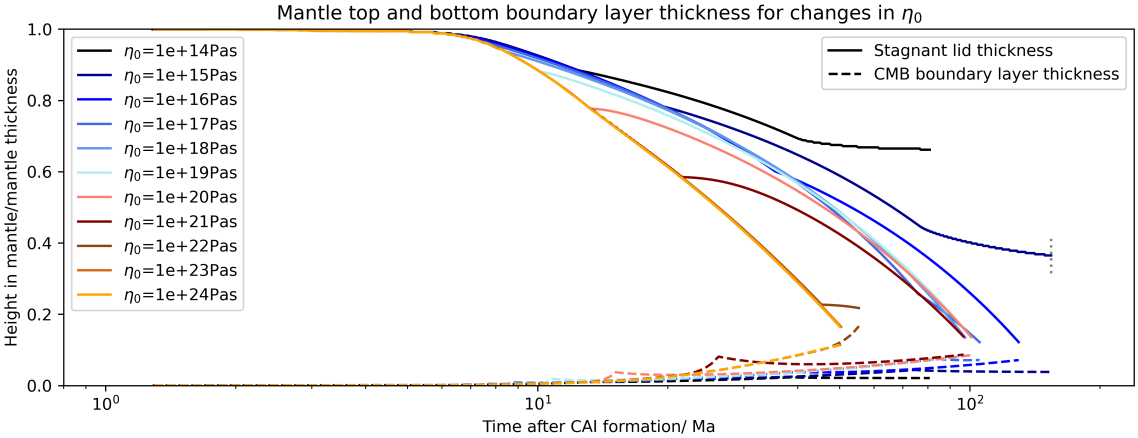

Figure B.5: Change in stagnant lid (solid) and CMB boundary layer (dashed) thickness for changes in reference viscosity, η_0, prior to the cessation of mantle convection. The vertical dotted grey lines on η_0 =10^{14},10^{15} Pas indicate the end of core solidification. Mantle convection ceases when the the stagnant lid and CMB boundary layer meet. Increasing η_0 increases the rate at which the stagnant lid thickens, ending mantle convection earlier.

B.3 Angrite paleomagnetism

There are multiple possibilities for the delay in onset of the angrite parent body dynamo relative to our model predictions. From these, a lower ^{60}Fe/^{56}Fe in the formation region of the angrites seems the most likely. Firstly, the angrite parent body may have been very large (up to Moon-size; Tissot et al., 2022), such that our assumptions to neglect the heat of accretion or mantle adiabat may be invalid. Secondly, ^{182}Hf/^{182}W measurements suggest angrite core formation occurred in multiple stages, not instantaneous as modelled in Chapter 3 (Kleine et al., 2012). However, gradual addition of material to the core reduces the degree of thermal stratification and enables earlier onset of a dynamo (Dodds et al., 2021). Additionally, heating by ^{60}Fe will rapidly remove thermal gradients from gradual accretion. Angrite core formation was complete ~ 2 Ma after CAI formation (Kleine et al., 2012), so late addition of material is unlikely to affect the dynamo a further $\sim$1.8 Ma after core formation (the time at which the volcanic angrites erupted; Wang et al., 2017). Thirdly, fractionation of iron isotopes during angrite core formation could have altered the proportion of ^{60}Fe in the core, but this is negligible due to the low pressures in planetesimal size bodies (Ni et al., 2022). Finally, as discussed in Chapter 3, ^{60}Fe/^{56}Fe may have been lower in the formation region of the angrites. Figure 3.11 displays the range of ^{60}Fe/^{56}Fe values which are consistent with the volcanic and plutonic angrite paleomagnetic record.

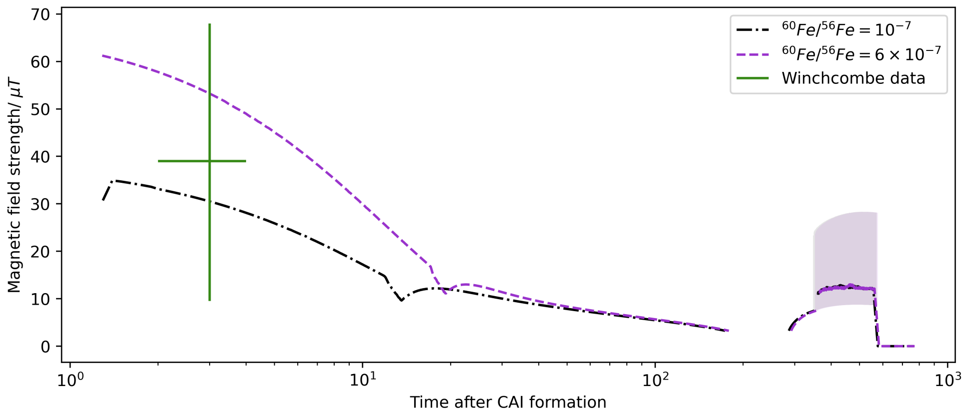

Figure B.6: Two example magnetic field histories, which match the intensity (without the factor of two correction) and timing of the paleomagnetic remanance recorded by the Winchcombe meteorite. Both runs are for a 500 km radius planetesimal, ^{60}Fe/^{56}Fe = 10^{-7} or 6×10^{-7} and all other parameters have the constant values in Table 1. Many other parameter combinations may fit the data, this plot aims to illustrate that it is feasible to generate a planetesimal at the correct time and strength to match the data.

Meteorite	Classification	Measured Phase	Age / Ma after CAI formation	Age method	Paleointensity / μT	Nebula correction	Possible origin	Reference
Allende	CV	chondrule	< 40	both	<8	False	dynamo	a)
Vigarano	CV	chondrule	3–11	radiometric	4 ± 1	False	dynamo	b)
DOM 08006 ALHA77307	CO	chondrule	1.7–3	radiometric	100 ± 50	True	nebula	c)
GRA 95229 LAP 02342	CR	chondrule	3.5–4	radiometric	8 ± 4	True	nebula	d)
Allende	CV	bulk	5–10	both	>20, ∼60	False	dynamo	e)
Allende	CV	QDM on bulk	2.5–3.5	radiometric	≥ 40	True	unconstrained	f)
Kaba	CV	bulk	4–6	radiometric	null	False	—	g)
Kaba	CV	bulk	6–40	both	3.8 ± 2.2	False	dynamo	g)
DOM 08006 ALHA77307	CO	bulk	2.7–5.1	radiometric	<0.9	False	—	h)
Winchcombe	CM	bulk	2.4–4	radiometric	78 ± 58	True	unconstrained	i)
CMs	CM	bulk	2.4–4	radiometric	4 ± 3	True	unconstrained	j)
WIS 91600	ungrouped chondrite	bulk	3.6–5	radiometric	4.4 ± 2.8	False	nebula	k)
Tagish lake	ungrouped chondrite	bulk	3–4	radiometric	<0.3	False	nebula	l)
Semarkona	LL3	chondrule	2–3	radiometric	54 ± 21	True	nebula	m)
Bjurböle	L/LL4	chondrule	80–140	model	9 ± 1	False	dynamo	b)
Portales Valley	H	bulk	80–130	radiometric	16 ± 14	False	dynamo	n)
PCA 91002	R	bulk	0–20	radiometric	12 ± 2	False	unconstrained	o)
LAP 03639	R	bulk	0–20	radiometric	$5pm1$	False	dynamo	o)

Table B.2: Meteorite paleomagnetic measurements of chondrites. ‘Age method’ refers to whether remanence acquisition is dated using radiometric dating or thermal evolution and dynamo generation modelling. ‘Nebula Correction’ refers to whether paleointensities were multiplied by a factor of two to account for the unknown angle between the nebula field and the remanent magnetisation. ‘Possible origin’ denotes previous interpretations of paleomagnetic measurements. Remanences $< 1\,\mu$T have been interpreted as null remanences so the timing of remanence acquisition and possible source are blank. a) Fu et al. (2012), b) Shah et al. (2017), c) Borlina et al. (2021), d) Fu et al. (2020), e) Carporzen et al. (2011), f) Fu et al. (2021), g) Gattacceca et al. (2016), h) Borlina et al. (2022), i) Bryson et al. (2023), j) Cournede et al. (2015), k) Bryson et al. (2020a), l) Bryson et al. (2020b), m) Fu et al. (2014b), n) Bryson et al. (2019b), o) Cournède et al. (2020)

Meteorite	Classification	Measured Phase	Age / Ma after CAI formation	Age method	Paleointensity / μT	Nebula correction	Possible origin	Reference
Odessa	IAB	cloudy zone	100–160	model	null	False	—	a)
Toluca	IAB	cloudy zone	100–160	model	null	False	—	a)
Colomera	IIE	cloudy zone	87–107	radiometric	15 ± 5	False	dynamo	b)
Techado	IIE	cloudy zone	65–91	radiometric	36 ± 11	False	dynamo	b)
Miles	IIE	cloudy zone	150–160	radiometric	33 ± 9	False	dynamo	c)
Steinbach	IVA	cloudy zone	2–8	radiometric	≥100	False	dynamo	d)
SJN silicate	IVA	bulk	—	—	null	False	—	d)
Imilac	MG pallasite	cloudy zone	149–170	model	80 ± 15	False	dynamo	e)
Esquel	MG pallasite	cloudy zone	162–217	model	64 ± 15	False	dynamo	e)
Springwater	MG pallasite	cloudy zone	122–141	model	22 ± 8	False	dynamo	e)
Marjalahti	MG pallasite	cloudy zone	86–109	model	null	False	—	e)
Brenham	MG pallasite	cloudy zone	100–130	model	null	False	—	e)
D'Orbigny	angrite	bulk	3.8–3.9	radiometric	< 0.6	True	—	f)
Sahara 99555	angrite	bulk	3.8–3.9	radiometric	< 0.6	True	—	f)
Asuka 881371	angrite	bulk	3.8–3.9	radiometric	< 0.4	True	—	f)
Angra dos Reis	angrite	bulk	11–11.1	radiometric	17 ± 8.5	False	dynamo	f)
ALHA81001	eucrite	bulk	> 870	radiometric	>2, ~12	False	crustal remanence	g)
NWA 7325	ungrouped achondrite	bulk	4–5	radiometric	< 1.7	False	—	h)
Erg Chech 002	ungrouped achondrite	bulk	1.7–2.3	radiometric	60 ± 18	True	nebula	i)

Table B.3: Meteorite paleomagnetic measurements of achondrites. 'Age method' refers to whether remanence acquisition is dated using radiometric dating or thermal evolution and dynamo generation modelling. 'Nebula Correction' refers to whether paleointensities were multiplied by a factor of two to account for the unknown angle between the nebula field and the remanent magnetisation. 'Possible origin' denotes previous interpretations of paleomagnetic measurements. Remanences $< 1\,\mu$T have been interpreted as null remanences so the timing of remanence acquisition and possible source are blank. MG stands for Main Group. a) Nichols et al. (2018), b) Maurel et al. (2020), c) Maurel et al. (2021), d) Bryson et al. (2017), e) Nichols et al. (2021), f) Wang et al. (2017), g) Fu et al. (2012), h) Weiss et al. (2017), i) Maurel and Gattacceca (2024)

Appendix C

Supplementary Information for Chapter 4

C.1 Minimum water content for a wet planetesimal

For my modification to the prefactor in the viscosity law (Section 4.2.3.2) to reduce the viscosity of the wet planetesimals requires

$$1 \geq \frac{10}{C_H^{\mathrm{sol}}}. \tag{C.1}$$

After substituting for C_H^{sol} in terms of C_H^{tot} and C_H^{tot} in terms of X_{w}, this becomes

$$1 \geq \frac{10(1 - \phi + \frac{\phi}{D_{\mathrm{w}}})}{2 \times 10^4 X_{\mathrm{w}} \frac{M_{\mathrm{min}}}{M_{H_2O}}} \tag{C.2}$$

For $\phi = 0.5$, $D_{\mathrm{w}} = 0.006$, and KLB-1 peridotite mineralogy ($M_{\mathrm{min}} = 55.1$), X_{w} must exceed 0.0136 wt%. Water contents below this value are so low they do not affect the viscosity and the dry viscosity law should be used.

Group	Volatile loss[a]	$\log(fO_2)$[b] $/\Delta IW$	$\sigma_{\log(fO_2)}$[b] $/\Delta IW$	$\frac{M_{\mathrm{core}}}{M_{\mathrm{total}}}$[c] /%	$\sigma_{\frac{M_{\mathrm{core}}}{M_{\mathrm{total}}}}$[c] /%	X_{S} /wt%	$\sigma_{X_{\mathrm{S}}}$ /wt%	$\frac{r_{\mathrm{c}}}{r}$	$\sigma_{\frac{r_{\mathrm{c}}}{r}}$
NC									
IC	No	-2.0	0.2	21	1	16.0	3.0	0.50	0.01
IIAB	No	-3.2	0.3	22	13	11.5	5.5	0.50	0.06
IIIAB	Yes	-1.8	0.2	21	3	7.0	5.0	0.48	0.01
IVA	Yes	-2.1	0.2	19	4	4.7	4.3	0.46	0.02
Mean	No	-2.6	0.2	21.5	6.5	13.8	3.1	0.50	0.03
CC									
IIC	No	-1.2	0.1	18	5	6.0	2.0	0.45	0.02
IID	No	-1.5	0.1	14	1	6.0	6.0	0.41	0.01
IIF	No	-1.2	0.1	14	2	8.5	4.5	0.42	0.01
SBT	No	-1.2	0.1	7	1	8.0	2.0	0.33	0.01
IIIF	Yes	-2.2	0.2	18	2	3.5	1.5	0.45	0.01
IVB	Yes	-2.0	0.2	4	2	0.5	0.5	0.26	0.02
Mean	No	-1.3	0.1	13	1	7.1	2.0	0.4	0.01

Table C.1: Parent body oxidation state, core mass fraction, and core radius fraction of iron meteorites. [a]Goldstein et al. (2009), [b]Grewal et al. (2024), [c]Hilton et al. (2022). Volatile loss was inferred from depletion of Ge relative to Ni (Goldstein et al., 2009). $\frac{r_{\mathrm{c}}}{r}$ was calculated in this work for a mantle density of $3000\,\mathrm{kgm^{-3}}$ and core density that depends on sulfur content (Equation 2.37). Core sulfur contents for a range of fractional crystallisation models were collated from Hilton et al. (2022), Zhang et al. (2024) and Hirschmann et al. (2021). The maximum and minimum values from this data was used to calculate $X_{\mathrm{S}} = (X_{\mathrm{S,max}} + X_{\mathrm{S,min}})/2$ and $\sigma_{X_{\mathrm{S}}} = (X_{\mathrm{S,max}} - X_{\mathrm{S,min}})/2$

Appendix D

Supplementary Information for Chapter 5

D.1 Maximum height of a ferrovolcanic intrusion

Ferrovolcanism occurs when pockets of less dense, Fe-FeS melt become trapped within the more dense, solid iron at the top of the core and the excess pressure forces Fe-FeS melt into the mantle. Unlike silicate volcanism where melt is buoyant, the Fe-FeS melt is more dense than surrounding mantle and its upwards motion is driven purely by the excess pressure within the core. Therefore, the maximum height of a ferrovolcanic intrusion within the mantle, h, is governed by the depth of the melt pocket within the core, D, and the relative densities of the melt, ρ_f, solid iron, ρ_s, and mantle, ρ_m, (Johnson et al., 2020a; Courville et al., 2025)

$$h = D\frac{(\rho_\mathrm{s} - \rho_\mathrm{f})}{(\rho_\mathrm{f} - \rho_\mathrm{m})}. \tag{D.1}$$

The maximum depth of a melt pocket within the core is determined by the fraction of the core that has solidified at a given time. An expression for this depth can be derived by combining Equations 2.23 and 2.27 and assuming all solidified material remains at the CMB ($m_\mathrm{frac} = 0$),

$$D_\mathrm{max} = r_\mathrm{c}\left(1 - \left(\frac{X_\mathrm{S,0}}{X_\mathrm{S}}\right)^{\frac{1}{3}}\right). \tag{D.2}$$

r_c is the core radius, $X_\mathrm{S,0}$ is the initial core sulfur content and X_S is the current core sulfur content, which increases during core crystallisation. Together, Equations D.1 and D.2 can be combined to give the maximum height of a ferrovolcanic intrusion for a given sulfur content

$$h = r_\mathrm{c}\left(1 - \left(\frac{X_\mathrm{S,0}}{X_\mathrm{S}}\right)^{\frac{1}{3}}\right)\frac{(\rho_s - \rho_f)}{(\rho_f - \rho_\mathrm{m})}. \tag{D.3}$$

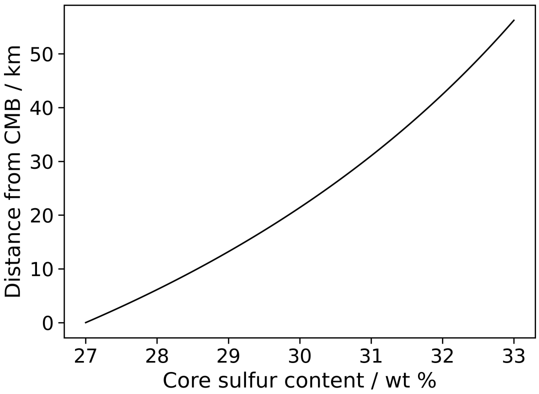

Figure D.1: Maximum distance of a ferrovolcanic intrusion above the CMB for the modal parameters of the Main Group pallasite parent body ($r = 400\,km$, $\frac{r_c}{r} = 0.5$). The initial core sulfur content is the minimum value consistent with the Main Group pallasite paleomagnetic record (27 wt%).

For the modal parameters of the Main Group pallasite parent body, the maximum value of h is 56 km (Figure D.1).

Appendix E

Code availability

The thermal evolution and dynamo generation model presented in this thesis is publicly available on the Hannah-RS/planetesimal-magnetic-history GitHub repository indexed by Zenodo (Sanderson, 2024). The parameter files for the runs presented in Chapter 2 and 3 are also available on this repository.

Code development and data analysis was undertaken using the following packages: Numpy (Harris et al., 2020), Scipy (Virtanen et al., 2020), and pandas (McKinney, 2010). Figures were made using Matplotlib (Hunter, 2007), seaborn (Waskom, 2021) and Crameri colormaps (Crameri, 2023).

Bibliography

Abrahams, J. N. and Nimmo, F. (2019). Ferrovolcanism: Iron Volcanism on Metallic Asteroids. *Geophysical Research Letters*, 46(10):5055–5064. Publisher: John Wiley & Sons, Ltd.

Agee, C. B., Li, J., Shannon, M. C., and Circone, S. (1995). Pressure-temperature phase diagram for the Allende meteorite. *Journal of Geophysical Research: Solid Earth*, 100(B9):17725–17740.

Alexander, C. M. O. (2019a). Quantitative models for the elemental and isotopic fractionations in chondrites: The carbonaceous chondrites. *Geochimica et Cosmochimica Acta*, 254:277–309.

Alexander, C. M. O. (2019b). Quantitative models for the elemental and isotopic fractionations in the chondrites: The non-carbonaceous chondrites. *Geochimica et Cosmochimica Acta*, 254:246–276.

Alexander, C. M. O., McKeegan, K. D., and Altwegg, K. (2018). Water Reservoirs in Small Planetary Bodies: Meteorites, Asteroids, and Comets. *Space Science Reviews*, 214(1):36.

Amano, K., Matsuoka, M., Nakamura, T., Kagawa, E., Fujioka, Y., Potin, S. M., Hiroi, T., Tatsumi, E., Milliken, R. E., Quirico, E., Beck, P., Brunetto, R., Uesugi, M., Takahashi, Y., Kawai, T., Yamashita, S., Enokido, Y., Wada, T., Furukawa, Y., Zolensky, M. E., Takir, D., Domingue, D. L., Jaramillo-Correa, C., Vilas, F., Hendrix, A. R., Kikuiri, M., Morita, T., Yurimoto, H., Noguchi, T., Okazaki, R., Yabuta, H., Naraoka, H., Sakamoto, K., Tachibana, S., Yada, T., Nishimura, M., Nakato, A., Miyazaki, A., Yogata, K., Abe, M., Okada, T., Usui, T., Yoshikawa, M., Saiki, T., Tanaka, S., Terui, F., Nakazawa, S., Watanabe, S.-i., and Tsuda, Y. (2023). Reassigning CI chondrite parent bodies based on reflectance spectroscopy of samples from carbonaceous asteroid Ryugu and meteorites. *Science Advances*, 9(49):eadi3789. Publisher: American Association for the Advancement of Science.

Asphaug, E. (2009). Growth and Evolution of Asteroids. *Annual Review of Earth and Planetary Sciences*, 37(Volume 37, 2009):413–448. Publisher: Annual Reviews.

Asphaug, E. and Reufer, A. (2014). Mercury and other iron-rich planetary bodies as relics of inefficient accretion. *Nature Geoscience*, 7(8):564–568. Publisher: Nature Publishing Group.

Aubert, J., Gastine, T., and Fournier, A. (2017). Spherical convective dynamos in the rapidly rotating asymptotic regime. *Journal of Fluid Mechanics*, 813:558–593. Publisher: Cambridge University Press.

Aubert, J., Labrosse, S., and Poitou, C. (2009). Modelling the palaeo-evolution of the geodynamo. *Geophysical Journal International*, 179(3):1414–1428. Publisher: Oxford Academic.

Aurnou, J. M. and King, E. M. (2017). The cross-over to magnetostrophic convection in planetary dynamo systems. *Proceedings of the Royal Society A: Mathematical, Physical and Engineering Sciences*, 473(2199):20160731. Publisher: Royal Society.

Badro, J., Siebert, J., and Nimmo, F. (2016). An early geodynamo driven by exsolution of mantle components from Earth's core. *Nature 2016 536:7616*, 536(7616):326–328. Publisher: Nature Publishing Group.

Bartels, K. S. and Grove, T. I. (1991). High pressure experiments on magnesian eucrite compositions: constraints on magmatic processes in the eucrite parent body. *Proceedings of Lunar and Planetary Science*, 21:351–365.

Bennett, N., Sio, C., Schauble, E., Lesher, C., Wimpenny, J., and Shahar, A. (2022). Iron isotope evidence of an impact origin for main-group pallasites. *Geochemical Perspectives Letters*, 23:6–10.

Bercovici, H. L., Elkins-Tanton, L. T., O'Rourke, J. G., and Schaefer, L. (2022). The effects of bulk composition on planetesimal core sulfur content and size. *Icarus*, 380:114976.

Bermingham, K. R., Füri, E., Lodders, K., and Marty, B. (2020). The NC-CC Isotope Dichotomy: Implications for the Chemical and Isotopic Evolution of the Early Solar System. *Space Science Reviews*, 216(8):133.

Bogard, D. D., Garrison, D. H., and McCoy, T. J. (2000). Chronology and petrology of silicates from IIE iron meteorites: evidence of a complex parent body evolution. *Geochimica et Cosmochimica Acta*, 64(12):2133–2154.

Bogdanovski, O. and Lugmair, G. W. (2004). Manganese-Chromium Isotope Systematics of Basaltic Achondrite Northwest Africa 011. In *35th Lunar and Planetary Science Conference*, page 1715. ADS Bibcode: 2004LPI....35.1715B.

Borlina, C. S., Weiss, B. P., Bryson, J. F. J., and Armitage, P. J. (2022). Lifetime of the Outer Solar System Nebula From Carbonaceous Chondrites. *Journal of Geophysical Research: Planets*, 127(7):e2021JE007139.

Borlina, C. S., Weiss, B. P., Bryson, J. F. J., Bai, X.-N., Lima, E. A., Chatterjee, N., and Mansbach, E. N. (2021). Paleomagnetic evidence for a disk substructure in the early solar system. *Science Advances*, 7(42):eabj6928. Publisher: American Association for the Advancement of Science.

Bottke, W. and Morbidelli, A. (2017). Using the Main Asteroid Belt to Constrain Planetesimal and Planet Formation. In Weiss, B. P. and Elkins-Tanton, L. T., editors, *Planetesimals: Early Differentiation and Consequences for Planets*, Cambridge Planetary Science, pages 38–68. Cambridge University Press, Cambridge.

Bottke, W. F., Walker, R. J., Day, J. M. D., Nesvorny, D., and Elkins-Tanton, L. (2010). Stochastic Late Accretion to Earth, the Moon, and Mars. *Science*, 330(6010):1527–1530. Publisher: American Association for the Advancement of Science.

Bouvier, A., Spivak-Birndorf, L. J., Brennecka, G. A., and Wadhwa, M. (2011). New constraints on early Solar System chronology from Al–Mg and U–Pb isotope systematics in the unique basaltic achondrite Northwest Africa 2976. *Geochimica et Cosmochimica Acta*, 75(18):5310–5323.

Braginsky, S. I. (1963). Structure of the F layer and reasons for convection in the Earth's core. *Soviet Phys. Dokl*, 149:8–10.

Bromiley, G., Varnam, M., Terasaki, H., Komabayashi, T., and Barosch, J. (2024). The extent of liquid immiscibility in planetesimal cores. *Geochemical Perspectives Letters*, 33:7–12.

Bromiley, G. D. (2023). The Geochemical Legacy of Low-Temperature, Percolation-Driven Core Formation in Planetesimals. *Earth, Moon, and Planets*, 127(2):4.

Bryson, J. F., Neufeld, J. A., and Nimmo, F. (2019a). Constraints on asteroid magnetic field evolution and the radii of meteorite parent bodies from thermal modelling. *Earth and Planetary Science Letters*, 521:68–78. Publisher: Elsevier B.V.

Bryson, J. F., Nichols, C. I., Herrero-Albillos, J., Kronast, F., Kasama, T., Alimadadi, H., Van Der Laan, G., Nimmo, F., and Harrison, R. J. (2015). Long-lived magnetism from solidification-driven convection on the pallasite parent body. *Nature 2015 517:7535*, 517(7535):472–475. Publisher: Nature Publishing Group.

Bryson, J. F. J., Nichols, C. I. O., and Mac Niocaill, C. (2023). A unified intensity of the magnetic field in the protoplanetary disk from the Winchcombe meteorite. *Meteoritics & Planetary Science*, n/a(n/a):1–22.

Bryson, J. F. J., Weiss, B. P., Biersteker, J. B., King, A. J., and Russell, S. S. (2020a). Constraints on the Distances and Timescales of Solid Migration in the Early Solar System from Meteorite Magnetism. *The Astrophysical Journal*, 896(2):103. Publisher: The American Astronomical Society.

Bryson, J. F. J., Weiss, B. P., Getzin, B., Abrahams, J. N. H., Nimmo, F., and Scholl, A. (2019b). Paleomagnetic Evidence for a Partially Differentiated Ordinary Chondrite Parent Asteroid. *Journal of Geophysical Research: Planets*, 124(7):1880–1898. _eprint: https://onlinelibrary.wiley.com/doi/pdf/10.1029/2019JE005951.

Bryson, J. F. J., Weiss, B. P., Harrison, R. J., Herrero-Albillos, J., and Kronast, F. (2017). Paleomagnetic evidence for dynamo activity driven by inward crystallisation of a metallic asteroid. *Earth and Planetary Science Letters*, 472:152–163.

Bryson, J. F. J., Weiss, B. P., Lima, E. A., Gattacceca, J., and Cassata, W. S. (2020b). Evidence for Asteroid Scattering and Distal Solar System Solids From Meteorite Paleomagnetism. *The Astrophysical Journal*, 892(2):126. Publisher: The American Astronomical Society.

Buffett, B. A., Huppert, H. E., Lister, J. R., and Woods, A. W. (1996). On the thermal evolution of the Earth's core. *Journal of Geophysical Research: Solid Earth*, 101(B4):7989–8006. Publisher: John Wiley & Sons, Ltd.

Buono, A. S. and Walker, D. (2011). The Fe-rich liquidus in the Fe–FeS system from 1bar to 10GPa. *Geochimica et Cosmochimica Acta*, 75(8):2072–2087.

Burkhardt, C., Dauphas, N., Hans, U., Bourdon, B., and Kleine, T. (2019). Elemental and isotopic variability in solar system materials by mixing and processing of primordial disk reservoirs. *Geochimica et Cosmochimica Acta*, 261:145–170.

Burns, J. A., Safronov, V. S., and Gold, T. (1973). Asteroid Nutation Angles. *Monthly Notices of the Royal Astronomical Society*, 165(4):403–411.

Bystricky, M., Lawlis, J., Mackwell, S., and Heidelbach, F. (2024). High-Temperature Deformation of Enstatite-Olivine Aggregates. *Journal of Geophysical Research: Solid Earth*, 129(3):e2023JB027699.

Cai, S., Qin, H., Wang, H., Deng, C., Yang, S., Xu, Y., Zhang, C., Tang, X., Gu, L., Li, X., Shen, Z., Zhang, M., He, K., Qi, K., Fan, Y., Dong, L., Hou, Y., Shi, P., Liu, S., Su, F., Chen, Y., Li, Q., Li, J., Mitchell, R. N., He, H., Li, C., Pan, Y., and Zhu, R. (2025). Persistent but weak magnetic field at the Moon's midstage revealed by Chang'e-5 basalt. *Science Advances*, 11(1):eadp3333. Publisher: American Association for the Advancement of Science.

Cambioni, S., Weiss, B. P., Biersteker, J. B., Asphaug, E., Elkins-Tanton, L. T., Courville, S. W., and Merayo, J. M. G. (2024). Formation of Asteroid (16) Psyche by a Giant Impact. In *AGU Fall Meeting 2024*, volume 2024, pages DI32A–03. ADS Bibcode: 2024AGUFMDI32A..03C.

Carporzen, L., Weiss, B. P., Elkins-Tanton, L. T., Shuster, D. L., Ebel, D., and Gattacceca, J. (2011). Magnetic evidence for a partially differentiated carbonaceous chondrite parent body. *Proceedings of the National Academy of Sciences*, 108(16):6386–6389. Publisher: Proceedings of the National Academy of Sciences.

Cassata, W. S., Renne, P. R., and Shuster, D. L. (2011). Argon diffusion in pyroxenes: Implications for thermochronometry and mantle degassing. *Earth and Planetary Science Letters*, 304(3):407–416.

Castillo-Rogez, J., Johnson, T. V., Lee, M. H., Turner, N. J., Matson, D. L., and Lunine, J. (2009). 26Al decay: Heat production and a revised age for Iapetus. *Icarus*, 204(2):658–662.

Castillo-Rogez, J. and Young, E. D. (2017). Origin and Evolution of Volatile-rich Asteroids. In *Planetesimals: Early Differentiation and Consequences for Planets*, pages 92–114. Cambridge University Press. Pages: 92-114 Publisher: Cambridge University Press.

Castillo-Rogez, J. C. and McCord, T. B. (2010). Ceres' evolution and present state constrained by shape data. *Icarus*, 205(2):443–459.

Cébron, D., Laguerre, R., Noir, J., and Schaeffer, N. (2019). Precessing spherical shells: flows, dissipation, dynamo and the lunar core. *Geophysical Journal International*, 219(Supplement_1):S34–S57.

Chabot, N. L. (2004). Sulfur contents of the parental metallic cores of magmatic iron meteorites. *Geochimica et Cosmochimica Acta*, 68(17):3607–3618.

Chabot, N. L. and Drake, M. J. (2000). Crystallization of magmatic iron meteorites: The effects of phosphorus and liquid immiscibility. *Meteoritics & Planetary Science*, 35(4):807–816.

Chapman, C. R., Veverka, J., Belton, M. J. S., Neukum, G., and Morrison, D. (1996). Cratering on Gaspra. *Icarus*, 120(1):231–245.

Cheng, J. S., Stellmach, S., Ribeiro, A., Grannan, A., King, E. M., and Aurnou, J. M. (2015). Laboratory-numerical models of rapidly rotating convection in planetary cores. *Geophysical Journal International*, 201(1):1–17.

Chladni, E. F. F. (1794). *Ueber den Ursprung der von Pallas gefundenen und anderer ihr ähnlicher Eisenmassen, und über einige damit in Verbindung stehende Naturerscheinungen.* bey Johann Friedrich Hartknoch.

Christensen, U. R. (2009). Dynamo Scaling Laws and Applications to the Planets. *Space Science Reviews 2009 152:1*, 152(1):565–590.

Christensen, U. R. (2015). Iron snow dynamo models for Ganymede. *Icarus*, 247:248–259. Publisher: Academic Press Inc.

Christensen, U. R. and Aubert, J. (2006). Scaling properties of convection-driven dynamos in rotating spherical shells and application to planetary magnetic fields. *Geophysical Journal International*, 166(1):97–114.

Clayton, R. N. and Mayeda, T. K. (1996). Oxygen isotope studies of achondrites. *Geochimica et Cosmochimica Acta*, 60(11):1999–2017.

Connelly, J. N., Bizzarro, M., Krot, A. N., Nordlund, Å., Wielandt, D., and Ivanova, M. A. (2012). The Absolute Chronology and Thermal Processing of Solids in the Solar Protoplanetary Disk. *Science*, 338(6107):651–655. Publisher: American Association for the Advancement of Science.

Cook, D. L., Meyer, B. S., and Schönbächler, M. (2021). Iron and Nickel Isotopes in IID and IVB Iron Meteorites: Evidence for Admixture of an SN II Component and Implications for the Initial Abundance of 60Fe. *The Astrophysical Journal*, 917(2):59. Publisher: The American Astronomical Society.

Corgne, A., Wood, B. J., and Fei, Y. (2008). C- and S-rich molten alloy immiscibility and core formation of planetesimals. *Geochimica et Cosmochimica Acta*, 72(9):2409–2416.

Cournede, C., Gattacceca, J., Gounelle, M., Rochette, P., Weiss, B. P., and Zanda, B. (2015). An early solar system magnetic field recorded in CM chondrites. *Earth and Planetary Science Letters*, 410:62–74.

Cournède, C., Gattacceca, J., Rochette, P., and Shuster, D. L. (2020). Paleomagnetism of Rumuruti chondrites suggests a partially differentiated parent body. *Earth and Planetary Science Letters*, 533:116042.

Courville, S. W., O'Rourke, J. G., Castillo-Rogez, J. C., Fu, R. R., Oran, R., Weiss, B. P., and Elkins-Tanton, L. T. (2022). Acquisition and Preservation of Remanent Magnetization in Carbonaceous Asteroids. *Nature Astronomy*, 6(12):1387–1397. Number: 12 Publisher: Nature Publishing Group.

Courville, S. W., Sanderson, H. R., Bierson, C. J., Elkins-Tanton, L. T., Oran, R., O'Rourke, J. G., Russell, C. T., Weiss, B. P., and Williams, D. A. (2025). Ferromagmatic Intrusions on Asteroid (16) Psyche May Be Magnetized. *Journal of Geophysical Research: Planets*, 130(8):e2025JE009031. _eprint: https://agupubs.onlinelibrary.wiley.com/doi/pdf/10.1029/2025JE009031.

Crameri, F. (2023). Scientific colour maps. Language: eng.

Dauphas, N., Hopp, T., and Nesvorný, D. (2024). Bayesian inference on the isotopic building blocks of Mars and Earth. *Icarus*, 408:115805.

Davaille, A. and Jaupart, C. (1993). Transient high-Rayleigh-number thermal convection with large viscosity variations. *Journal of Fluid Mechanics*, 253:141–166. Publisher: Cambridge University Press.

Davidson, P. A. (2013). Scaling laws for planetary dynamos. *Geophysical Journal International*, 195(1):67–74.

Davies, C. J., Bono, R. K., Meduri, D. G., Aubert, J., Greenwood, S., and Biggin, A. J. (2022). Dynamo constraints on the long-term evolution of Earth's magnetic field strength. *Geophysical Journal International*, 228(1):316–336.

Davies, C. J. and Pommier, A. (2018). Iron snow in the Martian core? *Earth and Planetary Science Letters*, 481:189–200. Publisher: Elsevier.

Davis, F. A., Tangeman, J. A., Tenner, T. J., and Hirschmann, M. M. (2009). The composition of KLB-1 peridotite. *American Mineralogist*, 94(1):176–180. Publisher: De Gruyter.

de Wijs, G. A., Kresse, G., Vočadlo, L., Dobson, D., Alfè, D., Gillan, M. J., and Price, G. D. (1998). The viscosity of liquid iron at the physical conditions of the Earth's core. *Nature*, 392(6678):805–807. Number: 6678 Publisher: Nature Publishing Group.

Deschamps, F. and Vilella, K. (2021). Scaling Laws for Mixed-Heated Stagnant-Lid Convection and Application to Europa. *Journal of Geophysical Research: Planets*, 126(10):e2021JE006963.

Devienne, J. A. P. M., Berndt, T. A., Williams, W., and Chen, S. (2024). From Disorder to Order: Inheritance of Magnetic Remanence in Tetrataenite-Bearing Meteorites From Multi-Phase Micromagnetic Modeling. *Journal of Geophysical Research: Planets*, 129(6):e2023JE008268.

Dibb, S. D., Asphaug, E., Bell, J. F., Binzel, R. P., Bottke, W. F., Cambioni, S., Christoph, J. M., Elkins-Tanton, L. T., Jaumann, R., Lawrence, D. J., Oran, R., O'Rourke, J. G., Polansky, C., Weiss, B. P., Wieczorek, M., and Williams, D. A. (2024). A Post-Launch Summary of the Science of NASA's Psyche Mission. *AGU Advances*, 5(2):e2023AV001077.

Dibb, S. D., Bell III, J. F., Elkins-Tanton, L. T., and Williams, D. A. (2023). Visible to Near-Infrared Reflectance Spectroscopy of Asteroid (16) Psyche: Implications for the Psyche Mission's Science Investigations. *Earth and Space Science*, 10(1):e2022EA002694.

Dodds, K. H. (2022). *Deciphering the thermal evolution of small planetary bodies.* PhD thesis, University of Cambridge, University of Cambridge.

Dodds, K. H. (2024). The Direction of Core Solidification in Asteroids: Implications for Dynamo Generation. In *AGU Fall Meeting 2024*, Washington DC.

Dodds, K. H., Bryson, J. F., Neufeld, J. A., and Harrison, R. J. (2021). The Thermal Evolution of Planetesimals During Accretion and Differentiation: Consequences for Dynamo Generation by Thermally-Driven Convection. *Journal of Geophysical Research: Planets*, 126(3). Publisher: Blackwell Publishing Ltd.

Dodds, K. H., Bryson, J. F. J., Neufeld, J. A., and Harrison, R. J. (2025). The direction of core solidification in asteroids: Implications for dynamo generation. *Icarus*, 425:116319.

Doyle, P. M., Jogo, K., Nagashima, K., Krot, A. N., Wakita, S., Ciesla, F. J., and Hutcheon, I. D. (2015). Early aqueous activity on the ordinary and carbonaceous chondrite parent bodies recorded by fayalite. *Nature Communications*, 6(1):7444. Publisher: Nature Publishing Group.

Drążkowska, J., Alibert, Y., and Moore, B. (2016). Close-in planetesimal formation by pile-up of drifting pebbles. *Astronomy & Astrophysics*, 594:A105. Publisher: EDP Sciences.

Drążkowska, J., Bitsch, B., Lambrechts, M., Mulders, G. D., Harsono, D., Vazan, A., Liu, B., Ormel, C. W., Kretke, K., and Morbidelli, A. (2022). Planet Formation Theory in the Era of ALMA and Kepler: from Pebbles to Exoplanets. In Inutsuka, S.-I., Aikawa, Y., Muto, T., Tomida, K., and Tamura, M., editors, *Protostars and Planets VII*, Astronomical Society of the Pacific. Astronommical Society of the Pacific, San Francisco. arXiv:2203.09759 [astro-ph].

Drążkowska, J. and Dullemond, C. P. (2018). Planetesimal formation during protoplanetary disk buildup. *Astronomy & Astrophysics*, 614:A62. Publisher: EDP Sciences.

Einsle, J. F., Eggeman, A. S., Martineau, B. H., Saghi, Z., Collins, S. M., Blukis, R., Bagot, P. A. J., Midgley, P. A., and Harrison, R. J. (2018). Nanomagnetic properties of the meteorite cloudy zone. *Proceedings of the National Academy of Sciences*, 115(49):E11436–E11445. Publisher: Proceedings of the National Academy of Sciences.

Elkins-Tanton, L. T., Asphaug, E., Bell III, J. F., Bercovici, H., Bills, B., Binzel, R., Bottke, W. F., Dibb, S., Lawrence, D. J., Marchi, S., McCoy, T. J., Oran, R., Park, R. S., Peplowski, P. N., Polanskey, C. A., Prettyman, T. H., Russell, C. T., Schaefer, L., Weiss, B. P., Wieczorek, M. A., Williams, D. A., and Zuber, M. T. (2020). Observations, Meteorites, and Models: A Preflight Assessment of the Composition and Formation of (16) Psyche. *Journal of Geophysical Research: Planets*, 125(3):e2019JE006296.

Elkins-Tanton, L. T., Weiss, B. P., and Zuber, M. T. (2011). Chondrites as samples of differentiated planetesimals. *Earth and Planetary Science Letters*, 305(1):1–10.

Evans, A. J. and Tikoo, S. M. (2022). An episodic high-intensity lunar core dynamo. *Nature Astronomy*.

Fang, L., Moynier, F., Chaussidon, M., Limare, A., Makhatadze, G. V., and Villeneuve, J. (2025). The initial solar system abundance of 60Fe and early core formation of the first asteroids. *Science Advances*, 11(2):eadp9381. Publisher: American Association for the Advancement of Science.

Faroughi, S. A. and Huber, C. (2015). A generalized equation for rheology of emulsions and suspensions of deformable particles subjected to simple shear at low Reynolds number. *Rheologica Acta*, 54(2):85–108.

Ferrick, A. L. and Korenaga, J. (2023). Generalizing Scaling Laws for Mantle Convection With Mixed Heating. *Journal of Geophysical Research: Solid Earth*, 128(5):e2023JB026398.

Frank-Kamenetskii, D. (1969). *Diffusion and Heat Exchange in Chemical Kinetics*. Plenum Press, New York. (translation by JP Appleton).

Fu, R. R. and Elkins-Tanton, L. T. (2014). The fate of magmas in planetesimals and the retention of primitive chondritic crusts. *Earth and Planetary Science Letters*, 390:128–137.

Fu, R. R., Kehayias, P., Weiss, B. P., Schrader, D. L., Bai, X.-N., and Simon, J. B. (2020). Weak Magnetic Fields in the Outer Solar Nebula Recorded in CR Chondrites. *Journal of Geophysical Research: Planets*, 125(5):e2019JE006260.

Fu, R. R., Lima, E. A., and Weiss, B. P. (2014a). No nebular magnetization in the Allende CV carbonaceous chondrite. *Earth and Planetary Science Letters*, 404:54–66.

Fu, R. R., Volk, M. W. R., Bilardello, D., Libourel, G., Lesur, G. R. J., and Dor, O. B. (2021). The Fine-Scale Magnetic History of the Allende Meteorite: Implications for the Structure of the Solar Nebula. *AGU Advances*, 2(3):e2021AV000486. Publisher: John Wiley & Sons, Ltd ISBN: 10.1029/2021.

Fu, R. R., Weiss, B. P., Lima, E. A., Harrison, R. J., Bai, X.-N., Desch, S. J., Ebel, D. S., Suavet, C., Wang, H., Glenn, D., Le Sage, D., Kasama, T., Walsworth, R. L., and Kuan, A. T. (2014b). Solar nebula magnetic fields recorded in the Semarkona meteorite. *Science*, 346(6213):1089–1092. Publisher: American Association for the Advancement of Science.

Fu, R. R., Weiss, B. P., Shuster, D. L., Gattacceca, J., Grove, T. L., Suavet, C., Lima, E. A., Li, L., and Kuan, A. T. (2012). An Ancient Core Dynamo in Asteroid Vesta. *Science*, 338(6104):238–241. Publisher: American Association for the Advancement of Science.

Fu, R. R., Young, E. D., Greenwood, R. C., and Elkins-Tanton, L. T. (2017). Silicate Melting and Volatile Loss During Differentiation in Planetesimals. In *Planetesimals: Early Differentiation and Consequences for Planets*, pages 115–135. Cambridge University Press.

Gattacceca, J., Weiss, B. P., and Gounelle, M. (2016). New constraints on the magnetic history of the CV parent body and the solar nebula from the Kaba meteorite. *Earth and Planetary Science Letters*, 455:166–175.

Ghosh, A. and McSween, H. Y. (1998). A Thermal Model for the Differentiation of Asteroid 4 Vesta, Based on Radiogenic Heating. *Icarus*, 134(2):187–206.

Ghosh, A. and McSween, H. Y. (1999). Temperature dependence of specific heat capacity and its effect on asteroid thermal models. *Meteoritics & Planetary Science*, 34(1):121–127.

Giordano, D., Russell, J. K., and Dingwell, D. B. (2008). Viscosity of magmatic liquids: A model. *Earth and Planetary Science Letters*, 271(1):123–134.

Goldberg, E., Uchiyama, A., and Brown, H. (1951). The distribution of nickel, cobalt, gallium, palladium and gold in iron meteorites. *Geochimica et Cosmochimica Acta*, 2(1):1–25.

Goldstein, J. I., Scott, E. R. D., and Chabot, N. L. (2009). Iron meteorites: Crystallization, thermal history, parent bodies, and origin. *Geochemistry*, 69(4):293–325.

Goldstein, J. I., Yang, J., and Scott, E. R. D. (2014). Determining cooling rates of iron and stony-iron meteorites from measurements of Ni and Co at kamacite–taenite interfaces. *Geochimica et Cosmochimica Acta*, 140:297–320.

Greenwood, R. C., Burbine, T. H., Miller, M. F., and Franchi, I. A. (2017). Melting and differentiation of early-formed asteroids: The perspective from high precision oxygen isotope studies. *Geochemistry*, 77(1):1–43.

Greenwood, R. C., Franchi, I. A., Jambon, A., Barrat, J. A., and Burbine, T. H. (2006). Oxygen Isotope Variation in Stony-Iron Meteorites. *Science*, 313(5794):1763–1765. Publisher: American Association for the Advancement of Science.

Grewal, D. S. and Manilal, V. (2025). Implications of Differentiated Late Accretion for the Volatile Inventory of the Bulk Silicate Earth. *The Planetary Science Journal*, 6(1):13. Publisher: IOP Publishing.

Grewal, D. S., Nie, N. X., Zhang, B., Izidoro, A., and Asimow, P. D. (2024). Accretion of the earliest inner Solar System planetesimals beyond the water snowline. *Nature Astronomy*, pages 1–8. Publisher: Nature Publishing Group.

Grott, M. and Breuer, D. (2008). The evolution of the martian elastic lithosphere and implications for crustal and mantle rheology. *Icarus*, 193(2):503–515.

Grott, M., Breuer, D., and Laneuville, M. (2011). Thermo-chemical evolution and global contraction of mercury. *Earth and Planetary Science Letters*, 307(1):135–146.

Guarguaglini, M., Soubiran, F., Hernandez, J.-A., Benuzzi-Mounaix, A., Bolis, R., Brambrink, E., Vinci, T., and Ravasio, A. (2021). Electrical conductivity of warm dense silica from double-shock experiments. *Nature Communications*, 12(1):840. Publisher: Nature Publishing Group.

Gubbins, D. (1977). Energetics of the Earth's core. *Journal of Geophysics*, 43(1):453–464.

Gubbins, D., Alfè, D., Masters, G., Price, G. D., and Gillan, M. J. (2003). Can the Earth's dynamo run on heat alone? *Geophysical Journal International*, 155(2):609–622.

Harries, D., Zhao, X., and Franchi, I. (2023). Upper limits of water contents in olivine and orthopyroxene of equilibrated chondrites and several achondrites. *Meteoritics & Planetary Science*, 58(5):705–721. _eprint: https://onlinelibrary.wiley.com/doi/pdf/10.1111/maps.13980.

Harris, C. R., Millman, K. J., van der Walt, S. J., Gommers, R., Virtanen, P., Cournapeau, D., Wieser, E., Taylor, J., Berg, S., Smith, N. J., Kern, R., Picus, M., Hoyer, S., van Kerkwijk, M. H., Brett, M., Haldane, A., del Río, J. F., Wiebe, M., Peterson, P., Gérard-Marchant, P., Sheppard, K., Reddy, T., Weckesser, W., Abbasi, H., Gohlke, C., and Oliphant, T. E. (2020). Array programming with NumPy. *Nature*, 585(7825):357–362. Publisher: Nature Publishing Group.

Hellmann, J. L., Van Orman, J. A., and Kleine, T. (2024). Hf-W isotope systematics of enstatite chondrites: Parent body chronology and origin of Hf-W fractionations among chondritic meteorites. *Earth and Planetary Science Letters*, 626:118518.

Henke, S., Gail, H. P., Trieloff, M., and Schwarz, W. H. (2013). Thermal evolution model for the H chondrite asteroid-instantaneous formation versus protracted accretion. *Icarus*, 226(1):212–228.

Henke, S., Gail, H.-P., Trieloff, M., Schwarz, W. H., and Kleine, T. (2012). Thermal evolution and sintering of chondritic planetesimals. *Astronomy & Astrophysics*, 537:A45. Publisher: EDP Sciences.

Hevey, P. J. and Sanders, I. S. (2006). A model for planetesimal meltdown by 26Al and its implications for meteorite parent bodies. *Meteoritics & Planetary Science*, 41(1):95–106.

Hilton, C. D., Ash, R. D., and Walker, R. J. (2022). Chemical characteristics of iron meteorite parent bodies. *Geochimica et Cosmochimica Acta*, 318:112–125.

Hilton, C. D., Bermingham, K. R., Walker, R. J., and McCoy, T. J. (2019). Genetics, crystallization sequence, and age of the South Byron Trio iron meteorites: New insights to carbonaceous chondrite (CC) type parent bodies. *Geochimica et Cosmochimica Acta*, 251:217–228.

Hirschmann, M. M. (2000). Mantle solidus: Experimental constraints and the effects of peridotite composition. *Geochemistry, Geophysics, Geosystems*, 1(10).

Hirschmann, M. M., Bergin, E. A., Blake, G. A., Ciesla, F. J., and Li, J. (2021). Early volatile depletion on planetesimals inferred from C–S systematics of iron meteorite parent bodies. *Proceedings of the National Academy of Sciences*, 118(13):e2026779118. Publisher: Proceedings of the National Academy of Sciences.

Hirschmann, M. M., Tenner, T., Aubaud, C., and Withers, A. C. (2009). Dehydration melting of nominally anhydrous mantle: The primacy of partitioning. *Physics of the Earth and Planetary Interiors*, 176(1):54–68.

Hirth, G. and Kohlstedt, D. (2003). Rheology of the Upper Mantle and the Mantle Wedge: A View from the Experimentalists. In *Inside the Subduction Factory*, volume 138 of *Geophysical Monograph Series*, pages 83–105. American Geophysical Union. doi:10.1029/138GM06.

Hirth, G. and Kohlstedt, D. L. (1996). Water in the oceanic upper mantle: implications for rheology, melt extraction and the evolution of the lithosphere. *Earth and Planetary Science Letters*, 144(1):93–108.

Howard, L. N. (1966). Convection at high Rayleigh number. In Görtler, H., editor, *Applied Mechanics*, pages 1109–1115, Berlin, Heidelberg. Springer.

Hu, X., Zhu, Z., Okuzumi, S., Bai, X.-N., Wang, L., Tomida, K., and Stone, J. M. (2019). Nonideal MHD Simulation of HL Tau Disk: Formation of Rings. *The Astrophysical Journal*, 885(1):36. Publisher: The American Astronomical Society.

Huguet, L., Le Bars, M., and Deguen, R. (2023). A Laboratory Model for Iron Snow in Planetary Cores. *Geophysical Research Letters*, 50(24):e2023GL105697.

Hunter, J. D. (2007). Matplotlib: A 2D Graphics Environment. *Computing in Science & Engineering*, 9(3):90–95.

Hutchison, R. (2004). *Meteorites: a petrologic, chemical and isotopic synthesis*. Number 2 in Cambridge planetary science. Cambridge University Press, Cambridge (GB).

Hyde, B. C., Moser, D. E., Tait, K. T., Darling, J. R., Yin, Q.-Z., Sanborn, M. E., Banerjee, N. R., Ali, A., Jabeen, I., and Moreira, H. (2022). A detailed record of early solar system melting in the carbonaceous achondrites Northwest Africa 7680 and 6962. *Meteoritics & Planetary Science*, 57(9):1722–1744.

Izidoro, A., Dasgupta, R., Raymond, S. N., Deienno, R., Bitsch, B., and Isella, A. (2022). Planetesimal rings as the cause of the Solar System's planetary architecture. *Nature Astronomy*, 6(3):357–366. Publisher: Nature Publishing Group.

Johansen, A., Blum, J., Tanaka, H., Ormel, C., Bizzarro, M., and Rickman, H. (2014). The multifaceted planetesimal formation process. In Beuther, H., Klessen, R., Dullemond, C. P., and Henning, T., editors, *Protostars and Planets VI*. University of Arizona Press. arXiv:1402.1344 [astro-ph].

Johnson, B. C., Sori, M. M., and Evans, A. J. (2020a). Ferrovolcanism on metal worlds and the origin of pallasites. *Nature Astronomy*, 4(1):41–44. Publisher: Nature Publishing Group.

Johnson, C. L., Mittelholz, A., Langlais, B., Russell, C. T., Ansan, V., Banfield, D., Chi, P. J., Fillingim, M. O., Forget, F., Haviland, H. F., Golombek, M., Joy, S., Lognonné, P., Liu, X., Michaut, C., Pan, L., Quantin-Nataf, C., Spiga, A., Stanley, S., Thorne, S. N., Wieczorek, M. A., Yu, Y., Smrekar, S. E., and Banerdt, W. B. (2020b). Crustal and time-varying magnetic fields at the InSight landing site on Mars. *Nature Geoscience*, 13(3):199–204. Publisher: Nature Publishing Group.

Joy, K. H., Gross, J., Korotev, R. L., Zeigler, R. A., McCubbin, F. M., Snape, J. F., Curran, N. M., Pernet-Fisher, J. F., and Arai, T. (2023). Lunar Meteorites. *Reviews in Mineralogy and Geochemistry*, 89(1):509–562.

Jung, J.-I., Tikoo, S. M., Burns, D., Váci, Z., and Krawczynski, M. J. (2024). Assessing lunar paleointensity variability during the 3.9 - 3.5 Ga high field epoch. *Earth and Planetary Science Letters*, 638:118757.

Kaminski, E., Limare, A., Kenda, B., and Chaussidon, M. (2020). Early accretion of planetesimals unraveled by the thermal evolution of the parent bodies of magmatic iron meteorites. *Earth and Planetary Science Letters*, 548:116469.

Karato, S.-i. and Wu, P. (1993). Rheology of the Upper Mantle: A Synthesis. *Science*, 260(5109):771–778. Publisher: American Association for the Advancement of Science.

Katz, R. F., Spiegelman, M., and Langmuir, C. H. (2003). A new parameterization of hydrous mantle melting. *Geochemistry, Geophysics, Geosystems*, 4(9).

Keil, K. (2012). Angrites, a small but diverse suite of ancient, silica-undersaturated volcanic-plutonic mafic meteorites, and the history of their parent asteroid. *Geochemistry*, 72(3):191–218.

Keil, K. and Wilson, L. (1993). Explosive volcanism and the compositions of cores of differentiated asteroids. *Earth and Planetary Science Letters*, 117(1):111–124.

Keller, T., Katz, R. F., and Hirschmann, M. M. (2017). Volatiles beneath mid-ocean ridges: Deep melting, channelised transport, focusing, and metasomatism. *Earth and Planetary Science Letters*, 464:55–68.

Kiefer, W. S., Filiberto, J., Sandu, C., and Li, Q. (2015). The effects of mantle composition on the peridotite solidus: Implications for the magmatic history of Mars. *Geochimica et Cosmochimica Acta*, 162:247–258.

Kleine, T., Hans, U., Irving, A. J., and Bourdon, B. (2012). Chronology of the angrite parent body and implications for core formation in protoplanets. *Geochimica et Cosmochimica Acta*, 84:186–203.

Kodolányi, J., Hoppe, P., Vollmer, C., Berndt, J., and Müller, M. (2022a). The Early Solar System Abundance of Iron-60: New Constraints from Chondritic Silicates. *The Astrophysical Journal*, 940(1):95. Publisher: The American Astronomical Society.

Kodolányi, J., Hoppe, P., Vollmer, C., Berndt, J., and Müller, M. (2022b). Iron-60 in the Early Solar System Revisited: Insights from In Situ Isotope Analysis of Chondritic Troilite. *The Astrophysical Journal*, 929(1):107. Publisher: The American Astronomical Society.

Konôpková, Z., McWilliams, R. S., Gómez-Pérez, N., and Goncharov, A. F. (2016). Direct measurement of thermal conductivity in solid iron at planetary core conditions. *Nature*, 534(7605):99–101. Publisher: Nature Publishing Group.

Kracher, A. and Wasson, J. T. (1982). The role of S in the evolution of the parental cores of the iron meteorites. *Geochimica et Cosmochimica Acta*, 46(12):2419–2426.

Krot, A. N., Keil, K., Scott, E. R. D., Goodrich, C. A., and Weisberg, M. K. (2014). 1.1 - Classification of Meteorites and Their Genetic Relationships. In Holland, H. D. and Turekian, K. K., editors, *Treatise on Geochemistry (Second Edition)*, pages 1–63. Elsevier, Oxford.

Kruijer, T. S., Burkhardt, C., Borg, L. E., and Kleine, T. (2022). Tungsten and molybdenum isotopic evidence for an impact origin of pallasites. *Earth and Planetary Science Letters*, 584:117440.

Kruijer, T. S., Kleine, T., and Borg, L. E. (2020). The great isotopic dichotomy of the early Solar System. *Nature Astronomy*, 4(1):32–40. Publisher: Nature Publishing Group.

Kruijer, T. S., Touboul, M., Fischer-Gödde, M., Bermingham, K. R., Walker, R. J., and Kleine, T. (2014). Protracted core formation and rapid accretion of protoplanets. *Science*, 344(6188):1150–1154. Publisher: American Association for the Advancement of Science.

Lambrechts, M., Johansen, A., and Morbidelli, A. (2014). Separating gas-giant and ice-giant planets by halting pebble accretion. *Astronomy & Astrophysics*, 572:A35. Publisher: EDP Sciences.

Landeau, M., Fournier, A., Nataf, H.-C., Cébron, D., and Schaeffer, N. (2022). Sustaining Earth's magnetic dynamo. *Nature Reviews Earth & Environment 2022*, pages 1–15. Publisher: Nature Publishing Group ISBN: 0123456789.

Lauretta, D. S., Connolly Jr, H. C., Aebersold, J. E., Alexander, C. M. O., Ballouz, R.-L., Barnes, J. J., Bates, H. C., Bennett, C. A., Blanche, L., Blumenfeld, E. H., Clemett, S. J., Cody, G. D., DellaGiustina, D. N., Dworkin, J. P., Eckley, S. A., Foustoukos, D. I., Franchi, I. A., Glavin, D. P., Greenwood, R. C., Haenecour, P., Hamilton, V. E., Hill, D. H., Hiroi, T., Ishimaru, K., Jourdan, F., Kaplan, H. H., Keller, L. P., King, A. J., Koefoed, P., Kontogiannis, M. K., Le, L., Macke, R. J., McCoy, T. J., Milliken, R. E., Najorka, J., Nguyen, A. N., Pajola, M., Polit, A. T., Righter, K., Roper, H. L., Russell, S. S., Ryan, A. J., Sandford, S. A., Schofield, P. F., Schultz, C. D., Seifert, L. B., Tachibana, S., Thomas-Keprta, K. L., Thompson, M. S., Tu, V., Tusberti, F., Wang, K., Zega, T. J., Wolner, C. W. V., and Team, t. O.-R. S. A. (2024). Asteroid (101955) Bennu in the laboratory: Properties of the sample collected by OSIRIS-REx. *Meteoritics & Planetary Science*, n/a(n/a).

Le Bars, M., Cébron, D., and Gal, P. L. (2015). Flows Driven by Libration, Precession, and Tides. *Annual Review of Fluid Mechanics*, 47(Volume 47, 2015):163–193. Publisher: Annual Reviews.

Le Bars, M., Wieczorek, M. A., Karatekin, Ö., Cébron, D., and Laneuville, M. (2011). An impact-driven dynamo for the early Moon. *Nature*, 479(7372):215–218. Publisher: Nature Publishing Group.

Lesher, C. E. and Spera, F. J. (2015). Chapter 5 - Thermodynamic and Transport Properties of Silicate Melts and Magma. In Sigurdsson, H., editor, *The Encyclopedia of Volcanoes (Second Edition)*, pages 113–141. Academic Press, Amsterdam.

Levison, H. F., Olkin, C. B., Noll, K. S., Marchi, S., Iii, J. F. B., Bierhaus, E., Binzel, R., Bottke, W., Britt, D., Brown, M., Buie, M., Christensen, P., Emery, J., Grundy, W., Hamilton, V. E., Howett, C., Mottola, S., Pätzold, M., Reuter, D., Spencer, J., Statler, T. S., Stern, S. A., Sunshine, J., Weaver, H., and Wong, I. (2021). Lucy Mission to the Trojan Asteroids: Science Goals. *The Planetary Science Journal*, 2(5):171. Publisher: IOP Publishing.

Lherm, V., Nakajima, M., and Blackman, E. G. (2024). Thermal and magnetic evolution of an Earth-like planet with a basal magma ocean. *Physics of the Earth and Planetary Interiors*, 356:107267.

Li, J. and Fei, Y. (2014). 3.15 - Experimental Constraints on Core Composition. In Holland, H. D. and Turekian, K. K., editors, *Treatise on Geochemistry (Second Edition)*, pages 527–557. Elsevier, Oxford.

Lichtenberg, T., Drążkowska, J., Schönbächler, M., Golabek, G. J., and Hands, T. O. (2021). Bifurcation of planetary building blocks during Solar System formation. *Science*, 371(6527):365–370. Publisher: American Association for the Advancement of Science.

Lichtenberg, T., Golabek, G. J., Burn, R., Meyer, M. R., Alibert, Y., Gerya, T. V., and Mordasini, C. (2019a). A water budget dichotomy of rocky protoplanets from 26Al-heating. *Nature Astronomy 2019 3:4*, 3(4):307–313.

Lichtenberg, T., Keller, T., Katz, R. F., Golabek, G. J., and Gerya, T. V. (2019b). Magma ascent in planetesimals: Control by grain size. *Earth and Planetary Science Letters*, 507:154–165.

Lister, J. R. (2003). Expressions for the dissipation driven by convection in the Earth's core. *Physics of the Earth and Planetary Interiors*, 140(1):145–158.

Lodders, K. (2021). Relative Atomic Solar System Abundances, Mass Fractions, and Atomic Masses of the Elements and Their Isotopes, Composition of the Solar Photosphere, and Compositions of the Major Chondritic Meteorite Groups. *Space Science Reviews*, 217(3):44.

Lovering, J. F., Nichiporuk, W., Chodos, A., and Brown, H. (1957). The distribution of gallium, germanium, cobalt, chromium, and copper in iron and stony-iron meteorites in relation to nickel content and structure. *Geochimica et Cosmochimica Acta*, 11(4):263–278.

Ma, N., Neumann, W., Néri, A., Schwarz, W., Ludwig, T., Trieloff, M., Klahr, H., and Bouvier, A. (2022). Early formation of primitive achondrites in an outer region of the protoplanetary disc. *Geochemical Perspectives Letters*, 23:33–37.

MacPherson, G. J., Davis, A. M., and Zinner, E. K. (1995). The distribution of aluminum-26 in the early Solar System—A reappraisal. *Meteoritics*, 30(4):365–386.

Marchi, S., Canup, R. M., and Walker, R. J. (2018). Heterogeneous delivery of silicate and metal to the Earth by large planetesimals. *Nature Geoscience*, 11(1):77–81. Publisher: Nature Publishing Group.

Maurel, C., Bryson, J. F. J., Lyons, R. J., Ball, M. R., Chopdekar, R. V., Scholl, A., Ciesla, F. J., Bottke, W. F., and Weiss, B. P. (2020). Meteorite evidence for partial differentiation and protracted accretion of planetesimals. *Science Advances*, 6(30):eaba1303. Publisher: American Association for the Advancement of Science.

Maurel, C., Bryson, J. F. J., Shah, J., Chopdekar, R. V., T. Elkins-Tanton, L., A. Raymond, C., and Weiss, B. P. (2021). A Long-Lived Planetesimal Dynamo Powered by Core Crystallization. *Geophysical Research Letters*, 48(6):e2020GL091917.

Maurel, C. and Gattacceca, J. (2023). Estimating Paleointensities From Chemical Remanent Magnetizations of Magnetite Using Non-Heating Methods. *Journal of Geophysical Research: Planets*, 128(6):e2023JE007779.

Maurel, C. and Gattacceca, J. (2024). A 4,565-My-old record of the solar nebula field. *Proceedings of the National Academy of Sciences*, 121(12):e2312802121. Publisher: Proceedings of the National Academy of Sciences.

Maurel, C., Weiss, B. P., and Bryson, J. F. J. (2019). Meteorite cloudy zone formation as a quantitative indicator of paleomagnetic field intensities and cooling rates on planetesimals. *Earth and Planetary Science Letters*, 513:166–175.

McCoy, T. J., Dickinson, T. L., and Lofgren, G. E. (1999). Partial melting of the Indarch (EH4) meteorite: A textural, chemical, and phase relations view of melting and melt migration. *Meteoritics & Planetary Science*, 34(5):735–746.

McCubbin, F. M. and Barnes, J. J. (2019). Origin and abundances of H2O in the terrestrial planets, Moon, and asteroids. *Earth and Planetary Science Letters*, 526:115771.

McKee, C. F. and Ostriker, E. C. (2007). Theory of Star Formation. *Annual Review of Astronomy and Astrophysics*, 45(Volume 45, 2007):565–687. Publisher: Annual Reviews.

McKinney, W. (2010). Data Structures for Statistical Computing in Python. In *Proceedings of the 9th Python in Science Conference*, pages 56–61, Austin, Texas.

McSween, H. Y., Mittlefehldt, D. W., Beck, A. W., Mayne, R. G., and McCoy, T. J. (2012). HED Meteorites and Their Relationship to the Geology of Vesta and the Dawn Mission. In Russell, C. and Raymond, C., editors, *The Dawn Mission to Minor Planets 4 Vesta and 1 Ceres*, pages 141–174. Springer, New York, NY.

Mei, S., Bai, W., Hiraga, T., and Kohlstedt, D. L. (2002). Influence of melt on the creep behavior of olivine–basalt aggregates under hydrous conditions. *Earth and Planetary Science Letters*, 201(3):491–507.

Merk, R., Breuer, D., and Spohn, T. (2002). Numerical Modeling of 26Al-Induced Radioactive Melting of Asteroids Considering Accretion. *Icarus*, 159(1):183–191.

Michaut, C. and Neufeld, J. A. (2022). Formation of the Lunar Primary Crust From a Long-Lived Slushy Magma Ocean. *Geophysical Research Letters*, 49(2):e2021GL095408.

Mittelholz, A. and Johnson, C. L. (2022). The Martian Crustal Magnetic Field. *Frontiers in Astronomy and Space Sciences*, 9.

Mittelholz, A., Johnson, C. L., Feinberg, J. M., Langlais, B., and Phillips, R. J. (2020). Timing of the martian dynamo: New constraints for a core field 4.5 and 3.7 Ga ago. *Science Advances*, 6(18):eaba0513. Publisher: American Association for the Advancement of Science.

Mittelholz, A., Johnson, C. L., and Morschhauser, A. (2018). A New Magnetic Field Activity Proxy for Mars From MAVEN Data. *Geophysical Research Letters*, 45(12):5899–5907.

Mittlefehldt, D. W. (2007). 1.11 - Achondrites. In Holland, H. D. and Turekian, K. K., editors, *Treatise on Geochemistry*, pages 1–40. Pergamon, Oxford.

Miyazaki, Y. and Korenaga, J. (2022). Inefficient Water Degassing Inhibits Ocean Formation on Rocky Planets: An Insight from Self-Consistent Mantle Degassing Models. *Astrobiology*, 22(6):713–734. Publisher: Mary Ann Liebert, Inc., publishers.

Monnereau, M., Guignard, J., Néri, A., Toplis, M. J., and Quitté, G. (2023). Differentiation time scales of small rocky bodies. *Icarus*, 390:115294.

Monteux, J., Golabek, G. J., Rubie, D. C., Tobie, G., and Young, E. D. (2018). Water and the Interior Structure of Terrestrial Planets and Icy Bodies. *Space Science Reviews*, 214(1):39.

Moore, W. B. and Webb, A. A. G. (2013). Heat-pipe Earth. *Nature 2013 501:7468*, 501(7468):501–505. Publisher: Nature Publishing Group.

Morard, G., Bouchet, J., Rivoldini, A., Antonangeli, D., Roberge, M., Boulard, E., Denoeud, A., and Mezouar, M. (2018). Liquid properties in the Fe-FeS system under moderate pressure: Tool box to model small planetary cores:. *American Mineralogist*, 103(11):1770–1779. Publisher: De Gruyter.

Morbidelli, A., Baillié, K., Batygin, K., Charnoz, S., Guillot, T., Rubie, D. C., and Kleine, T. (2022). Contemporary formation of early Solar System planetesimals at two distinct radial locations. *Nature Astronomy*, 6(1):72–79. Publisher: Nature Publishing Group.

Morbidelli, A., Kleine, T., and Nimmo, F. (2025). Did the terrestrial planets of the solar system form by pebble accretion? *Earth and Planetary Science Letters*, 650:119120.

Morschhauser, A., Grott, M., and Breuer, D. (2011). Crustal recycling, mantle dehydration, and the thermal evolution of Mars. *Icarus*, 212(2):541–558.

Moskovitz, N. and Gaidos, E. (2011). Differentiation of planetesimals and the thermal consequences of melt migration. *Meteoritics & Planetary Science*, 46(6):903–918.

Murphy Quinlan, M., Walker, A. M., and Davies, C. J. (2023). Reconciling fast and slow cooling during planetary formation as recorded in the main group pallasites. *Earth and Planetary Science Letters*, 618:118284.

Murphy Quinlan, M., Walker, A. M., Davies, C. J., Mound, J. E., Müller, T., and Harvey, J. (2021). The Conductive Cooling of Planetesimals With Temperature-Dependent Properties. *Journal of Geophysical Research: Planets*, 126(4):e2020JE006726.

Muxworthy, A. R., Bland, P. A., Davison, T. M., Moore, J., Collins, G. S., and Ciesla, F. J. (2017). Evidence for an impact-induced magnetic fabric in Allende, and exogenous alternatives to the core dynamo theory for Allende magnetization. *Meteoritics & Planetary Science*, 52(10):2132–2146.

Nakamura, T., Matsumoto, M., Amano, K., Enokido, Y., Zolensky, M. E., Mikouchi, T., Genda, H., Tanaka, S., Zolotov, M. Y., Kurosawa, K., Wakita, S., Hyodo, R., Nagano, H., Nakashima, D., Takahashi, Y., Fujioka, Y., Kikuiri, M., Kagawa, E., Matsuoka, M., Brearley, A. J., Tsuchiyama, A., Uesugi, M., Matsuno, J., Kimura, Y., Sato, M., Milliken, R. E., Tatsumi, E., Sugita, S., Hiroi, T., Kitazato, K., Brownlee, D., Joswiak, D. J., Takahashi, M., Ninomiya, K., Takahashi, T., Osawa, T., Terada, K., Brenker, F. E., Tkalcec, B. J., Vincze, L., Brunetto, R., Aléon-Toppani, A., Chan, Q. H. S., Roskosz, M., Viennet, J.-C., Beck, P., Alp, E. E., Michikami, T., Nagaashi, Y., Tsuji, T., Ino, Y., Martinez, J., Han, J., Dolocan, A., Bodnar, R. J., Tanaka, M., Yoshida, H., Sugiyama, K., King, A. J., Fukushi, K., Suga, H., Yamashita, S., Kawai, T., Inoue, K., Nakato, A., Noguchi, T., Vilas, F., Hendrix, A. R., Jaramillo-Correa, C., Domingue, D. L., Dominguez, G., Gainsforth, Z., Engrand, C., Duprat, J., Russell, S. S., Bonato, E., Ma, C., Kawamoto, T., Wada, T., Watanabe, S., Endo, R., Enju, S., Riu, L., Rubino, S., Tack, P., Takeshita, S., Takeichi, Y., Takeuchi, A., Takigawa, A., Takir, D., Tanigaki, T., Taniguchi, A., Tsukamoto, K., Yagi, T., Yamada, S., Yamamoto, K., Yamashita, Y., Yasutake, M., Uesugi, K., Umegaki, I., Chiu, I., Ishizaki, T., Okumura, S., Palomba, E., Pilorget, C., Potin, S. M., Alasli, A., Anada, S., Araki, Y., Sakatani, N., Schultz, C., Sekizawa, O., Sitzman, S. D., Sugiura, K., Sun, M., Dartois, E., De Pauw, E., Dionnet, Z., Djouadi, Z., Falkenberg, G., Fujita, R., Fukuma, T., Gearba, I. R., Hagiya, K., Hu, M. Y., Kato, T., Kawamura, T., Kimura, M., Kubo, M. K., Langenhorst, F., Lantz, C., Lavina, B., Lindner, M., Zhao, J., Vekemans, B., Baklouti, D., Bazi, B., Borondics, F., Nagasawa, S., Nishiyama, G., Nitta, K., Mathurin, J., Matsumoto, T., Mitsukawa, I., Miura, H., Miyake, A., Miyake, Y., Yurimoto, H., Okazaki, R., Yabuta, H., Naraoka, H., Sakamoto, K., Tachibana, S., Connolly, H. C., Lauretta, D. S., Yoshitake, M., Yoshikawa, M., Yoshikawa, K., Yoshihara, K., Yokota, Y., Yogata, K., Yano, H., Yamamoto, Y., Yamamoto, D., Yamada, M., Yamada, T., Yada, T., Wada, K., Usui, T., Tsukizaki, R., Terui, F., Takeuchi, H., Takei, Y., Iwamae, A., Soejima, H., Shirai, K., Shimaki, Y., Senshu, H., Sawada, H., Saiki, T., Ozaki, M., Ono, G., Okada, T., Ogawa, N., Ogawa, K., Noguchi, R., Noda, H., Nishimura, M., Namiki, N., Nakazawa, S., Morota, T., Miyazaki, A., Miura, A., Mimasu, Y., Matsumoto, K., Kumagai, K., Kouyama, T., Kikuchi, S., Kawahara, K., Kameda, S., Iwata, T., Ishihara, Y., Ishiguro, M., Ikeda, H., Hosoda, S., Honda, R., Honda, C., Hitomi, Y., Hirata, N., Hirata, N., Hayashi, T., Hayakawa, M., Hatakeda, K., Furuya, S., Fukai, R., Fujii, A., Cho, Y., Arakawa, M., Abe, M., Watanabe, S., and Tsuda, Y. (2022). Formation and evolution of carbonaceous asteroid Ryugu: Direct evidence from returned samples. *Science*, 0(0):eabn8671. Publisher: American Association for the Advancement of Science.

Nakamura, T., Noguchi, T., Tanaka, M., Zolensky, M. E., Kimura, M., Tsuchiyama, A., Nakato, A., Ogami, T., Ishida, H., Uesugi, M., Yada, T., Shirai, K., Fujimura, A., Okazaki, R., Sandford, S. A., Ishibashi, Y., Abe, M., Okada, T., Ueno, M., Mukai, T., Yoshikawa, M., and Kawaguchi, J. (2011). Itokawa Dust Particles: A Direct Link Between S-Type Asteroids and Ordinary Chondrites. *Science*, 333(6046):1113–1116. Publisher: American Association for the Advancement of Science.

Nanne, J. A. M., Nimmo, F., Cuzzi, J. N., and Kleine, T. (2019). Origin of the non-carbonaceous–carbonaceous meteorite dichotomy. *Earth and Planetary Science Letters*, 511:44–54.

Néri, A., Guignard, J., Monnereau, M., Bystricky, M., Perrillat, J.-P., Andrault, D., King, A., Guignot, N., Tenailleau, C., Duployer, B., Toplis, M. J., and Quitté, G. (2020). Reevaluation of metal interconnectivity in a partially molten silicate matrix using 3D microtomography. *Physics of the Earth and Planetary Interiors*, 308:106571.

Néri, A., Monnereau, M., Guignard, J., Bystricky, M., Tenailleau, C., Duployer, B., Toplis, M. J., and Quitté, G. (2021). Textural evolution of metallic phases in a convecting magma ocean: A 3D microtomography study. *Physics of the Earth and Planetary Interiors*, 319:106771.

Neufeld, J. A., Bryson, J. F., and Nimmo, F. (2019). The Top-Down Solidification of Iron Asteroids Driving Dynamo Evolution. *Journal of Geophysical Research: Planets*, 124(5):1331–1356. Publisher: John Wiley & Sons, Ltd.

Neumann, W., Breuer, D., and Spohn, T. (2012). Differentiation and core formation in accreting planetesimals. *Astronomy & Astrophysics*, 543:A141. Publisher: EDP Sciences.

Neumann, W., Breuer, D., and Spohn, T. (2014). Differentiation of Vesta: Implications for a shallow magma ocean. *Earth and Planetary Science Letters*, 395:267–280. Publisher: Elsevier.

Neumann, W., Henke, S., Breuer, D., Gail, H.-P., Schwarz, W. H., Trieloff, M., Hopp, J., and Spohn, T. (2018). Modeling the evolution of the parent body of acapulcoites and lodranites: A case study for partially differentiated asteroids. *Icarus*, 311:146–169.

Neumann, W., Luther, R., Trieloff, M., Reger, P. M., and Bouvier, A. (2023). Fitting Thermal Evolution Models to the Chronological Record of Erg Chech 002 and Modeling the Ejection Conditions of the Meteorite. *The Planetary Science Journal*, 4(10):196. Publisher: IOP Publishing.

Neumann, W., Ma, N., Bouvier, A., and Trieloff, M. (2024). Recurrent planetesimal formation in an outer part of the early solar system. *Scientific Reports*, 14(1):14017. Publisher: Nature Publishing Group.

Newcombe, M. E., Nielsen, S. G., Peterson, L. D., Wang, J., Alexander, C. M. O., Sarafian, A. R., Shimizu, K., Nittler, L. R., and Irving, A. J. (2023). Degassing of early-formed planetesimals restricted water delivery to Earth. *Nature*, 615(7954):854–857. Number: 7954 Publisher: Nature Publishing Group.

Ni, P., Shahar, A., Badro, J., Yang, J., Bi, W., Zhao, J., Hu, M. Y., and Alp, E. E. (2022). Planet Size Controls Fe Isotope Fractionation Between Mantle and Core. *Geophysical Research Letters*, 49(20):e2022GL098451.

Nichols, C. I., Bryson, J. F., Cottrell, R. D., Fu, R. R., Harrison, R. J., Herrero-Albillos, J., Kronast, F., Tarduno, J. A., and Weiss, B. P. (2021). A Time-Resolved Paleomagnetic Record of Main Group Pallasites: Evidence for a Large-Cored, Thin-Mantled Parent Body. *Journal of Geophysical Research: Planets*, 126(7):e2021JE006900. Publisher: John Wiley & Sons, Ltd ISBN: 10.1029/2021.

Nichols, C. I., Bryson, J. F., Herrero-Albillos, J., Kronast, F., Nimmo, F., and Harrison, R. J. (2016). Pallasite paleomagnetism: Quiescence of a core dynamo. *Earth and Planetary Science Letters*, 441:103–112. Publisher: Elsevier.

Nichols, C. I. O., Krakow, R., Herrero-Albillos, J., Kronast, F., Northwood-Smith, G., and Harrison, R. J. (2018). Microstructural and paleomagnetic insight into the cooling history of the IAB parent body. *Geochimica et Cosmochimica Acta*, 229:1–19.

Nimmo, F. (2007). Energetics of the Core. In *Treatise on geophysics*, volume 8, pages 33–62. Elsevier, Amsterdam ; Boston, 1st ed edition.

Nimmo, F. (2009). Energetics of asteroid dynamos and the role of compositional convection. *Geophysical Research Letters*, 36(10). Publisher: John Wiley & Sons, Ltd.

Nimmo, F., Kleine, T., Morbidelli, A., and Nesvorny, D. (2024). Mechanisms and timing of carbonaceous chondrite delivery to the Earth. *Earth and Planetary Science Letters*, 648:119112.

Nimmo, F. and Stevenson, D. J. (2000). Influence of early plate tectonics on the thermal evolution and magnetic field of Mars. *Journal of Geophysical Research: Planets*, 105(E5):11969–11979.

Noack, L. and Breuer, D. (2013). First- and second-order Frank-Kamenetskii approximation applied to temperature-, pressure- and stress-dependent rheology. *Geophysical Journal International*, 195(1):27–46.

O'Brien, T., Tarduno, J. A., Anand, A., Smirnov, A. V., Blackman, E. G., Carroll-Nellenback, J., and Krot, A. N. (2020). Arrival and magnetization of carbonaceous chondrites in the asteroid belt before 4562 million years ago. *Communications Earth & Environment*, 1(1):1–7. Publisher: Nature Publishing Group.

Opeil, C. P., Consolmagno, G. J., and Britt, D. T. (2010). The thermal conductivity of meteorites: New measurements and analysis. *Icarus*, 208(1):449–454.

Oran, R., Weiss, B. P., and Cohen, O. (2018). Were chondrites magnetized by the early solar wind? *Earth and Planetary Science Letters*, 492:222–231.

O'Rourke, J. G. and Stevenson, D. J. (2016). Powering Earth's dynamo with magnesium precipitation from the core. *Nature*, 529(7586):387–389.

Pallas (1778). *Reise durch verschiedene Provinzen des russischen Reichs in einem ausfuehrlichen Auszuge*. J.G. Fleischer.

Peterson, L. D., Newcombe, M. E., Alexander, C. M. O., Wang, J., Klein, F., Bekaert, D. V., and Nielsen, S. G. (2023). The H content of aubrites: An evaluation of bulk versus in situ methods for quantifying water in meteorites. *Earth and Planetary Science Letters*, 620:118341.

Piralla, M., Villeneuve, J., Schnuriger, N., Bekaert, D. V., and Marrocchi, Y. (2023). A unified chronology of dust formation in the early solar system. *Icarus*, 394:115427.

Poirier, J.-P. (1994). Light elements in the Earth's outer core: A critical review. *Physics of the Earth and Planetary Interiors*, 85(3):319–337.

Pommier, A., Davies, C. J., and Zhang, R. (2020). A Joint Experimental-Modeling Investigation of the Effect of Light Elements on Dynamos in Small Planets and Moons. *Journal of Geophysical Research: Planets*, 125(8):e2020JE006492.

Pommier, A., Leinenweber, K., and Tasaka, M. (2015). Experimental investigation of the electrical behavior of olivine during partial melting under pressure and application to the lunar mantle. *Earth and Planetary Science Letters*, 425:242–255.

Pozzo, M., Davies, C., Gubbins, D., and Alfè, D. (2013). Transport properties for liquid silicon-oxygen-iron mixtures at Earth's core conditions. *Physical Review B*, 87(1):014110. Publisher: American Physical Society.

Rayman, M. D. (2022). Dawn at Ceres: The first exploration of the first dwarf planet discovered. *Acta Astronautica*, 194:334–352.

Raymond, C. A., Russell, C. T., and McSween, H. Y. (2017). Dawn at Vesta: Paradigms and Paradoxes. In Weiss, B. P. and Elkins-Tanton, L. T., editors, *Planetesimals: Early Differentiation and Consequences for Planets*, Cambridge Planetary Science, pages 321–339. Cambridge University Press, Cambridge.

Rider-Stokes, B. G., Stephant, A., Anand, M., Franchi, I. A., Zhao, X., White, L. F., Yamaguchi, A., Greenwood, R. C., and Jackson, S. L. (2024). Evidence against water delivery by impacts within 10 million years of planetesimal formation. *Earth and Planetary Science Letters*, 642:118860.

Rider-Stokes, B. G., Zhao, X., Jackson, S. L., Suttle, M. D., Franchi, I. A., White, L. F., Greenwood, R. C., Whitehouse, M. J., Riches, L., Anand, M., Hoefnagels, B., and Grady, M. M. (2025). Rapid protoplanet formation in the outer Solar System recorded in a dunite from the carbonaceous chondrite reservoir. *Communications Earth & Environment*, 6(1):524. Publisher: Nature Publishing Group.

Rubie, D. C., Jacobson, S. A., Morbidelli, A., O'Brien, D. P., Young, E. D., de Vries, J., Nimmo, F., Palme, H., and Frost, D. J. (2015). Accretion and differentiation of the terrestrial planets with implications for the compositions of early-formed Solar System bodies and accretion of water. *Icarus*, 248:89–108.

Rubin, A. E. (2018). Carbonaceous and noncarbonaceous iron meteorites: Differences in chemical, physical, and collective properties. *Meteoritics & Planetary Science*, 53(11):2357–2371.

Rückriemen, T., Breuer, D., and Spohn, T. (2015). The Fe snow regime in Ganymede's core: A deep-seated dynamo below a stable snow zone. *Journal of Geophysical Research: Planets*, 120(6):1095–1118. Publisher: John Wiley & Sons, Ltd.

Rückriemen, T., Breuer, D., and Spohn, T. (2018). Top-down freezing in a Fe–FeS core and Ganymede's present-day magnetic field. *Icarus*, 307:172–196.

Ruedas, T. (2017). Radioactive heat production of six geologically important nuclides. *Geochemistry, Geophysics, Geosystems*, 18(9):3530–3541.

Rushmer, T., Minarik, W. G., and Taylor, G. J. (2000). Physical Processes of Core Formation. In Canup, R. M. and Righter, K., editors, *Origin of the Earth and Moon*, pages 227–244. University of Arizona Press.

Russell, C. T., Raymond, C. A., Ammannito, E., Buczkowski, D. L., De Sanctis, M. C., Hiesinger, H., Jaumann, R., Konopliv, A. S., McSween, H. Y., Nathues, A., Park, R. S., Pieters, C. M., Prettyman, T. H., McCord, T. B., McFadden, L. A., Mottola, S., Zuber, M. T., Joy, S. P., Polanskey, C., Rayman, M. D., Castillo-Rogez, J. C., Chi, P. J., Combe, J. P., Ermakov, A., Fu, R. R., Hoffmann, M., Jia, Y. D., King, S. D., Lawrence, D. J., Li, J.-Y., Marchi, S., Preusker, F., Roatsch, T., Ruesch, O., Schenk, P., Villarreal, M. N., and Yamashita, N. (2016). Dawn arrives at Ceres: Exploration of a small, volatile-rich world. *Science*, 353(6303):1008–1010. Publisher: American Association for the Advancement of Science.

Ruzicka, A. (2014). Silicate-bearing iron meteorites and their implications for the evolution of asteroidal parent bodies. *Geochemistry*, 74(1):3–48.

Sahijpal, S., Soni, P., and Gupta, G. (2007). Numerical simulations of the differentiation of accreting planetesimals with 26Al and 60Fe as the heat sources. *Meteoritics & Planetary Science*, 42(9):1529–1548.

Samuel, H. and Tackley, P. J. (2008). Dynamics of core formation and equilibration by negative diapirism. *Geochemistry, Geophysics, Geosystems*, 9(6).

Sanborn, M. E., Wimpenny, J., Williams, C. D., Yamakawa, A., Amelin, Y., Irving, A. J., and Yin, Q.-Z. (2019). Carbonaceous achondrites Northwest Africa 6704/6693: Milestones for early Solar System chronology and genealogy. *Geochimica et Cosmochimica Acta*, 245:577–596.

Sanderson, H. (2024). A refined, versatile model for planetesimal thermal evolution and dynamo generation, doi: 10.5281/zenodo.12771396.

Sandu, C. and Kiefer, W. S. (2012). Degassing history of Mars and the lifespan of its magnetic dynamo. *Geophysical Research Letters*, 39(3).

Scheinberg, A., Elkins-Tanton, L. T., Schubert, G., and Bercovici, D. (2016). Core solidification and dynamo evolution in a mantle-stripped planetesimal. *Journal of Geophysical Research: Planets*, 121(1):2–20. Publisher: John Wiley & Sons, Ltd.

Scheinberg, A. L., Soderlund, K. M., and Elkins-Tanton, L. T. (2018). A basal magma ocean dynamo to explain the early lunar magnetic field. *Earth and Planetary Science Letters*, 492:144–151.

Schubert, G. and Soderlund, K. M. (2011). Planetary magnetic fields: Observations and models. *Physics of the Earth and Planetary Interiors*, 187(3):92–108.

Schubert, G., Turcotte, D. L., and Olson, P. (2001). *Mantle Convection in the Earth and Planets*. Cambridge University Press, Cambridge, United Kingdom.

Schwaiger, T., Gastine, T., and Aubert, J. (2021). Relating force balances and flow length scales in geodynamo simulations. *Geophysical Journal International*, 224(3):1890–1904.

Scott, E. R. D. (1977a). Formation of olivine-metal textures in pallasite meteorites. *Geochimica et Cosmochimica Acta*, 41(6):693–710.

Scott, E. R. D. (1977b). Pallasites—metal composition, classification and relationships with iron meteorites. *Geochimica et Cosmochimica Acta*, 41(3):349–360.

Scott, E. R. D. (2020). Iron Meteorites: Composition, Age, and Origin. In *Oxford Research Encyclopedia of Planetary Science*. Oxford University Press.

Scott, T. and Kohlstedt, D. L. (2006). The effect of large melt fraction on the deformation behavior of peridotite. *Earth and Planetary Science Letters*, 246(3-4):177–187.

Shah, J., Bates, H. C., Muxworthy, A. R., Hezel, D. C., Russell, S. S., and Genge, M. J. (2017). Long-lived magnetism on chondrite parent bodies. *Earth and Planetary Science Letters*, 475:106–118.

Shepard, M. K., Richardson, J., Taylor, P. A., Rodriguez-Ford, L. A., Conrad, A., de Pater, I., Adamkovics, M., de Kleer, K., Males, J. R., Morzinski, K. M., Close, L. M., Kaasalainen, M., Viikinkoski, M., Timerson, B., Reddy, V., Magri, C., Nolan, M. C., Howell, E. S., Benner, L. A. M., Giorgini, J. D., Warner, B. D., and Harris, A. W. (2017). Radar observations and shape model of asteroid 16 Psyche. *Icarus*, 281:388–403.

Soderlund, K. M., Stanley, S., Cao, H., Calkins, M. A., and Browning, M. K. (2025). Puzzles in Planetary Dynamos: Implications for Planetary Interiors. *Annual Review of Earth and Planetary Sciences*. Publisher: Annual Reviews.

Solomatov, V. S. (1995). Scaling of temperature-and stress-dependent viscosity convection. *Physics of Fluids*, 7:266.

Spitzer, F., Burkhardt, C., Kruijer, T. S., and Kleine, T. (2025). Comparison of the earliest NC and CC planetesimals: Evidence from ungrouped iron meteorites. *Geochimica et Cosmochimica Acta*, 397:134–148.

Spitzer, F., Burkhardt, C., Nimmo, F., and Kleine, T. (2021). Nucleosynthetic Pt isotope anomalies and the Hf-W chronology of core formation in inner and outer solar system planetesimals. *Earth and Planetary Science Letters*, 576:117211.

Spohn, T. (1991). Mantle differentiation and thermal evolution of Mars, Mercury, and Venus. *Icarus*, 90(2):222–236.

Stanley, S. (2016). Planetary dynamos: updates and new frontiers. In Schrijver, C. J., Bagenal, F., and Sojka, J. J., editors, *Heliophysics*, pages 126–146. Cambridge University Press, Cambridge.

Sterenborg, M. G. and Crowley, J. W. (2012). Thermal evolution of early solar system planetesimals and the possibility of sustained dynamos. *Physics of the Earth and Planetary Interiors*.

Stevenson, D. J. (2003). Planetary magnetic fields. *Earth and Planetary Science Letters*, 208(1):1–11.

Stevenson, D. J. (2010). Planetary Magnetic Fields: Achievements and Prospects. *Space Science Reviews*, 152:651–664.

Stixrude, L., Scipioni, R., and Desjarlais, M. P. (2020). A silicate dynamo in the early Earth. *Nature Communications*, 11(1):935. Publisher: Nature Publishing Group.

Sturtz, C., Limare, A., Chaussidon, M., and Kaminski, É. (2022a). Structure of differentiated planetesimals: A chondritic fridge on top of a magma ocean. *Icarus*, 385:115100.

Sturtz, C., Limare, A., Tait, S., and Kaminski, É. (2022b). Birth and Decline of Magma Oceans in Planetesimals: 2. Structure and Thermal History of Early Accreted Small Planetary Bodies. *Journal of Geophysical Research: Planets*, 127(12):e2021JE007020.

Suttle, M. D., King, A. J., Schofield, P. F., Bates, H., and Russell, S. S. (2021). The aqueous alteration of CM chondrites, a review. *Geochimica et Cosmochimica Acta*, 299:219–256.

Tachibana, S., Sawada, H., Okazaki, R., Takano, Y., Sakamoto, K., Miura, Y. N., Okamoto, C., Yano, H., Yamanouchi, S., Michel, P., Zhang, Y., Schwartz, S., Thuillet, F., Yurimoto, H., Nakamura, T., Noguchi, T., Yabuta, H., Naraoka, H., Tsuchiyama, A., Imae, N., Kurosawa, K., Nakamura, A. M., Ogawa, K., Sugita, S., Morota, T., Honda, R., Kameda, S., Tatsumi, E., Cho, Y., Yoshioka, K., Yokota, Y., Hayakawa, M., Matsuoka, M., Sakatani, N., Yamada, M., Kouyama, T., Suzuki, H., Honda, C., Yoshimitsu, T., Kubota, T., Demura, H., Yada, T., Nishimura, M., Yogata, K., Nakato, A., Yoshitake, M., Suzuki, A. I., Furuya, S., Hatakeda, K., Miyazaki, A., Kumagai, K., Okada, T., Abe, M., Usui, T., Ireland, T. R., Fujimoto, M., Yamada, T., Arakawa, M., Connolly, H. C., Fujii, A., Hasegawa, S., Hirata, N., Hirata, N., Hirose, C., Hosoda, S., Iijima, Y., Ikeda, H., Ishiguro, M., Ishihara, Y., Iwata, T., Kikuchi, S., Kitazato, K., Lauretta, D. S., Libourel, G., Marty, B., Matsumoto, K., Michikami, T., Mimasu, Y., Miura, A., Mori, O., Nakamura-Messenger, K., Namiki, N., Nguyen, A. N., Nittler, L. R., Noda, H., Noguchi, R., Ogawa, N., Ono, G., Ozaki, M., Senshu, H., Shimada, T., Shimaki, Y., Shirai, K., Soldini, S., Takahashi, T., Takei, Y., Takeuchi, H., Tsukizaki, R., Wada, K., Yamamoto, Y., Yoshikawa, K., Yumoto, K., Zolensky, M. E., Nakazawa, S., Terui, F., Tanaka, S., Saiki, T., Yoshikawa, M., Watanabe, S., and Tsuda, Y. (2022). Pebbles and sand on asteroid (162173) Ryugu: In situ observation and particles returned to Earth. *Science*, 375(6584):1011–1016. Publisher: American Association for the Advancement of Science.

Tang, H. and Dauphas, N. (2012). Abundance, distribution, and origin of 60Fe in the solar protoplanetary disk. *Earth and Planetary Science Letters*, 359-360:248–263.

Tarduno, J. A., Cottrell, R. D., Nimmo, F., Hopkins, J., Voronov, J., Erickson, A., Blackman, E., Scott, E. R., and McKinley, R. (2012). Evidence for a Dynamo in the Main Group Pallasite Parent Body. *Science*, 338(6109):939–942. Publisher: American Association for the Advancement of Science.

Tarduno, J. A., O'Brien, T. M., Blackman, E. G., and Smirnov, A. V. (2017). Magnetization of CV Meteorites in the Absence of a Parent Body Core Dynamo. In *48th Annual Lunar and Planetary Science Conference*, page 2850.

Tassin, T., Gastine, T., and Fournier, A. (2021). Geomagnetic semblance and dipolar–multipolar transition in top-heavy double-diffusive geodynamo models. *Geophysical Journal International*, 226(3):1897–1919.

Tauxe, L. (2010). *Essentials of paleomagnetism.* University of California press, Berkeley.

Telus, M., Huss, G. R., Ogliore, R. C., Nagashima, K., and Tachibana, S. (2012). Recalculation of data for short-lived radionuclide systems using less-biased ratio estimation. *Meteoritics & Planetary Science*, 47(12):2013–2030.

Thiriet, M., Breuer, D., Michaut, C., and Plesa, A.-C. (2019). Scaling laws of convection for cooling planets in a stagnant lid regime. *Physics of the Earth and Planetary Interiors*, 286:138–153.

Tissot, F. L. H., Collinet, M., Namur, O., and Grove, T. L. (2022). The case for the angrite parent body as the archetypal first-generation planetesimal: Large, reduced and Mg-enriched. *Geochimica et Cosmochimica Acta*, 338:278–301.

Tosi, N., Grott, M., Plesa, A.-C., and Breuer, D. (2013). Thermochemical evolution of Mercury's interior. *Journal of Geophysical Research: Planets*, 118(12):2474–2487.

Trinh, K. T., Bierson, C. J., and O'Rourke, J. G. (2023). Slow evolution of Europa's interior: metamorphic ocean origin, delayed metallic core formation, and limited seafloor volcanism. *Science Advances*, 9(24):eadf3955. Publisher: American Association for the Advancement of Science.

Udry, A., Howarth, G. H., Herd, C. D. K., Day, J. M. D., Lapen, T. J., and Filiberto, J. (2020). What Martian Meteorites Reveal About the Interior and Surface of Mars. *Journal of Geophysical Research: Planets*, 125(12):e2020JE006523.

Ulff-Møller, F. (1998). Effects of liquid immiscibility on trace element fractionation in magmatic iron meteorites: A case study of group IIIAB. *Meteoritics & Planetary Science*, 33(2):207–220.

Vernazza, P. and Beck, P. (2017). Composition of Solar System Small Bodies. In Weiss, B. P. and Elkins-Tanton, L. T., editors, *Planetesimals: Early Differentiation and Consequences for Planets*, Cambridge Planetary Science, pages 269–297. Cambridge University Press, Cambridge.

Virtanen, P., Gommers, R., Oliphant, T. E., Haberland, M., Reddy, T., Cournapeau, D., Burovski, E., Peterson, P., Weckesser, W., Bright, J., Van Der Walt, S. J., Brett, M., Wilson, J., Millman, K. J., Mayorov, N., Nelson, A. R. J., Jones, E., Kern, R., Larson, E., Carey, C. J., Polat, İ., Feng, Y., Moore, E. W., VanderPlas, J., Laxalde, D., Perktold, J., Cimrman, R., Henriksen, I., Quintero, E. A., Harris, C. R., Archibald, A. M., Ribeiro, A. H., Pedregosa, F., Van Mulbregt, P., SciPy 1.0 Contributors, Vijaykumar, A., Bardelli, A. P., Rothberg, A., Hilboll, A., Kloeckner, A., Scopatz, A., Lee, A., Rokem, A., Woods, C. N., Fulton, C., Masson, C., Häggström, C., Fitzgerald, C., Nicholson, D. A., Hagen, D. R., Pasechnik, D. V., Olivetti, E., Martin, E., Wieser, E., Silva, F., Lenders, F., Wilhelm, F., Young, G., Price, G. A., Ingold, G.-L., Allen, G. E., Lee, G. R., Audren, H., Probst, I., Dietrich, J. P., Silterra, J., Webber, J. T., Slavič, J., Nothman, J., Buchner, J., Kulick, J., Schönberger, J. L., De Miranda Cardoso, J. V., Reimer, J., Harrington, J., Rodríguez, J. L. C., Nunez-Iglesias, J., Kuczynski, J., Tritz, K., Thoma, M., Newville, M., Kümmerer, M., Bolingbroke, M., Tartre, M., Pak, M., Smith, N. J., Nowaczyk, N., Shebanov, N., Pavlyk, O., Brodtkorb, P. A., Lee, P., McGibbon, R. T., Feldbauer, R., Lewis, S., Tygier, S., Sievert, S., Vigna, S., Peterson, S., More, S., Pudlik, T., Oshima, T., Pingel, T. J., Robitaille, T. P., Spura, T., Jones, T. R., Cera, T., Leslie, T., Zito, T., Krauss, T., Upadhyay, U., Halchenko, Y. O., and Vázquez-Baeza, Y. (2020). SciPy 1.0: fundamental algorithms for scientific computing in Python. *Nature Methods*, 17(3):261–272.

Walte, N. P. and Golabek, G. J. (2022). Olivine aggregates reveal a complex collisional history of the main group pallasite parent body. *Meteoritics & Planetary Science*, 57(5):1098–1115.

Walte, N. P., Howard, C. M., and Golabek, G. J. (2023). Mantle fragmentation and incomplete core merging of colliding planetesimals as evidenced by pallasites. *Earth and Planetary Science Letters*, 617:118247.

Walte, N. P., Solferino, G. F. D., Golabek, G. J., Silva Souza, D., and Bouvier, A. (2020). Two-stage formation of pallasites and the evolution of their parent bodies revealed by deformation experiments. *Earth and Planetary Science Letters*, 546:116419.

Wang, H., Weiss, B. P., Bai, X.-N., Downey, B. G., Wang, J., Wang, J., Suavet, C., Fu, R. R., and Zucolotto, M. E. (2017). Lifetime of the solar nebula constrained by meteorite paleomagnetism. *Science*, 355(6325):623–627. Publisher: American Association for the Advancement of Science.

Wardle, M. (2007). Magnetic fields in protoplanetary disks. *Astrophysics and Space Science*, 311(1):35–45.

Warren, P. H. (2011). Stable-isotopic anomalies and the accretionary assemblage of the Earth and Mars: A subordinate role for carbonaceous chondrites. *Earth and Planetary Science Letters*, 311(1):93–100.

Waskom, M. (2021). seaborn: statistical data visualization. *Journal of Open Source Software*, 6(60):3021.

Wasson, J. T. (1967). The chemical classification of iron meteorites: I. A study of iron meteorites with low concentrations of gallium and germanium. *Geochimica et Cosmochimica Acta*, 31(2):161–180.

Wasson, J. T. and Choi, B.-G. (2003). Main-group pallasites: chemical composition, relationship to IIIAB irons, and origin. *Geochimica et Cosmochimica Acta*, 67(16):3079–3096.

Weidenschilling, S. J. (2019). Accretion of the asteroids: Implications for their thermal evolution. *Meteoritics & Planetary Science*, 54(5):1115–1132.

Weisberg, M. K. and Kimura, M. (2012). The unequilibrated enstatite chondrites. *Geochemistry*, 72(2):101–115.

Weiss, B. P., Bai, X.-N., and Fu, R. R. (2021). History of the solar nebula from meteorite paleomagnetism. *Science Advances*, 7(1):eaba5967. Publisher: American Association for the Advancement of Science.

Weiss, B. P. and Elkins-Tanton, L. T. (2013). Differentiated Planetesimals and the Parent Bodies of Chondrites. *Annual Review of Earth and Planetary Sciences*, 41(1):529–560.

Weiss, B. P., Gattacceca, J., Stanley, S., Rochette, P., and Christensen, U. R. (2010). Paleomagnetic Records of Meteorites and Early Planetesimal Differentiation. *Space Science Reviews*, 152(1):341–390.

Weiss, B. P. and Tikoo, S. M. (2014). The lunar dynamo. *Science*, 346(6214). Publisher: American Association for the Advancement of Science.

Weiss, B. P., Wang, H., Sharp, T. G., Gattacceca, J., Shuster, D. L., Downey, B., Hu, J., Fu, R. R., Kuan, A. T., Suavet, C., Irving, A. J., Wang, J., and Wang, J. (2017). A nonmagnetic differentiated early planetary body. *Earth and Planetary Science Letters*, 468:119–132.

Wieczorek, M., Weiss, B., Breuer, D., Cébron, D., Fuller, M., Garrick-Bethell, I., Gattacceca, J., Halekas, J., Hemingway, D., Hood, L., Wieczorek, M. A., Weiss, B. P., Halekas, J. S., Hemingway, D. J., Hood, L. L., Laneuville, M., Nimmo, F., Oran, R., Purucker, M. E., Rückriemen, T., Soderlund, K. M., and Tikoo, S. M. (2022). Lunar magnetism. *HAL Open Science*.

Williams, J. P. and Cieza, L. A. (2011). Protoplanetary Disks and Their Evolution. *Annual Review of Astronomy and Astrophysics*, 49(Volume 49, 2011):67–117. Publisher: Annual Reviews.

Williams, Q. (2009). Bottom-up versus top-down solidification of the cores of small solar system bodies: Constraints on paradoxical cores. *Earth and Planetary Science Letters*, 284(3-4):564–569. Publisher: Elsevier.

Williams, Q. (2025). A note on the direction of core solidification in asteroids, the iron melting curve, and phase equilibria parameterizations. *Icarus*, 427:116381.

Wilson, L., Goodrich, C. A., and Van Orman, J. A. (2008). Thermal evolution and physics of melt extraction on the ureilite parent body. *Geochimica et Cosmochimica Acta*, 72(24):6154–6176.

Windmill, R. J., Franchi, I. A., Hellmann, J. L., Schneider, J. M., Spitzer, F., Kleine, T., Greenwood, R. C., and Anand, M. (2022). Isotopic evidence for pallasite formation by impact mixing of olivine and metal during the first 10 million years of the Solar System. *PNAS Nexus*, 1(1):pgac015.

Yang, J. and Goldstein, J. I. (2005). The formation of the Widmanstätten structure in meteorites. *Meteoritics & Planetary Science*, 40(2):239–253.

Yang, J., Goldstein, J. I., and Scott, E. R. D. (2007). Iron meteorite evidence for early formation and catastrophic disruption of protoplanets. *Nature*, 446(7138):888–891. Publisher: Nature Publishing Group.

Yang, J., Goldstein, J. I., and Scott, E. R. D. (2010). Main-group pallasites: Thermal history, relationship to IIIAB irons, and origin. *Geochimica et Cosmochimica Acta*, 74(15):4471–4492.

Yang, L. and Ciesla, F. J. (2012). The effects of disk building on the distributions of refractory materials in the solar nebula. *Meteoritics & Planetary Science*, 47(1):99–119.

Yomogida, K. and Matsui, T. (1984). Multiple parent bodies of ordinary chondrites. *Earth and Planetary Science Letters*, 68(1):34–42.

Zhang, B., Chabot, N. L., and Rubin, A. E. (2022). Compositions of carbonaceous-type asteroidal cores in the early solar system. *Science Advances*, 8(37):eabo5781. Publisher: American Association for the Advancement of Science.

Zhang, B., Chabot, N. L., and Rubin, A. E. (2024). Compositions of iron-meteorite parent bodies constrain the structure of the protoplanetary disk. *Proceedings of the National Academy of Sciences*, 121(23):e2306995121. Publisher: Proceedings of the National Academy of Sciences.

Zhao, Y. H., Zimmerman, M. E., and Kohlstedt, D. L. (2009). Effect of iron content on the creep behavior of olivine: 1. Anhydrous conditions. *Earth and Planetary Science Letters*, 287(1-2):229–240.

Zhao, Y. H., Zimmerman, M. E., and Kohlstedt, D. L. (2018). Effect of iron content on the creep behavior of Olivine: 2. Hydrous conditions. *Physics of the Earth and Planetary Interiors*, 278:26–33. Publisher: Elsevier.